Faculté des Sciences, Département de Physique

Thèse de doctorat

Présentée et soutenue publiquement par

Pierre Nickmilder

Pour obtention du grade de docteur en Science

Spécialité : Science des matériaux

Elaboration and Characterization of Hybrid Ferroelectric Nanocomposites using Advanced Scanning Probe Microscopy and Spectroscopy

Soutenue le 16 février 2026

Jury

Prof. Philippe Leclère, Université de Mons	**Promoteur**
Prof. Michel Voué, Université de Mons	**Président**
Prof. Stephanos Konstantinidis, Université de Mons	**Secrétaire**
Prof. Brice Gautier, INL/INSA Lyon	**Membre**
Prof. Isabelle Royaud, Université de Lorraine	**Membre**

Année Universitaire 2025 – 2026

Abstract

Ferroelectric and piezoelectric devices have seen a steady expansion in low-power electronic applications over recent years. However, their development increasingly relies on complex and heterogeneous material systems, for which reliable nanoscale characterization of electromechanical behaviour remains a major challenge. In particular, understanding how geometry, surface roughness, and multiphase interfaces influence the interpretation of Piezoresponse Force Microscopy (PFM) measurements is essential.

In this work, PVDF–TrFE/$BiFeO_3$ (BFO) thin film nanocomposites were selected as a model system and were elaborated by spin coating, enabling the production of uniform films compatible with SPM-based characterisation. BFO nanoparticles synthesised via a sol–gel route were embedded either in a conductive PEDOT:PSS matrix or directly within the ferroelectric polymer matrix.

A combination of structural, mechanical, and electrical characterisation techniques confirmed the phase purity, morphology, and electrical integrity of the samples. Conventional PFM revealed well-defined ferroelectric domains in PVDF–TrFE but proved unreliable for BFO containing composites due to strong mechanical heterogeneity and pronounced surface roughness. Advanced PFM approaches, including dual-frequency resonance tracking (DFRT-PFM), switching-spectroscopy (ssPFM) combined with clustering analysis, and DataCube-PFM, were therefore exploited to improve measurement stability and to discriminate genuine ferroelectric responses from artefactual signals.

Switching-spectroscopy measurements demonstrated robust and reproducible ferroelectric switching in PVDF–TrFE, whereas BFO nanoparticles exhibited highly heterogeneous and environment-dependent behaviour. DataCube-PFM enabled spatially resolved reconstruction of apparent surface displacement while simultaneously accessing local mechanical properties.

Overall, this work establishes a robust methodological framework for a more reliable interpretation of PFM data in complex ferroelectric nanocomposite systems.

Keywords

Ferroelectric hybrid Material, SPM, PFT, C-AFM, PFM, DFRT-PFM, ssPFM, Datacube PFM, Electrostatic forces, Mechanical heterogeneity

IA declaration

I, Pierre Nickmilder I declare that I used AI software while writing this manuscript as a tool for rephrasing and spell checking.

Acknowledgement

Me voici à conclure l'écriture de cette thèse par, paradoxalement, la section qui sera la première (et pour beaucoup la seule !) que l'on lira. L'écriture de ce manuscrit n'est pas seulement l'aboutissement de quatre années de thèse, mais bien de près de dix ans (une décennie, rien que ça !) passés au sein de l'Université de Mons. Au cours de cette période, j'ai eu la chance de faire de nombreuses rencontres, avec des personnes issues d'horizons très différents, dont les échanges et la bienveillance ont contribué à faire de moi la personne que je suis aujourd'hui. La section qui suit se veut un hommage à toutes ces rencontres.

Comme le veut l'usage, mes premiers remerciements vont à mon promoteur. Philippe, je te remercie pour toutes les opportunités que tu m'as offertes. De mon mémoire à cette thèse, du CMN à la création du LPNE, en passant par les différents déménagements qui ont suivi, quelques appareils endommagés (je plaide coupable pour la balance), une production parfois en dents de scie et des embûches impromptues, nous voilà enfin au bout. Merci sincèrement pour ta confiance et ces opportunités. Je remercie également le Fonds de la Recherche Scientifique (FRS-FNRS) pour le financement de ce projet (PDR PiezoFlexoTronics).

Restons au LPNE, où il est de bon augure de remercier l'ensemble des membres actuels, en commençant par l'autre dernier membre encore présent depuis la construction du laboratoire : Joséphine, dont la démarche, bien que pas toujours assurée, l'a menée à réaliser une quantité impressionnante de travail. Je tiens à te remercier, la plus sicilienne des Belges, pour l'aide précieuse que tu m'as apportée au cours de toutes ces années de collaboration. Poursuivons les remerciements en Méditerranée, avec un Catalan égaré à Mons. Sergio, voilà un an que tu as rejoint le labo, et tu en es déjà devenu un rouage essentiel. Merci pour tous les efforts fournis pour m'aider, ainsi que pour nos nombreuses discussions passionnantes, tantôt scientifiques, tantôt orientées jeux vidéo. Gaudiu de la vostra estada a Mons ! Les remerciements suivants ne nous emmèneront pas bien loin, puisqu'ils s'adressent à un Marocain. Ismail, tu as repris la lourde tâche d'assistant, mais ta persévérance et ta rigueur me laissent convaincu que tu la mèneras à bien. أتمنى لك الشجاعة والسعادة في السنوات القادمة. On peut enfin s'éloigner de la Méditerranée pour remercier le dernier membre du laboratoire, Dingrui. Man, I hope you keep enjoying your stay in Mons and that you will continue trying to learn a few words of French!

En plus des membres encore présents, je souhaite remercier toutes celles et ceux qui sont passés par le LPNE, et le moins que l'on puisse dire, c'est que la liste est longue : Quynh, qui apportait toujours sa bonne humeur au labo (et des gâteaux maison à tomber par terre), Stéphane, dont l'inventivité frôlait parfois la folie, Dang, dont l'aplomb n'avait d'égal que la motivation, Thomas et son obsession marquée pour les échecs, Eva, qui a survécu à l'explosion de la boîte à Gand (j'exagère à peine), Pierre Bayart, que je surnommais PB (ce qui était un peu ridicule, car j'étais le seul à utiliser ce surnom pour

distinguer les Pierre du labo), François, dont les talents en programmation m'ont sauvé plus d'une fois, Romain et ses simulations qui mettait à genoux l'ordinateur du labo, Martin et sa débrouillardise remarquable…

Cette liste déjà longue est complétée par une pléthore de stagiaires : Emeline 1, Adrien, Elliot, Romain, Emeline 2, Mathis, Mael, Nelson, Myriam, Killian, Romain, Hugo, Fabian, Antonin, Leriche, Julien, Elias, Sahad, Alex, Valérian, Brick… À vous toutes et tous (et à ceux que j'ai sûrement oubliés), merci pour ces excellents moments passés ensemble.

La section suivante s'adresse aux personnes qui ont fait de ces neuf années à l'UMons quelques-uns des plus beaux souvenirs de ma vie. Je parle bien entendu de la bande à Pierrot ! Lorsque j'ai commencé mon parcours universitaire, j'ai eu la chance de rencontrer des personnages plus hauts en couleur les uns que les autres : Louis, l'homme d'initiative, à l'origine de notre projet de kot commun et de bien d'autres événements que nous avons organisés ; David, le fou des pâtes carbonara, dont les précédents remerciements de thèse m'ont mis une certaine pression ; Barnabé, à jamais indissociable, dans nos esprits, du Choukas et du ricard ; Quentin, qui, je l'espère, utilise encore régulièrement la voiture électrique que je lui ai offerte ; Amandine, dite « la chérie », qui, je l'espère, n'utilise plus le pull du concert de Rammstein suite à un malencontreux accident impliquant des métalleux alcoolisés ; Nathan, dont la langue bien pendue ferait de lui un syndicaliste hors pair, et son inséparable Clara, que je surnommais « l'incruste » à l'époque de la colocation (même si elle était techniquement plus présente que certains de nos colocataires) ; Thomas, le dernier arrivé, dont l'humour gras parvient même à surpasser le mien ! Ensemble nous avons vécu temps d'aventure (La côte belge, Rome et le magnifique Two Ducks, la ducasse d'Ath, le Doudou, …) que je ne pourrais certainement pas leurs rendre justice en si peu de mot. N'oublions pas non plus de rendre hommage au temple de ce groupe : la Taverne 44, où le goût légendaire des frites est inversement proportionnel à l'empressement des serveurs. À vous tous, mes amis, merci pour tous ces moments formidables partagés au cours de ces neuf années.

Enfin, je souhaite conclure ces remerciements en m'adressant aux personnes à qui je dois le plus : mes parents. Papa, je sais que mon caractère n'a pas toujours été facile à supporter, surtout mes tendances défaitistes, mais je te remercie de m'avoir appris à me dépasser et à toujours continuer sans jamais rien lâcher. Maman, même si ces dernières années ont été extrêmement éprouvantes, je suis heureux que tu puisses lire ces mots et voir l'aboutissement de mes études. Le parcours n'a pas été facile, mais en voici la fin. Merci papa et maman d'avoir toujours été là pour moi. Je vous aime.

Scientific activity during the PhD

Attended conferences

1. **P. Nickmilder**, H. Valloire, L. Borowik, and Ph. Leclère. "Study of the electromechanical properties of hybrid piezoelectric nanocomposite materials." **Oral presentation** done at Belgian Polymer Group, Houffalize, Belgium, 26 June 2025.

2. **P. Nickmilder**, H. Valloire, L. Borowik, and Ph. Leclère. "Etude des propriétés électromécaniques de matériaux nanocomposites hybrides piezoélectriques." **Oral presentation** done at Forum de Microscopie à sonde locale, Spa, Belgium, 02 April 2025.

3. **P. Nickmilder**, I. Ben Khaled, and P.h Leclère. "On the characterization of electromechanical organic-inorganic hybrid active materials." **Poster session** presented at 2024 EDT MAIN/NanoWal PhD Scientific Day, Louvain-la-Neuve, Belgium, 31 October 2024.

4. **P. Nickmilder**. "On the electromechanical properties of hybrid piezoelectric nanocomposites by Scanning Probe Microscopy." **Oral presentation** done at Workshop Eunice, Catania, Italy, 06 July 2024.

5. **P. Nickmilder** and Ph. Leclère. "Caractérisation des propriétés électromécaniques de nanocomposites hybrides ferroélectriques." **Poster session** presented at Forum des Microscopies à Sonde Locale 2024, Ecully, France, 22 April 2024.

6. **P. Nickmilder**, E. Schmidt, A. Edoire, M.-H. Chambrier, A. Da Costa, A. Ferri, R. Desfeux, and Ph. Leclère. "Exploring the Nanoscale Ferroelectric Properties of Lead-free Lanthanide Oxide Thin Films for Energy Applications." **Poster session** presented at Mardi des Chercheurs 2024, Mons, Belgium, 26 March 2024.

7. **P. Nickmilder**. "On the nanoscale mechanical and viscoelastic properties of high Impact polymer composites." **Oral presentation** done at Complexurf, Bruxelles, Belgium, 01 February 2024.

8. **P. Nickmilder**, E. Schmidt, M. Lefèbre, M.-H. Chambrier, A. Da Costa, A. Ferri, R. Desfeux, and Ph. Leclère. "On the electro-mechanical Property Characterization of piezoelectric inorganic and hybrid material for energy harvesting systems." **Poster session** presented at MRS Fall Meeting 2023, Boston, USA, 28 November 2023.

9. **P. Nickmilder**, J. Mathurin, A. Dazzi, and Ph. Leclère. "Study of the mechanical, viscoelastic, and chemical properties of polymer blend-based thin films by dynamic atomic force microscopy." **Poster session** presented at First EUNICE Workshop for Multi-Functional Materials : From Synthesis to Applications, Lille, France, 27 June 2023.

10. **P. Nickmilder**, Ph. Leclère, Yang Lanti, and T. De Muijlder. "Study of the mechanical and viscoelastic properties of complex heterogeneous polymeric systems at the nanoscale and automated population identification." **Oral presentation** done at Forum des microscopies à sonde locale, Obernai, France, 07 April 2023.

11. **P. Nickmilder**, Ph. Leclère, J. Mathurin, and A. Dazzi. "Study of the mechanical, viscoelastic, and chemical properties of polymer blendbased thin films by dynamic atomic force microscopy." **Poster session** presented at EDT-MAIN PhD Scientific Day / NanoWal annual meeting, Namur, Belgium, 31 January 2023.

Publication during the thesis

Published

1. A. Dazzi, J. Mathurin, Ph. Leclère, **P. Nickmilder**, P. De Wolf, M. Wagner, Q. Hu, A. Deniset-Besseau, Photothermal AFM-IR Depth Sensitivity: An Original Pathway to Tomographic Reconstruction, Anal. Chem. 96 (**2024**) 17931–17940. *https://doi.org/10.1021/acs.analchem.4c01969*.

2. M. Petrov, D. Canena, N. Kulachenkov, N. Kumar, **P. Nickmilder**, Ph. Leclère, I. Sokolov, Mechanical spectroscopy of materials using atomic force microscopy (AFM-MS), Materials Today 80 (2024) 218–225. *https://doi.org/10.1016/j.mattod.2024.08.021*.

3. G. Seychal, **P. Nickmilder**, V. Lemaur, C. Ocando, B. Grignard, Ph. Leclère, C. Detrembleur, R. Lazzaroni, H. Sardon, N. Aranburu, J.-M. Raquez, A novel approach to design structural natural fiber composites from sustainable CO 2 -derived polyhydroxyurethane thermosets with outstanding properties and circular features, Composites Part A: Applied Science and Manufacturing 185 (**2024**) 108311. *https://doi.org/10.1016/j.compositesa.2024.108311*.

4. L. Yang, **P. Nickmilder**, H. Verhoogt, T. Hoeks, Ph. Leclère, Probing Viscoelastic Properties and Interfaces in High-Density Polyethylene Vitrimers at the Nanoscale Using Dynamic Mode Atomic Force Microscopy, ACS Appl. Mater. Interfaces 16 (**2024**) 38501–38510. *https://doi.org/10.1021/acsami.4c06809*.

5. D. Siniscalco, L. Pessoni, L. Billon, A. Boussonnière, A.-S. Castanet, J.-F. Bardeau, **P. Nickmilder**, Ph. Leclère, N. Delorme, Measurement of the Transition Temperature Governing the Photoinduced Reversible Solid-to-Liquid Transition of Azobenzene-Containing Polymers, ACS Appl. Polym. Mater. 5 (**2023**) 7358–7363. *https://doi.org/10.1021/acsapm.3c01256*.

6. J. Zveny, A. Remy, **P. Nickmilder**, A. Delchambre, A. Nonclercq, Ph. Leclère, F. Reniers, Evaluating Cold Atmospheric Plasma for Endoscope Decontamination: Feasibility and Impact Analysis on PTFE Surfaces, Plasma Med (**2024**). *https://doi.org/10.1615/PlasmaMed.2024054997*.

Submitted

1. J. Rojas, C. Collange, V. Phan, **P. Nickmilder**, Ph. Leclère, P. De Wolf, M. Wagner, A. Deniset-Besseau, J. Mathurin, A. Dazzi, Frequency sweep force volume operating mode: a mechanical artifact free AFM-IR technique. **Submitted** to Journal of Applied Physics (JAP).

2. **P. Nickmilder**, S. Gonzalez-Casal, Ph. Leclère, Distinguishing nanoscale electromechanical properties in hybrid ferroelectric systems: insights from Bismuth Ferrite and PVDF-TrFE flexible nanocomposites. **Submitted** to ACS Omega.

Abbreviations

AFM – Atomic Force Microscopy
AM – Amplitude Modulation
BFO – Bismuth Ferrite Oxide ($BiFeO_3$)
BTO – Barium Titanate ($BaTiO_3$)
C-AFM – Conductive Atomic Force Microscopy
CR-PFM – Contact Resonance Piezoresponse Force Microscopy
DC – Direct Current
DFRT – Dual-Frequency Resonance Tracking
DFRT-PFM – Dual-Frequency Resonance Tracking Piezoresponse Force Microscopy
DMA – Dynamic Mechanical Analysis
DMT – Derjaguin–Muller–Toporov (contact mechanics model)
ESEM – Environmental Scanning Electron Microscopy
ESBS – Electrostatic Blind Spot
FM – Frequency Modulation
ITO – Indium Tin Oxide
JKR – Johnson–Kendall–Roberts (contact mechanics model)
KPFM – Kelvin Probe Force Microscopy
LDOS – Local Density of States
LPFM – Lateral Piezoresponse Force Microscopy
OBD – Optical Beam Deflection
PEDOT:PSS – Poly(3,4-ethylenedioxythiophene):poly(styrenesulfonate)
PFM – Piezoresponse Force Microscopy
PF-PFM – PeakForce Piezoresponse Force Microscopy
PFT – PeakForce Tapping
PZT – Lead Zirconate Titanate
PVDF – Poly(vinylidene fluoride)
PVDF–TrFE – Poly(vinylidene fluoride-co-trifluoroethylene)
SEM – Scanning Electron Microscopy
SHO – Simple Harmonic Oscillator
SPM – Scanning Probe Microscopy
ssPFM – Switching Spectroscopy Piezoresponse Force Microscopy
STM – Scanning Tunnelling Microscopy
VPFM – Vertical Piezoresponse Force Microscopy
XRD – X-Ray Diffraction
ZnO – Zinc Oxide

Chapter 1: Introduction

1.1 Piezoelectric effect for energy harvesting and electronics

The recent years have been highlighted by an energy crisis always more pressing, emphasizing the urgent need to shift towards alternative energy sources. Traditional fossil fuels and their negative environmental impacts have raised major concerns, triggering the development of cleaner and more sustainable energy options such as thermal, wind and solar energy (**Figure 1**) [1]. In parallel, technological advancements in electronic device miniaturization and energy-efficient technologies have led to the creation of low-power systems, operating with minimal energy consumption. For this reason, mechanical energy harvesting, based on renewable vibrational energy, has emerged as a promising low-power sensor networks and wearable electronics [2,3].

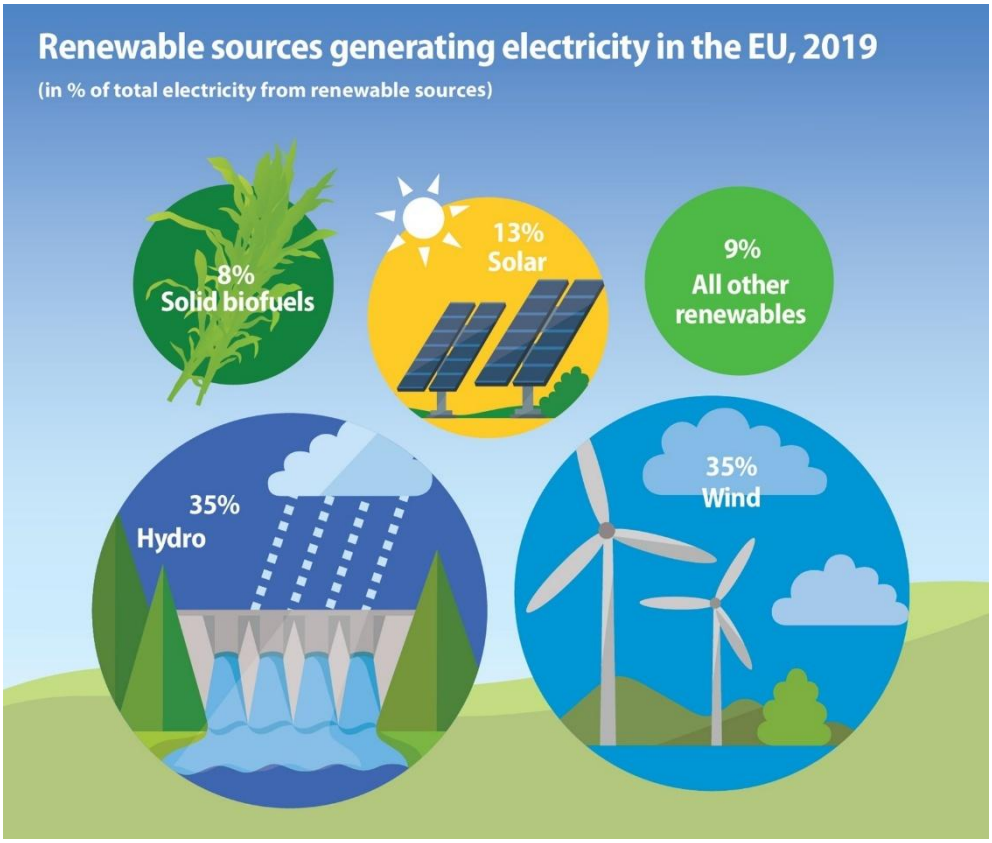

***Figure 1** : Repartition of electricity production of the different renewable sources in the EU, 2019. Figure adapted from [4].*

Piezoelectric devices can be used to transform the vibrational mechanical energy, ubiquitous in our environment, into electrical energy through the direct piezoelectric effect. Consequently, piezoelectric materials have garnered significant interest in recent years for the creation of piezoelectric harvester [5]. Due to their straightforward design offering high power density and scalability [6,7], they are easily integrated within sensors and other electronic devices. For instance, flexible piezoelectric devices have

demonstrated power densities sufficient to drive low-power electronics, highlighting their relevance in emerging technologies (**Figure 2**) [8].

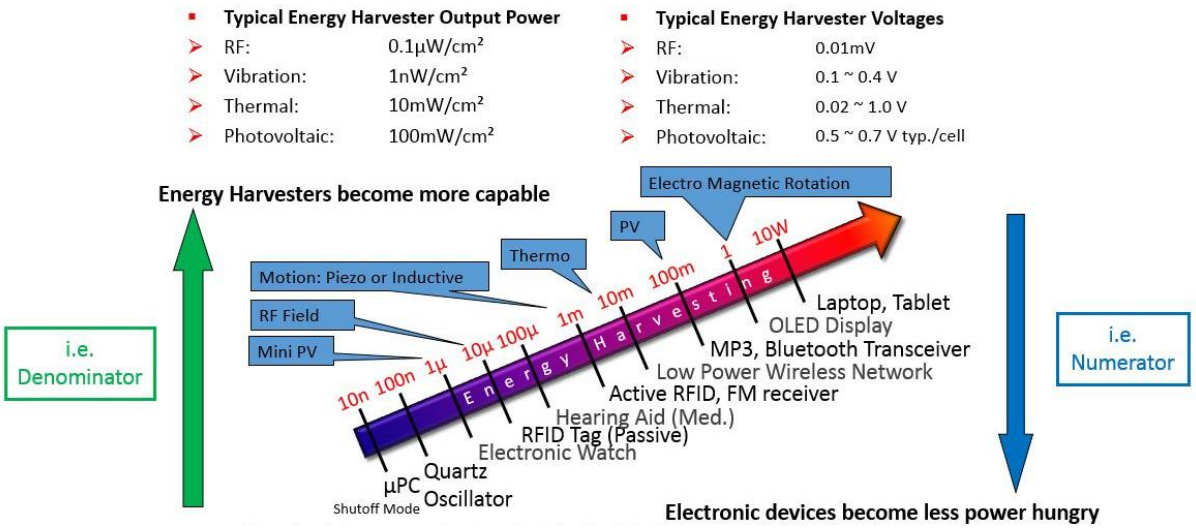

***Figure 2** : Power consumption as a function of the size of the electronic device.*

Despite these advances, challenges remain in optimizing piezoelectric materials and device architectures to enhance energy conversion efficiency and mechanical flexibility [9]. The specific problem addressed is the need for lead-free, environmentally friendly alternative piezoelectric materials compared to the current commonly used ones, with improved performance and integration capabilities for energy harvesting applications [10,11]. A critical knowledge gap exists in understanding the synergistic effects of novel piezoelectric composites, nanostructures, and hybrid energy harvesting systems, as well as in balancing trade-offs between piezoelectric coefficients, mechanical robustness, and device scalability [9,12–15] Controversies persist regarding the relative merits of inorganic versus polymeric piezoelectric materials, with ceramics offering higher piezoelectric coefficients but lower flexibility, and polymers providing mechanical compliance but lower energy conversion efficiency [16]. This gap limits the deployment of piezoelectric harvesters in flexible and wearable electronics, potentially constraining the realization of self-powered systems [6].

The present thesis focuses on the development and characterization of electro-mechanically active nanostructures by combining inorganic ferroelectric nanofillers with an organic matrix of ferroelectric polymer. We concentrate on the analysis of these nanostructures and their *in situ* mechanisms, using local advanced Scanning Probe Microscopy (SPM) and spectroscopy characterization techniques, to evaluate the mechanical and electromechanical performance of that system, offering a global aspect of characterization on nanoscale properties of such hybrid system.

1.2 Electromechanical properties

1.2.1 Dielectric materials

A dielectric material is defined as an electrical insulator that will polarize under the application of an electric field. When such a field is applied, positive charges are displaced in the direction of the field, while negative charges shift in the opposite direction. This charge displacement phenomenon is referred to as polarisation [17].

At the microscopic scale, the separation of opposite charges gives rise to an electric dipole, which constitutes the fundamental microscopic origin of dielectric polarisation. The quantity describing this separation is the electric dipole moment, defined as:

$$\vec{p} = Q * \vec{l}$$

Eq. 1

where $\vec{p}$ is the dipole moment, Q is the magnitude of positive or negative charge and $\vec{l}$ is the vector distance between two charges.

The dipole moment appearing in a solid, during the application of a field $\vec{E}$ is proportional to it. It can be expressed as:

$$\vec{P} = \varepsilon_0 \alpha \vec{E}$$

Eq. 2

Where α is the atomic polarizability and ε_0 is the vacuum permittivity.

At the macroscopic scale, the relevant physical quantity is the polarisation $\vec{\mathrm{P}}$, defined as the dipole moment per unit volume:

$$\vec{\mathrm{P}} = \frac{\mathrm{d}\vec{\mathrm{p}}}{dV}$$

Eq. 3

where $\vec{p}$ represents the individual microscopic dipole moments within a representative volume V.

Every dipole in a dielectric material is like a vector whose direction is along the applied electric field (or from negative to positive charge of a dipole) and dipole density or macroscopic polarisation $\vec{\mathrm{P}}$ (C m^{-2}) is a vector field. Reversing the direction of electric field leads to depolarisation and re-polarisation of dielectric material in opposite direction [18].

There are two types of dielectrics:

- Polar dielectric, containing permanent dipole that can be aligned by an electrical field.

- Non-polar dielectric, not presenting any permanent dipole but can be induced.

Dielectric polarisation in homogeneous materials occurs via four primary mechanisms [19] (**Figure 3**):

- *Electronic polarisation*: The displacement of the centre of the negatively charged electron cloud to their relative nucleus in each atom. This phenomenon is observable in all dielectrics submit to an electric field.
- *Ionic polarisation*: When an ionic crystal material is put under an electrical field, the cation and the anions will be moved to opposite direction. This gives rise to a net dipole moment.
- *Orientation polarisation*: This effect arises only in systems presenting permanent dipole. Those will align to the direction of the applied electric field. (At ambient temperature, they tend to have a static distribution).
- *interfacial space charge polarisation*: It arises from the accumulation of mobile charges at structural surfaces and interfaces. This is not an intrinsic property of material, as it arises from heterostructures and hence is not discussed further here.

All those polarisations can either be reversible or irreversible.

Polarisation involves the alignment of dipoles within the material, which creates an internal electric field that opposes the applied field, thus storing energy [20,21]. The efficiency and capacity of energy storage in dielectrics depend on several factors, including the dielectric constant, breakdown strength, and the material's ability to handle high electric fields without degradation [22].

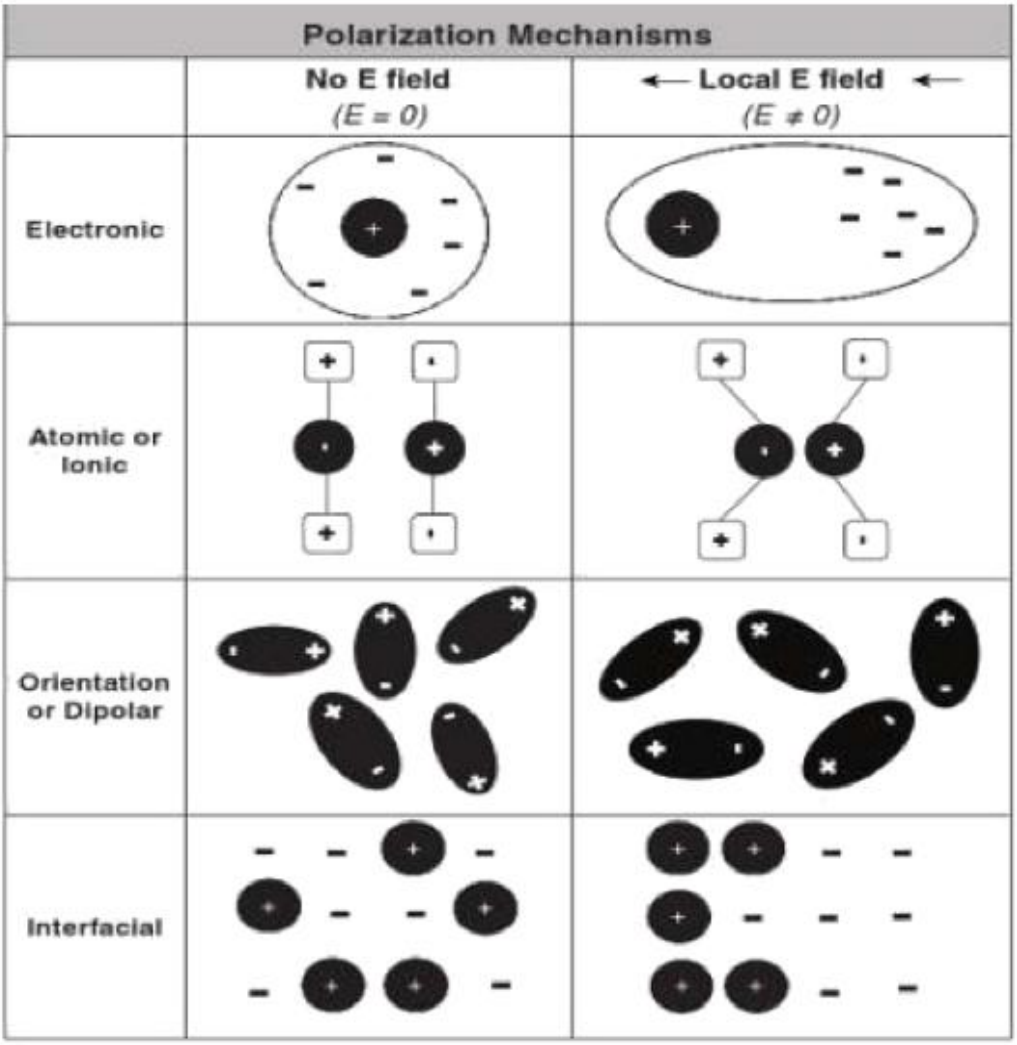

Figure 3 *: Representation of the four types of polarisation mechanisms. Figure adapted from* [23].

1.2.2 Piezoelectricity

A piezoelectric material is a dielectric material not only polarizable by an electrical field but also by a mechanical stress. The discovery of this effect is attributed to the Curie brothers [24], that observed in 1880 that electrical charge was induced in a quartz crystal when pressure was applied. This conversion, from mechanical to electrical energy, is called the direct piezoelectric effect. The opposite effect, the mechanical deformation of an object under an electrical stress, is called the inverse piezoelectric effect and was discovered a year later by Lippman [25].

Piezoelectricity has been found in a wide range of materials ranging from inorganic to organic materials, natural or human made. Piezoelectricity has a different origin depending on the material group. For crystalline structures such in inorganic piezoelectric materials and semicrystalline polymers, this arise from a non-centrosymmetric crystal structure, as illustrated in **Figure 4**: In steady state, piezoelectric materials usually have

their centre of charges that coincide, so they are electrically neutral. When they are put under mechanical stress, there is separation of the mass centre of charges resulting in a dipole moment. This effect is observed on 21 of the 32 crystalline classes, each of them showing a lack of inversion symmetry. On the other hand, piezoelectric effect of organic materials and amorphous polymers arise from the molecular dipole reorientation under electrical or mechanical stress [26]. This polarity arises from the polarity of molecular element originating from the difference of electronegativity between atoms [27].

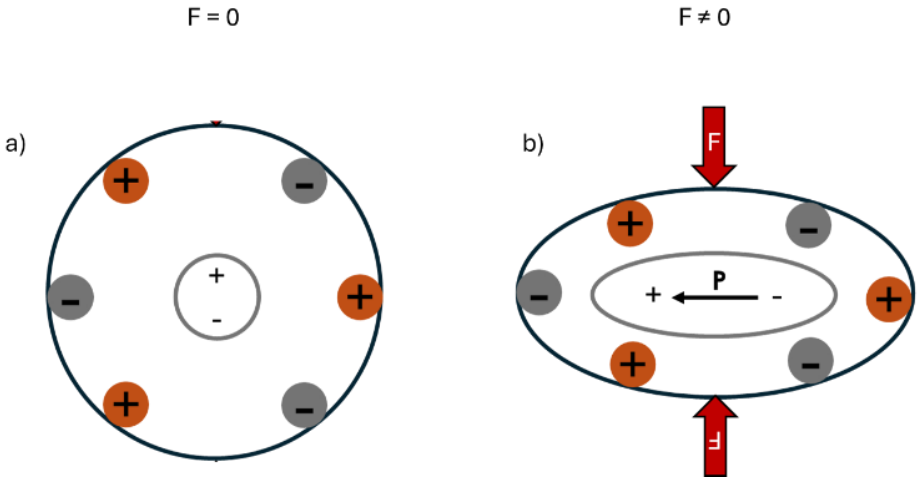

***Figure 4** : Representation of a purely piezoelectric structure. a) At rest, where the mass centres of charges are superposed, and b) Under mechanical stress, where the separation of mass centres of charges induces a polarisation.*

The piezoelectric effect corresponds to the addition of mechanical and dielectric effect. The first can be expressed by the Hooke's law and the second by the dielectric effect [28];

$$D = \varepsilon E$$

Eq. 4

$$S = s\sigma$$

Eq. 5

where D is the displacement tensor of charge density or dielectric displacement (N/V), ε is the dielectric permittivity tensor (N/V^2) and E the applied electric field (V/m).

where S is the strain, s is the compliance (m^2/N) and σ is the stress (N/m^2).

By combining those two fundamental equations, we can extract the two fundamental laws of piezoelectricity:

$$S = [s^E]\{\sigma\} + [d]\{E\}$$

Eq. 6

$$D = [d^t]\{\sigma\} + [\varepsilon^\sigma]\{E\}$$

Eq. 7

where [d] is the direct piezoelectric effect matrix, [d_t] is the matrix which describes the converse piezoelectric effect

It can be simplified as:

$$D_i = d_{ij}\sigma_j + \varepsilon_{ik}E_k$$

Eq. 8

$$S_j = s_{jl}\sigma_l + d_{ji}E_i$$

Eq. 9

In the context of the linear piezoelectric effect, Voigt notation is used to reduce the complete tensor notation to a more compact matrix form. This notation is based on the symmetries of the deformation tensor and is not a general tensor notation.

The piezoelectric coefficient tensor d_{ij} (3 x 6) is the most commonly used when discussing piezoelectric properties of materials (**Figure 5 a**). The first subscript *i* (ranging from 1–3) denotes the direction of the applied electric field (or the applied mechanical stress) while the second subscript *j* denotes the direction of the induced strain (or poling) corresponding to the external stimuli in the direction *i*. Components of d_{ij} for *j* =1→ 3 are considered as 'normal' modes since they couple an electric field to a normal (tensile or compressive) strain and *vice versa*. Components of d_{ij} for *j* = 4 → 6 are shear modes since they relate to shear strains in the material (**Figure 5 b**).

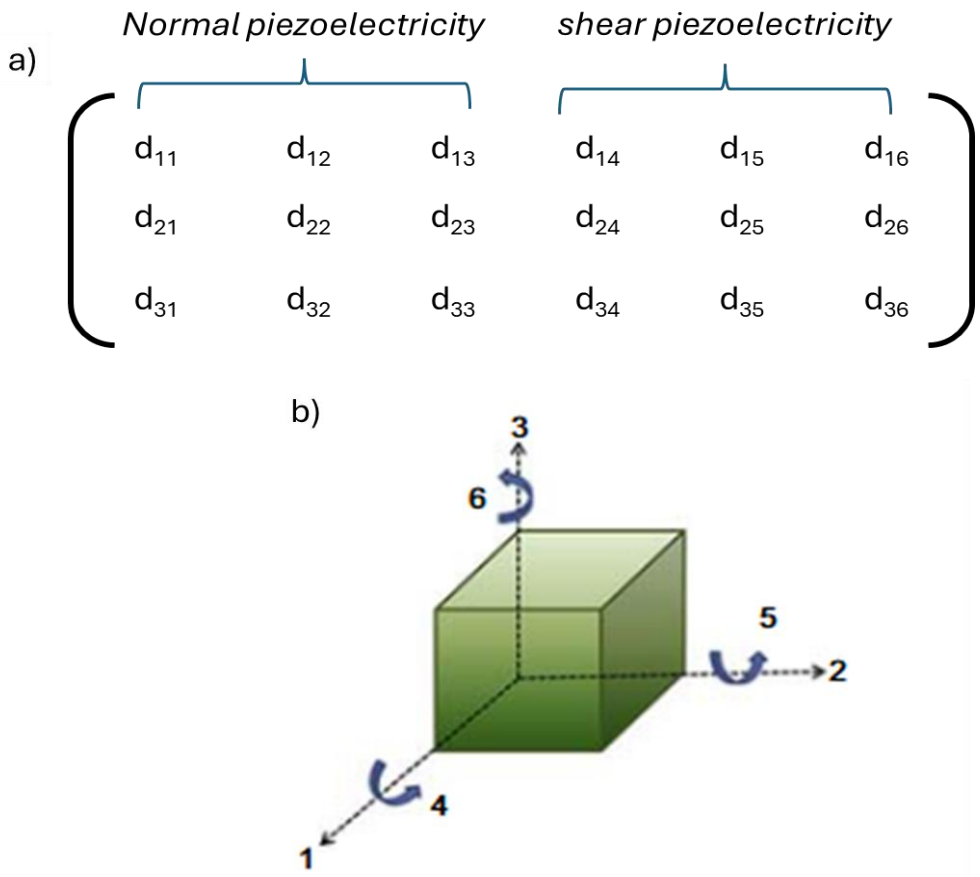

***Figure 5** : (a) Piezoelectric matrix. Figure adapted from* [29]. *(b) Schematic representation of the Voigt notation used to defined piezoelectric coefficient. Figure adapted from* [30].

The tensor nature of the piezoelectric coefficient, that arises from the directionality of the response of the materials has a function of the direction the applied stress, implies that there is different coefficient depending on the orientation of the response to the applied stress. The most commonly considered are the d_{33}, where the deformation is in the direction of the stress and the d_{13}, perpendicular to the stress. d_{ij} is typically expressed in C/N or m/V.

1.2.3 Pyroelectricity

Pyroelectric materials are a sub-class of piezoelectrics that present a spontaneous nonzero macroscopic polarisation in their pristine state [31,32]: there is naturally a separation of the mass center of charges inside the material. when those materials are uniformly heated ($\Delta T \neq 0$), there is a change in their polarisation state, from which charges will develop on the surface, hence the pyroelectric name (**Figure 6**). However, the polarity of the unit cell is sustained only over a certain temperature range (Curie temperature).

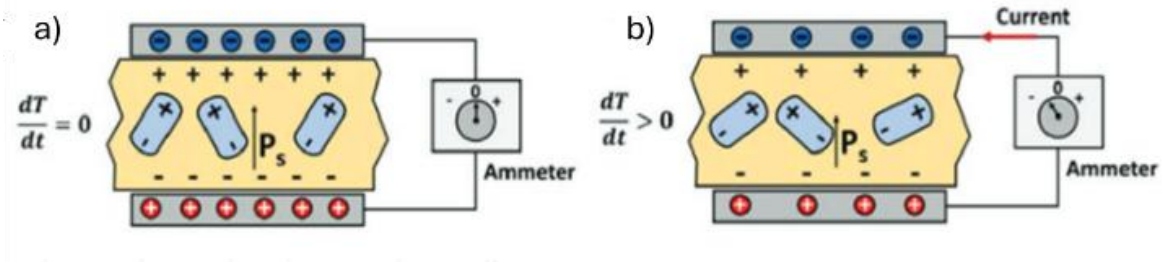

***Figure 6** : Representation of the pyroelectric effect, a) When dT/dt=0, system is at the equilibrium, and b) When dT/dt≠0, modification of the spontaneous polarisation, causing a migration of electron. Figure adapted from* [33].

Pyroelectricity is used in a wide range of application, from energy harvesting to thermal imaging, with the possibility to use it for temperature and light sensor [33].

1.2.4 Ferroelectricity

Ferroelectricity was discovered in 1921 in Rochelle salt by Valasek [34]. Ferroelectric materials are a sub-class of pyroelectric materials which exhibit spontaneous polarisation without assistance of an electric field that can be switched with the application of an electric field [35]. The term ferroelectrics was coined by analogy with ferromagnetic, mainly because ferroelectrics show a hysteretic displacement loop under the electric field that looks like that of magnetization loop of ferromagnetic under magnetic fields.

Ferroelectrics are characterized by their natural switchable spontaneous polarisation, whose direction can be changed by the application of an external electric field. This is illustrated in **Figure 7**. Initially, dipoles in the material are relatively disordinate. At low enough electric field (E_c), ferroelectrics behave just like all other linear dielectrics, exhibiting linear behavior of polarisation (P) in response to the electric field. Once a critical value known as the coercive field (E_{coer}) is reached, the dipoles start to align themselves with the electric field, inducing a net dipole in the material. Polarisation reaches a maximum value at high fields, where the polarisation saturates (P_{sat}). As the field is decreased to zero, the polarisation decreases accordingly but does not go to zero at zero field, since the dipole keeps a preferential orientation. The non-null polarisation at this point is called the remanent polarisation (P_r). When the orientation of the electric field is inverted the same observations can be made.

Ferroelectric materials present a critical temperature after which they lose their ferroelectric properties. The Curie temperature (T_c) corresponds to the transition temperature from ferroelectric to paraelectric, from which materials switch from a non-centrosymmetric structure to a centrosymmetric one, inducing the disappearance of any remanent polarisation and exhibits a dielectric behavior.

The presence of the piezoelectric and pyroelectric properties coupled with the existence of remnant polarisation makes ferroelectric materials prominent materials for a wide application range, energy harvesting, sensor, photovoltaic devices and non-volatile memories [36]

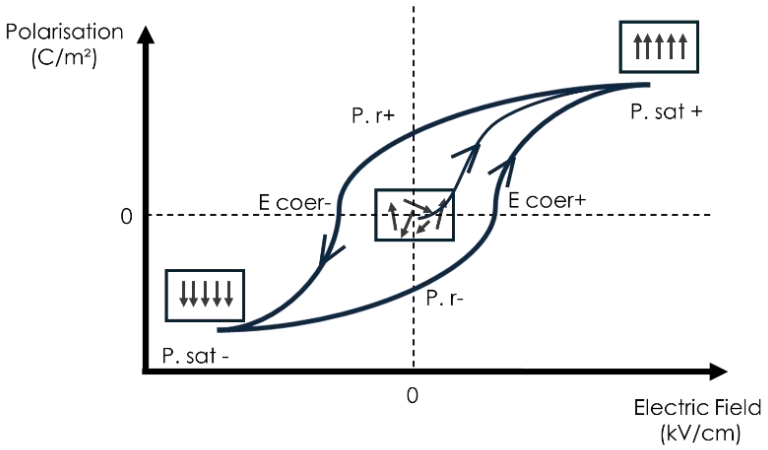

Figure 7 *:Schematic representation of a ferroelectric P-E loop with key parameters and dipole orientation presented.*

From the different polar symmetries and polarisation conditions, a ferroelectric material exhibits not only reversible polarizability but also pyroelectric, piezoelectric and dielectric properties.

To summarise, the relation between all the crystalline structures is presented in **Figure 8**.

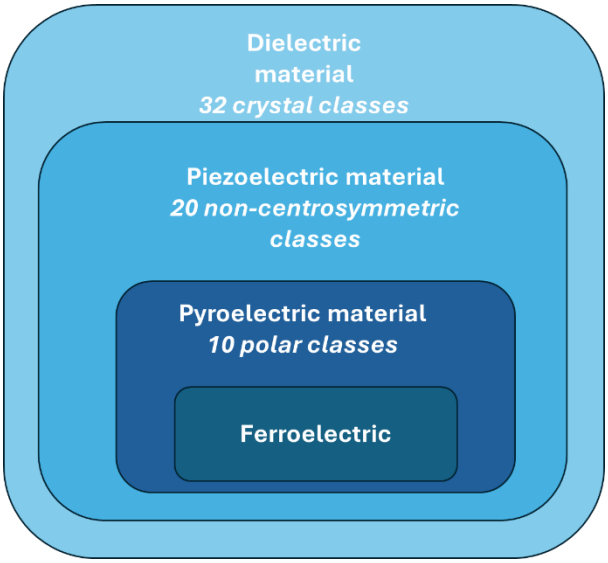

Figure 8 *: Relationship between piezo, pyro and ferroelectric materials. Figure inspired from* [37].

1.2.5 Flexoelectricity

Flexoelectricity, also called the nonlocal piezoelectric effect, is a physical phenomenon in which an electric polarisation is induced in a dielectric material by an strain gradient [38]. Flexoelectricity was first observed in 1964 [39]. Unlike piezoelectricity, which requires a material to lack a centre of symmetry, flexoelectricity can occur in all dielectric materials, including centrosymmetric ones (**Figure 9**). This effect can be expressed as:

$$P_i = \mu_{ijkl} \frac{d\varepsilon_{jk}}{dx_l}$$

Eq. 10

where P_i is the flexoelectric polarisation,μ_{ijkl} the flexoelectric coefficient, ε_{jk} the elastic strain, and x_l the coordinate.

Although it is an universal electromechanical coupling effect, it is typically minimal in bulk materials, resulting in it being considered more as a scientific curiosity than a practical physical property. The rise of nanotechnology and the scale-down of materials, however, renewed scientific interest in flexoelectricity as it became clear that the effect could be significant at small dimensions, opening the path for small energy harvesting and sensing devices [40,41].

Strain gradients, which are typically negligible in bulk material, can be extremely large in nanostructures such as thin films, nanowires, and nanotubes. In these systems, the flexoelectric polarisation can reach magnitudes comparable to or even exceeding those of traditional piezoelectric materials. This effect has been observed in a variety of materials, including perovskite oxides (like $SrTiO_3$ and $BaTiO_3$), polymers, and biological membranes. This effect becomes more important in materials with high dielectric constant (such as ferroelectric one).

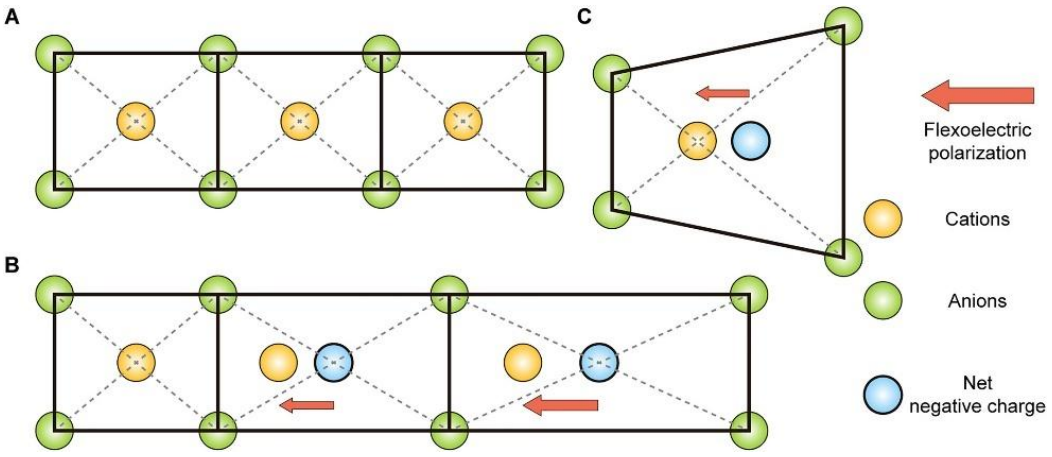

***Figure 9** : Flexoelectric effect in centrosymmetric materials. (A) Unstrained 2D ionic structure with zero net dipole moment. (B) Each unit cell is uniformly stretched by various strains, and the strain gradient generates an uncompensated dipole moment. (C) A net dipole moment produced by an inhomogeneous deformation of a unit cell. Figure adapted from* [42].

1.3 Piezoelectric and ferroelectric materials

As indicated before, the first piezoelectric material ever studied was the quartz by the Curie brothers [24]. One and an half century later, the quantity and diversity of piezoelectric materials has greatly increased, with dozens of piezoelectric materials used for energy harvesting [6,28,43]. They can be classified in 3 main categories in function of their chemical nature (**Table 1**):

- Inorganic: containing both single crystal and ceramic.
- Organic: containing both biomaterials as well as synthetic piezoelectric polymer.
- Hybrid: a combination of the two previous ones.

The choice of a piezoelectric material depends of its intrinsic piezoelectric properties but also the requirements of the targeted application, as well as additional parameters such as design flexibility, operation frequency and available volume.

***Table 1** : Different types of piezoelectric materials*

Chemical nature	Types of Material		Examples	
			Name	**d_{ij} (pC/N)**
Inorganic	Piezoelectric single crystal		quartz Rochelle salt	2.3 (d_{11}) [44] 225 (d_{14}) [45]
	Piezoelectric ceramic	Lead	PZT PMNPt	400 (d_{33}) [46] 600-700 (d_{33}) [47]
		Lead-free	ZnO $BiFeO_3$	6-13 (d_{33}) [48] 20-60 (d_{33}) [49,50]
Organic	Bio-piezoelectric material		wood Silk	0.1-0.3 (d_{11}) [51] -1.5 (d_{14}) [52]
	Piezoelectric polymer		PVDF PLLA	-20 (d33) [46] 10 (d_{14}) [53]
Hybrid	Piezoelectric nanocomposite		PVDF/PZT PVDF-TrFE/BFO	90 [54] 30 [55]

1.3.1 Inorganic piezoelectric materials

Inorganic piezoelectric materials are generally divided into two main categories: piezoelectric crystals and piezoelectric ceramics. Piezoelectric crystals consist of a single, continuous crystal lattice that exhibits piezoelectricity due to its inherent asymmetrical structure. In contrast, piezoelectric ceramics are polycrystalline materials composed of numerous small grains with random orientations. These ceramics only display piezoelectric behaviour after a polarisation process, typically done by applying a strong electric field that aligns the dipole orientations of the crystallites.

The discovery of piezoelectric and ferroelectric effects in natural crystals such as quartz, topaz, or Rochelle salt laid to the foundation for modern understanding of piezoelectricity. Although their piezoelectric coefficients are considerably lower than those of synthetic materials some of them, particularly the quartz (SiO_2), remain widely used in industrial applications like resonators and sensors, due to their natural abundance and usability.

The first piezoelectric ceramic ever observed was barium titanate ($BaTiO_3$, BTO), discovered in 1947 [49]. This finding was revolutionary, as it was the first polycrystalline material that could exhibit permanent piezoelectricity after a poling process. BTO and later developed synthetic ceramics were classified as ferroelectrics. The piezoelectric constant (d_{33}) of ferroelectrics was significantly greater than that of natural materials. Common ferroelectric families include perovskite, ilmenite, tungsten bronze, and various other metal oxides [36]. Among them, perovskite is the prominent piezoceramic crystal structure with outstanding performance.

Perovskites possess a general formula ABX_3, where A is a large metallic cation, B a smaller metallic cation, and X an anion [56] (**Figure 10**). The high symmetry of the perovskite lattice enables flexible deformation of the unit cell, giving rises to several ferroelectrically active non-cubic phases, such as tetragonal and rhombohedral structures [57] (see **Figure 11**). The versatility of perovskites arises from the diverse distortions their crystal lattice can undertake, which allows for extensive tunability of their functional properties.

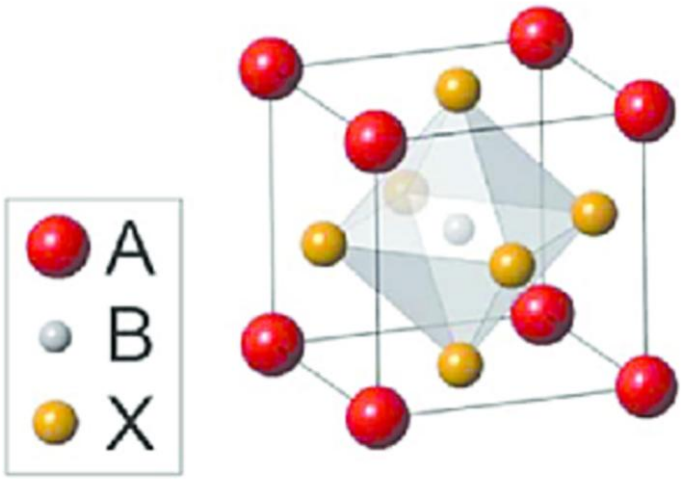

***Figure 10** : General 3D structure of perovskite. Figure adapted from* [58].

Today, the most widely used piezoelectric materials are lead zirconate titanate ($PbZrO_3$–$PbTiO_3$, PZT) ceramics, a perovskite solid solution. PZT exhibits a piezoelectric response three to ten times stronger than of conventional piezoelectric ceramics, making it ideal for a wide range of applications. However, growing environmental and health concerns regarding the toxicity of lead have driven research toward lead-free alternatives, such as barium titanate (BTO) and bismuth ferrite oxide ($BiFeO_3$, BFO).

Among those, bismuth Ferrite oxide (BFO) stands out as a room-temperature multiferroic material, meaning that this perovskite exhibits both ferroelectric and antiferromagnetic properties simultaneously, which is a rather unique occurrence. It presents high spontaneous polarisation and high Curie temperature, while being lead-free, making it a

great candidate for a variety of applications such as energy conversion, electric storage and even photovoltaics. It can easily be synthesized in laboratory following a sol-gel process (*vide infra* ***section 4.1.1***). BFO nanoparticles will be considered in this thesis.

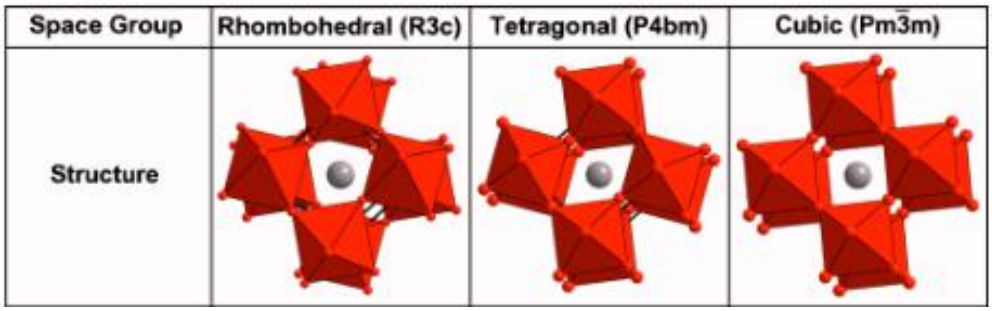

Figure 11 *: Structural properties of the rhombohedral, tetragonal, and cubic phases reported for pure BNT. Figure adapted from* [57].

1.3.2 Organic piezoelectric materials

The first organic material being reported as presenting piezoelectric properties was the wood in the fifties [59]. In the past 70 years, piezoelectricity has been confirmed in a variety of other biological materials, such as bone, long-chain peptides, proteins, polysaccharides [26,60], as well as in different synthetic organic polymer such as polyvinylidene fluoride (PVDF) and its copolymers, poly (L-lactic acid) (PLLA) [61], odd numbered nylon [62], etc..... The linear piezoelectricity inherent to these systems originates from complex dipolar properties and dipole–dipole interactions mediated by intricate hydrogen-bond networks exhibiting different levels of self-assembly and hierarchy [63].

When comparing piezoelectric coefficient outputs, it appears that inorganic piezoelectric materials are by far more efficient than their organic counterparts. However, their widespread utilization is limited because of their low biocompatibility, brittleness, complex and expensive processing and intrinsic rigidness [64,65]. On the other hand, even though organic piezoelectric materials exhibit relatively modest piezoelectric properties, their applications in specific domains such as biomedical and smart electronics hold great promise due to their intrinsic biocompatibility, great flexibility, cost-effectiveness, lightweight, and ease to process in a diversity of form [26,66,67].

After the discovery of piezoelectricity in bio-organic materials, it was seen more as a curiosity because of the extremely low value of piezoelectric coefficient. Interest in piezoelectric organics from the wider scientific community began in 1969 when Heiji Kawai discovered “strong” piezoelectric effects in the synthetic polymer poly(vinylidene fluoride) (PVDF) [68]. PVDF is known as a highly non-reactive thermoplastic semi-crystalline polymer that presents as a repeating unit (CH_2-CF_2). It possesses five distinct crystalline phases depending on the conditions and post-treatment: α, β, γ, δ and ε.

Among all the crystalline phases, α, β, and γ phases are the most studied and frequently employed polymorphs of PVDF [69] (**Figure 12**).

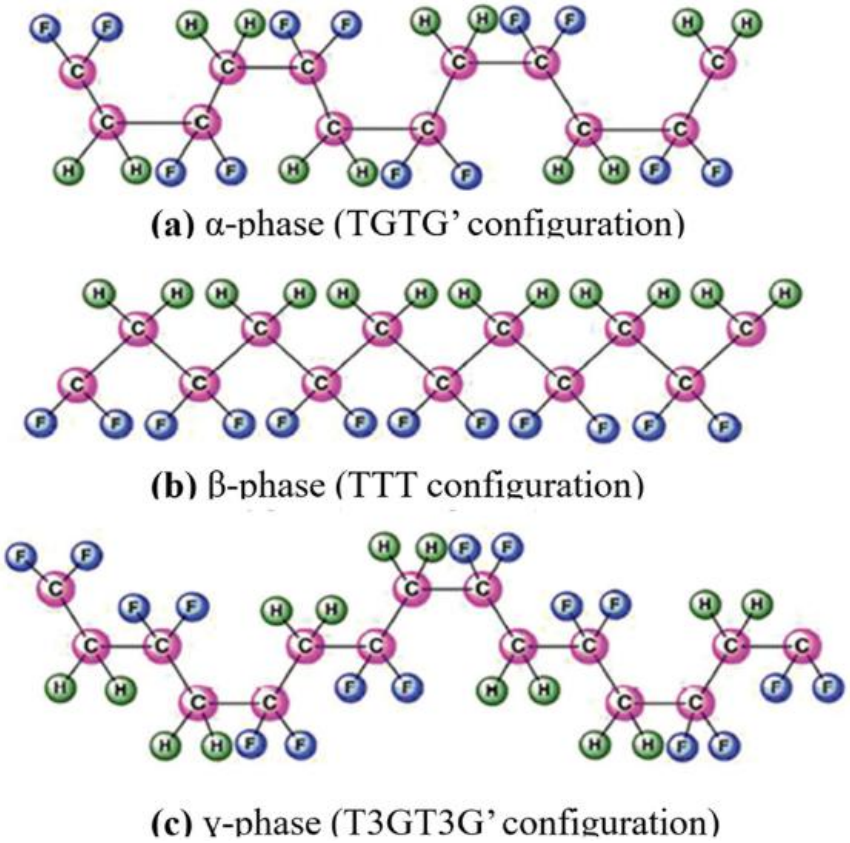

***Figure 12** : Chemical structure of the three main phases of PVDF. Figure adapted from* [70].

- α phase is electrically inactive, with an antiparallel arrangement of dipoles (trans-gauche-trans-gauche, TGTG/conformation) that cancels any net dipole moment in the structure. This phase is the most favourable thermodynamically.

- β (all trans TTTT chain conformations) and γ (T3GT3G/conformations) phases are both electrically active as their dipoles are aligned parallels to each other, leading to a nonzero dipole moment. The β phase, in particular, possesses a very high polarisation, showing strong piezo and ferroelectric properties. Favouring the highest concentration of β phase possible is a prerequisite to obtain a resulting material highly responsive to the applied stress/strain [70].Electric poling is one of the most important ways to obtain the β-phase. Other ways to improve β phase are stretching, high-energy irradiation and annealing at high pressure [71].

Copolymerization is another effective process to tune the polymorph structure as well as the electro-active phase nucleation of PVDF. The addition of other electronegative species along the polymer chain axis is used to promote one of the crystalline phases.

Poly(vinylidene fluoride-co-trifluoroethylene) or P(VDF-TrFE) is the most popular of those copolymers. The introduction of the third fluoride atom in the TrFE [CHF-CF_2] induces polar β-phase by arranging the molecular chain in all-trans conformation. This steric hindrance allows to favour the presence of β phase only as a function of the TrFE unit proportion independently of the processing conditions and electrical poling [72]. Other known electroactive copolymers of PVDF are P(VDF-HFP) and P(VDF-CTFE) (**Figure 13**).

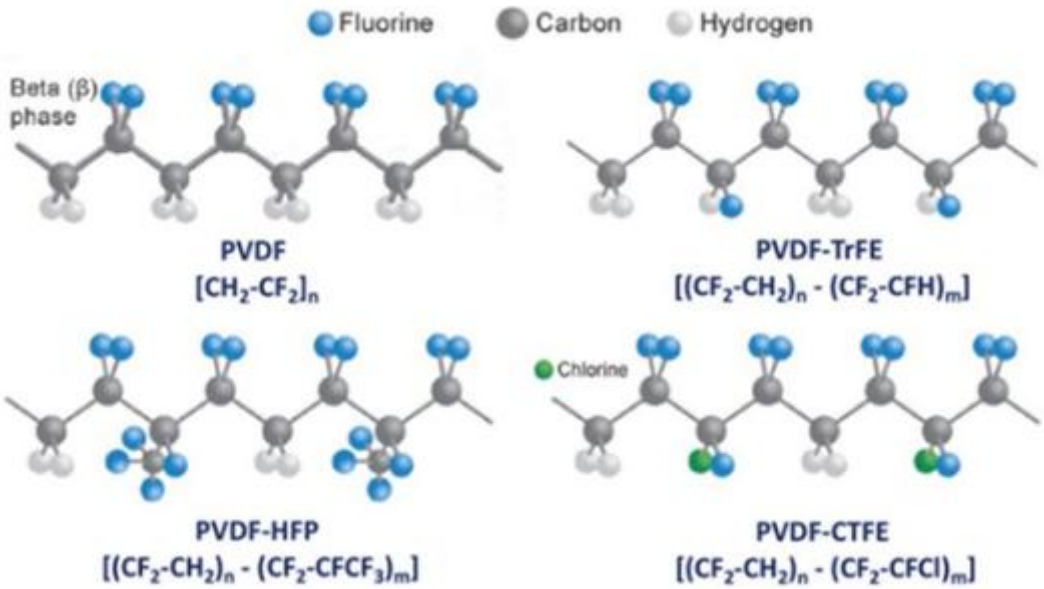

Figure 13 *:Structural configuration of PVDF and its copolymers: P(VDF–TrFE), P(VDF–HFP), and P(VDF–CTFE). Figure adapted from [73].*

Unlike most of the common piezoelectric materials, both PVDF and its copolymers present a negative piezoelectric coefficient (between -10 to-40 pm/V) meaning that an electric field parallel to the dipole orientation leads to compression instead of expansion, and vice versa.

1.3.3 Nanocomposites

Both the organic and inorganic component present some drawbacks: despite the outstanding piezoelectric performance of ceramics, their inherent brittleness limits their applications in flexible devices. Moreover despite the satisfactory flexibility of polymers, their poor piezoelectric properties restrict their use in high energy density applications [7]. To overcome that challenge, one proposed solution is the development of piezoelectric composite materials, where nanofillers are integrated into a polymer matrix to improve both structural and electromechanical performance.

Polyvinylidene fluoride (PVDF) and its copolymers are among the most researched matrices for ferroelectric nanocomposites. The addition of nanofillers significantly enhances the mechanical-to-electrical energy conversion efficiency through two primary

mechanisms. First, the presence of these particles serves as nucleation agents that promote the formation of the β-phase within the polymers. Second, the inclusion of nanoparticles modifies the dielectric properties of the system, effectively increasing the dielectric permittivity, crucial for efficient energy conversion processes [74].

Various types of fillers have been investigated for their potential benefits. Piezoelectric fillers, such as PZT , ZnO , BFO, and BTO, have been thoroughly studied as a way to help in nucleation and dipole alignment [75–78]. Even purely conductive (non-ferroelectric) fillers such as graphene or carbon nanotubes have been investigated to enhance nucleation and to aid the transfer of generated charges [79–81].

Most studies on piezoelectric or ferroelectric nanocomposites focus primarily on macroscale characterisation, evaluating how the incorporation of nanofillers modifies the overall response of the material [82–84]. Only a limited number of works attempt to probe their local behaviour, and even fewer exploit the full capabilities of SPM for nanoscale analysis. In many cases, SPM is used merely as a global diagnostic tool [85–88] rather than a precise nanoscale probe capable of resolving the structural and functional heterogeneity of such complex materials.

1.4 Objectives of the thesis

The objective of our thesis is to develop and demonstrate reliable methodologies for preparing, measuring, and interpreting the nanoscale ferroelectric and mechanical properties of polymer–nanoparticles heterostructures using advanced SPM (Scanning Probe Microscopy) techniques. This work aims to establish sample-preparation strategies that produce thin films and composite architectures compatible with a wide range of SPM modes, while preserving the intrinsic behaviour of the materials. This includes the fabrication of uniform ferroelectric PVDF-TrFE thin films, the dispersion and immobilisation of isolated $BiFeO_3$ (BFO) nanoparticles in a conductive polymer matrix for single-particles analysis, and the preparation of hybrid ferroelectric nanocomposites combining both components.

Beyond sample preparations, the central objective is to characterise both the individual materials and their composites at the nanoscale, with particular emphasis on understanding how complex geometries, roughness, and multi-phase interfaces influence PFM-based ferroelectric measurements. Instead of relying solely on classical PFM mode for global assessment, this research explores advanced PFM modes, such as Dual-Frequency Resonance Tracking (DFRT), switching-spectroscopy PFM (ssPFM) cartography, and frequency DataCube (DCube) mode to enable a more accurate and spatially resolved quantification of piezoelectric and mechanical responses within heterogeneous structures.

A further objective of the thesis is to critically assess the origin of the PFM signal in such systems. Because nanoscale PFM measurements are highly susceptible to artifacts, such as electrostatic forces, tip–sample crosstalk, phase flipping, or resonance instabilities. This work proposes a set of practical diagnostic checks to distinguish genuine ferroelectric behaviours from non-ferroelectric artifacts. These procedures are

first validated through reference ferroelectric and non-ferroelectric materials, and subsequently applied to the PVDF-TrFE films, BFO nanoparticles, and their composites.

Chapter 2: Nanoscopic characterization: Scanning Probe Microscopy

“Scanning probe microscopy” (abbreviated SPM) encompasses all microscopy techniques that use a microscopic probe apparatus to achieve surface property mapping. The first technique developed in this field was Scanning Tunneling Microscopy (STM) [89] in 1981. It is based on the measurement of the current resulting from the tunnel effect (a quantum effect, whereby a microscopic particle, an electron in this case, passes through a potential barrier) between the tip of the probe and the surface being studied. To carry out this type of measurement, a conducting tip is brought close to the surface of the sample, which is also conductive. These two conductive parts thus act as electrodes. A voltage is applied between the two, allowing the electrons to cross the vacuum separating them. The resulting current depends not only on the voltage applied, but also on the distance between the tip and the surface and the Local Density Of State (LDOS) of the sample [90]. This technique enables the morphology of the studied sample, and the distinction of present species with atomic precision.

One of the techniques derived from STM is Atomic Force Microscopy (AFM). Developed in 1986 by G. Binnig, C. Quate, and C. Gerber [91], this technique was originally designed for measuring the topography of surfaces with nanometric resolution, without any limitation on the conductive nature of the surfaces.

Almost forty years later, its modes and applications have diversified. SPM is now applicable to a wide range of samples, from rigid materials as ceramics to cell cultures or polymer materials [92–94]. AFM is now able to probe a large range of physical and chemical properties at the nanoscale [95–101].

The experimental set-up conditions as well as calibration procedures for the different SPM-type measurements presented in this section will be described in **Section 4.3.**

2.1 Set-up and working principle

A typical SPM set-up consists of three different parts: The probe, the scanning apparatus, and the detection system [102] (see **Figure 14**).

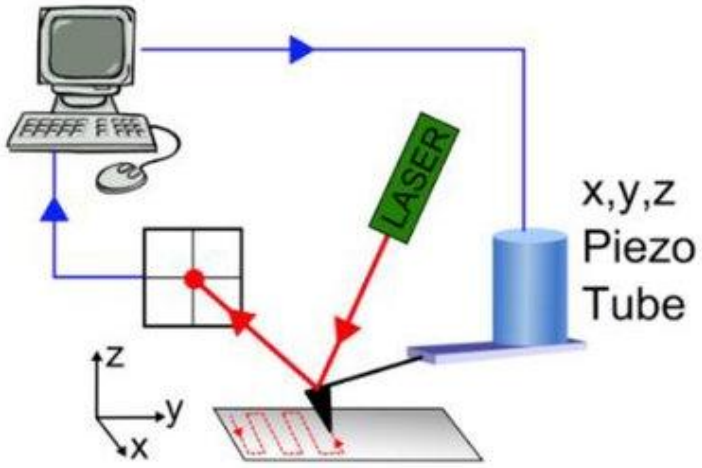

***Figure 14**: Basic SPM set-up. Figure adapted from* [103].

- The probe itself consists of two parts: the tip and the cantilever. The tip is the key element that interacts with the sample. SPM tips are generally fabricated as sharp as possible to achieve the highest lateral resolution. Typically made of silicon nitride, they can also be made of other materials or coated with a conductive layer, such as PtIr (Platinum-Iridium), to allow the measurement of local electrical properties. The cantilever acts as a force transducer, converting tip-sample interaction forces into measurable deflections. Its backside is reflective to facilitate laser-based deflection measurement. The mechanical properties of the tips are defined by their dimension, length l, and width w, as well as their spring constant k.
- The scanning system relies on a piezoelectric tube, which enables precise movement in the X, Y, and Z directions. This setup allows highly accurate displacement, from several micrometres down to sub-nanometre levels. The piezoelectric element can also induce controlled oscillations of the tip required for dynamic SPM modes at a defined frequency.
- Detection in SPM is based on the Optical Beam Deflection (OBD) system. A laser is reflected from the back of the cantilever toward a quadrant photodetector. The photodetector generates voltage signals corresponding to cantilever deflections in both vertical and lateral directions. These signals are processed by the feedback controller.

The core of all SPM techniques is monitoring the interaction between the tip and the sample surface. The interaction forces between both can be measured by the bending of the cantilever, that will trigger a trackable deflection of the laser spot on the photodiode. Furthermore, the feedback controller monitors those forces, from which it extracts the vertical Z-displacement and, therefore, generates topographic images.

2.1.1 SPM modes

AFM operation modes can be classified into two categories as a function of the cantilever movement: static mode and dynamic mode.

2.1.1.1 Static modes

The static mode, also called contact mode, was the first AFM mode developed [91]. In it, the cantilever deflection is maintained at a constant value while the tip scans across the sample surface. A feedback loop adjusts the vertical position of the cantilever to maintain this constant deflection, providing a direct measure of surface topography. This mode can generate significant friction, potentially damaging soft samples or abrading the tip. Despite these limitations, static mode remains essential for characterizing local physical properties such as electrical conductivity and piezoelectric response, where maintaining continuous electrical contact is necessary.

2.1.1.2 Dynamic modes

The dynamic mode or vibrating mode is divided into 2 sub-categories: intermittent contact mode (tapping) and non-contact mode.

In intermittent contact, the cantilever oscillates near its fundamental flexural resonant frequency while monitoring the amplitude and phase. The interaction between the tip and the sample will cause a shift in the amplitude and phase values. The shift is continually compensated by the feedback system that adjusts the scanner position following the surface morphology. This mode allows to reduce the contact time between the tip and the sample, reducing in the process the surface damage and abrasion risk.

In non-contact mode, the tip oscillates close to the sample surface without making contact, avoiding any repulsive forces. The cantilever vibrates at its resonant frequency in air, and the amplitude of this oscillation is tracked. Attractive interactions alter the resonant frequency, thereby affecting the oscillation amplitude. This mode is ideal for imaging soft and delicate samples because it eliminates repulsive forces. However, non-contact mode can be disrupted by contaminant layers that interfere with the oscillation, so it is typically conducted in ultra-high vacuum conditions.

2.2 “Forces” in atomic force microscopy

Understanding the interacting forces between the probing tip and the analysed sample is a prerequisite for the interpretation of any SPM measurement. There is a force gradient between the two objects that depends on the distance between them. The different constituents of this force gradient are short-range and long-range forces and can be either attractive or repulsive [104]. For instance, the contact mode is characterized by short-range repulsive forces, while the non-contact mode is characterized by long-range attractive forces. Intermittent contact mode works in the two regimes. This interaction can be represented by a Lennard-Jones potential (see **Figure 15**).

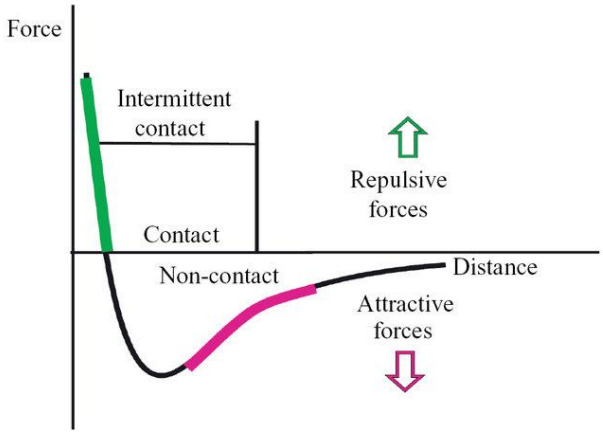

***Figure 15**: Interaction Forces arising in each AFM mode. Figure adapted from* [105].

A brief summary of the common forces between the tip and sample surface is provided below.

Long-range interactions in AFM are typically van der Waals forces [106,107], originating from electric dipole interactions, either between permanent or induced dipoles. There are three possible dipole interactions: interaction between two permanent dipoles called the Keesom force, interaction between a permanent and an induced one called the Debye force, and the interaction between a spontaneously generated induced dipole called the London force. Although the weakest of the three, the London force is the predominant part of the van der Waals forces due to its universal presence at the molecular and atomic scale.

The net van der Waals force is the sum of all individual dipole interactions between the tip and the surface. Van der Waals forces between two identical bodies in a medium are always attractive, while the force between two different bodies can be attractive or repulsive. Van der Waals forces are expressed in the following equation:

$$F_{vdw} = \frac{HR}{6D^2}$$

Eq. 11

where H is the Hamaker constant, R is the tip radius, and D is the instantaneous tip-surface distance.

This expression is expressed under the condition that the tip has a spherical edge, and the sample is a flat surface. From the expression of this force, it is interpreted that the van der Waals forces should tend to infinity when the tip and the sample are in contact, which is not realistic. The empirical value used to represent the distance in the case of mechanical contact is D_0= 0.165 nm.

Short-range repulsive forces arise from the Pauli exclusion principle: when two atoms are brought close to each other, their electron clouds come closer too and start repelling each other. In AFM, the probe-surface interaction occurs not between two atoms but thousands of them. Continuum approaches are necessary to describe the effective repulsive force.

Capillary forces appear when water condenses spontaneously on hydrophilic surfaces under ambient conditions, forming a meniscus around the tip [108,109]. The arising capillary forces can significantly impact measurement. To minimize those capillary forces, it is advisable to work in the least humid atmosphere possible. Conversely, these forces can be eliminated by completely immersing the sample in a liquid. However, working in liquid introduces other interactions, known as DLVO forces (Derjaguin, Landau, Verwey, and Overbeek) [110]. These are electrostatic forces comprising VdW forces between two surfaces (attractive in SPM measurements), repulsion due to ions in the solution near the sample, and the solvation effect, defined as the minimization of contact between the hydrophilic environment (the solution) and the hydrophobic space composed of the measurement tip and the sample surface.

Another force that can influence the bending of the cantilever is the electrostatic force [111,112]. Those arise from different phenomena: the surface potential difference between the tip and the sample, and the charge applied to the system in electrical SPM modes. Those forces can either be attractive or repulsive. Those forces will be developed in the section consecrated to PFM artifacts (*vide infra,* **section 3.2**).

Other forces can also significantly influence the cantilever bending. These include steric force [102] when a polymeric solid is compressed (reduction of free volume between chains) and the "bridging effect," which is an attraction between the tip and sample surfaces with common free interaction sites.

2.3 Nano-mechanical characterization with AFM

The characterization of nanoscale properties is typically done by collecting a force curve corresponding to the approach-retract movement of the tips onto the surface. Those curves are expressed as a function of time or distance. Those curves are typically divided into several segments (**Figure 16**). Initially, when the tip is still far from the sample (position A), the system is at equilibrium with no force in play. Then, as the tip is brought closer, attractive vDW forces start to arise. At some point, that force is so great that it provokes a jump-in of the tips into the surface (position B), establishing the contact tip-sample. After that, the tip is further pushed into the sample until the maximum forces are reached. The different contact repulsive steric forces arise at that point (position C). The tip can be held at this maximum of force set-point for a defined period of time (defined as the hold time. Next, the tip is moved up, with a progressive decrease of the repulsive forces and an increase of the attractive forces, consisting of vDW forces and capillary

forces. As the pull-out force exerted on the cantilever exceeds the attractive forces between the tip and the surface, it will jump out of contact (position D) before going back to a forceless equilibrium.

Analysing the contact portion of these curves (between positions C and D) using contact mechanics models allows the extraction of quantitative mechanical properties, such as elastic modulus and contact stiffness. Ramp is performed in a triangular wave with a typical ramp rate around 1 Hz.

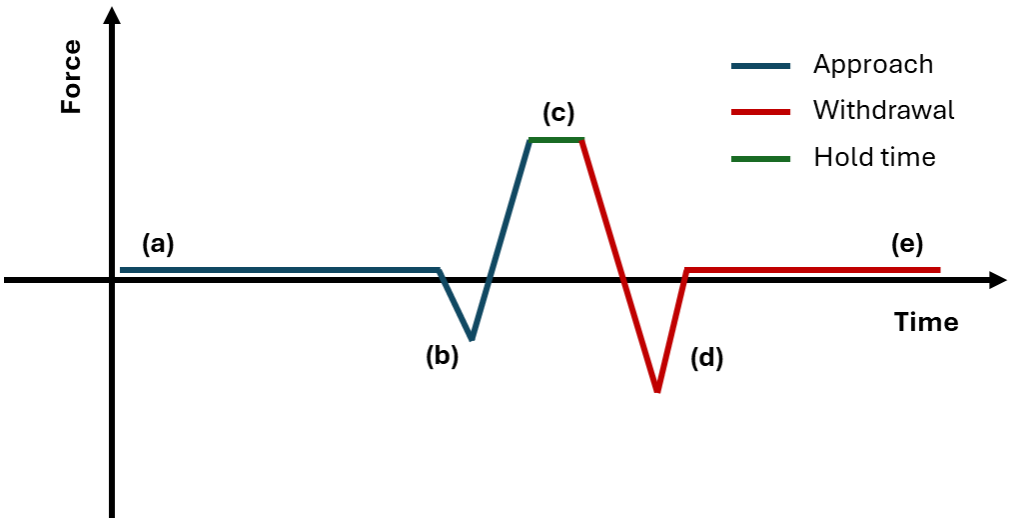

Figure 16 *:Principle of* Force-distance curve *operation with the tip trajectory.*

2.3.1 Peak Force Tapping

The Peak Force Tapping (PFT) is a more rapid and simple technique that allows quantitative measurement of the mechanical properties of a wide range of materials [113]. It is based on the obtention of local cartography, where each pixel corresponds to a force curve generated by the tip approach-retract motion. Different mechanical properties can be extracted from those measurements such as the adhesion, the deformation or the young modulus (**Figure 17-b**).

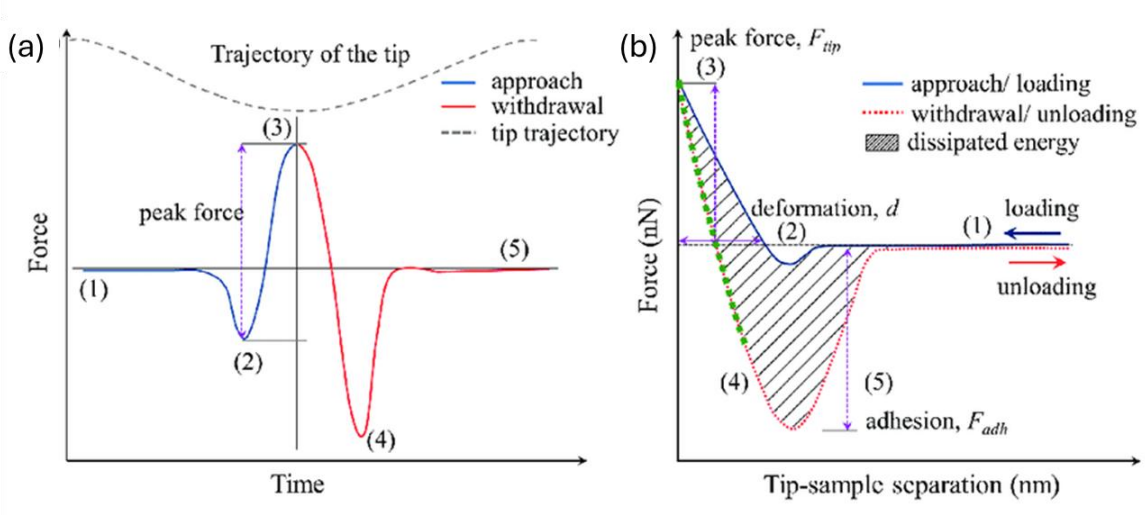

Figure 17: *(a) Principle of Peak Force Tapping operation with the tip trajectory, (b) Schematic of force-distance curve obtained at each tapping cycle. Figure adapted from* [114].

The movement occurs at a frequency much lower (500 Hz-2 kHz) than the resonance of the lever (50-300 kHz) to avoid dynamic effects characteristic of resonance AFM modes (e.g., Tapping mode). It can be considered quasi-static (with no dynamic solicitation), thereby limiting the information to the elastic aspects of the response.

In PFT, a non-destructive aspect is combined with direct control over the forces at play. Additionally, the lever undergoes a sinusoidal wave displacement. This modulation enables smoother tip movements than a triangular wave, with a gentle approach, retraction, and zero velocity during displacement. This method ensures effective control of force curves and stable responses due to the low forces involved.

2.3.2 Mechanical model

Interpreting the force curves from an AFM measurement requires using a theoretical model adjusted to these curves to extract the mechanical properties (green area in ***Figure 17 b***). However, to date, no model comprehensively describes all behaviours. The choice of model depends on the specific characteristics of the situation being studied.

2.3.2.1 Hertz et Sneddon

The first model for interpreting SPM measurements is based on the Hertz model (developed in the 1880s). It describes the deformation δ (indentation) caused by the contact between a spherical probe and an elastic surface [115].

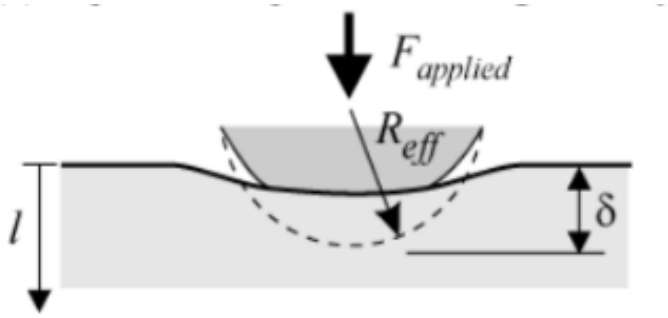

Figure 18: *Indentation of a rigid flat surface by a spherical probe. Figure adapted from* [116].

This model is based on the following preliminary assumptions:

- The surface and the tip are homogeneous;
- The surface is isotropic and semi-infinite;
- There is no friction;
- The deformation is small (δ << R);
- Adhesion forces are zero (F_{adh} = 0).

The relationships between the parameters obtained are:

$$F(h) = \begin{cases} 0 & for\ h \geqslant 0 \\ \frac{4}{3} E^* \sqrt{Rh^3} & for\ h < 0 \end{cases}$$

Eq. 12

$$a = \left(\frac{FR}{E^*}\right)^{\frac{1}{3}}$$

Eq. 13

where E* is the reduced modulus, R is the tip radius, and a is the contact radius. Because there are no adhesion forces in this model, the contact area when no force is applied is zero, a_0 = 0. h is the distance between the tip and the surface.

In the 1960s, Sneddon developed a model close to Hertz's, generalizing the expressions for indentation depth and force to various solid probe geometries of revolution [117]. To do this, he derived the following general equations:

$$h = \int_0^1 \frac{f'(x)}{\sqrt{1-x^2}} dx$$

Eq. 14

$$F = E^* a \int_0^1 \frac{x^2 f\prime(x)}{\sqrt{1-x^2}} dx$$

Eq. 15

where (f(x)) represents the tip geometry, (x) is a dimensionless parameter (between 0 and 1).

- For a spherical tip, the geometry can be expressed as

$$f(x) = R - \sqrt{R^2 - a^2 x^2}$$

Eq. 16

This equation can be simplified as $f(x) = \frac{a^2 x^2}{2R}$ for small indentation. Substituting this into the integrals yields the same Hertz solutions.

F(x) can be adapted to other tip geometries [118] (**Figure 19**):

- For flat-ended cylindrical tip;

$$F(h) = 2a_c E^* h$$

Eq. 17

where (a_c) is the radius of contact of the cylinder.

- For conical tip;

$$F(h) = \frac{2}{\pi} E^* h^2 tan\theta$$

Eq. 18

where (θ) is the apex angle of the cone.

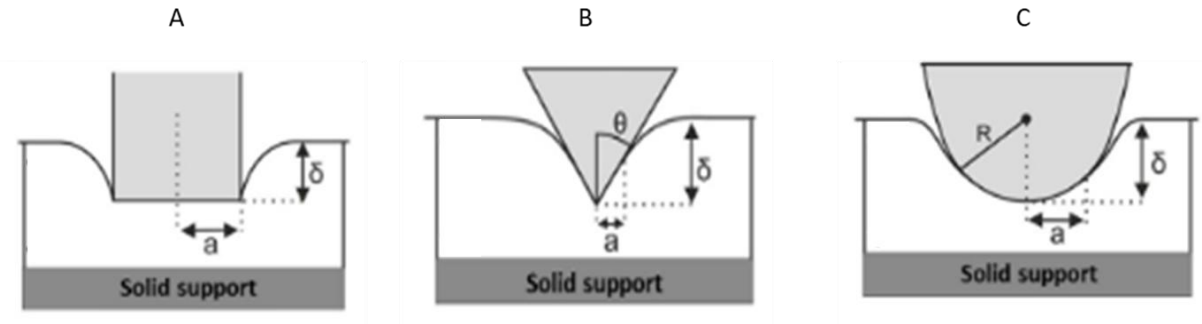

***Figure 19**: Representation of indentation of a surface by tips of different geometries:(a) flat-ended cylindrical probe(b), conical probe, (c) paraboloid (spherical) probe. Figure adapted from* [118].

Due to their relative simplicity, the Hertz and Sneddon models are still frequently used today to obtain approximations of the Young's modulus of rigid surfaces, even though some of their assumptions, such as the absence of friction or surface adhesion, are rarely valid.

2.3.2.2 DMT (Derjaguin, Muller, Toporov)

Various models have been developed to improve upon the Hertz model [116]. Among these is the Derjaguin, Muller, and Toporov (DMT) model [119], in which the authors take into account adhesion forces outside the contact region between the tip and the surface. These forces, however, remain relatively weak, and the Hertzian contact remains valid (**Figure 20**).

Adhesion forces are considered as a contribution to the total load, which allows the following relations to be derived:

$$F(h) = \begin{cases} F_{adh} & pour\ h \geqslant D_0 \\ F_{adh} + \frac{4}{3}\, E^* \sqrt{Rh^3} & pour\ h < D_0 \end{cases}$$

Eq. 19

$$a = \left(\frac{R}{E^*}(F - F_{adh})\right)^{1/3}$$

Eq. 20

Adhesion forces are generally expressed in terms of surface energy:

$$F_{adh} = -2\pi \Delta\gamma R$$

Eq. 21

where $\Delta\gamma$ is the work of adhesion per unit area [N/m].

The presence of this adhesion component results in a non-zero contact area when no force is applied:

$$a_0 = \left(\frac{2\pi R^2 \Delta\gamma}{E^*}\right)^{1/3}$$

Eq. 22

2.3.2.3 JKR (Johnson-Kendall-Roberts)

Another adaptation of the Hertz theory is the Johnson, Kendall, and Roberts (JKR) model [120], which accounts for adhesion forces within the contact region between the tip and the surface (**Figure 20**). This is expressed by the following equations:

$$F_{JKR} = \frac{4E^* a^3}{3R} - \sqrt{8\pi\Delta\gamma E^* a^3}$$

Eq. 23

$$h = \frac{-a^2}{R} + \sqrt{\frac{2\pi\Delta\gamma a}{E^*}}$$

Eq. 24

Although similar to the DMT model, the force expression in the JKR model introduces additional complexity. This includes the consideration of the contact area, which is expressed by the formula:

$$a = \left[\frac{3R}{4E^*}\left(F + 3\pi R\Delta\gamma + \sqrt{6\pi R\Delta\gamma + (3\pi R\Delta\gamma)^2}\right)\right]^{1/3}$$

Eq. 25

where $F_{adh} = -\frac{3}{2}\pi\Delta\gamma R$

Similar to the DMT model, the contact area without applied force is non-zero:

$$a_0 = \sqrt[3]{\frac{6\pi\Delta\gamma R_{eff}{}^2}{E^*}}$$

Eq. 26

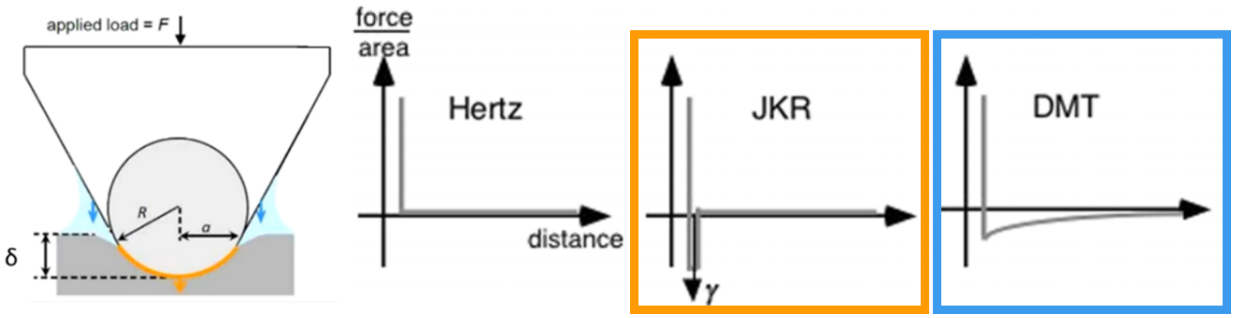

***Figure 20** : Representation of adhesion forces acting in DMT model and JKR model. Figure adapted from [121].*

2.3.2.4 Maugis-Dugdale

The DMT and JKR models have long been considered as distinct models from each other. However, Maugis demonstrated that they are «extremes» of the same theory [122]. The DMT model applies to rigid surfaces with low adhesion force and a small contact radius,

whereas the JKR model applies to soft surfaces with a higher adhesion force and a larger contact area.

To choose the most appropriate model for each sample, a parameter μ, known as the Tabor parameter, can be determined [123].

$$\mu = \left(\frac{R_{eff}\Delta\gamma^2}{E^{*2}z_{equ}^3}\right)^{1/3}$$

Eq. 27

where z_{equ} is the interatomic equilibrium distance between the surface and the tip.
$\Delta\gamma$ is derived from the expression of the adhesion force.

If μ tends toward 0 (less than 0.1), it is preferable to use the DMT model. If it tends toward infinity (or greater than 5), the JKR model is more suitable. Between these two values, Maugis' theory is used. Many systems fall within this intermediate zone. However, Maugis' model does not offer a simple analytical solution like DMT and JKR do. It requires solving the following parametric equations:

$$F = \frac{E^* a^3}{R} - \lambda a^2 \left(\frac{\pi\gamma E^{*2}}{R}\right)^{1/3} \left[\sqrt{m^2-1} + m^2 arctg\sqrt{m^2-1}\right]$$

Eq. 28

$$h = \frac{a^2}{R} - \frac{4\lambda a}{3}\left(\frac{\pi\gamma}{RE^*}\right)^{\frac{1}{3}}\sqrt{m^2-1}$$

Eq. 29

where m is a dimensionless parameter corresponding to the ratio of the maximal area where attractive forces are felt to the contact radius between the tip and the surface.

To solve these equations, it is necessary to work iteratively by varying the value of m. This complicates data processing.

2.4 Electrical properties by SPM

2.4.1 Conductive AFM

Conductive AFM (C-AFM) [124] is a mode that measures the flow of current in a material at the nanoscale. Developed in 1993 [125], this mode is based on a conductive tip serving as a top electrode to close the circuit, which is driven on top of the sample surface, either in contact mode or in peak-force mode [126], while applying a voltage. The resulting current is mapped, providing information on the local conductivity of the sample in correlation with morphology.

In addition to imaging mode, I(V) spectroscopic curves can be recorded. It is done by applying a voltage ramp after fixing the position of the cantilever on top of the sample. The resulting curves are used to comprehend the local conductivity of the sample.

The current measure in this type of measurement is typically low, ranging from picoamperes to microamperes. This is why a supplementary module, a preamplifier, is added to the AFM scanner to be able to detect the electrical flow.

C-AFM can particularly be used on dielectric materials to determine their injection threshold, i.e., the voltage at which thin materials start to allow current passage or experience electrical breakdown.

2.4.2 Kelvin Probe Force Microscopy

Kelvin Probe Force Microscopy (KPFM) is an AFM technique to measure the Contact Potential Difference (V_{CPD}) between a conducting tip and a sample [127]. This measurement provides insights into the work function of the sample, a key parameter to understand surface electric properties.

The V_{CPD} is defined as:

$$V_{CPD} = \frac{\varphi_{tip} - \varphi_{sample}}{e}$$

Eq. 30

where φ_{tip} and φ_{sample} are respectively the work functions of the tip and the sample, and e is the elementary charge. φ_{tip} is usually determined using a reference sample of known work function (**Table 2**).

***Table 2** : Work function of conventional calibration materials.*

Materials	ϕ (eV)
Aluminum (Al)	4.28 [128]
Gold (Au)	5.1 [128]
Silicon (Si)	4.6 [129]

Initially, when the tip and sample are separated and not electrically connected, their Fermi levels differ (**Figure 21 a**). When the tip and sample approach each other, their Fermi levels align through electron tunnelling, leading to an equilibrium state where the system reaches a stable configuration, creating an apparent V_{CPD}(**Figure 21 b**). This V_{CPD} generates an electrical force in the contact area, which can be nullified by applying an external bias V_{DC}. When the bias has the same magnitude but opposite direction as the V_{CPD}. The applied bias that nullifies the electrical force due to the V_{CPD} is equal to the work function difference between the tip and the sample (**Figure 21 c**).

In addition to the nulling voltage V_{DC}, a probing voltage V_{AC} is also applied. The V_{AC} generates oscillating electrical forces, while V_{DC} nullifies these forces, allowing the quantification of the V_{CPD}. The electrostatic force between the tip and the sample (F_{es}) is given by the equation:

$$F_{es} = \frac{1}{2}\frac{dC(z)}{dz}\Delta V$$

Eq. 31

where C is the capacity of the system, z the distance and ΔV the difference between the contact potential and the applied potential between the tip and the sample.

ΔV is given by:

$$\Delta V = V_{DC} + V_{AC}\, sin(\omega t) - V_{CPD}$$

Eq. 32

So, the electrostatic force at working frequency ω is:

$$F_{es\omega} = \frac{dC(z)}{dz}(V_{DC} - V_{CPD})V_{AC}\, sin(\omega t)$$

Eq. 33

KPFM measurement is typically divided into two measurement steps: a first step to measure the topography and a second step in lift mode (at a certain distance from the sample) to measure the electrostatic forces.

A lock-in amplifier measures $F_{es\omega}$ to determine the V_{CPD} by nullifying the oscillating electrical force. By adjusting V_{DC} so that the output amplitude signal of the lock-in amplifier is zero, the V_{CPD} can be accurately mapped across the sample surface.

KPFM can operate in two main modes: **Amplitude Modulation (AM)** and **Frequency Modulation (FM)**.

In AM mode, the electrostatic force is measured directly from the amplitude of the cantilever oscillation at ω. The CPD is determined by applying V_{DC} to nullify the measured oscillation amplitude, thus measuring the work function.

In FM mode, the force gradient is detected through the frequency shift of the cantilever oscillation. The CPD is measured by applying V_{DC} to nullify this frequency shift, offering higher spatial resolution compared to AM mode.

To improve the quality of the measurement and limit capacitive crosstalk, an alternative AM-KPFM mode, the heterodyne KPFM [130], has been developed. Contrary to its predecessor, the measurement is done in a single pass. The measurement is driven in Tapping mode at the free resonance frequency ω_0, while the probing voltage Vac for the

modulation is driven at $\omega_{ac}= \omega_1-\omega_0$, where ω_1 is the second resonance frequency of the cantilever. The electrostatic force in this mode is expressed by the equation:

$$F_{esH} \approx [\frac{A}{2}\frac{dC^2(z)}{dz^2}](V_{DC} - V_{CPD})V_{AC}\, cos(\omega_1 t)$$

Eq. 34

From this final expression, it is noted that the demodulation of the signal is done at ω_1, independently of the contact mechanics, and is dependent of the second derivative of the capacitance, making it more sensitive to the surface than the previous techniques.

KPFM is widely used to map the work function or surface potential of materials, particularly in the study of semiconductors and other electronic materials. The technique provides valuable insights into surface properties, such as charge distribution, local potential variations, and electronic structure. This is useful to determine charge injection inside the sample after a poling process [131–133].

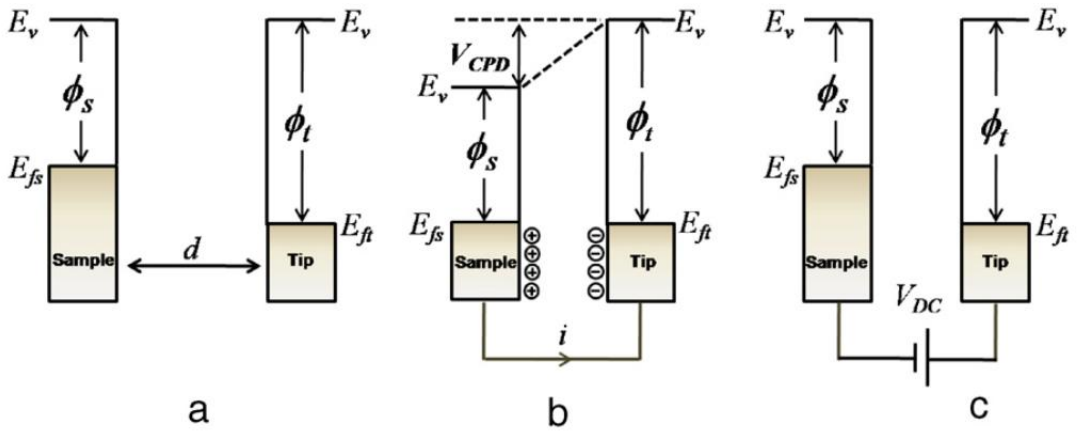

Figure 21 *:Electronic energy levels of the sample and AFM tip for three cases: (a) tip and sample are separated by distance d with no electrical contact, (b) tip and sample are in electrical contact, and (c) external bias (V_{dc}) is applied between tip and sample to nullify the VCPD and, therefore, the tip–sample electrical force. E_v is the vacuum energy level. E_{fs} and E_{ft} are Fermi energy levels of the sample and tip, respectively. Figure adapted from [127].*

Chapter 3: Piezoresponse Force Microscopy

As highlighted in the introduction, the growing demand for miniaturized electronics in various fields has intensified research on nanomaterials and nanoscale components, making the precise characterization of their electro-mechanical properties increasingly important.

Conventional optical-based techniques for piezoelectric evaluation at small scale such as laser interferometry [134] or polarized light microscopy [135] are inadequate for studying nanomaterials and nanocomposites. Their spatial resolution is fundamentally limited by the wavelength of light, and they generally lack the sensitivity required to detect the weak piezoelectric coefficients characteristic of biological, organic, or hybrid materials. These limitations have created the need for high-resolution, highly sensitive methods capable of probing electromechanical behaviour at the nanoscale.

The invention of Piezoresponse Force Microscopy (PFM) in 1991 [136] marked a major breakthrough in this context. PFM combines the nanoscale spatial resolution and non-destructive operation of SPM with the ability to map local electromechanical deformation induced by an applied electric field. It enables quantitative and qualitative assessment of piezoelectric amplitude, polarisation orientation, ferroelectric domain structure, and switching behaviour [137–139].

As such, PFM has become a key technique for characterizing a broad range of functional materials from inorganic ferroelectrics [133] to organic films [72], nanocomposites [140], and even biological systems [141].

The experimental set-up condition as well as calibration procedures for the different PFM type measurement presented in this section will be described in **Section 4.3.**

3.1 Working Principle of PFM

Piezoresponse Force Microscopy (PFM) is a local probe microscopy technique based on the inverse piezoelectric effect (*vide supra,* **section 1.2.2**): the deformation of a piezoelectric material is induced by an electrical stress, as described by the following formula in Voigt notation:

$$S_{ij} = d_{ij}E_j$$

Eq. 35

where S_{ij} is the strain tensor, d_{ij} is the piezoelectric tensor, and E_i is the electrical field.

A conductive tip serves both as the upper electrode and the detector for this deformation. The tip is put in contact mode with the sample with a constant load force, while at the same time an AC bias voltage is applied to generate a localized electric field at the tip apex. The piezoelectric material will then deform (expand or contract, depending on the sign of its piezoelectric coefficient). A lock-in amplifier system is used to simultaneously

record the topography and the electromechanical response, namely the amplitude and phase signals (**Figure 22**).

Those values are directly linked to the magnitude of the piezoelectric coefficient as well as the domain polarisation direction under the tip. Assuming that the probing voltage bias V is applied to a piezoelectric sample:

$$V = V_{DC} + V_{AC}\, sin(\omega t)$$

Eq. 36

where V_{DC} is the optional polarisation or switching bias (often set to 0), V_{AC} is the measurement or probing bias, and ω is the AC bias driving frequency.

Under the solicitation of the electric field, the sample oscillates at the driving frequency of the AC voltage is expressed

$$A_{piezo} = A_0 + A_{1\omega} sin(\omega t + \varphi)$$

Eq. 37

where A_0 represents the static surface displacement, and φ is the phase shift between the driving voltage V_{AC} and the voltage-induced deformation $A_{1\omega}$. The PFM response amplitude, $A_{1\omega}$, is proportional to the sample deformation and therefore reflects the strength of the local electromechanical coupling.

The PFM phase, φ, represents the phase lag of the material response compared to the AC driving voltage. It provides information about the polarisation direction in the material under the tip. If the polarisation direction aligns with the applied field, the vibration will be in-phase with the V_{ac}, and φ will be 0. Conversely, if the polarisation direction is opposite to the applied field, the vibration will be is out-of-phase, and φ will be equal to 180°.

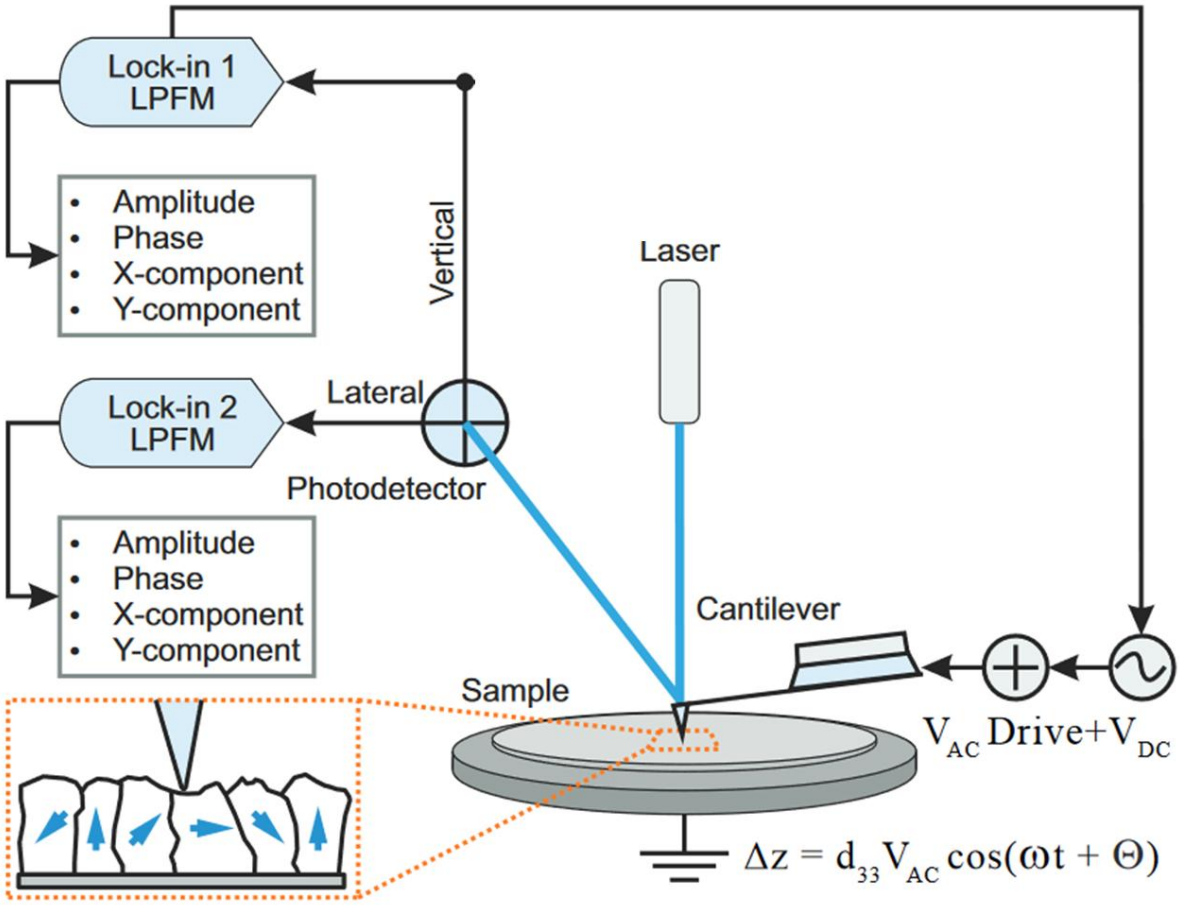

***Figure 22**: Representation of a PFM set-up. Figure adapted from [142].*

3.1.1 Vertical and Lateral PFM

PFM typically measures the vertical deflection of the cantilever, which contains information on the vertical component of the polarisation normal to the surface. This measurement corresponds to the piezoelectric coefficient d_{33}, and the method is known as vertical PFM (VPFM). In VPFM, the application of a uniform electric field along the polarisation axis results in either elongation or contraction of the domain, depending on the polarisation direction.

In the absence of electrostatic forces, the deformation along the vertical axis is described as:

$$\Delta Z = d_{33} V = d_{33} V_{AC} sin(\omega t + \varphi) + \Delta Z_{topo}$$

Eq. 38

where ΔZ is the surface deformation along the z-axis, d_{33} is the piezoelectric coefficient in the z-direction, and V is the applied voltage. The detection of the

electromechanical vibration is coupled with the z-axis detection of the sample's topography (ΔZ_{topo}).

PFM also detects movements of ferroelectric domains oriented parallel to the sample surface, known as lateral PFM (LPFM). LPFM is based on the detection of the torsional movement of the cantilever. An alternating voltage generates a shear deformation, causing lateral vibration of the tip. This shear movement is transmitted to the tip in contact with the surface, resulting in cantilever torsion. The lateral displacement from the shear movement is defined as:

$$\Delta X = d_{15} V_{ac} sin\,(\omega t + \varphi)$$

Eq. 39

Where ΔX is the lateral deformation, and d_{15} is the in-plane piezoelectric coefficient.

3.1.2 Ferroelectric analysis in PFM

Piezoelectric, non-ferroelectric materials are relatively straightforward to analyse by PFM. The piezoresponse amplitude and phase are recorded, either as images or spectroscopic curves, under the application of an AC voltage (V_{ac}). Since the amplitude is directly proportional to the applied voltage, the piezoelectric coefficient is estimated simply by performing a linear regression of the amplitude as a function of V_{ac}.

In contrast, the characterization of ferroelectric properties requires a more careful and elaborate approach. Probing nanoscale ferroelectric domains or acquiring reliable ferroelectric hysteresis loops involves additional considerations related to tip–sample interactions, electrostatics, and switching dynamics, making the analysis significantly more complex than for simple piezoelectric materials.

3.1.2.1 Imaging mode

The imaging mode makes it possible to reconstruct the ferroelectric domains naturally occurring in a sample from the amplitude and phase collected during a scan. It is also possible to write domains using a poling procedure. This procedure requires the application of a DC voltage during a complete scan, forcing alignment under the tip in the direction of the applied electric field. It requires the applied voltage to be greater than the coercive voltage of the sample, yet low enough to avoid generating artifacts or damaging the surface.

PFM requires the tip to be in contact with the sample to serve as the same time of top electrode and a surface displacement sensor. The studied deformation in PFM is usually extremely small (a few picometers for an applied voltage of 1 V), making it sometimes hard to distinguish it from background noise. To increase the signal-to-noise/ratio, the simplest solution is to increase the reading voltage. Another solution adopted by the PFM community is to work in resonance-enhanced PFM mode (**Figure 23 a**).

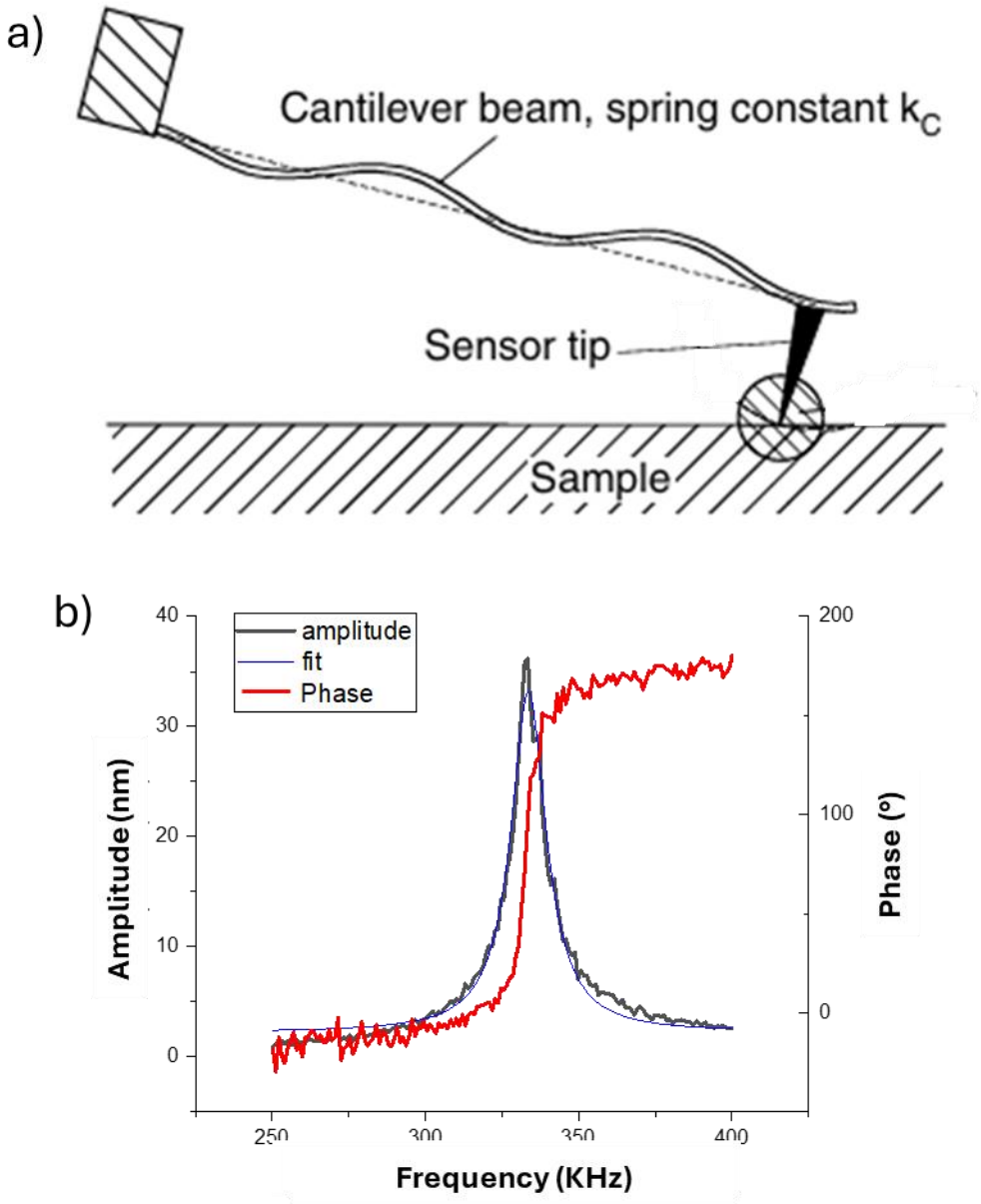

***Figure 23**: a) Illustration of AFM measurement in contact resonance mode. Figure adapted from [143]. b) Illustration of the signal amplification from a frequency ramp collected on a PZT sample.*

3.1.2.2 Spectroscopy mode

Local spectroscopic measurements can be performed to provide specific information on the local dynamics of domain switching and remanence of polarisation state. This mode is called switching spectroscopy PFM (ssPFM) [138].

In ssPFM, the electromechanical deformation and domain orientation are continuously monitored using a fixed V_{AC}, while a series of V_{DC} pulses is applied to the sample at a fixed position (see **Figure 24 a**). The pulse incrementally increases until reaching the desired maximum voltage (V_{max}). The pulses then decrease to $-V_{max}$ before returning to zero. Between each pulse, the V_{DC} voltage is released to allow measurement of the remnant response. The measure can be repeated at different V_{DC0} values with a fixed interval. The contact area during this stationary measurement is small, enabling the characterization of the coercive voltage, amplitude, and the phase of the material with high spatial resolution.

Those measurements give access to two different spectroscopic information: the off-field results and the on-field results.

The off-field measurement captures the material response once the DC voltage is released. The remnant polarisation is used to reconstruct ferroelectric hysteresis loops with minimal electrostatic artifacts, ensuring that only the intrinsic remnant polarisation is analysed. It is expected for a ferroelectric material that the vibration amplitude of domains polarised up and domains polarised down to be equal, with phase data separated by 180°. A transition is observed from one to another at the coercive voltages (see **Figure 24 b**).

The on-field measurement, on the other hand, captures the material response while DC voltage is applied. The resulting polarisation presents a slope compared to the off-field results originating from the supplementary electrostatic forces in presence (**Figure 24 c**).

Spectroscopic measurements are conventionally performed in Contact mode, during which a series of frequency sweeps of the applied AC excitation is collected. Each sweep is then fitted using a **Simple Harmonic Oscillator (SHO) model**, allowing extraction of the relevant contact-resonance parameters: the amplitude, phase, and amplification factor at the optimal (resonant) frequency (**Figure 23 b**).

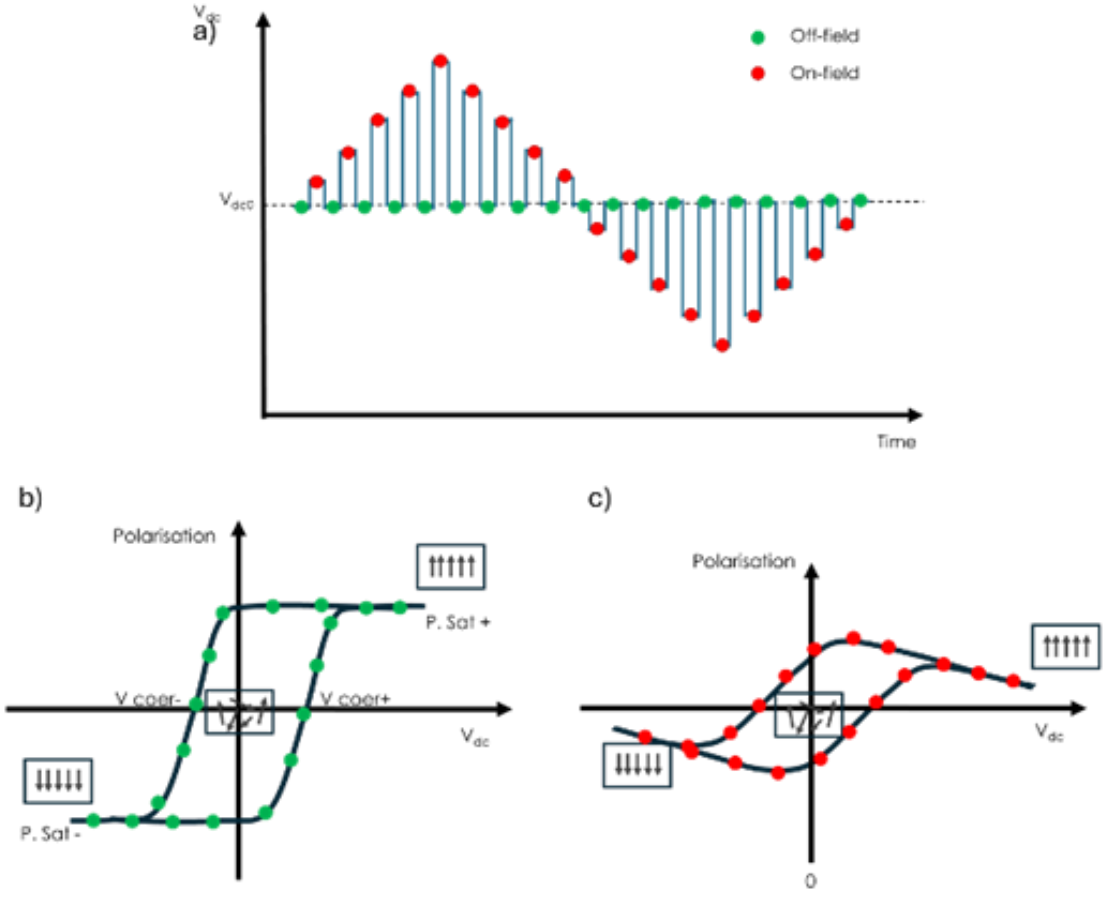

***Figure 24**:Representation of the V_{dc} pulses applied during an ssPFM measurement while V_{ac} is maintained constant. Reconstruction of the hysteresis loops from those pulse b) off-field and c) on-field.*

3.1.3 PFM operations mode

3.1.3.1 Single frequency PFM

Historically, PFM measurements were performed at a single low, non-resonant drive frequency, but this approach proves challenging for samples with weak piezoelectric responses. Due to the inherently low signal-to-noise ratio, the genuine piezoelectric signal is often masked by instrumental noise. To improve this ratio, measurements can instead be performed at the contact resonance frequency of the tip–sample system.

In contact resonance [143–145], the tip contacts the surface and is vibrated at one of its own vibration modes (see **Figure 23 a**). These contact resonance frequencies are directly dependent on the effective stiffness of the contact (k^*), derived from the tip-sample mechanical interaction. Operating at contact resonance significantly amplifies the electromechanical response, with the amplitude multiplied by the quality factor Q.

Depending on the material and environment, *Q* can range from several tens to several hundreds, producing a substantial enhancement of the detected signal (**Figure 23 b**).

Conventional CR-PFM imaging is performed at a fixed resonance frequency during the scan. Despite the large amplification, CR-AFM suffers from a major limitation: the resonance frequency is highly sensitive to variations in contact stiffness. Surface roughness or material heterogeneity alters the contact conditions, causing resonance shifts that generate topographic crosstalk. In heterogeneous systems such as nanocomposites, where constituents have distinct elastic moduli, local changes in stiffness further complicate a correct interpretation of the acquisition.

3.1.3.2 Dual-Frequency-Resonance-Tracking (DFRT)

A possible solution to overcome the potential shift problem in CR-PFM is to use a resonance tracking technique called **Dual-Frequency-Resonance-Tracking (DFRT)** [146].

In DFRT-PFM, the cantilever is driven using a linear combination of two sinusoidal voltages, one at a frequency below (f_1) and one above (f_2) the resonance frequency (f_0). The difference between these two drive frequencies (f_1-f_2) is typically maintained between 5-10 kHz. A position-sensitive detector measures the resulting motion of the cantilever, while two lock-in amplifiers extract the corresponding amplitudes (A_1, A_2) and phases (φ_1,φ_2). The resonance frequency is then tracked using a PID (Proportional, Integral, Differential) gain by maintaining A_1-A_2 = 0 at each point on the surface, ensuring that the system continuously adjusts to any shifts in resonance caused by changes in the sample's topography (**Figure 25**).

DFRT-PFM significantly enhances the signal-to-noise ratio, making it possible to study materials with low piezoelectric coefficients. With constant excitation, DFRT-PFM provides a much stronger signal than traditional PFM, allowing a reduction in the excitation amplitude, which in turn minimizes electrostatic forces. The ability to track the resonance frequency in real-time also protects DFRT-PFM from frequency shifts caused by topographical variations and electrostatic forces, leading to more accurate and reliable measurements.

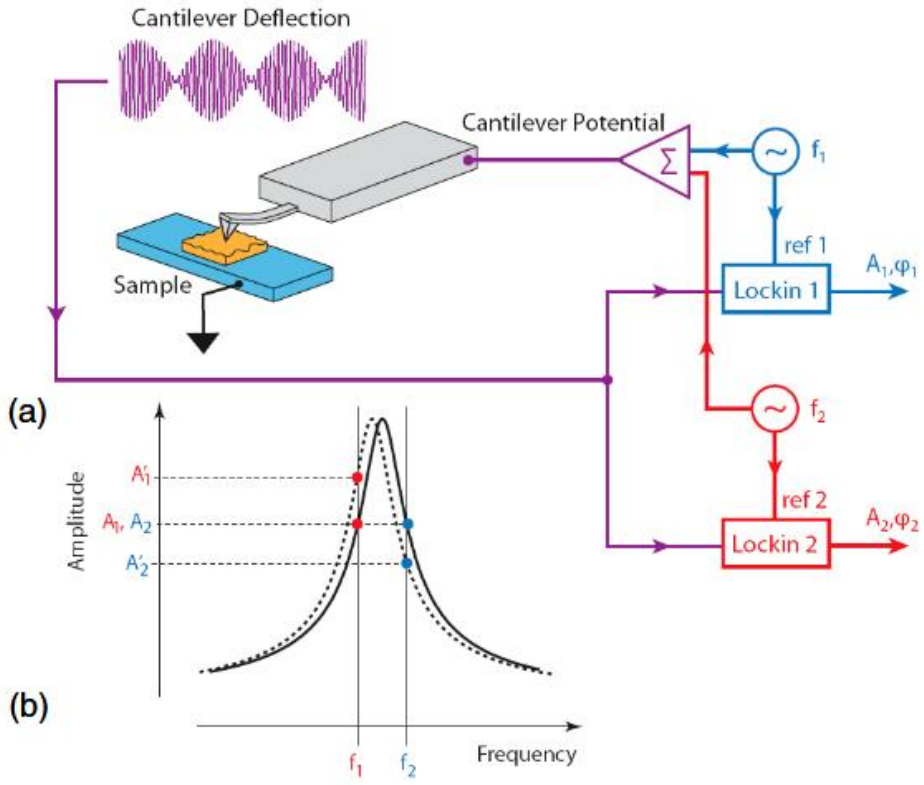

Figure 25 : (a) Schematic diagrams of the experimental set-up. (b) Principle of the dual-frequency excitation-based resonant-amplitude tracking. Figure from [146].

3.1.3.3 DataCube PFM

A recently developed method for probing local ferroelectricity is DataCube PFM [147,148]. DataCube CR-PFM is a hyperspectral Force-Volume technique that records at each pixel a force curve including a hold in contact segment. During this hold period, a frequency sweep of the AC excitation is performed, and the resulting response is fitted with a Simple Harmonic Oscillator (SHO) model. This allows direct extraction of key contact-resonance parameters (frequency, amplitude, phase, and Q-factor) from which quantitative CR-PFM maps can be generated. The force-curve portion of each DataCube simultaneously provides mechanical properties such as modulus and adhesion (Figure 2b), enabling multidimensional characterization from a single measurement.

Because the sweep duration, range, and sampling rate are user-defined, DataCube offers high accuracy and an excellent signal-to-noise ratio, with parameter extraction based on hundreds of data points. Compared to dual-frequency resonance tracking, this leads to substantial improvements, particularly in Q-factor determination. Moreover, since DataCube relies on Force-Volume imaging, the tip does not drag across the surface between pixels, eliminating lateral forces that typically damage sensitive samples and degrade probe sharpness. As a result, DataCube provides more consistent vertical measurements and is suitable for complex nanostructure normally harder to image in PFM.

3.2 Artifacts in PFM measurements

Even though Piezoresponse Force Microscopy is designed to detect electromechanical deformation, the measured signal is affected by several non-piezoelectric contributions, often referred to as artifacts [149]. These parasitic effects arise from the application of a local electric field and can even produce ferroelectric-like hysteresis loops on non-ferroelectric samples.

3.2.1 Electrostatic effect

Whenever an electrical bias is applied between a tip and the sample, electrostatic forces will arise[111,131]. Those forces are constituted of a local term, corresponding to the one between the apex of the tip and the sample, and a non-local one, corresponding to the one between the cantilever and the surface.

Those forces arise from the surface potential difference between the tip and the sample, their capacitive interaction, and the charge injection into the sample.

The general equation to represent the electrostatic force between the tip and the sample is the same as the one presented in KPFM [111] (**Eq. 31**). The electrostatic force at working frequency ω is expressed by the same expression as in **Eq. 32**.

Out of all artifacts, this one is considered the most problematic because it can be predominant (possibly overcoming the piezoelectric contribution), can induce ferro-like response on a non-ferroelectric sample [150], and the induced tip binding does not correspond to actual surface displacement.

Since this arises from the measurement set-up itself, complete removal of that effect is impossible. Still, a lot of work has been done to try to minimize the electrostatic contribution as much as possible.

To reduce the charge injection in the sample, the most obvious way is to apply the smallest possible voltage to the sample. It is also recommended after poling to scan the sample without bias to try to "release" all trapped charges at the surface.

To compensate for the surface potential difference between the tip and the sample V_{cpd}, measurement can be performed using a compensation bias $V_{dc0,}$ equal to the V_{cpd} value [132]. To do so complementary KPFM measurements are needed. Be careful that this value will change during the measurement because of the charge injection!

To minimize the capacitive interaction, the most direct method is to work with an optimised tip, with high rigidity and low "active cantilever surface", but often at the expense of the sensitivity [112,151]. A simple, effective solution proposed by Killgore *et al*. is to optimize the laser position on the cantilever so that it becomes insensitive to the bending specific to this effect [152]. This spot is called the ElectroStatic Blind Spot (ESBS).

The tip displacement associated with the electrostatic effect in PFM can be written as:

$$A_{es} = \frac{1}{k^*}\frac{dC(z)}{dz}(V_{DC} - V_{CPD})V_{ac}$$

Eq. 40

where k* is the effective rigidity of the tip sample system.

3.2.2 Vegard strain

Another important artifact in PFM is the Vegard strain effect. This effect arises from the presence of water at the surface of the sample, which leads to an electrochemical reaction under the electric field [153]. The application of the electric field causes the injection and ionic migration of species such as oxygen vacancies that are associated with a volumetric change under the tip. That reaction can damage the surface. This effect is mostly observed in ionically active materials.

The best way to reduce that effect to a minimum, besides working in a controlled environment, is to reduce the tension between the tip and the sample so that the activation energy threshold is not overcome. It is also recommended to work at high frequency, since it is based on slow ionic displacement [150]. Working at low temperatures is another solution.

The tip displacement associated with the Vegard strain effect in PFM is written as [154,155]:

$$A_{Veg} = \frac{2\frac{D(T)}{\omega}^{\frac{1}{2}}(1+\upsilon)\beta}{\eta V_{AC}}$$

Eq. 41

where *D(T)* is the diffusion coefficient, β is the Vegard coefficient, υ is the Poisson coefficient, η is extracted from the linear relation between chemical potential and the applied electric field, and ω is the working frequency.

3.2.3 electrostriction

Electrostriction is an intrinsic dielectric effect that, similarly to piezoelectricity, is the shape change of a material under an electrical field. The presence of this electric field induces an ionic displacement within the crystalline structure, creating a charge gradient. This charge difference induces an attractive Coulomb force between the two ends of the domain, resulting in the compression of the material [156]. Unlike piezoelectricity, there is no direct-reverse reciprocity.

As with the Vegard effect, this one is based on ionic displacement. The same type of precautions is therefore necessary: work at low voltage, high frequency, and low temperature.

This effect is more important when the sample is thin. It is therefore interesting to work on relatively thick samples.

The tip displacement associated with the electrostriction effect in PFM is written as [157]:

$$A_{est} = 2\frac{M_{333}}{t}V_{AC}V_{DC}$$

Eq. 42

where M_{333} is the electrostriction coefficient.

This coefficient being generally far lower than the piezoelectric one, the electrostrictive term is often ignored. The piezoelectric term is sometimes referred to as the electrostrictive term in literature, which can be quite confusing.

3.2.4 Joule effect

The Joule effect occurs when an electrical current is applied to a conductive material. The interaction between the electron flux and the atoms making up the material causes energy to be dissipated in the form of heat [158]. In PFM measurements, this is accompanied by thermal expansion of the material that is perceived by the tip.

There is no real solution to avoid this effect.

The tip displacement associated with the Joule effect in PFM is written as:

$$A_{jou} = \frac{\beta_{jou}}{R}2V_{AC}V_{DC}$$

Eq. 43

where β_{jou} is the transduction factor (which allows to go from a power to a displacement: $\Delta Z=\beta_{jou}P$) and R is the resistance of the material.

3.2.5 Flexoelectricity

Flexoelectricity is a property present in every dielectric, which is independent of the internal symmetry of the system. The inverse flexoelectric effect is the deformation of the sample under an electrical field gradient and is written as:

$$\sigma = \mu\Delta E$$

Eq. 44

where σ is the mechanical constraint, and μ is the flexoelectric tensor of order 4.

This effect is known to be extremely weak but becomes relevant at the nanoscale [159,160].

Since this effect is gradient-dependent, the best way to minimize it is to minimize the gradient. A good way to do so is to reduce the tension between the tip and the sample, working on a thick sample or increasing the tip sample surface area by working at low forces or by increasing the radius of the tip.

The tip displacement associated with the flexoelectric effect in PFM is written as:

$$A_{flex} = \mu_{3333} V_{AC}$$

Eq. 45

The resulting global displacement of the tip in PFM is:

$$A_{total} = A_{piezo} + A_{es} + A_{Veg} + A_{est} + A_{jou} + A_{flex}$$

Eq. 46

Those different artifacts are summarized in **Table 3**.

***Table 3**: Summary of PFM artifacts, their supposed origin, and solution to reduce them.*

Artifact	Origin	minimisation
Electrostatic effect	Charge difference Charge injection Capacitive coupling	ΔV minimisation Increase contact stiffness ESBS
Vegard strain	Ionic migration	ΔV minimisation Working at high frequency
Electrostriction	Dipole alignment	ΔV minimisation Working at high frequency Thick sample
Flexoelectricity	Polarisation under stress gradient	electrical gradient reduction (ΔV minimisation, increase contact surface area, work with thick sample, ...)
Joule	Thermic dilatation	/

3.3 Verification of the true ferroelectric nature of the signal

Historically, the presence of a hysteresis loop after an off-field measurement was considered as the definitive proof of the ferroelectric nature of the response. However, it has since been recognized that artifacts can create fake ferroelectric-like hysteresis

loops, even in non-ferroelectric materials [131,161,162]. Different precautions need to be undertaken to improve the quality of the signal (**Table 3**). Complementary measurements are performable to ensure the true ferroelectric nature of the measured signal.

3.3.1 On-off-field comparison

A first straightforward approach is to check for the presence of hysteresis in both on-field and off-field measurements. Although the on-field loop is typically distorted by electrostatic contributions, resulting in a sloped or asymmetric shape and reduction of the apparent coercive voltage, the simultaneous observation of switching in both modes strengthens confidence in a ferroelectric origin. Nevertheless, this criterion alone is often insufficient, especially for materials with low piezoelectric coefficients or strong ionic activity.

3.3.2 Contact Kelvin Probe Force Microscopy (cKPFM)

Another spectroscopic approach described in the literature is contact Kelvin Probe Force Microscopy (cKPFM), introduced by Balke *et al*. [163]. This method provides valuable insight into the true ferroelectric origin of the measured signal. cKPFM is conceptually derived from ssPFM: by collecting a series of off-field hysteresis loops at different values of the applied DC "writing voltage" (V_{dc_0}), it becomes possible to reconstruct the piezoresponse as a function of the writing voltage for each polarisation step (see **Figure 26**). From this dataset, the contact surface potential is defined as the value of the applied potential at which the electrostatic responses is nulled. This parameter reflects charge dynamics at the tip–sample interface and is analysed to distinguish ferroelectric switching from electrostatic or ionic contributions.

Additionally, the evolution of the piezoresponse as a function of the writing voltage provides valuable insight into the genuine ferroelectric nature of the measured signal. In a manner analogous to conventional ferroelectric hysteresis loop measurements based on a DC bias, a true ferroelectric material is expected to exhibit a well-defined bistability between two stable polarization states. When the applied writing voltage V_{dc0} exceeds the coercive voltage V_{dc} the piezoresponse reaches a saturation regime corresponding to complete dipole switching, leading to a plateau in the measured response **(Figure 26 b).**

In contrast, materials that do not exhibit intrinsic ferroelectricity typically show a continuous and gradual evolution of the piezoresponse with increasing writing voltage, without any clear saturation or stable plateau. Such behaviour reflects the absence of switchable polarization states and is characteristic of non-ferroelectric or purely electrostatic or piezoelectric responses **(Figure 26 c)**.

This qualitative distinction between bistable and continuous voltage-dependent responses constitutes a robust criterion for discriminating genuine ferroelectric

behaviour from artefactual or non-ferroelectric contributions in PFM-based measurements.

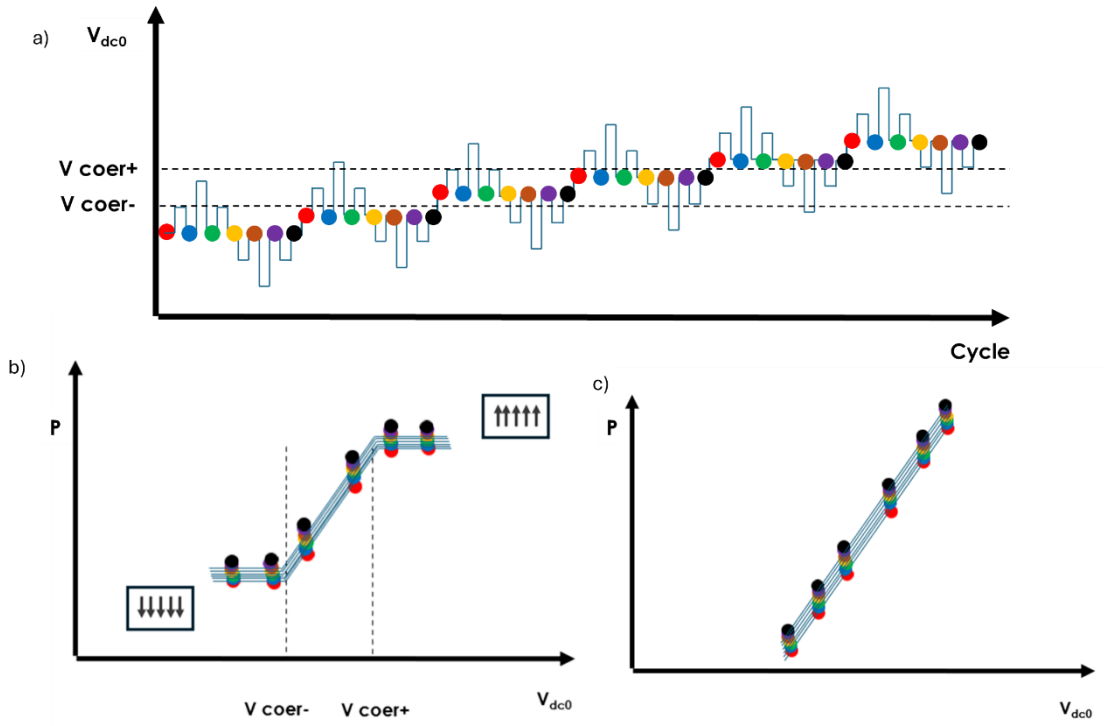

***Figure 26**: (a) Illustration of DC waveform used in cKPFM, where the reading voltage varies between each cycle and the waveform is repeated for measuring the response at different V_{dc0} voltages. Expected responses as a function of V_{dc0} (b) on a ferroelectric sample and (c) on a non-ferroelectric sample.*

Chapter 4: Materials and Methods

4.1 Sample preparation

This section details the synthesis of ferroelectric nanoparticles and the fabrication of polymer and composite thin films. The preparation protocols are optimized to ensure homogeneous dispersion, controlled thickness, and suitable electrical and mechanical properties for reliable AFM-based nanoscale characterization.

4.1.1 Ferroelectric nanoparticles synthesis

Ferroelectric bismuth ferrite oxide ($BiFeO_3$, BFO) nanoparticles are synthesized at the LPNE laboratory following an adapted sol–gel route inspired by several procedures reported in the literature.

The synthesis begins with the dissolution of bismuth nitrate pentahydrate [$Bi(NO_3)_3{\cdot}5H_2O$] (Aldrich, CAS:10035-06-0) and iron nitrate nonahydrate [$Fe(NO_3)_3{\cdot}9H_2O$] (Aldrich, CAS:7782-61-8) in equimolar proportions in ethylene glycol (Aldrich, CAS:107-21-1). Upon dissolution, both precursors dissociate into their respective metal cations and nitrate anions:

$$Bi(NO_3)_3.5H_2O\ (s) \xrightarrow{H_2O} Bi^{3+} + 3NO_3{}^{-} + 5H_2O$$

$$Fe(NO_3)_3.9H_2O\ (s) \xrightarrow{H_2O} Fe^{3+} + 3NO_3{}^{-} + 9H_2O$$

Ethylene glycol is selected as a solvent due to its favourable chelating properties and its tendency to promote phase purity [164,165] over other commonly used solvents, like acetic acid [166], and 2-methoxyethanol [167]. The precursor solution is magnetically stirred at 80 °C for 2 hours, leading to a homogeneous reddish solution.

During subsequent heating and solvent evaporation, hydrolysis reactions occur, forming metal hydroxide species:

$$Bi^{3+} + H_2O \rightarrow Bi(OH)^{2+} + H^{+}$$

$$Fe^{3+} + H_2O \rightarrow Fe(OH)^{2+} + H^{+}$$

These species undergo progressive condensation reactions, resulting in the formation of a three-dimensional metal–oxygen network:

$$M{-}OH + HO{-}M \rightarrow M{-}O{-}M + H_2O\ (M = Bi \text{ or } Fe)$$

Drying at 150 °C yields a xerogel, during which volatile by-products such as NO_2 and H_2O vapour are released. The xerogel is then annealed at 600 °C for 1 hour under a nitrogen atmosphere, promoting crystallization of the perovskite $BiFeO_3$ R-phase [168]. This can be summarised as:

$$BiFe(OH)_6 \rightarrow BiFeO_3 + 9H_2O$$

After thermal treatment, the resulting powder is finely ground in an agate mortar and leached in dilute nitric acid to remove secondary phases, followed by washing and centrifugation [169]. The complete synthesis process is summarized in **Figure 27**.

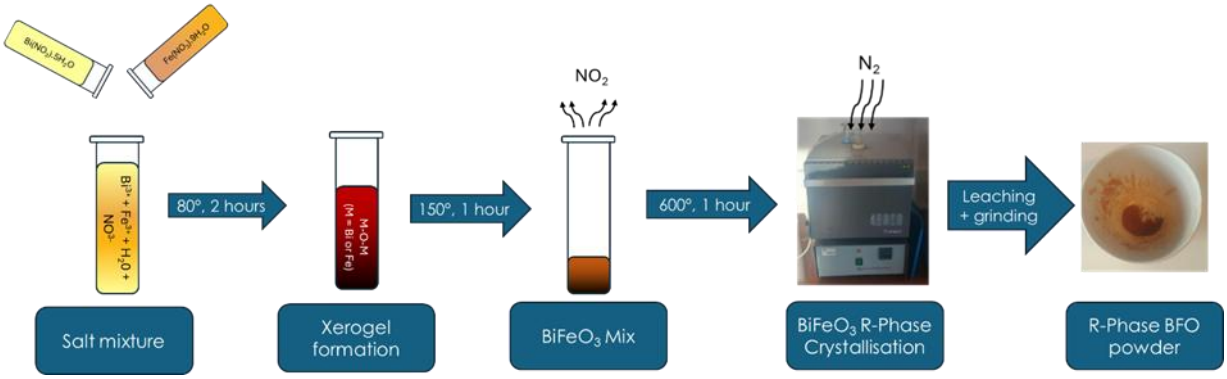

***Figure 27** : Sol-gel fabrication process of BFO particles.*

4.1.2 Polymer thin film for SPM measurements

A wide range of procedures has been explored for the preparation of PVDF-based samples, including electrospinning [140], spin-coating [170], dip-coating [171], solvent casting [172], and 3D printing [173], particularly. To ensure that studied samples are easily analysed in SPM modes while requiring only a relatively low voltage range, they are prepared in the form of thin films. Among the various fabrication methods available, spin-coating and dip-coating represent the most cost-effective techniques to produce uniform polymer films with a controlled thickness [174]. Among the methods enabling the deposition of homogeneous and reproducible layers suitable for nanoscale characterization. However, after several optimization trials, the spin-coating proves to be the best technique for the preparation of our composite films. The integration of particles inside the polymer matrix is by far more effective with spin-coating, although dip-coating allows for a more uniform layer of polymer (*vide infra*, **section 5.2**).

Pure PVDF-TrFE thin films are prepared using a 5 wt.% solution of PVDF-TrFE 70:30 (Piezotech – Arkema, FC 30, CM5758) dissolved in a DMF–acetone mixture (Aldrich, CAS:68-12-2 and CAS:67-64-1). This solution is magnetically stirred for several hours to ensure complete dissolution of the polymer. The samples are then spin-coated at 4000 rpm for 30 s with an acceleration of 300 rpm/s onto conductive ITO-coated glass substrates (R = 70–100 Ω/sq, Aldrich CAS:50926-11-9). The substrates are previously cleaned in an RBS bath, rinsed with distilled water, and dried under N_2 flux.

PVDF-TrFE/BFO composite thin films are produced using the same polymer solution (5 wt.%) with the addition of BFO powder to obtain a composite containing 5 wt.%. BFO relative to PVDF-TrFE. This proportion results in relatively small and well-dispersed particle aggregates in the matrix [13]. The mixture is sonicated in water bath for 2 hours to

achieve uniform dispersion of the particles prior to spin-coating onto ITO substrates. The same spin-coating parameters as for the pure PVDF-TrFE films are used.

BFO particles are also prepared as a thin film of conductive polymer matrix, maintaining the isolated particles. This matrix serves to mechanically stabilize the particles during AFM measurements to ensure an electrical connection between the polymer and the ITO surface. An aqueous PEDOT:PSS solution is chosen for this purpose [175]. BFO powder is added to reach 0.25 wt.%. The mixture is then sonicated in water bath for 2 hours to ensure uniform dispersion of the particles before spin-coating onto ITO substrates.

All thin film samples are annealed at 140 °C for 2 hours with a heating and cooling rate of 1 °C/min. For the PVDF-TrFE-based films, annealing at this temperature increases the proportion of the β-crystalline phase (confirmed by Raman spectra) [176] and thereby enhances the intrinsic ferroelectric properties of the polymer [177,178]. For the PEDOT:PSS-based films, annealing at this temperature decreases the resistivity of PEDOT:PSS [179].

No supplementary poling procedure is necessary to observe ferroelectric domains in PVDF-TrFE films. Film thicknesses are measured by making a scratch measured by AFM and further confirmed by ellipsometry.

4.2 Structural characterization

In addition to SPM-based measurements, complementary characterization techniques were used to evaluate the structural, morphological, and optical properties of the samples. X-ray diffraction, spectroscopic ellipsometry, and environmental SEM provide essential validation of phase purity, film thickness, and morphology, supporting the interpretation of nanoscale electromechanical measurements.

4.2.1 X-Ray Diffraction

X-ray diffraction (XRD) measurements are based on the scattering of incident X-rays by the periodic arrangement of atoms within a crystalline material. When X-rays interact with the electron clouds surrounding the atoms, they are diffracted in specific directions determined by the crystal structure. The resulting diffracted beams are collected by a detector, producing a diffractogram that displays the intensity of the scattered X-rays as a function of the diffraction angle. This pattern provides information about the atomic arrangement and crystalline phases present in the material.

X-ray diffraction measurements rely on the Bragg model of diffraction. In this model, each reflection is associated with a family of crystallographic planes, regularly spaced atomic layers visualized as sheets passing through the lattice. Bragg's law establishes the relationship between the interplanar spacing d, the X-ray wavelength λ, and the angle of incidence θ according to the following equation:

$$n\lambda = 2dsin(\theta)$$

Eq. 47

where *n* is the order of diffraction.

The position and intensity of the diffracted peaks depend on the crystal structure and symmetry (space group) of the analysed material, enabling both phase identification and quantitative analysis of crystalline components.

In this thesis, XRD analysis is performed on an Panalytical Empyrean diffractometer with a Cu kα radiation source and a detector PIXcel1D (RTMS detector). It is employed to determine the crystalline phases of the BFO particles synthesized via the sol–gel method. Those measurements were performed in the "Service de Science des Matériaux" at the University of Mons with the help of Prof. Maurice Gonon.

4.2.2 Ellipsometry

Ellipsometry is an optical characterization technique used to analyse thin films and surfaces by measuring the changes in the polarisation state of light upon reflection or transmission through a sample. In this technique, a beam of polarized light is directed at the sample surface at an oblique angle of incidence. The polarisation state of the reflected or transmitted light varies depending on the film thickness, refractive index, and absorption properties (**Figure 28**).

These variations are described by two measurable parameters: Ψ (psi) representing the amplitude ratio and Δ (Delta) representing the phase difference between the in-plane (p-polarized) and out-of-plane (s-polarized) light components. By analysing Ψ and Δ as a function of wavelength or angle of incidence, it is possible to determine the film optical constants (refractive index n and extinction coefficient k) and thickness with high precision.

This determination is indirect because Ψ and Δ cannot be directly converted into the optical constants of the material. Instead, a model-based fitting approach is required in which theoretical data are iteratively compared to experimental measurements until the best agreement is achieved.

$$\rho = tan\,(\psi)e^{i\Delta}$$

Eq. 48

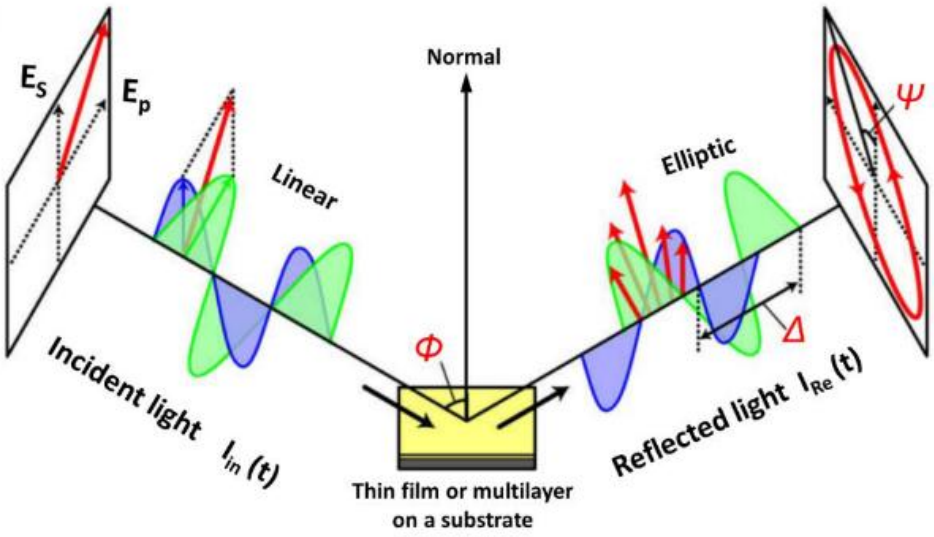

***Figure 28** : Schematic illustration of a spectroscopic ellipsometry set-up. Figure adapted from [180].*

The ellipsometry measurements are carried out on a Park Accurion EP4 spectroscopic imaging ellipsometer. The EP4 is operated in PCSA mode in a 400-800 nm spectral range. The angle of incidence is set to 50 degrees. The signal is collected through a Nikon Plan SLWD 10X\0.21.

The modelling of the ellipsometry data is done with the EP4-Model software (Park-Accurion), assuming sharp interfaces between the layers. Roughness is handled within the Effective Medium Approximation (EMA). Those measurements were performed in the Laboratory of Physics of Materials and Optics (LPMO, UMONS), with the help of Prof. Michel Voué.

4.2.3 environmental Scanning Electron Microscopy (eSEM)

Scanning Electron Microscopy (SEM) is an imaging technique that uses a focused beam of high-energy electrons under high vacuum to examine the surface structure of a sample. When the incident electron beam interacts with the atoms of the sample surface, it generates various signals such as secondary electrons, backscattered electrons, and characteristic X-rays. These signals are collected and analysed to produce detailed structure images and chemical composition images. The intensity of emitted secondary electrons provides high-resolution topographical contrast, allowing visualisation of surface morphology at the nanoscale.

Conventional SEM analysis requires the sample to be electrically conductive or coated with a thin conductive layer to prevent electrostatic charging under the electron beam. In contrast, environmental SEM (eSEM) mitigates this limitation by operating in a controlled gaseous environment at a much higher pressure than conventional SEM systems (**Figure 29**). This configuration relies on differential pressure chambers and a metallic enclosure to maintain stable imaging conditions. That enables the examination of non-conductive or hydrated samples without the need for conductive coating, making this is type of measurement compatible with AFM measurement.

In this work, eSEM measurements are employed as a complementary technique to AFM, providing detailed imaging of the film structure and confirming the dispersion and integration of BFO nanoparticles within the polymer matrix. Measurements are performed using a ThermoFisher Quattro S instrument. All measurements were performed in high vacuum, detecting the secondary electron.

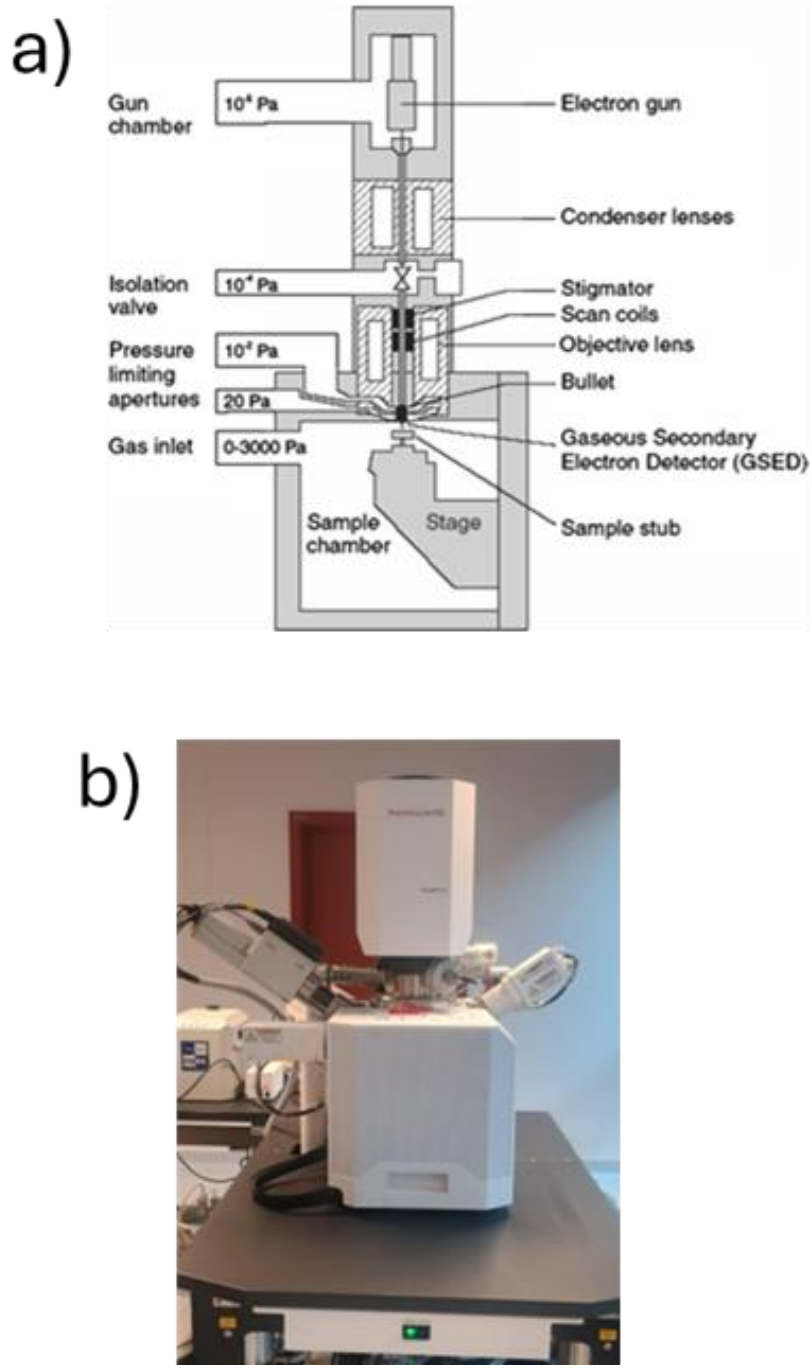

Figure 29 *:(a) Schematic representation of an eSEM apparatus. Figure adapted from [181]. (b) Thermofisher quattro S eSEM apparatus coupled with an EDX detector present in the LPNE lab.*

4.3 Scanning Probe Microscopy experimental conditions

All mechanical, electrical, and electro-mechanical AFM measurements in this study are performed with a Dimension Icon AFM instrument (**Figure 30 a**) (Bruker Nano Inc., Santa Barbara, CA, USA). Specific cantilevers and supplementary modules are employed depending on the measurement mode. Data analysis is carried out using Nanoscope Analysis® 3.0 (Bruker) and Mountains® 11.2 (DigitalSurf) software.

Electrical contact is established between the conductive AFM tip (top electrode) and the ITO-coated glass substrate (bottom electrode), with a metallic pin connecting an exposed area of the ITO to the AFM circuitry.

A supplementary module HFL2LI from Zurich Instruments (Zurich, Switserland) is used for KPFM and DFRT measurement. The control of this system is based on the LabOne® software.

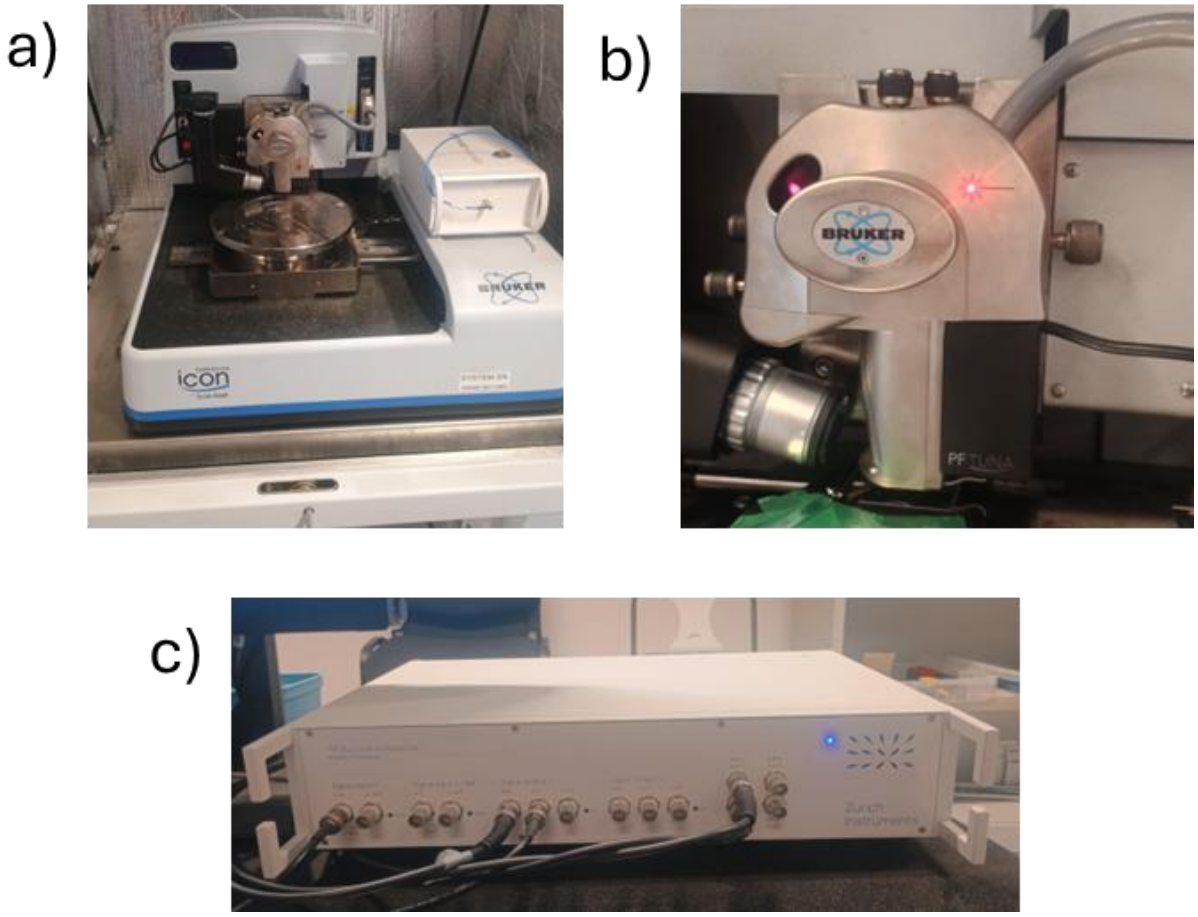

***Figure 30**: (a) Dimension icon AFM used for all the different AFM measurements, (b) Pre-amplifier module attached to the AFM scanner head, necessary for C-AFM-type measurement and (c) HF2LI lock-in from Zurich instrument used both for heterodyne-KPFM and DFRT-PFM.*

4.3.1 Peak Force QNM

Morphology and mechanical properties of the samples are investigated using PeakForce Quantitative Nanomechanical Mapping (PF-QNM) mode. The cantilevers used for these measurements are RTESPA-300-30 probes (Bruker) with a nominal spring constant of approximately 40 N/m and a tip radius of around 30 nm.

To proceed with the peak force measurement, the tip is calibrated in two steps.

First, the deflection sensitivity is determined from force–distance curves acquired on a rigid reference sample (sapphire). It is the conversion parameter from the voltage measured on the photodiode and the actual tip displacement. Since the sapphire does not deform under the applied force, the measured z-displacement corresponds directly to the cantilever deflection. The exact spring constant of the tip is then refined from these measurements.

Secondly, a semi-quantitative calibration is performed to determine the Young's modulus of the studied samples. A conventional PeakForce measurement is carried out on a calibration sample with a known modulus like that of the investigated material. The effective contact radius and other parameters are adjusted until the measured modulus matches the expected value. For this purpose, a PMMA film (E = 3.1 GPa) is used for the calibration.

The measurement parameters are optimized to ensure accurate spectroscopic data. The oscillation amplitude is between 20 to 50 nm, the scan rate is approximately 0.4 Hz, and the force setpoint is between 20 to 60 nN. This range provides sufficient indentation (a few nanometres) for accurate measurement while maintaining elastic deformation. Data are collected at 256 × 256 pixel resolution. The choice of the mechanical model and the extraction of the Young's modulus is performed with a Python code, PyCAROS, developed in the laboratory [182,183].

4.3.2 Conductive AFM (C-AFM)

The local conductivity of our samples is investigated using conductive AFM (C-AFM). This technique requires an additional current preamplifier module (see **Figure 30 b**) to detect currents in the picoampere range. To increase the stability of the measurement and assess the current measurement over a range of voltage, data were collected as DataCube C-AFM. Each pixel is a Force curve with the application of a voltage ramp during a fixed hold time. It allows the reconstruction of current maps at different voltages.

Measurements are performed using PFTUNA probes (Bruker), which are Pt/Ir-coated silicon nitride tips with a triangular geometry and a spring constant of 0.4 N/m. The setpoint is fixed around 20 nN to ensure stable contact. A hold time of 50 ms is applied during I–V mapping, with voltage going from -10V up to 10V. Data are acquired with 32 × 32 or 64 × 64-pixels resolution.

4.3.3 Kelvin Probe Force Microscopy (KPFM)

The surface potential of our sample is determined with heterodyne KPFM. The tips used for those measurements are SCM-PIT-V2 tips (Bruker), (k = 3N/m) tips with a conductive coating of Pt/Ir.

As explained in **section 2.4.2**, this measurement mode requires tracking two specific frequencies (ω_0 and ω_1). Because the Icon-AFM cannot perform this directly, an external HF2LI lock-in amplifier (Zurich Instrument) is integrated into the setup to detect the frequency difference between the frequencies (**Figure 30 c**).

The setup AFM-HF2LI for heterodyne KPFM measurement is described in (**Figure 31**). The HF2LI module receives in input the vertical signal from the AFM through the vertical output of the Signal Access Module (SAM) (indicated in red). From this signal, both the amplitude and the ω_0 are collected. The HF2LI takes control of the V_{ac} $(\omega_1-\omega_0)$ signal by sending it to the output to the sample bias input of the SAM (indicated in blue). The PID system adjusts the V_{DC} value to nullify the difference between the V_{DC} and the V_{CPD}. The V_{DC} signal is sent back to the HF2LI to add the V_{DC} to the V_{AC} signal (indicated in green). The resulting measurement of the surface potential is transferred to the Nanoscope controller input from the auxiliary output of the HF2LI (indicated in yellow)

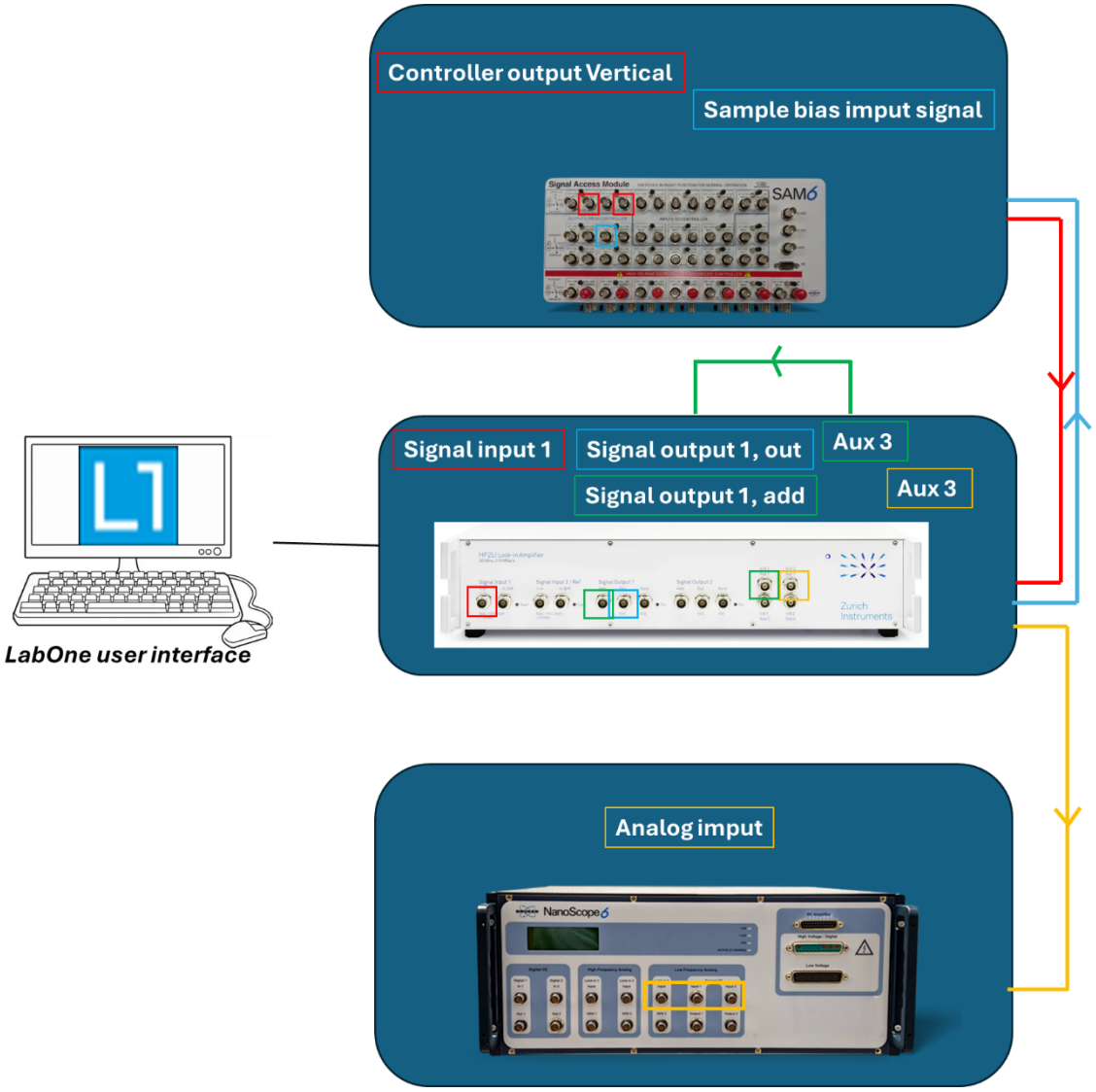

***Figure 31** : Coupling of the HF2LI to the AFM set-up for heterodyne KPFM measurement.*

Before all KPFM measurements, the tip work function is calibrated using a reference sample composed of three metallic strips (gold, aluminium, and silicon) with known work functions. The measured surface potential over these materials is used to determine the effective work function of the tip.

4.3.4 Piezoresponse Force Microscopy (PFM)

All PFM measurements performed in this work are carried out in contact resonance (CR-PFM) mode using SCM-PIT-V2 tips. The setpoint force is adjusted between 40–80 nN,

resulting in contact resonance frequencies ranging from 200–350 kHz (vertical) and 600–800 kHz (lateral), depending on the sample. Unless stated otherwise, all measurements are performed at a probing voltage of 1V and a scan angle of 0°.

For CR-PFM imaging, the resonance frequency is first identified by recording a single frequency sweep from which a Simple Harmonic Oscillator (SHO) fit extracts the CR-Frequency. The excitation frequency is then set slightly below the maximum resonance peak to avoid phase shift artifacts.

For frequency-tracking mode, the same HF2LI lock-in amplifier is used in KPFM measurements and is connected to the AFM. It enables real-time tracking of resonance shifts while maintaining the amplitude difference at 0. PFM images are recorded at a 256 × 256 pixel resolution.

The setup AFM-HF2LI for DFRT-PFM measurement is described in **Figure 32**. The HF2LI module receives as input the vertical or the lateral signal from the AFM through the vertical/lateral output of the SAM (indicated in red). Both can be collected at the same time. The HF2LI takes control of the V_{ac} signal by sending it to the output to the sample bias input of the SAM (indicated in blue). The lock-in system allows the generation of the two satellite frequencies around the resonance frequency, while the PID tracks and keeps the difference of amplitude of those two frequencies null. The resulting measurement of the vertical and/or lateral amplitude and phase signal is transferred to the Nanoscope controller input from the auxiliary output of the HF2LI (indicated in yellow).

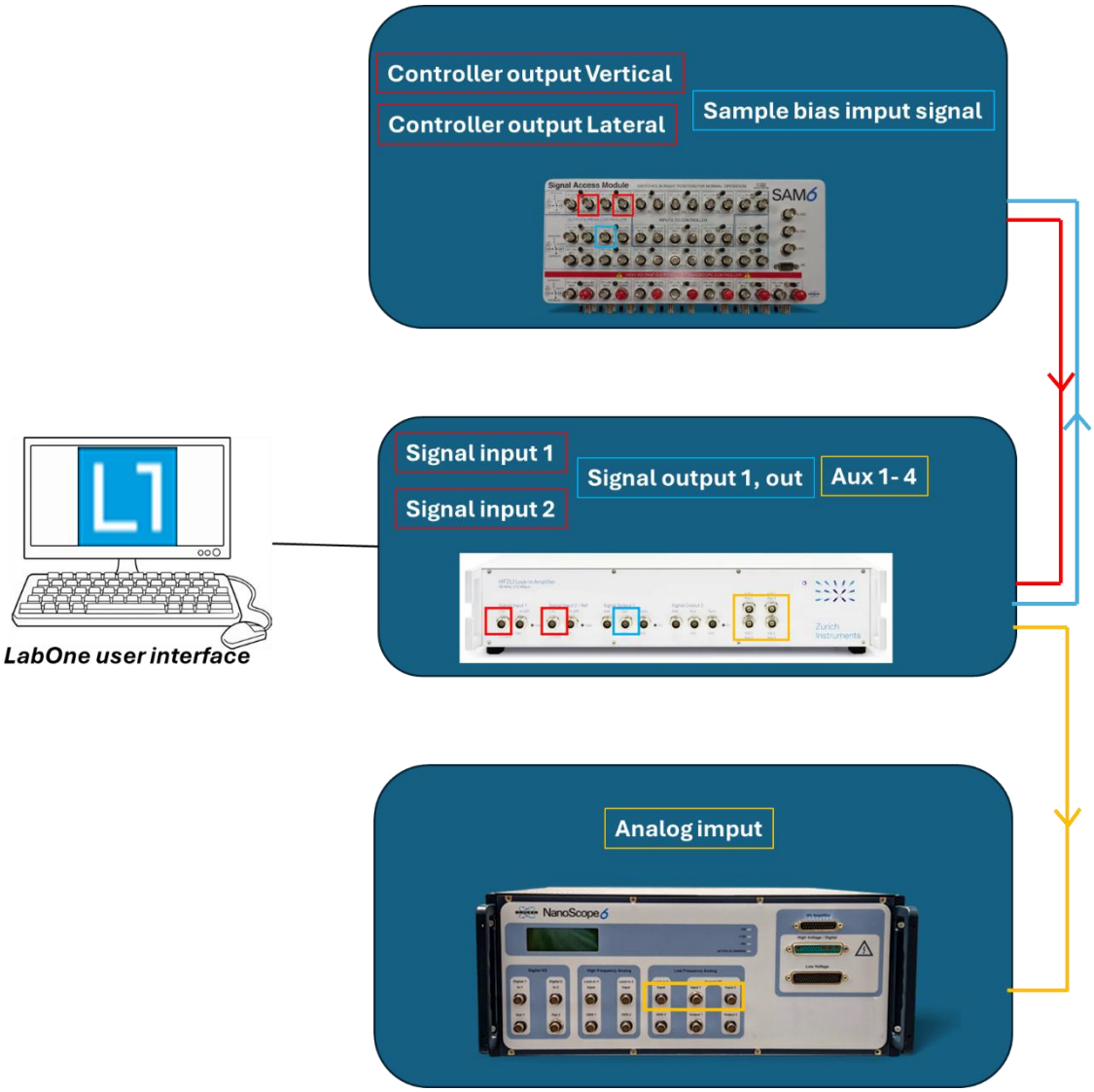

***Figure 32** : Coupling of the HF2LI to the AFM set-up for DFRT-PFM measurement.*

Local hysteresis loops are measured using the ssPFM mode. Measurement parameters (setpoint and frequency range) are like those used for conventional PFM imaging. Each loop consists of up to 10 voltage cycles, with polarisation voltage being between −10 V and +10 V. The reading voltage of each cycle is either kept constant at a 0 value or at several volts for the cKPFM measurement. Both on-field and off-field responses are recorded. The hold time for each sweep ranges from 10 to 30 ms. The measurements are performed either in a single location or as grids. The grids are analysed with the help of the pyssPFM software [184] to analyse and to map the ferroelectric distribution.

Local apparent d_{33} evaluations (d_{33}^{app}) are carried out on pre-identified regions of interest. Successive frequency sweeps are performed after local polarisation. Using the ssPFM function with zero-polarisation voltage, thousands of frequency sweeps are saved in a single measurement while reducing the presence of electrostatic forces. Apparent surface displacement D (corresponding to A_{piezo}) is extracted from SHO data using $A_{piezo} = A_0 + A_{1\omega} sin(\omega t + \varphi)$

Eq. *37*. d_{33}^{app} is determined from the linear regression of D as a function of V_{ac}.

The distribution of apparent surface displacement D across samples is investigated using DataCube PFM (DataCube PFM or FFV PFM) [147]. In this spectroscopic mode, force curves are recorded at each pixel, maintaining a short contact period (30 ms) during which a frequency sweep is applied. SHO fit measures different PFM parameters. The resulting parameter maps allow reconstruction of D as well as access to local mechanical parameters such as adhesion and local contact resonance. DataCube PFM mappings are recorded with a resolution of 64 × 64 or 128 × 128 pixels.

Before all PFM measurements, the position of the laser reflection on the cantilever is optimised to coincide with the electrostatic blind spot (ESBS) located approximately at two-thirds of the cantilever length (see **Figure 33**) to minimise electrostatic artifacts (*vide supra,* **section 3.2**). The deflection sensitivity and spring constant of the tips are determined following the same calibration procedure as in Peak Force measurements. Phase calibration is performed on a reference PZT sample exhibiting well-defined up and down ferroelectric domains (see **Figure 34**) [185].

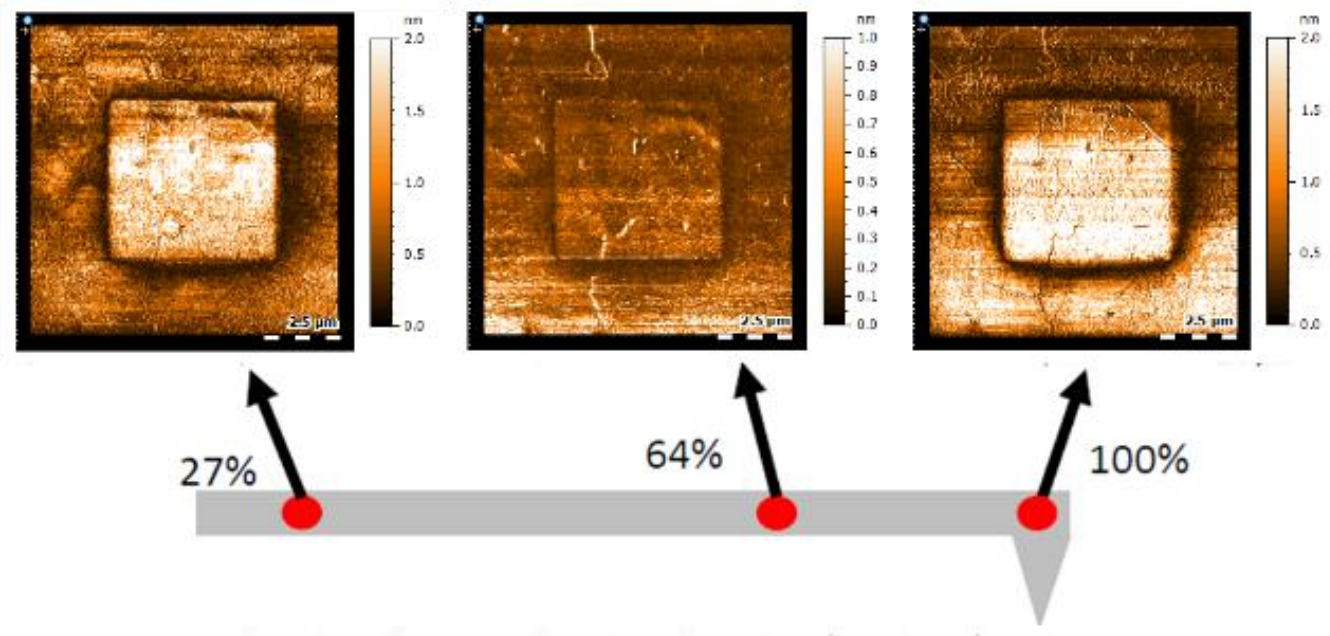

Figure 33 *: Demonstration of the electrostatic blind-spot on a PZT sample after poling square in opposite direction. Amplitude image collected after moving the laser reflection on the cantilever of the tip at 1/3, 2/3, and the end of the cantilever.*

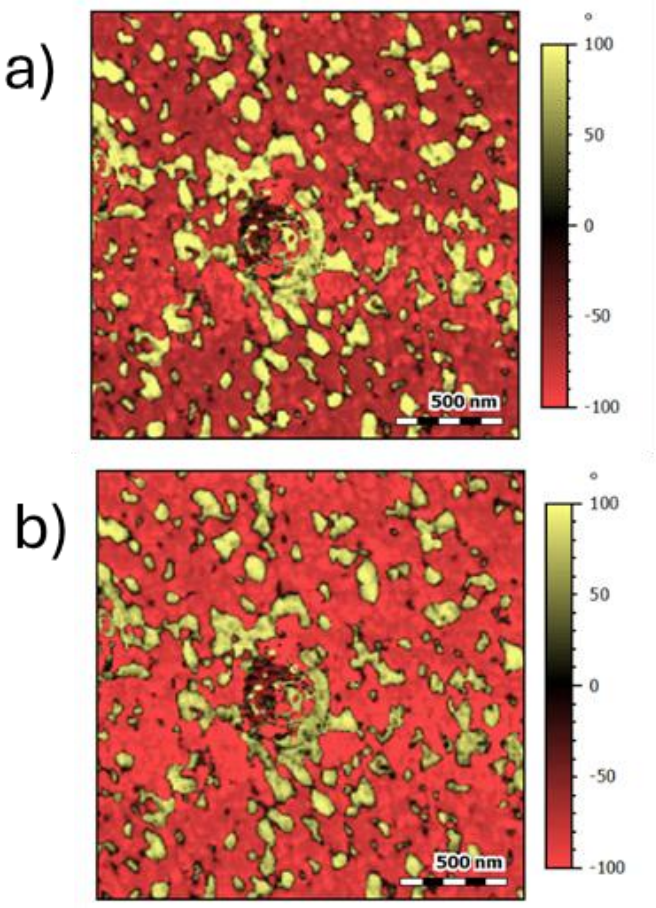

Figure 34 *: Illustration phase offset correction: (a) Phase image without phase correction, (b) Phase image after applying a phase offset correction.*

Chapter 5: Structural, mechanical and electrical characterisation of thin films

5.1 Structural characterisation by eSEM imaging and X-Ray diffraction

5.1.1 PVDF-TrFE thin film

A known limitation of conventional SEM is the need to coat organic samples with a thin conductive layer, typically gold or carbon, to prevent charging and obtain usable images. Environmental SEM (eSEM) overcomes this constraint by operating at pressures significantly higher than those of conventional systems, enabling the imaging of insulating materials without surface metallization.

The eSEM images acquired on the PVDF–TrFE thin films reveal a uniform fibrillar morphology (**Figure 35 a-b**), with features on the order of several tens of nanometres. This structure is consistent with the lamellar arrangements usually reported for spin-coated PVDF-based films, which arise from the intrinsic crystalline organization of the polymer [186]. In some zones, isolated areas appear devoid of polymer, likely due to slight non-uniformities during deposition or local redistribution of polymer chains during solvent evaporation.

The same characteristic morphology is also visible in the AFM topography images (see **Figure 41 a**), further confirming the nanoscale fibrillar structure of the films.

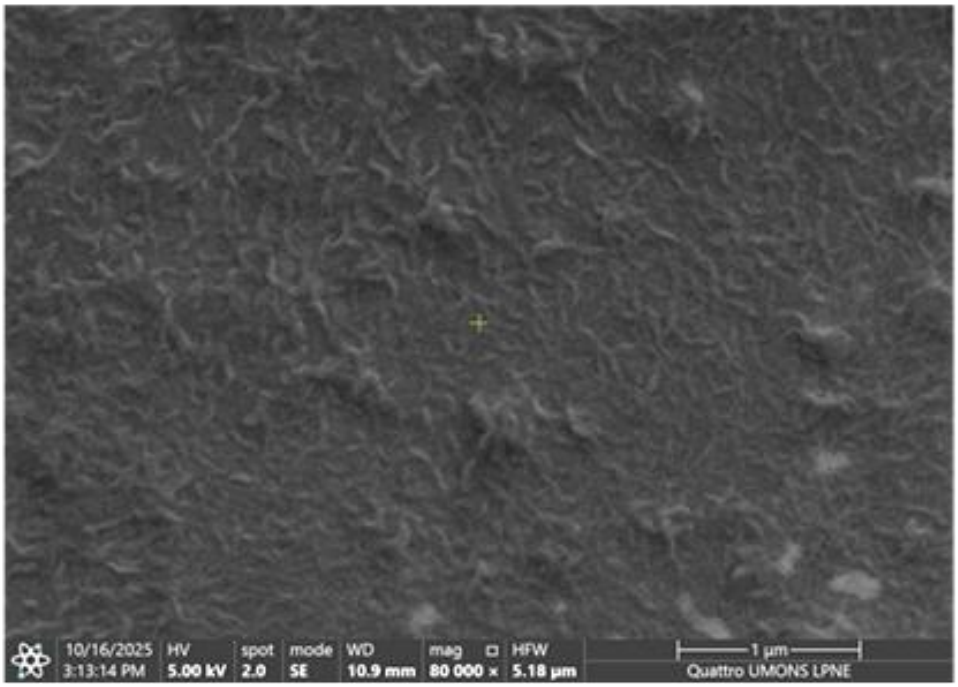

***Figure 35** : eSEM image of the PVDF-TrFE spin-coated thin film.*

5.1.2 BFO particles

As described in the previous chapter, the BFO particles were synthesized using a sol–gel route. The X-ray diffraction pattern of the cleaned BFO powder (**Figure 36 a**) confirms that the dominant phase is the rhombohedral (R) perovskite phase, which corresponds to the main ferroelectric form of $BiFeO_3$ (JCPDS No. 71-2494). In addition to this main phase, minor residual fractions of a cubic BFO-related phase ($Bi_{36}Fe_{24}O_{57}$) and hematite (Fe_2O_3) were detected, indicating incomplete phase purification through the cleaning protocol.

Environmental SEM imaging performed on the calcined powder (**Figure 36 b**) shows that the synthesized BFO particles have sizes ranging from approximately 50 to 200 nm with an average around 120 nm, and are relatively dispersed. It is consistent with the expected morphology for BFO obtained via sol–gel synthesis.

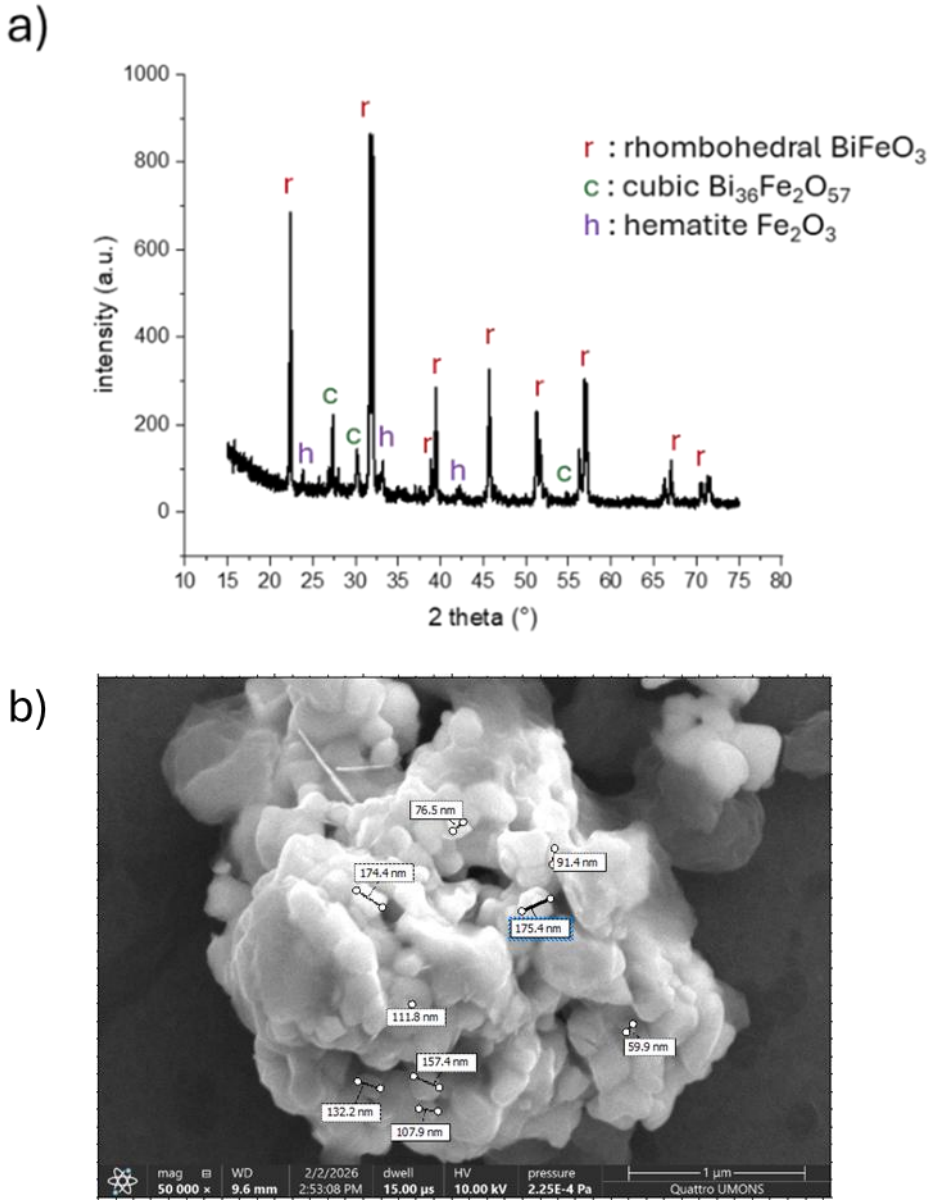

Figure 36 *: (a) DRX spectra of BFO powder produced following a sol-gel procedure and (b) eSEM imaging of BFO particles trapped in a polymer matrix (PVDF-TrFE), with size of a few representative particles highlighted.*

5.1.3 Ferroelectric hybrid nanocomposites

Environmental SEM imaging of the nanocomposite reveals several noteworthy features. First, despite the grinding and sonication steps applied during preparation, micron-sized particle aggregates are still present, in some cases reaching up to 20 µm (**Figure 37 a**). These large clusters are too rough to be probed reliably by AFM. When focusing on regions containing smaller aggregates, it becomes clear that the BFO particles are embedded within the polymer matrix, appearing immobilized. In these areas, aggregate sizes range

from individual nanoparticles to micrometric clusters. Several of the last ones are highlighted with white circles (**Figure 37 b**).

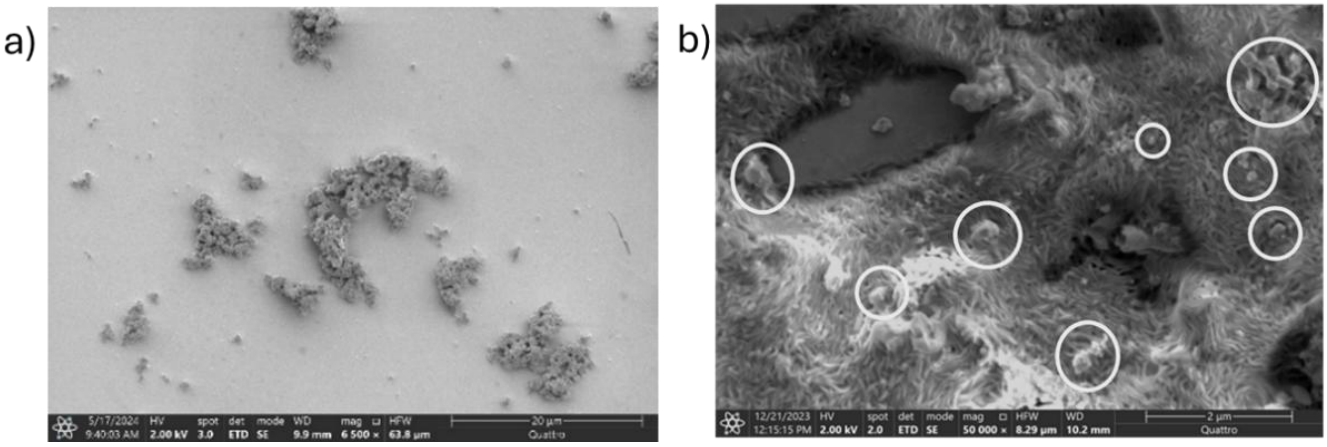

***Figure 37** : eSEM imaging of BFO/ PVDF-TrFE nanocomposites, (a) 20 µm scale and (b) 2 µm scale, with circled in white some of the BFO aggregates put in evidence*

The overall surface roughness of the composite is also noticeably higher than that of the pure polymer film. Several areas show exposed ITO substrate, likely resulting from local rearrangements of the polymer during drying or from particle ejection during the spin-coating process.

Local EDX analysis performed on fine-grained regions confirms the BFO composition of the particles (Bi signal) and the presence of the polymer matrix (C signal) (**Figure 38**).

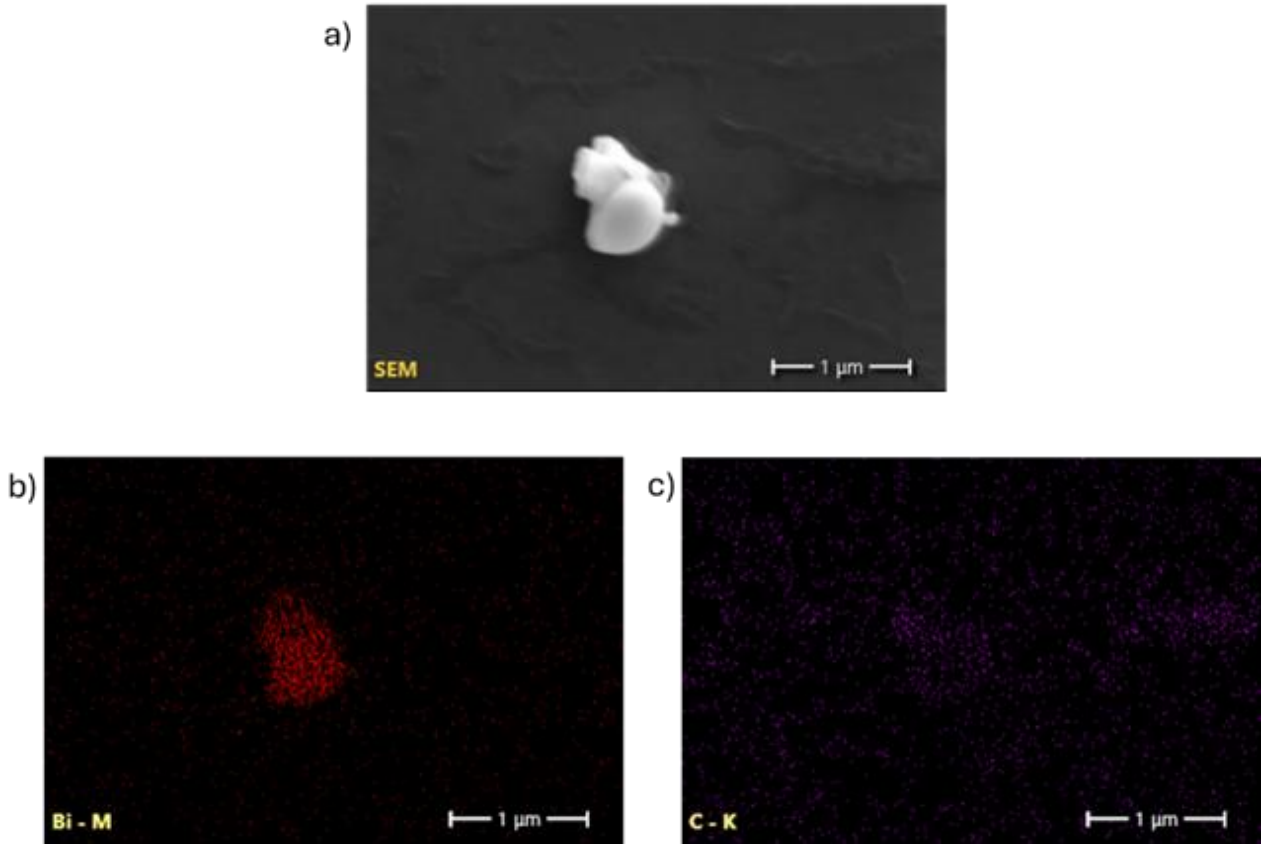

***Figure 38** : EDX-SEM imaging on an isolated particles of BFO embedded in the PVDF-TrFE matrix (a) imaging, (b) Bismuth signal in red and (c) Carbon signal in purple.*

5.2 Thickness measurement

Film thickness is first evaluated following a scratch in which the polymer layer was locally removed using a razor blade, and the resulting topographical step is measured by AFM. This height difference corresponds to the film thickness. As shown in **Figure 39 c**, the measured step indicates a thickness of approximately 40 nm. To confirm that the measurement really reflects the height difference between the polymer and the bare substrate, the experiment is performed in Peak-Force Tapping. This technique clearly distinguishes both materials through their contrasting mechanical responses. The ITO region appears more rigid and uniform (**Figure 39 b**).

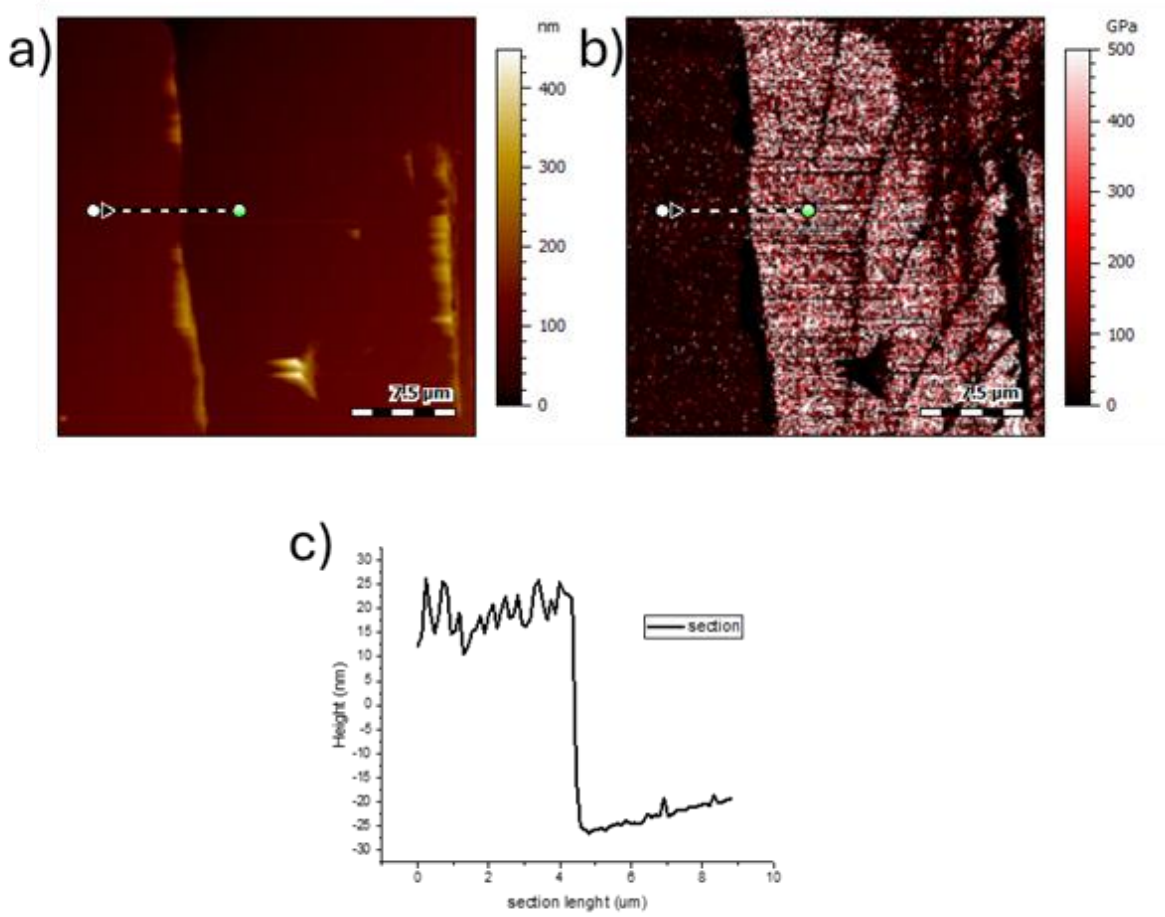

***Figure 39** : Illustration of a cross-section measurement after a scratch a) Topographic image and b) Young modulus image collected in PFT. c) Resulting cross-section of the topography.*

The thickness values obtained from the scratch are further validated by ellipsometry, which gives consistent thicknesses (**Figure 40 d-e**). Optical constants are taken from the literature and from online databases and are additionally checked from thick reference films deposited on silicon. The resulting fit shows coherent results on our data.

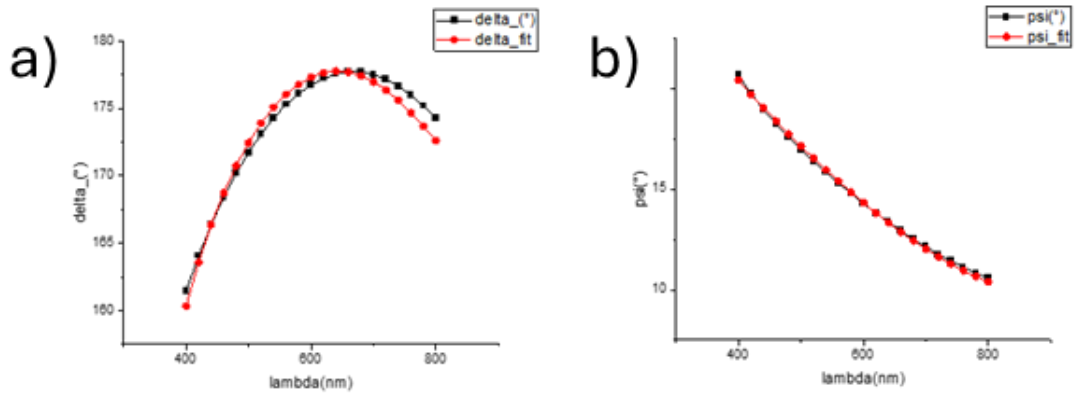

Figure 40 *:Ellipsometry parameters and their fit of the theoretical model d) Δ, and e) ψ.*

Taken together, both approaches indicate that dip-coated films yield relatively uniform thicknesses of around 40 nm whereas spin-coated films show a larger spatial variation between 20 and 60 nm, depending on the location on the sample (**Table 4**). Scratch tests performed on the nanocomposite films revealed thickness variations like those observed in the pure polymer films.

Although dip-coating generally produces more uniform polymer films than spin-coating, this technique proves less reliable for the nanocomposites. Several post-processing strategies are attempted, such as depositing an additional polymer layer with a semi-compatible solvent. However, these approaches are ineffective and often lead to poorly integrated or mechanically unstable nanoparticle regions. They are non-responsive in PFM measurements and easily removed by scratching.

For these reasons, we ultimately chose to continue using spin-coated nanocomposite solutions containing the polymer and the particles. Samples are more reproducible and stable during the electromechanical characterization. For comparison purposes, all measurements presented on PVDF-TrFE films are collected on spin-coated films.

Table 4 *: Results of the thickness test on thin polymer film of PVDF-TrFE*

	Spin-coating	**Dipcoating**
Scratch test	39±17 nm	33±6 nm
Ellipsometry	40±24 nm	36±9 nm

5.3 Mechanical characterization of the sample using Peak-Force Tapping

The local morphology of the PVDF-TrFE thin film is shown in **Figure 41 a**. The fibrillar polymer structure observed previously by SEM is also visible in AFM, more easily distinguishable at higher magnification (**Figure 41 b**). The fibrillar "Rice-like" structuration of the PVDF-TrFE is the same as that previously described and arises when the system is annealed at 140°C [187]. This structure has been reported as being the most stable in terms of ferroelectric properties. Beyond providing a stable and high-resolution topographic map, PeakForce Tapping (PFT) also gives access to local mechanical properties through its force-curve–based spectroscopic measurements. Parameters such as adhesion (**Figure 41 d**) and Young's modulus can then be extracted from them.

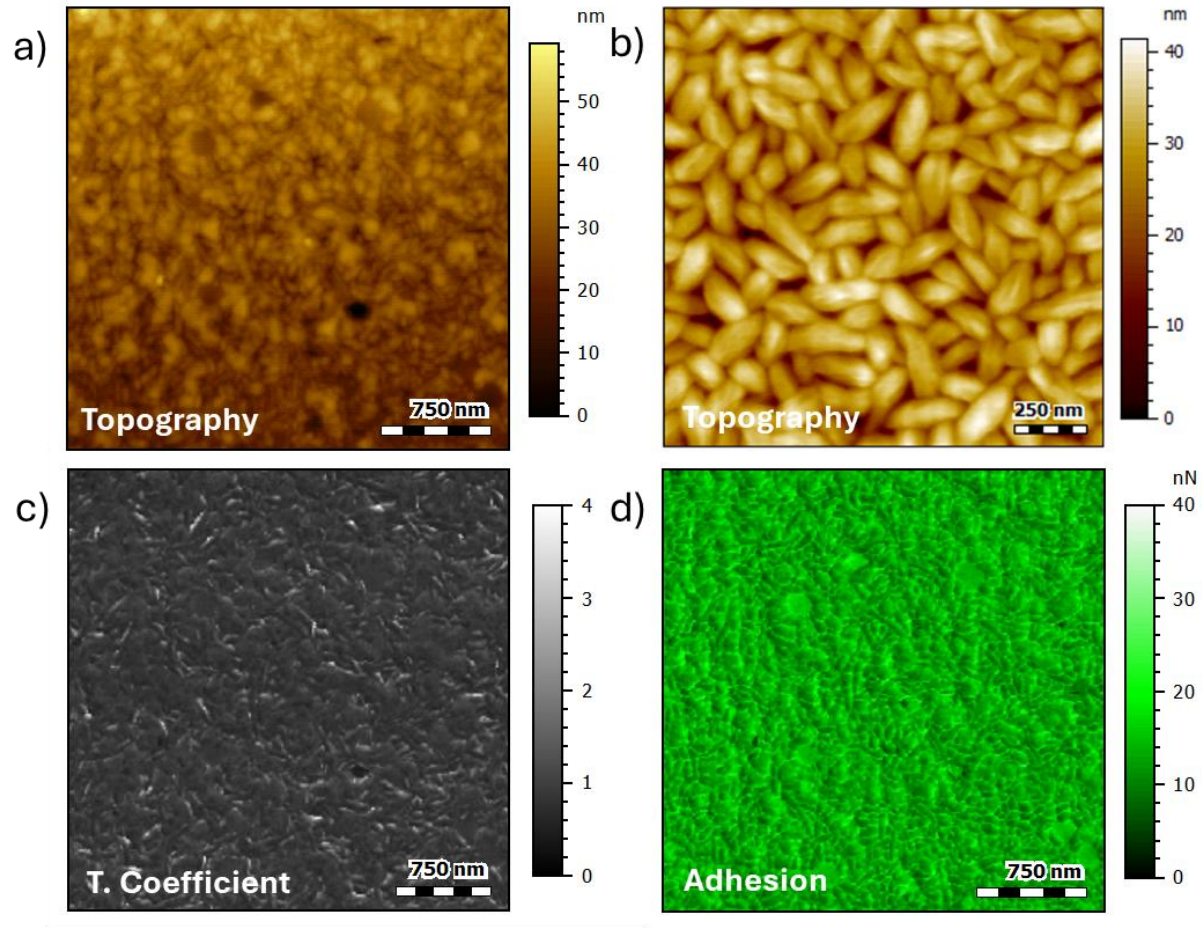

***Figure 41** : Image collected on the PVDF-TrFE thin film in PFT mode (a) Topography over a 3.5 µm ² area and (b) Topography over a 1 µm ² area. (c) "Recalculated" Tabor coefficient and (d) Adhesion measured by PFT.*

Determining the Young's modulus requires fitting the retract portion of each force curve. Several contact-mechanics models exist. Each relies on different assumptions (see **2.3.2**). As expected, the calculated modulus varies significantly and depends on the chosen model (**Figure 42**). To identify the most appropriate one, we compute the Tabor parameter for every force curve using a custom-built software tool and then recalculate the modulus. The resulting Tabor-parameter map indicates that the Maugis–Dugdale model is the most suitable for our polymer system (**Figure 41 c**).

Using this model, the Young's modulus of the PVDF-TrFE film is estimated at around 3.5 GPa. It is consistent with values reported for this material [188]. Overall, the mechanical response is spatially uniform across the film except for the edges of some fibrils where the tip–sample contact is unstable, leading to less reliable data.

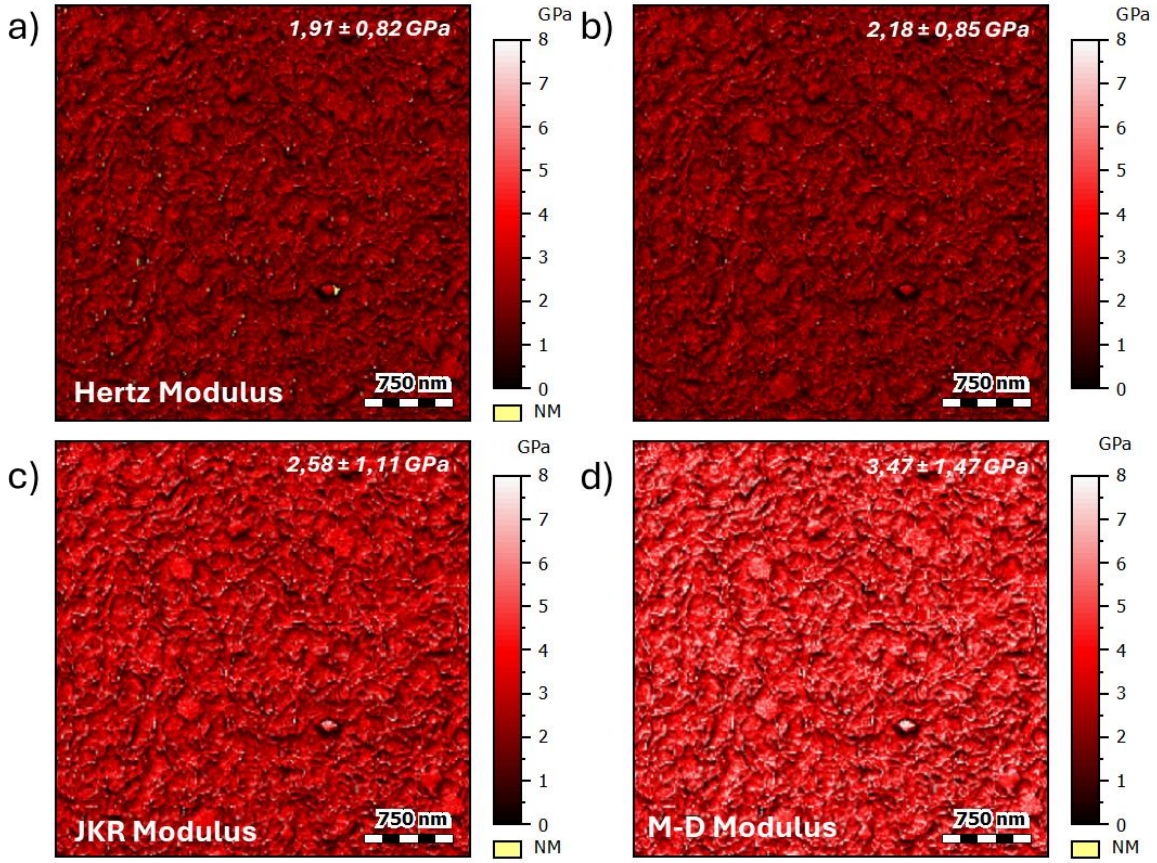

***Figure 42** : Recalculated Young modulus of PVDF-TrFE from PFT measurement following different fitting model: (a) Hertz, (b) DMT, (c) JKR, and (d) Maugis-Dugdale.*

A noticeable feature in the PVDF–BFO nanocomposites is the presence of well-dispersed particle aggregates of various sizes embedded within the polymer matrix (**Figure 43 a**), already observed with SEM imaging. The characteristic fibrillar morphology of the PVDF-TrFE matrix remains visible (**Figure 43 b**). The adhesion map of a small particle cluster, in more detail, shows that the polymer matrix exhibits values that are near the ones

measured in the pure film. However, the BFO particles present slightly lower adhesion (**Figure 44 b, d**).

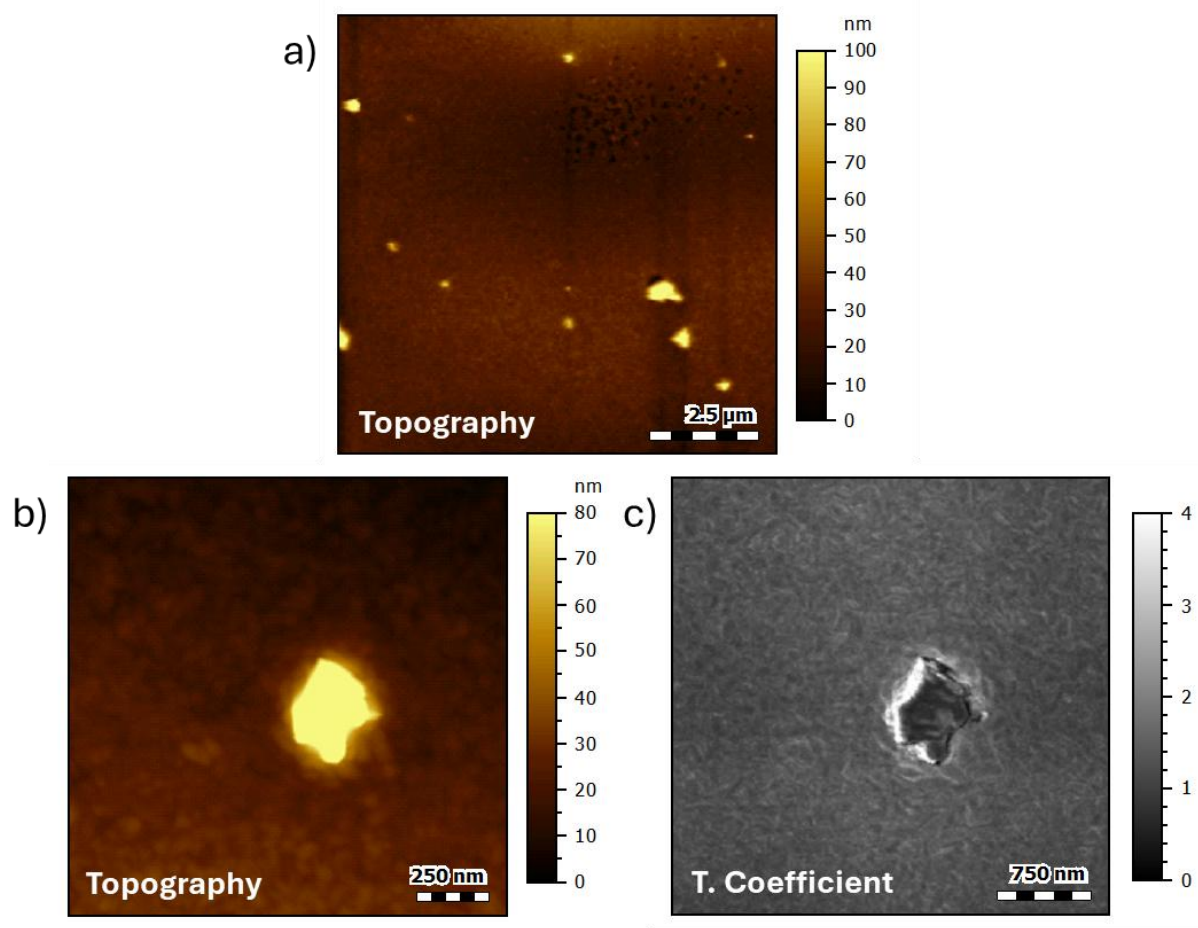

Figure 43 *: (a) Topographic image of the BFO-PVDF-TrFE manocomposites,10 µm ^{2}, (b) Topographic image of the BFO-PVDF-TrFE manocomposites,1 µm ^{2} and (c) Tabor coefficient mapping.*

The Tabor-parameter mapping further confirms this difference. The particles display distinctly lower Tabor values than the surrounding polymer, although all values still fall within the range where the Maugis–Dugdale model remains valid (**Figure 43 c**). The corresponding Young's modulus map is shown in **Figure 44 a**. The BFO particles appear only slightly stiffer than the polymer matrix. However, it is relatively modest due to the large mechanical contrast expected between the materials. This reduced contrast likely results from the fact that the particles are small, stiff objects embedded within a softer matrix. Furthermore, the edge of the particles appears to have a lower modulus than the centre of the particle. Particular care must be taken near the edges of aggregates where tip–sample instabilities generate artificial increases or decreases in the signal (**Figure 44 c)**.

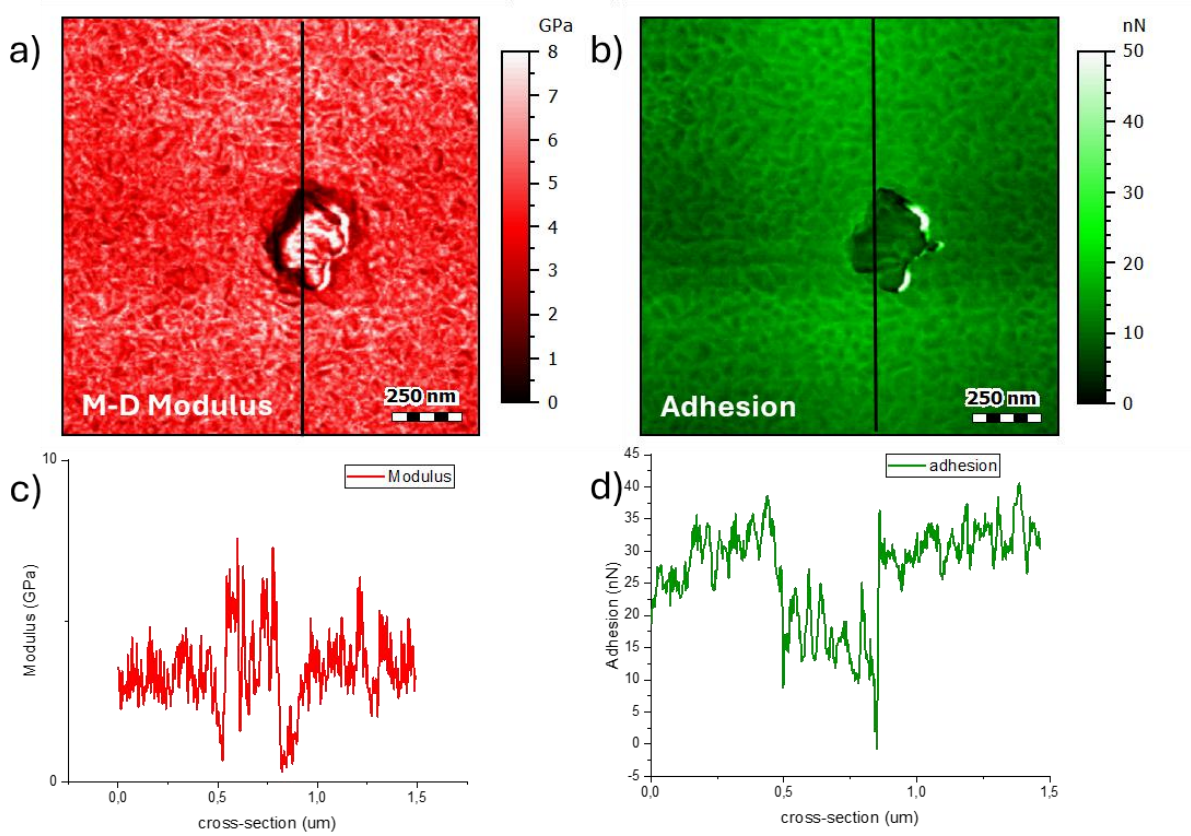

Figure 44 *: (a) Maugis modulus mapping on the composite, (b) Adhesion mapping on the composite, (c) Adhesion section, and (d) Young modulus section.*

For larger particle aggregates, another instability is observed: Some regions appear hardly analysable. Inspection of the raw force curves in these zones reveals a poor curve quality. This effect most likely arises from the extremely rough topographies of those structures and from the partial mobility of the aggregates, causing unstable tip–sample contact. An analogous phenomenon is also observed for BFO particles embedded in the PEDOT:PSS matrix (**Figure 45**).

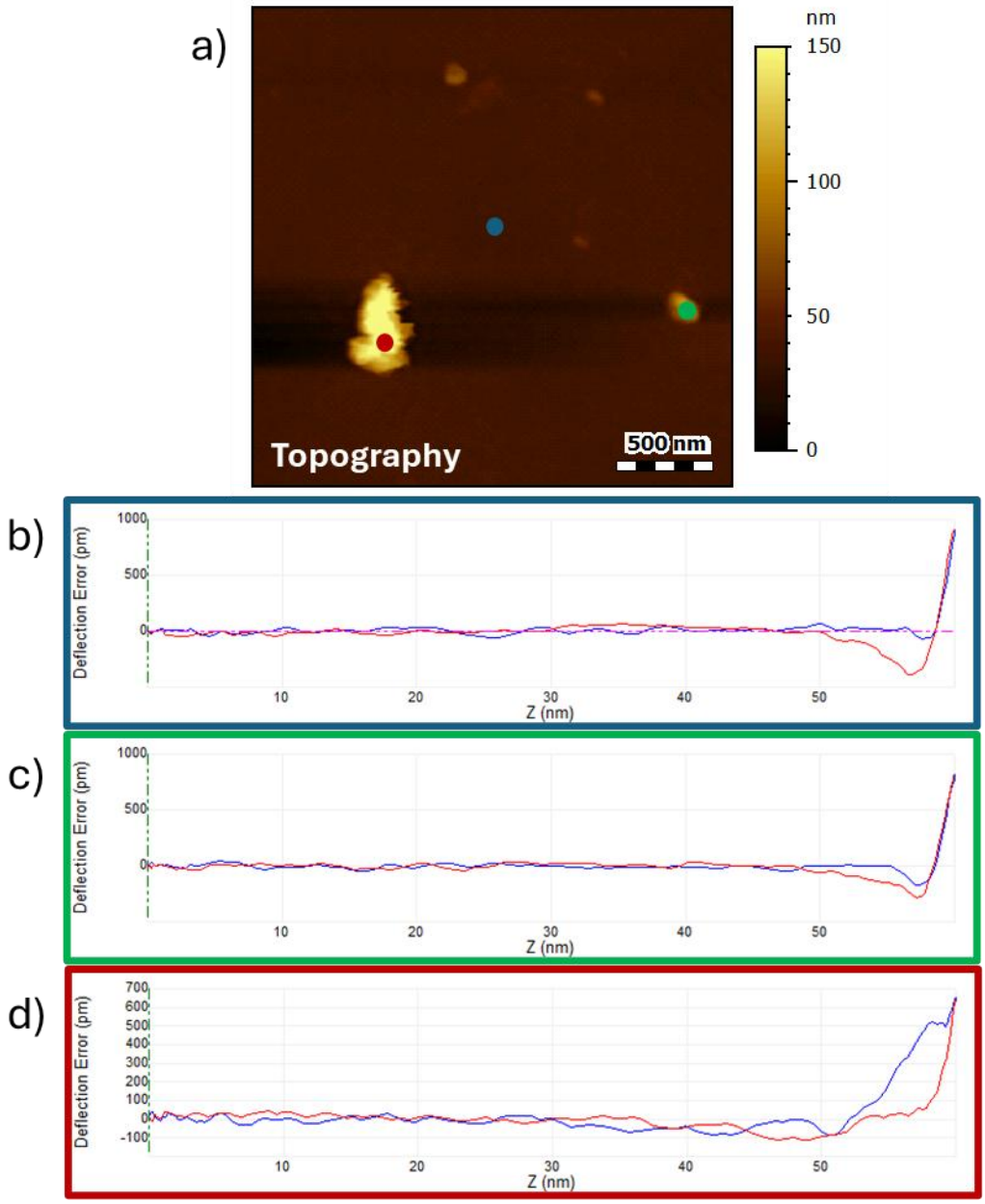

Figure 45 *: (a) Topography of the BFO-PEDOT:PSS film. (b-d) Forces curves collected in different positions of the film, indicated in the topography image. In blue, an area of the polymer, in green, an area of a stable particle, and in red, an area of unstable (big aggregate) particles.*

5.3.1 Leakage current verification by C-AFM

Before proceeding with the electromechanical characterization of our samples, it is essential to verify that they can be safely polarized within the voltage range used in our experiments (–10 to +10 V) without reaching the leakage threshold. Exceeding this threshold could generate Joule effect that could be misinterpreted as piezoresponse signals [189].

To assess this, we performed cAFM measurement using the DataCube mode of the AFM. Therein, each pixel corresponds to a complete I(V) curve. For the sake of clarity, leakage-current maps are reconstructed by extracting the current values of applied voltages at both extrema.

For the PVDF-TrFE films, measurements are acquired along the sample edge to probe regions of varying thickness and to compare their response with that of the underlying ITO substrate (**Figure 46**). The resulting I(V) maps indicate that no electrical breakdown occurs within the applied voltage range for either polarity, even in the thinnest regions (< 10 nm). At -10 V, the ITO part appears extremely responsive in bright yellow while the whole area corresponding to the polymer is in brown, showing an absence of leakage current (**Figure 46 b**). The same observation can be done at 10V, except that ITO shows some non-responsive area, likely arising from a lack of contact stability in these (**Figure 46 c**).

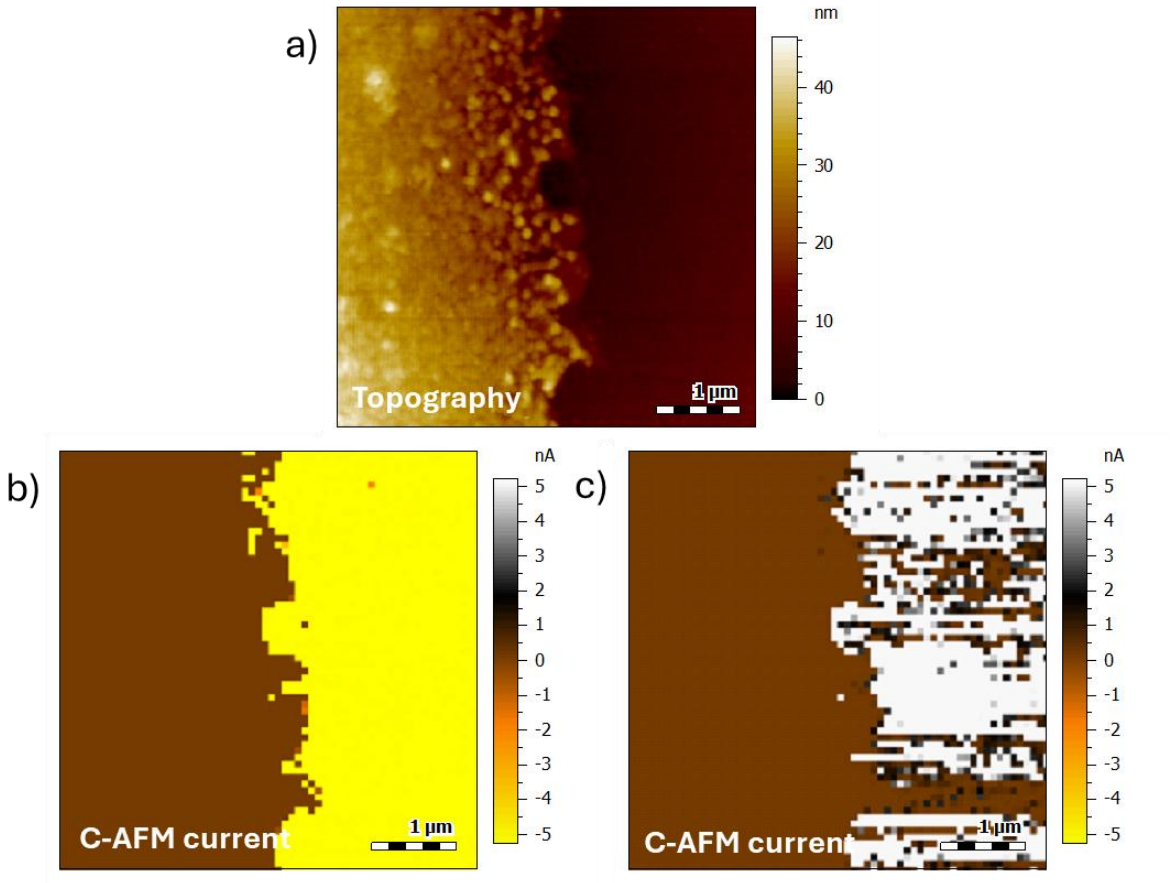

***Figure 46** : FV-cAFM measurement over the thin film of PVDF-TrFE sample (a) Topography, (b) Resulting current when -10 V are applied, b) Resulting current when 10 V are applied.*

The BFO–PEDOT:PSS system is evaluated with the same procedure after annealing the films at 140 °C to optimize the conductivity of PEDOT:PSS [179]. The leakage current map

at -10V (**Figure 47 b**) shows that the different areas identifiable as nanoparticles in the topography image (**Figure 47 a**) exhibit no detectable leakage, while the PEDOT:PSS matrix shows an expected strong and stable conductive response. The same observation can be done at 10V (**Figure 47 c**).

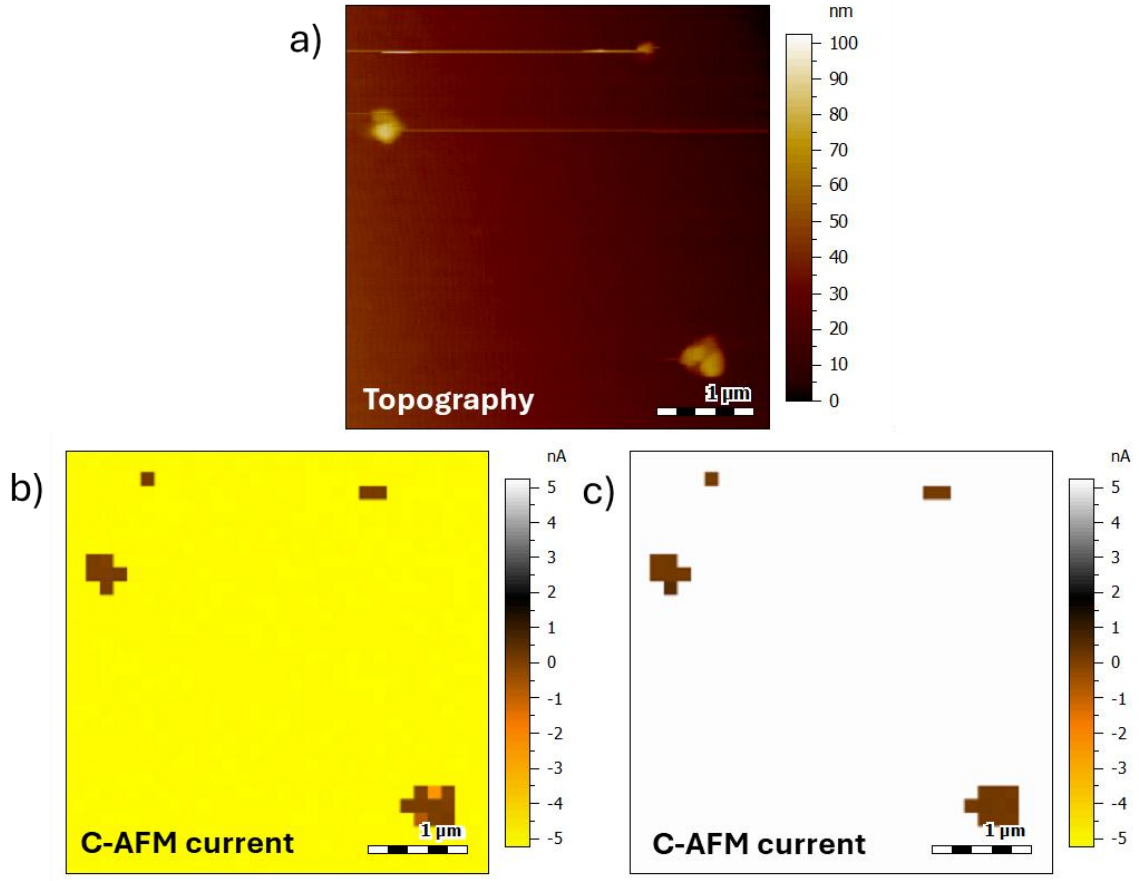

***Figure 47** : FV-cAFM measurement over the thin film of BFO-PEDOT:PSS (a) Topography, (b) resulting current when a -10 V voltage is applied, and (c) resulting current when a 10 V voltage is applied.*

Since none of the individual components displays leakage within the applied voltage window, the complete hybrid nanocomposite shows no sign of electrical breakdown. It confirms that PFM measurements are safely conducted without inducing electrostatic artifacts.

5.4 Conclusion

This chapter presented the fabrication and structural characterisation of PVDF–TrFE/BFO nanocomposite thin films designed for AFM-based electromechanical investigations. X-

ray diffraction confirmed the successful synthesis of rhombohedral-phase BFO nanoparticles, while eSEM and AFM imaging evidenced their effective incorporation within the polymer matrices. Although some degree of particle aggregation and surface roughness was observed, mechanical mapping performed by Peak Force Tapping demonstrated clear contrast between the polymer and ceramic phases. Thickness measurements obtained from AFM scratch tests and ellipsometry indicated nanometric films compatible with low-voltage PFM experiments. Finally, conductive-AFM measurements confirmed the absence of leakage currents within the investigated voltage range. Together, these results validated the structural integrity and electrical suitability of the prepared samples for subsequent ferroelectric characterisation.

Chapter 6: Domain imaging by PFM

Understanding the nanoscale electromechanical behaviour of ferroelectric materials relies on accurate visualisation of their domain structures and on distinguishing genuine ferroelectric signals from artifacts related to topography, mechanical heterogeneity, and electrostatic effects. This chapter presents a detailed characterisation of naturally occurring domain configurations and local switching in PVDF-TrFE, BFO particles, and their corresponding hybrid nanocomposites, using piezoresponse force microscopy (PFM) as an imaging tool. To improve stability and reliability in complex three-dimensional heterostructures, a dual-frequency resonance-tracking (DFRT) module is also used.

6.1 Conventional CR-PFM characterization

6.1.1 PVDF-TrFE

At large scale, CR-PFM imaging of PVDF-TrFE reveals a relatively uniform topography (**Figure 48 a**). At higher magnification, the characteristic fibrillar or "rice-like'' morphology previously reported becomes apparent (**Figure 48 b**). After identifying the optimal contact-resonance frequency by performing a frequency sweep, both amplitude and phase images are acquired (**Figure 48 c-d**). The maps reveal randomly distributed up and down polarized domains with elongated shapes with 10–50 nm in width and over several hundred nanometres in length. The relative fraction of up and down domains is not constant and varies depending on the area examined.

Combining the phase image with the topography shows that the naturally occurring ferroelectric domains do not follow the underlying fibrillar structure (**Figure 48 e**) as it is already described by research teams that report that vertically orientated domains can already be presented before annealing, although annealing at 140 °C generally enhances the ferroelectric response [190,191].

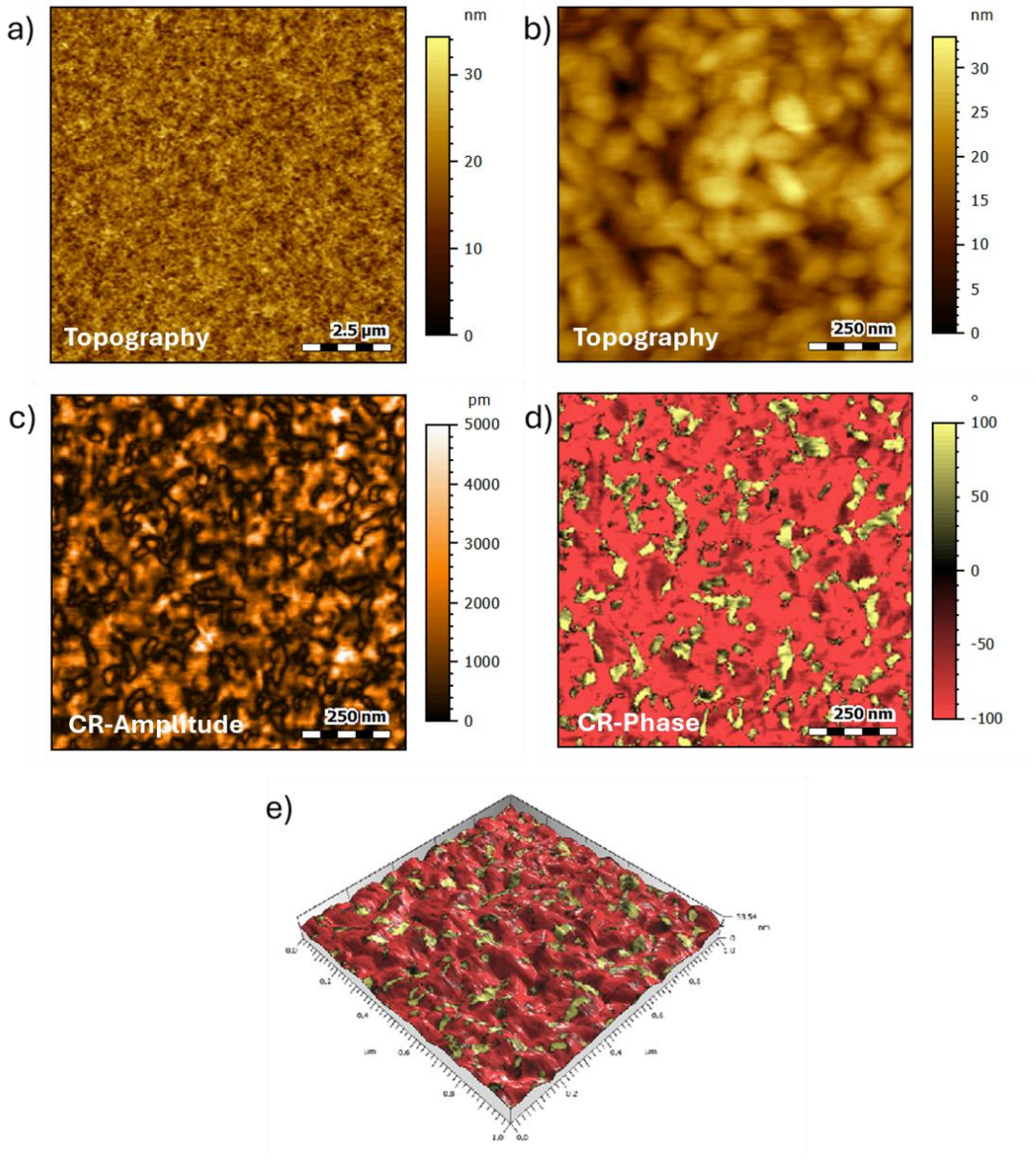

Figure 48 *: .CR-PFM image of PVDF-TrFE thin film. (a) Topography on 10 µm², (b) Topography on 1 µm². (c) Amplitude and (d) Phase at CR frequency = 289 kHz. (e) 3D superposition of phase on topography.*

A switching experiment was performed to confirm the reversibility of those domains in the studied range. A 4 µm² square was first poled at +10 V, followed by a second 3 µm² square at –10 V in the upper-right corner of the intern square (**Figure 49**). The resulting PFM amplitude increases overall (**Figure 49 b**), while the phase presents two zones of opposite polarisation: negative voltage produces a positive phase, and positive voltage produces a negative phase (**Figure 49 c**), consistent with a negative piezoelectric coefficient.

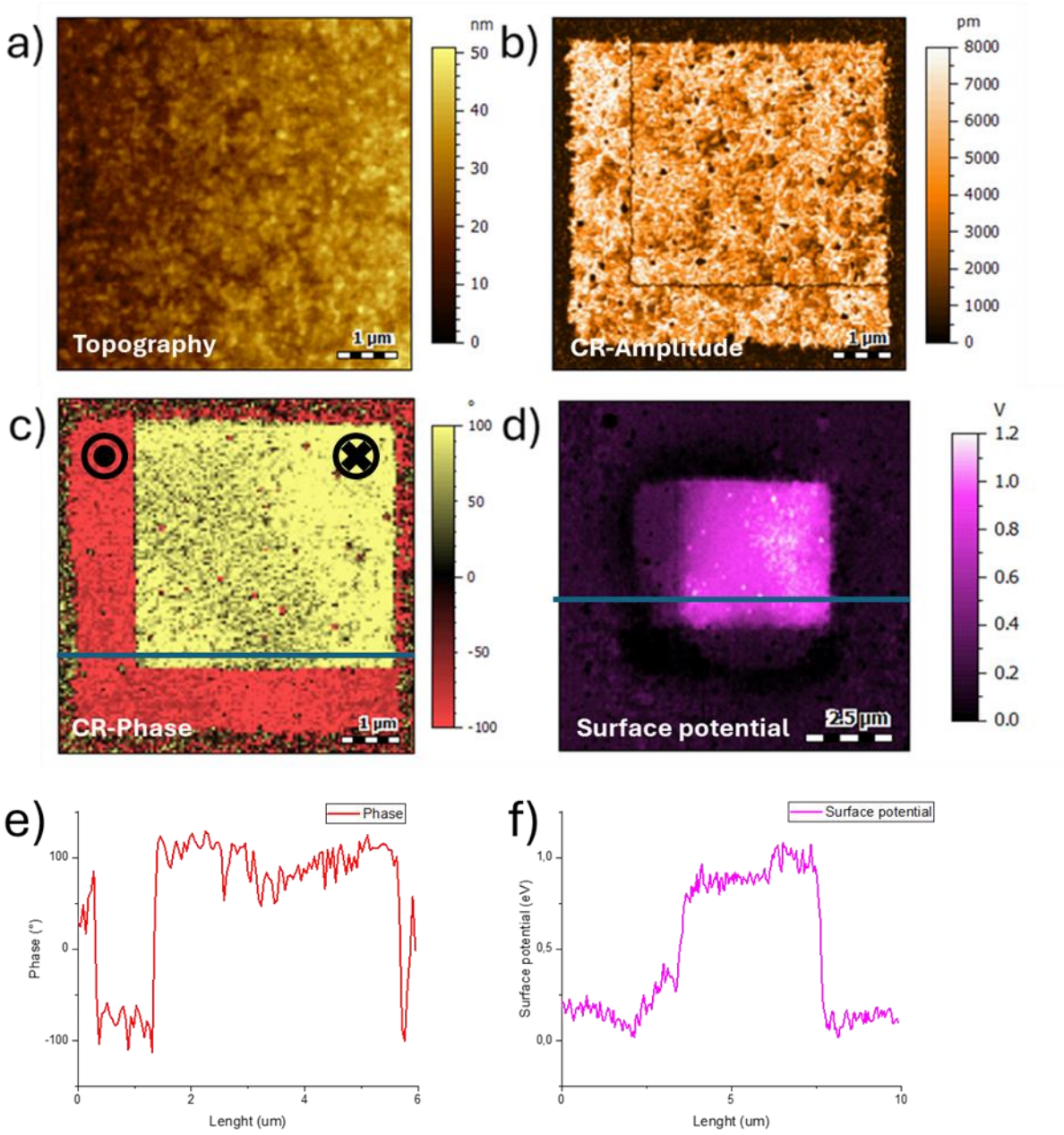

Figure 49 *: CR-PFM after local poling at CR frequency = 290 kHz: (a) Topography, (b) Amplitude, (c) Phase. (d) Heterodyne KPFM Surface potential after poling. (e) Section of the phase image and (f) Section of the surface potential image.*

A closer inspection of poled areas reveals a diffuse border between poled and unpoled regions. This blurring is likely due to the fibrillar morphology. Nine fixed spots are locally poled at –10 V to further examine this behaviour (**Figure 50 a**). These experiments confirm that the polarisation is not sharply confined. The poled region spreads laterally, with an apparent radius of about 200 nm, much larger than the 25 nm tip radius (**Figure 50 b-c**). The shape of the poled areas also appears influenced, either constrained or extended, by the underlying "rice-grain'' microstructure.

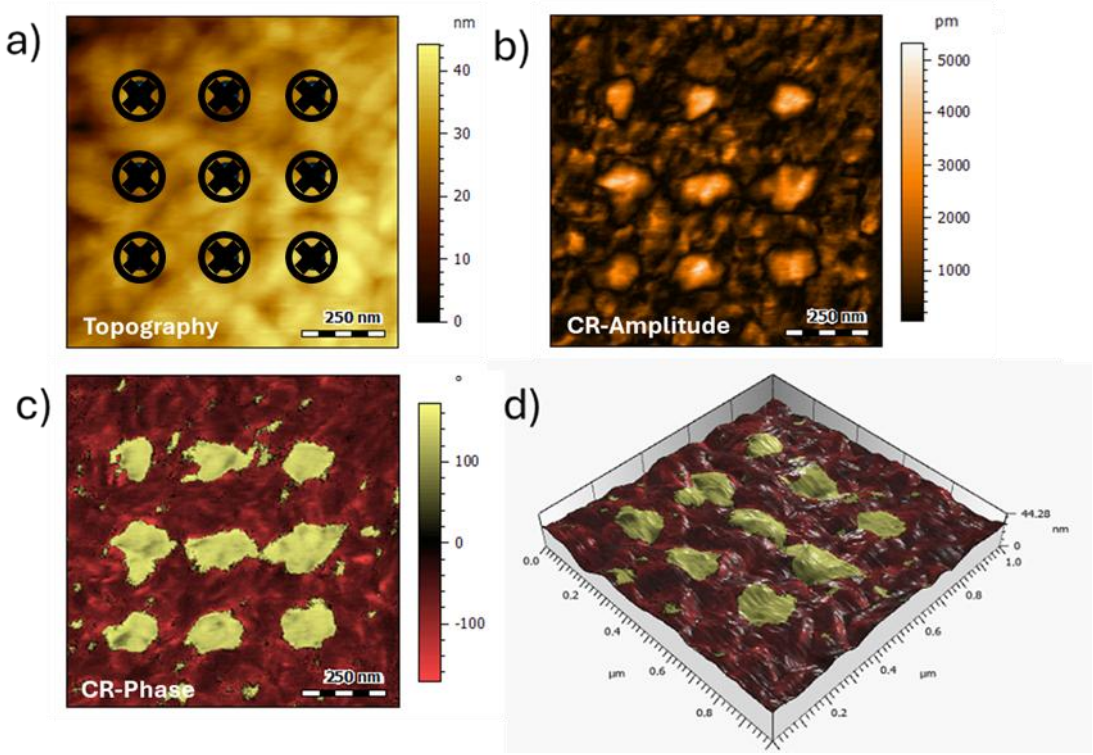

Figure 50 *:CR-PFM after local poling of nine positions at CR frequency = 285 kHz: (a) Topography with highlighted positions, (b) Amplitude, (c) Phase, (d) 3D phase superposition.*

Although no detectable topographic modification occurs after local poling, the surface potential varies due to injected charges (**Figure 49 d**). The last poled square (the right corner one) exhibits a significant charge accumulation. A diffuse "cloudy'' section is also observed around the poled square, suggesting charge migration within the polymer film (**Figure 49 f**). These electrostatic effects likely contribute to the apparent domain size and contrast, indicating that not all observed changes originate solely from ferroelectric switching.

6.1.2 BFO Particles in PEDOT:PSS

CR-PFM imaging of BFO–PEDOT:PSS shows that only a fraction of particles from all particles identifiable from the topographic images exhibit a measurable PFM amplitude signal (**Figure 51 a–b**). This incomplete activity may partly reflect non-ferroelectric secondary BFO phases, but is more plausibly attributable to insufficient electrical coupling between some particles and the ITO bottom electrode. As previously observed in AFM and eSEM, the larger aggregates present high roughness and mechanical instability, complicating reliable imaging in CR-PFM measurements.

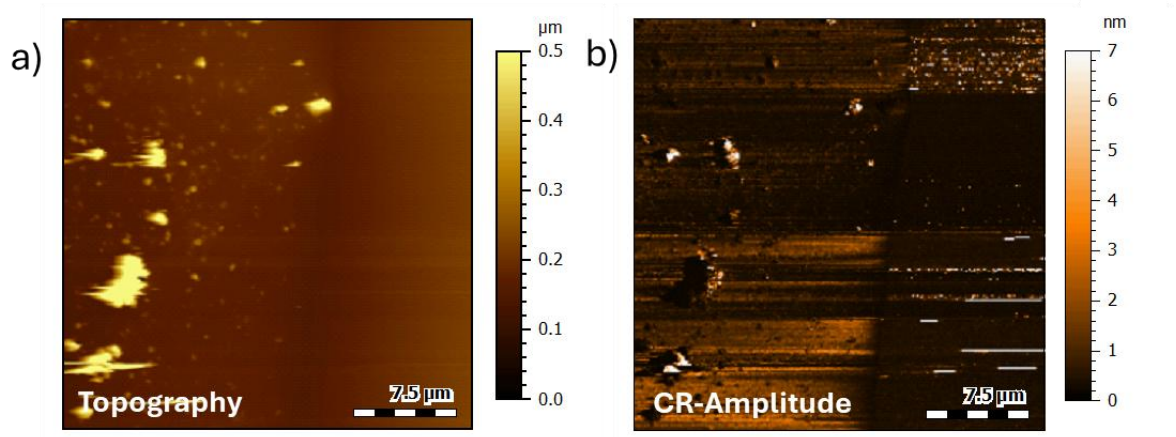

***Figure 51** : CR-PFM on 10 µm² of BFO–PEDOT:PSS at CR-frequency = 310 kHz: (a) Topography, (b) Amplitude.*

Focusing on a smaller and responsive particle cluster exhibits clear ferroelectric behaviour, with up- and down-polarised domains distributed across the aggregate (**Figure 52 b-c**). There is no detectable piezoresponse from the surrounding PEDOT:PSS matrix. Most BFO grain appear to possess their own polarisation state when relating individual domains with specific particles. Adjacent particles share the same polarisation direction, although they exhibit a sharp amplitude discontinuity. This fact could be misinterpreted as a domain wall. However, some domains observed are extremely small (less than 20 nm) than the expected particle size. Moreover, some of them exhibit naturally multiple ferroelectric orientations.

The phase contrast becomes largely uniform across the aggregates after poling at –10 V, except one edge region (**Figure 52 d–e**). Poor electrical contact and/or non-switchable grain in the polarisation range contribute to this fact. On the other hand, amplitude remains comparable before and after poling, though slightly blurred, likely due to some tip wear.

Given the marked topographical variations and mechanically heterogeneous nature of the aggregates, conventional CR-PFM does not provide an optimal representation of such complex systems. More advanced or robust spectroscopic approaches are required for accurate interpretation.

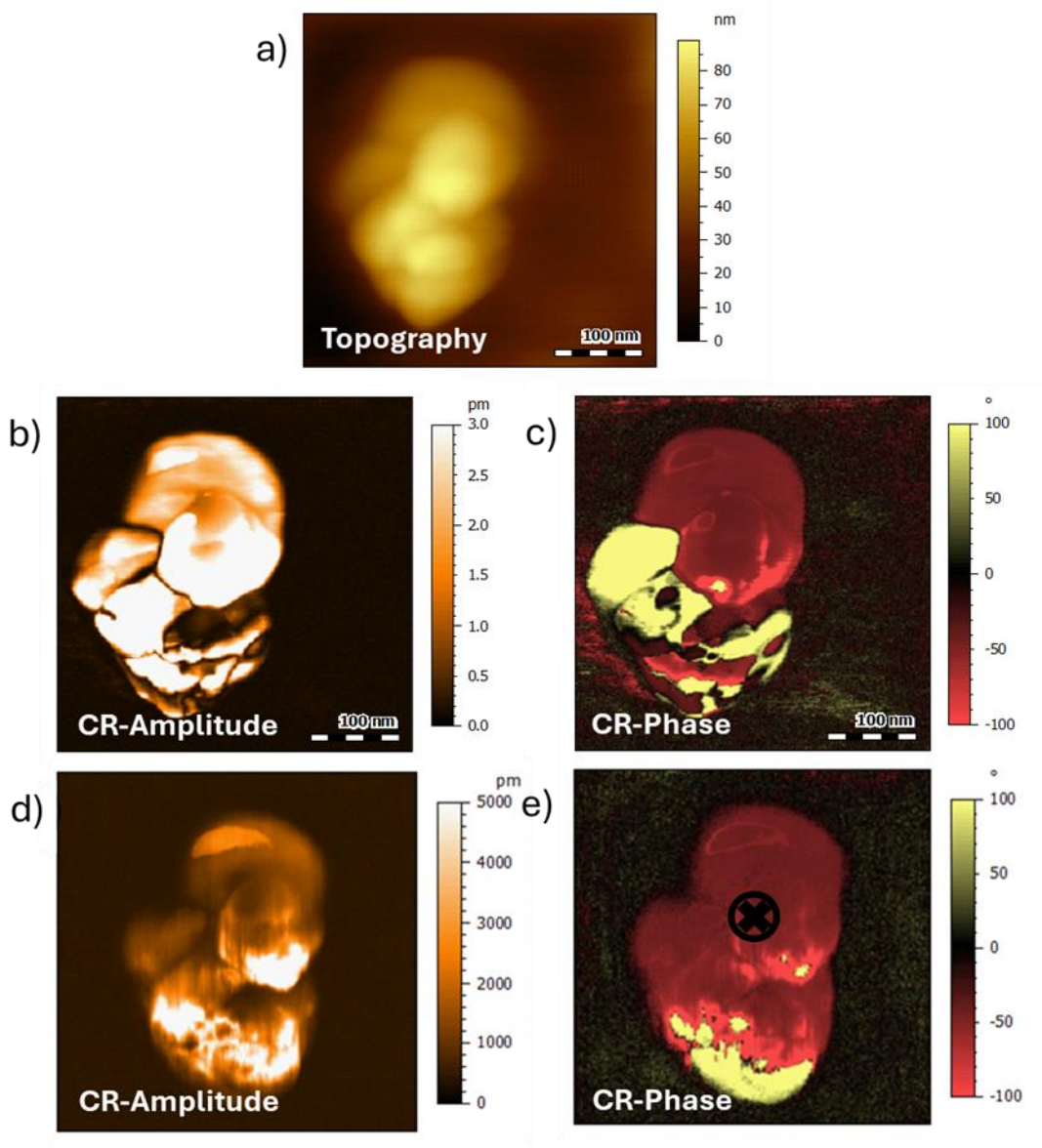

Figure 52 *: CR-PFM on 400 nm² BFO–PEDOT:PSS at CR Frequency = 310 kHz: (a) Topography, (b) Amplitude, (c) Phase, (d) Amplitude and (e) Phase after polarisation at –10 V.*

6.1.3 PVDF-TrFE / BFO Nanocomposites

At larger scale, the PVDF-TrFE/BFO nanocomposite shows holes and discontinuities in the polymer film (**Figure 53 a**). These defects likely arise from uneven deposition caused by the presence of BFO particles and by the partial removal of poorly embedded particles during spin-coating. Nevertheless, more particles display electromechanical activity than in the PEDOT:PSS system, although several remain non-responsive (**Figure 53 b**). As described before, the largest aggregates display surface roughness, preventing reliable CR-PFM analysis.

Local frequency sweep collected on the particles and on the matrix shows the expected difference of amplitude value (**Figure 53 c**), but also an important shift of CR-Frequency between the two materials. The PVDF-TrFE shows a CR-Frequency around 290 kHz, while the BFO value is more around 315 kHz. This difference can be explained by the mechanical differences between the two materials.

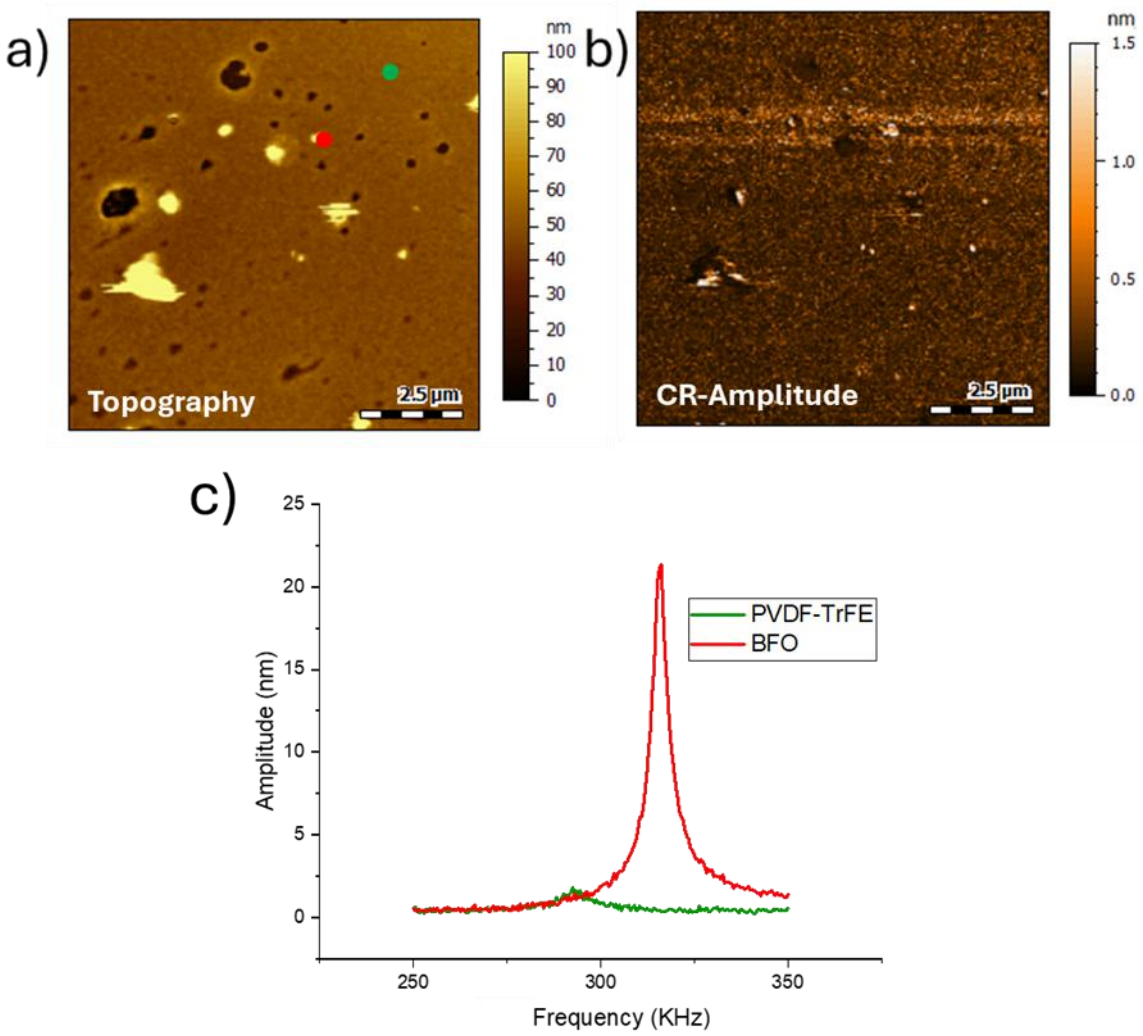

***Figure 53** : CR-PFM on 10 µm² PVDF-TrFE/BFO at CR-frequency = 310 kHz: (a) Topography, (b) Amplitude. (c) Frequency sweeps ramp on the two areas indicated in the topography. In red, the area corresponding to the BFO, and in green, the area corresponding to the PVDF-TrFE.*

Zooming into smaller aggregates, we encounter a restriction. The measurement conditions (frequency, setpoint, and gain) can be optimized for one element at a time, but not for both simultaneously. At a frequency of 315 kHz, optimal for BFO, the particles show strong amplitude and a clear phase contrast, but likely due to phase overshoot, as no domain structure is visible in amplitude (**Figure 54 a-c**). The polymer matrix displays only a very weak ferroelectric response in amplitude and in phase. Some zones of the

particle cluster appear almost non-responsive and could be interpreted as either a poor electrical connection between electrode and particle or non-ferroelectric properties of the BFO grain, or presence of polymer above the grain.

The polymer shows a stronger and more uniform response after poling and re-tuning the resonance to 290 kHz, which is optimal for PVDF-TrFE. At this level, the particle signal becomes weaker and consequently more difficult to interpret (**Figure 54 d-e**). However, the problematic grain does not show any measurable response, supporting a non-responsiveness rather than a polymer accumulation.

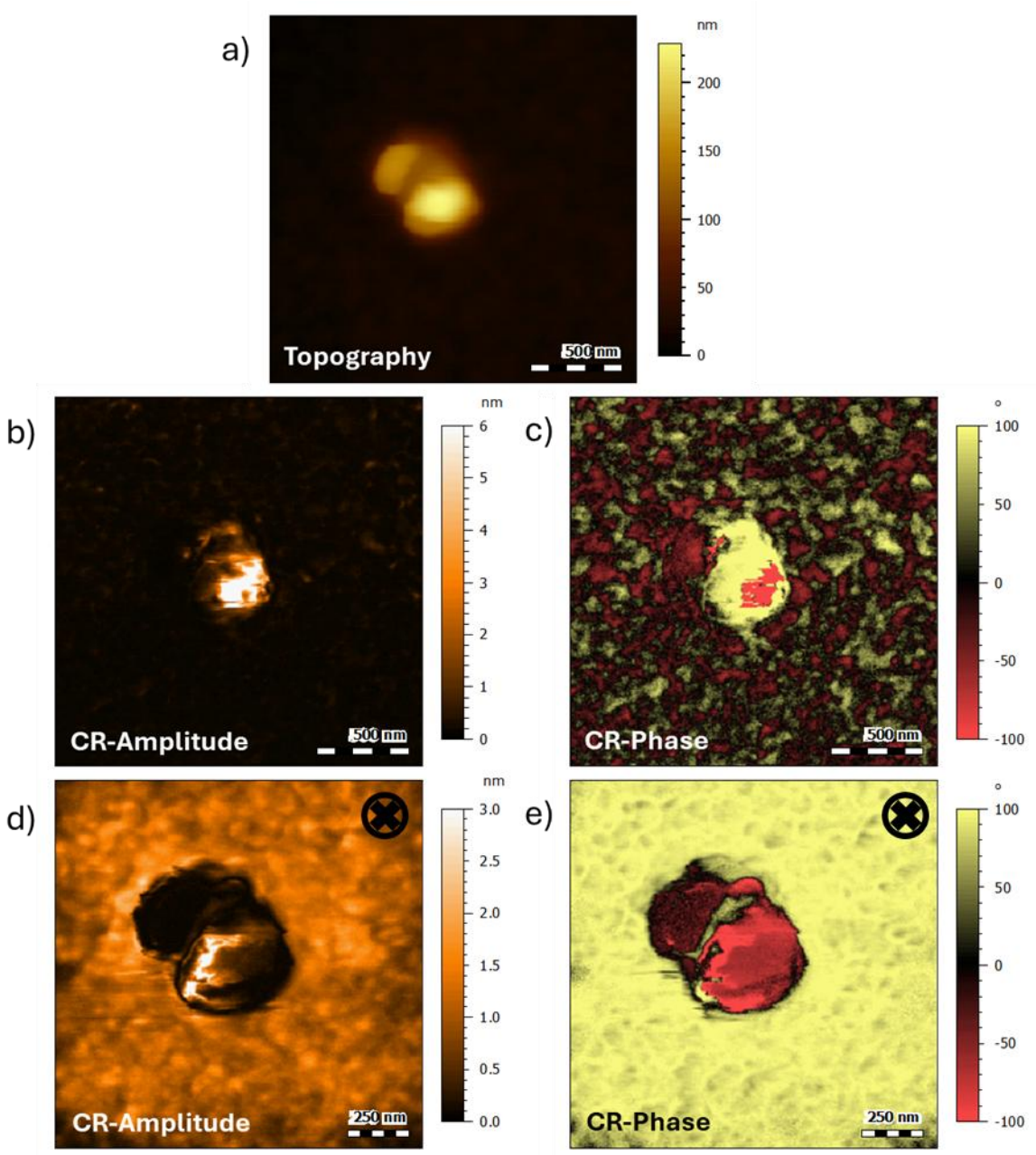

Figure 54 *: CR-PFM on a 2 µm ^{2} area of BFO-PVDF-TrFE nanocomposites at CR frequency = 315 kHz. (a) Topography, (b) Amplitude, and (c) Phase. CR-PFM on a pooled*

$1um^2$ area of BFO-PVDF-TrFE nanocomposites at CR frequency = 295 kHz. (d) Amplitude, and (e) Phase.

6.2 DFRT-PFM

Working at the resonance frequency significantly enhances the signal-to-noise ratio in PFM measurements. However, this approach also has several limits, notably an increased sensitivity to surface roughness and local variations in contact mechanics, effects that become particularly problematic in heterogeneous samples or highly uneven 3D structures. To mitigate these issues, a dual-frequency resonance tracking (DFRT) module (Zurich Instruments, Zurich, Switzerland) is employed. By continuously adjusting the excitation to the local resonance, this method stabilises the measurement and enables more reliable visualisation of vertical ferroelectric domains in complex structures. An additional advantage is the greatly improved accessibility of lateral PFM imaging, which is otherwise difficult to achieve under conventional single-frequency resonance conditions.

Because the tracking system operates by monitoring the amplitude difference between both drive frequencies, the measured amplitude cannot be directly converted into a physical displacement in nanometres. Therefore, all DFRT-PFM responses are reported in arbitrary units.

6.2.1 PVDF-TrFE

DFRT-PFM imaging of the ferroelectric polymer reveals domain features consistent with those obtained using conventional CR-PFM. Elongated ferroelectric domains are again clearly resolved in the out-of-plane channel (**Figure 55 a-c**). The corresponding in-plane images show similar domain structures, although located in different regions (**Figure 55 d-e**). No link is observed between the orientation of the in-plane and out-of-plane domains and between those and the topography. The presence of ferroelectric domains in both in-plane and out-of-plane orientations in PVDF-TrFE has been previously reported [192]. The amplitude contrast is not entirely uniform across the surface, with some locations showing a stronger vertical than lateral response, or vice versa.

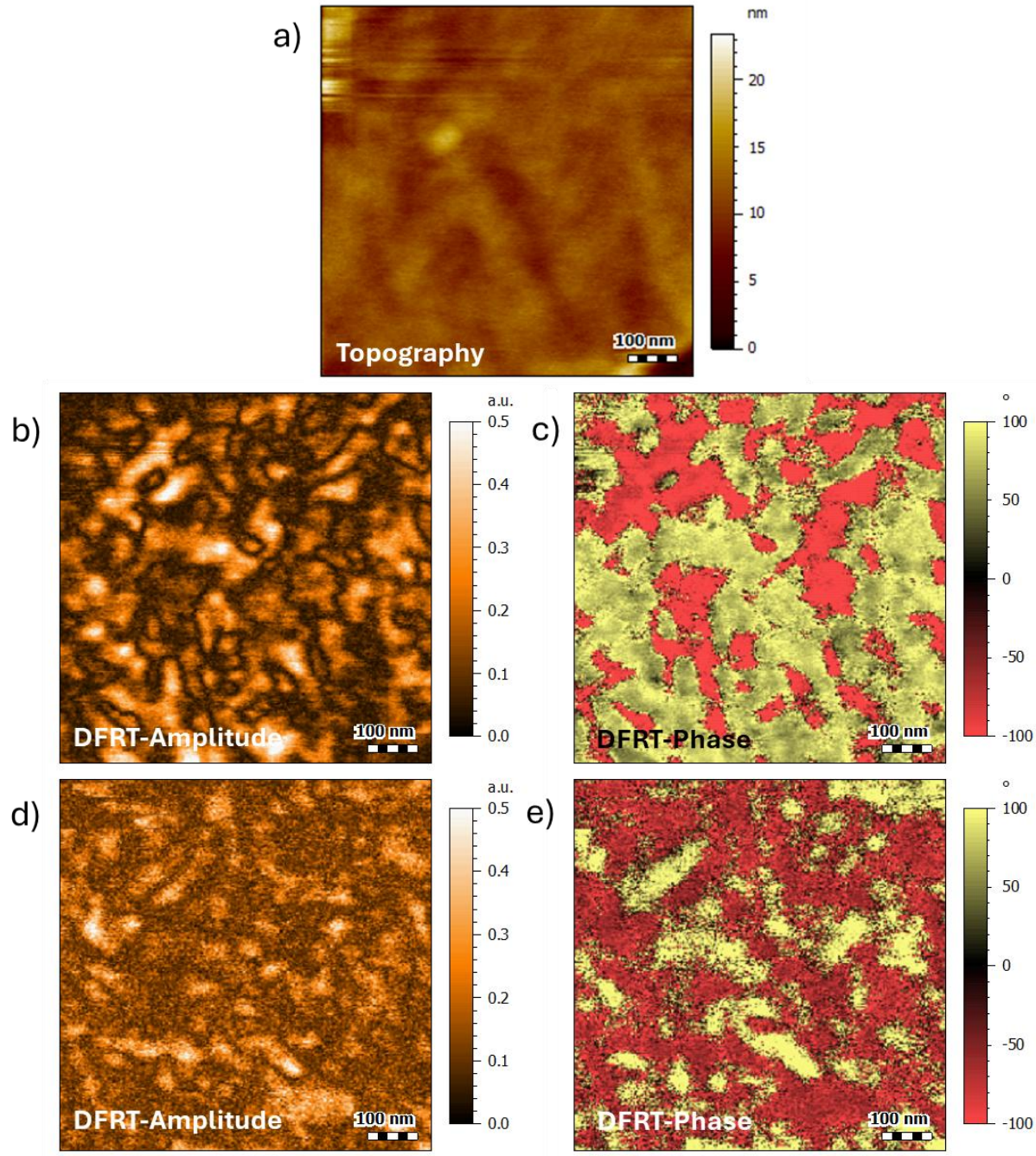

Figure 55 *: DFRT-PFM imaging of the PVDF–TrFE film. Vertical mode (CR Frequency range 250–350 kHz): (a) Topography, (b) Amplitude, and (c) Phase. Lateral mode (CR Frequency range 600–800 kHz): (d) Amplitude and (e) Phase.*

During extended measurements, an excessively high set-point is found to induce local scratching of the polymer (**Figure 56 a**). This mechanical disturbance also distorts the ferroelectric domain arrangement. The initially balanced up- and down-domain distribution becomes biased towards one polarity (**Figure 56 b-c**). The effect is even more pronounced in lateral PFM imaging, where the relative proportion of the two in-plane orientations significantly changes (**Figure 56 d-g**). This stronger alteration of the lateral

domain pattern is probably attributed to the horizontal component of the scratching forces, which may also induce mechanically driven domain switching besides changing the topography [193].

These observations highlight the need to optimise PFM measurements with relatively low set-point values in order to prevent tip-induced modification of the ferroelectric structure, but keeping it high enough to ensure a stable tip–sample contact.

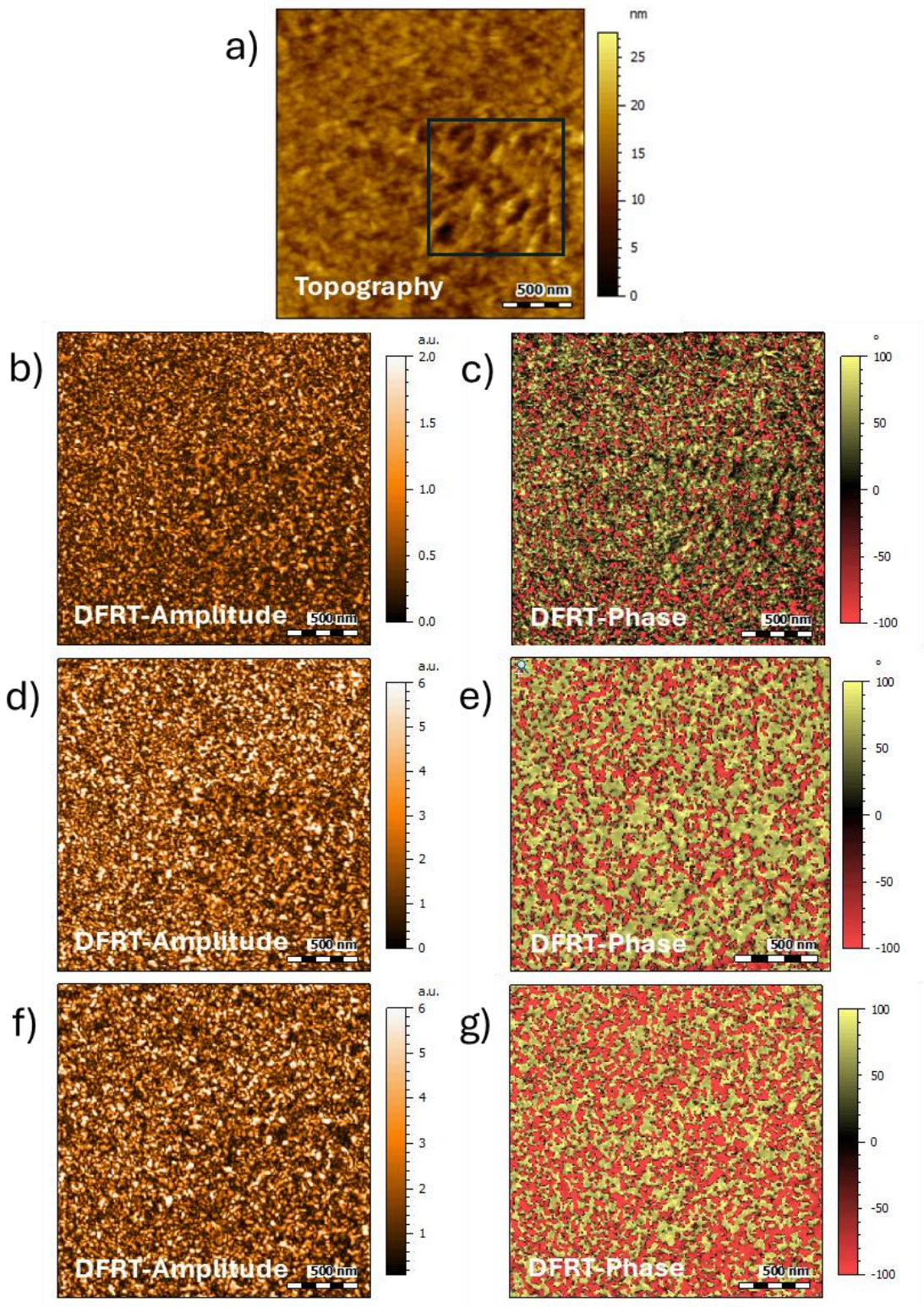

Figure 56 *: Effect of high set-point scanning on PVDF–TrFE in DFRT-PFM. (a) Topography showing the region previously scanned at 60 nN (highlighted in blue). Vertical DFRT-PFM (CR frequency range 250–350 kHz): (b) Amplitude and (c) Phase. Lateral DFRT-PFM (CR frequency range 600–800 kHz) at 0° scan orientation: (d) Amplitude and (e) Phase; and at 90° scan orientation: (f) Amplitude and (g) Phase.*

6.2.2 BFO Particles in PEDOT:PSS

DFRT-PFM imaging of the BFO–PEDOT:PSS system confirms that not all topographically identifiable aggregates exhibit a measurable piezoresponse, as in CR-PFM (**Figure 57 a-b**). As it was already previously suggested, this likely results from insufficient electrical contact between certain particles and the bottom electrode. Only particles visibly emerging from the matrix tend to show a detectable response.

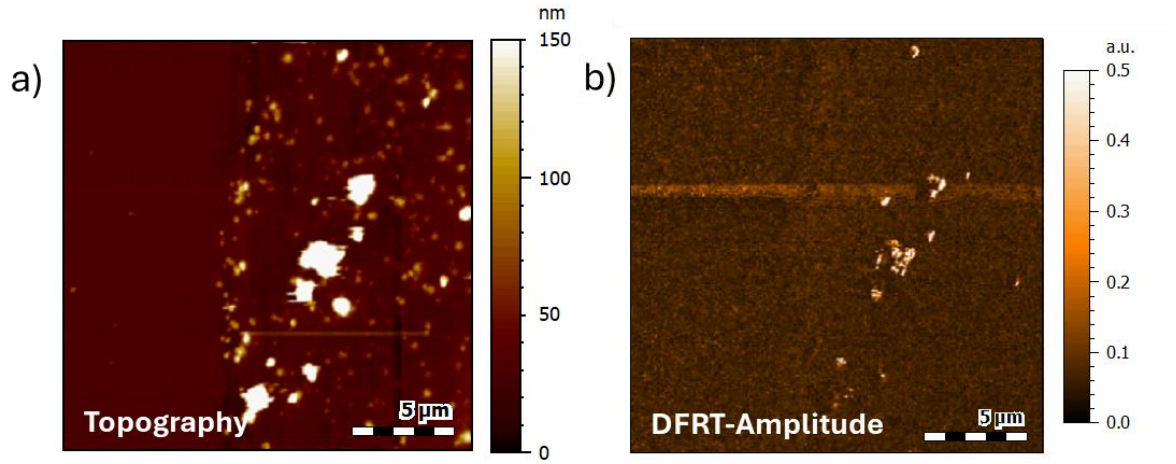

***Figure 57** : DFRT-PFM imaging of BFO–PEDOT:PSS over a 20 µm² area (CR frequency range 250–350 kHz). (a) Topography and (b) Vertical Amplitude.*

Focusing on a larger, responsive aggregate, the particles display a generally coherent amplitude signal with the phase images revealing distinct up- and down-domains (**Figure 58 a-c**). However, some particles within the aggregate exhibit a noticeably weaker out-of-plane phase contrast compared to the others. Examination of the corresponding in-plane images reveals the opposite behaviour. The regions with weak out-of-plane phase show stronger in-plane phase contrast (**Figure 58 d-e**). This inversion is consistent with a distribution of randomly oriented BFO grains within the aggregate.

Although the overall behaviour resembles that observed in CR-PFM, some anomalous features also appear. In certain zones, up- and down-domain phase contrast arises without a corresponding domain wall in the amplitude channel. This raises questions regarding the authenticity of these phase features. That part of the observed contrast originates from phase-flip artifacts caused likely by mechanical instabilities within the aggregate. Such instability prevents the PID controller from maintaining a stable lock, producing artificial phase switching rather than genuine ferroelectric contrast. Additional crosstalk between the vertical and lateral channels may further contribute to these effects.

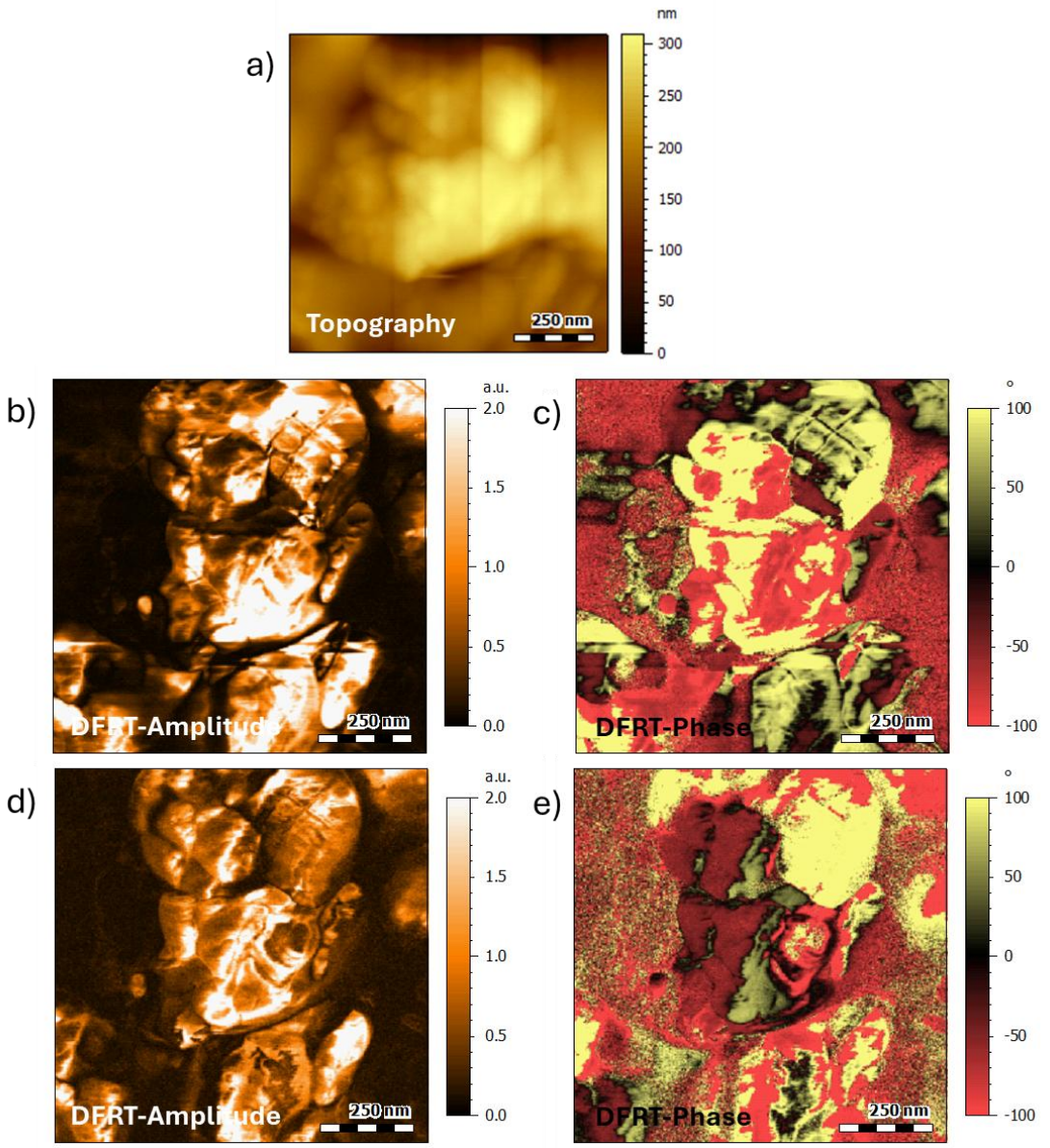

***Figure 58** : DFRT-PFM imaging of a responsive BFO aggregate over a 1 µm² area. Vertical mode (CR Frequency range 250–350 kHz): (a) Topography, (b) Amplitude, and (c) Phase. Lateral mode (CR Frequency range 600–800 kHz): (d) Amplitude and (e) Phase.*

6.2.3 PVDF-TrFE / BFO Nanocomposites

DFRT-PFM imaging performed on an isolated BFO grain within the ferroelectric nanocomposites demonstrates the possibility to successfully image both material phases simultaneously in both vertical and lateral modes (**Figure 59**). Clear ferroelectric domains can be assigned to each component. However, the image stability remains limited due to local variations in topography and mechanical modulus. To maintain stable tracking on these aggregates, a higher set-point was required, which occasionally caused minor scratching of the polymer and potential tip-induced domain reorientation. This effect is faintly visible in the phase maps.

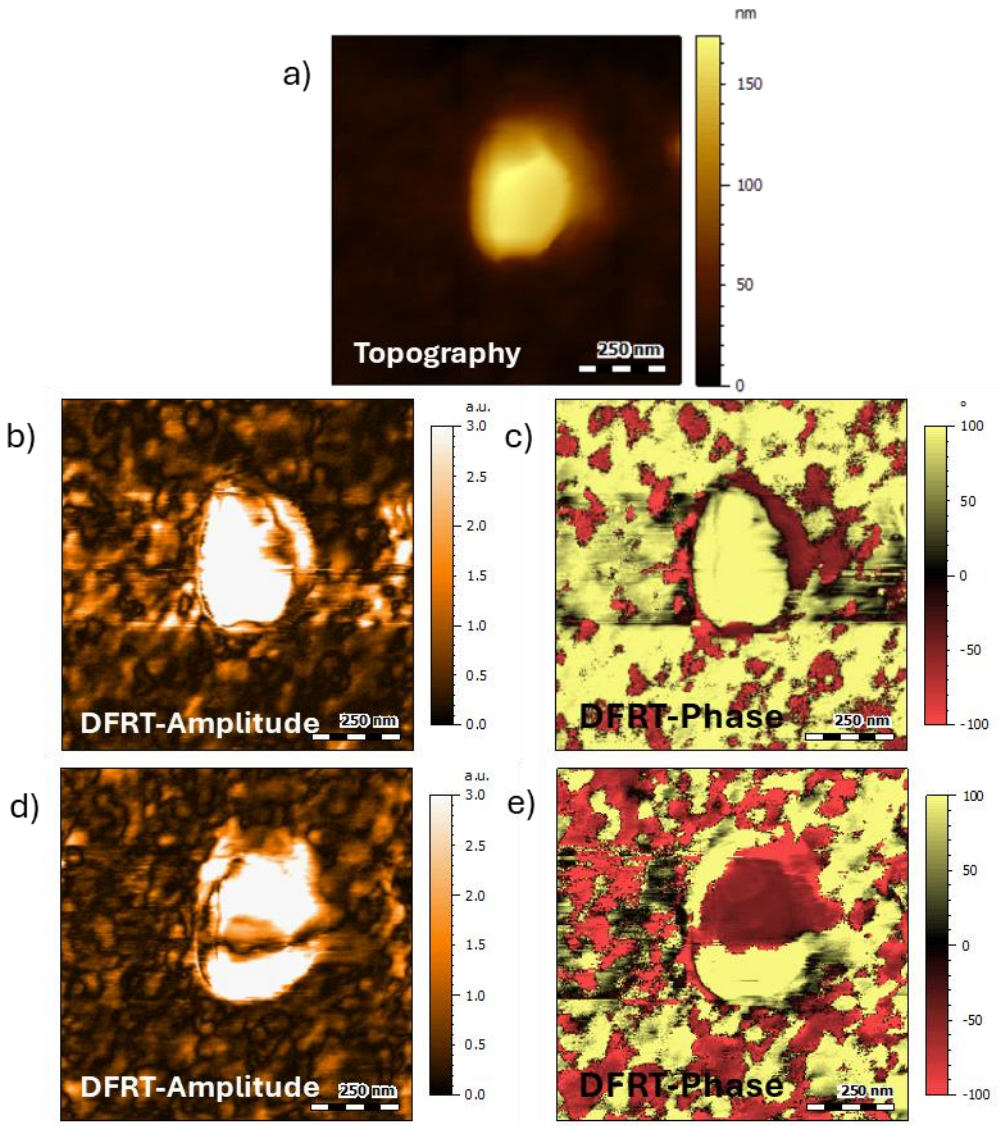

Figure 59 *:DFRT-PFM imaging of an isolated BFO particle embedded in PVDF–TrFE. Vertical mode (CR frequency range 250–350 kHz): (a) Topography, (b) Amplitude, and (c) Phase. Lateral mode (CR frequency range 600–800 kHz): (d) Amplitude and (e) Phase.*

Analysis of a multi-grain aggregate (**Figure 60**) reveals more diverse responses. Some particles show a clear amplitude response, whereas others appear non-responsive (centre right particle) (**Figure 60 b-c**). The inverted phase behaviour observed in isolated grains also appears here. Regions with weak out-of-plane phase contrast may show stronger in-plane response (**Figure 60 d-e**).

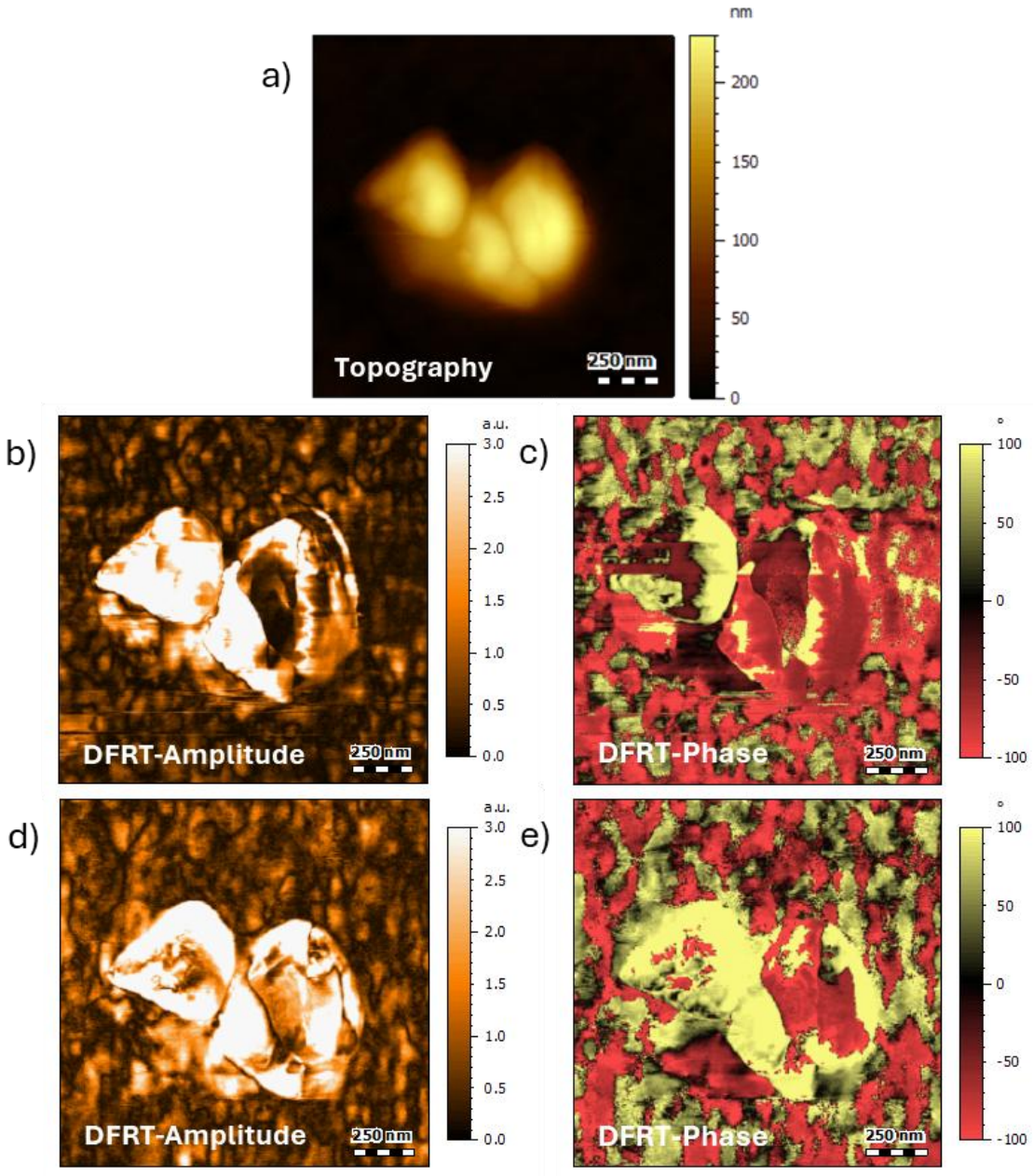

***Figure 60** : DFRT-PFM imaging of a multi-grain BFO aggregate embedded in PVDF–TrFE. Vertical mode (CR Frequency range 250–350 kHz): (a) Topography, (b) Amplitude, and (c) Phase. Lateral mode (CR Frequency range 600–800 kHz): (d) Amplitude and (e) Phase.*

As in the previous measurements on BFO particles, a part of the observed phase contrast appears to be artefactual because several regions exhibit phase inversion without any corresponding amplitude domain wall. This conduct most likely originates from phase-flip artifacts induced by local mechanical instabilities, rather than from a genuine ferroelectric domain structure. To confirm that these data were acquired over the same physical area, additional scans were performed with a scan angle of 90° (**Figure 61 a–b**). The ferroelectric domain structure of the polymer matrix remains largely unchanged,

whereas the apparent domain configuration located on top of the particles is significantly altered. More specifically, regions exhibiting phase contrast without associated amplitude walls are modified.

The pronounced surface roughness does not allow enough time for the PID controller to adapt and leads to phase overshoot phenomena. This overshoot becomes more evident when the phase scale is extended (**Figure 61 c–d**). It appears that the non-physical domain regions correspond to phase values exceeding ±90°, which can only be explained by signal inversion caused by instrumental overshoot rather than by a real polarisation state.

No restructuring of the ferroelectric domains surrounding the embedded particles is observed across all datasets, large-area or zoomed-in, CR-PFM or DFRT-PFM. The only regular effect is a degradation of data quality in regions where mechanical instabilities arising from topographic variations reduced the reliability of the contact resonance.

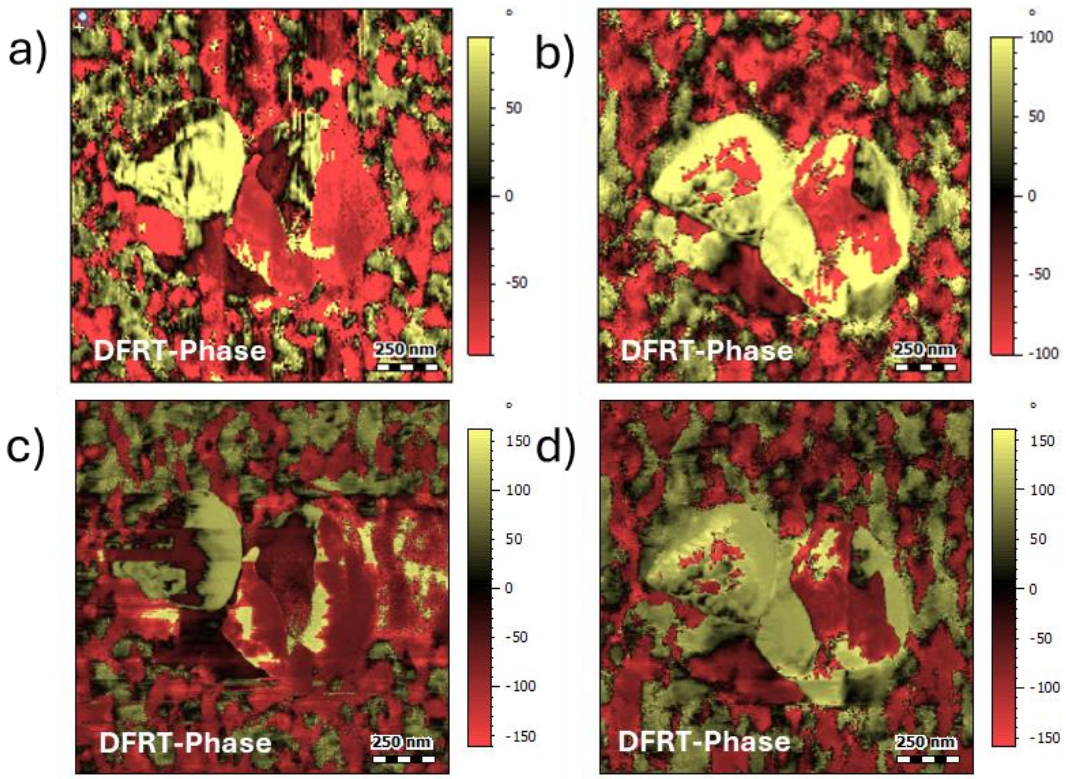

Figure 61 *:DFRT-PFM phases images corresponding to* ***Figure 60****. (a) Phase image in vertical mode (CR frequency range 250–350 kHz), scanned at 90°. (b)Phase image in lateral mode (CR frequency range 600–800 kHz), scanned at 90°.*

(c)Phase image in vertical mode (CR frequency range 250–350 kHz), scanned at 0 °. (d) Phase image in lateral mode (CR frequency range 600–800 kHz), scanned at 0°.

6.3 Conclusion

This chapter investigated the ability of PFM-based imaging techniques to resolve ferroelectric domains in both homogeneous and heterogeneous systems. Conventional CR-PFM enabled the observation of well-defined ferroelectric domain structures in PVDF–TrFE thin films, largely independent of surface morphology. However, its application to BFO-containing systems proved significantly more challenging due to surface roughness and local mechanical instabilities, leading to ambiguous amplitude and phase contrasts. The use of DFRT-PFM improved resonance tracking and allowed simultaneous vertical and lateral imaging, partially mitigating these limitations. Nevertheless, phase-flip artefacts and instability-related effects were frequently observed in heterogeneous regions, restricting the reliability of domain interpretation. These results highlight the intrinsic limitations of PFM imaging for complex nanocomposites and the need for complementary approaches.

Chapter 7: Spectroscopic measurements of the ferroelectric responses

As stated in **section 3.2**, the interpretation of the ferroelectric nature of a measured response at the nanoscale is a tedious process because numerous concurrent artifacts are present. For a long time, the collection of local poling PFM images and the local hysteresis loop of a sample was considered as a definitive proof of the ferroelectric nature of the sample. Since then, several cases of non-ferroelectric materials have shown ferroelectric-like hysteresis response in PFM. This common occurrence led to the wrong interpretation and classification of certain materials as ferroelectrics.

Several precautions are taken into consideration to reduce those undesirable effects to the minimum (**Table 3**), but this is often not enough of a solution. It is important to collect supplementary measurements, such as on-field hysteresis loop and cKPFM, to verify the true ferroelectric nature of the measured signal.

In this chapter, we present a detailed analysis of ssPFM measurements performed on well-defined ferroelectric (PZT) and non-ferroelectric (ZnO) reference systems, followed by their application to our systems, polymer films, oxide nanoparticles, and hybrid nanocomposites. Particular attention is given to the interpretation of both on- and off-field responses, the identification of heterogeneous behaviours, and the limitations inherent to single-point measurements. The chapter concludes with an extended analysis enabled by clustering-based ssPFM cartography.

Because the research team of the National Institute of Standards and Technology (NIST, USA) [161] has proposed that a set of simple measures is able to confirm or refute the ferroelectric nature of the response, comparison between on- and off-field results and the approach of cKPFM measurements have grabbed our attention. Those measurements are illustrated on a known ferroelectric (PZT) and a known non-ferroelectric (ZnO) on which ssPFM measurements were made, “optimizing” parameters to observe ferroelectric-like hysteresis. After that, the results on the sample of this thesis are presented as well as results on other samples encountered during this work. This “double-check” is essential to ensure that what is measured is not artifactual.

7.1 Illustration of ssPFM measurement on known ferroelectric PZT and non-ferroelectric ZnO

The simplest qualitative way to visualise the influence of electrostatic forces on an ssPFM measurement is to compare the off- and on-field results. When measurements are performed on a well-known ferroelectric sample, such as a PZT (**Figure 62 a**), a clear and stable off-field piezoresponse loop is obtained. The corresponding on-field loop exhibits a similar open hysteresis with an additional pronounced slope arising from electrostatic forces induced by surface charging.

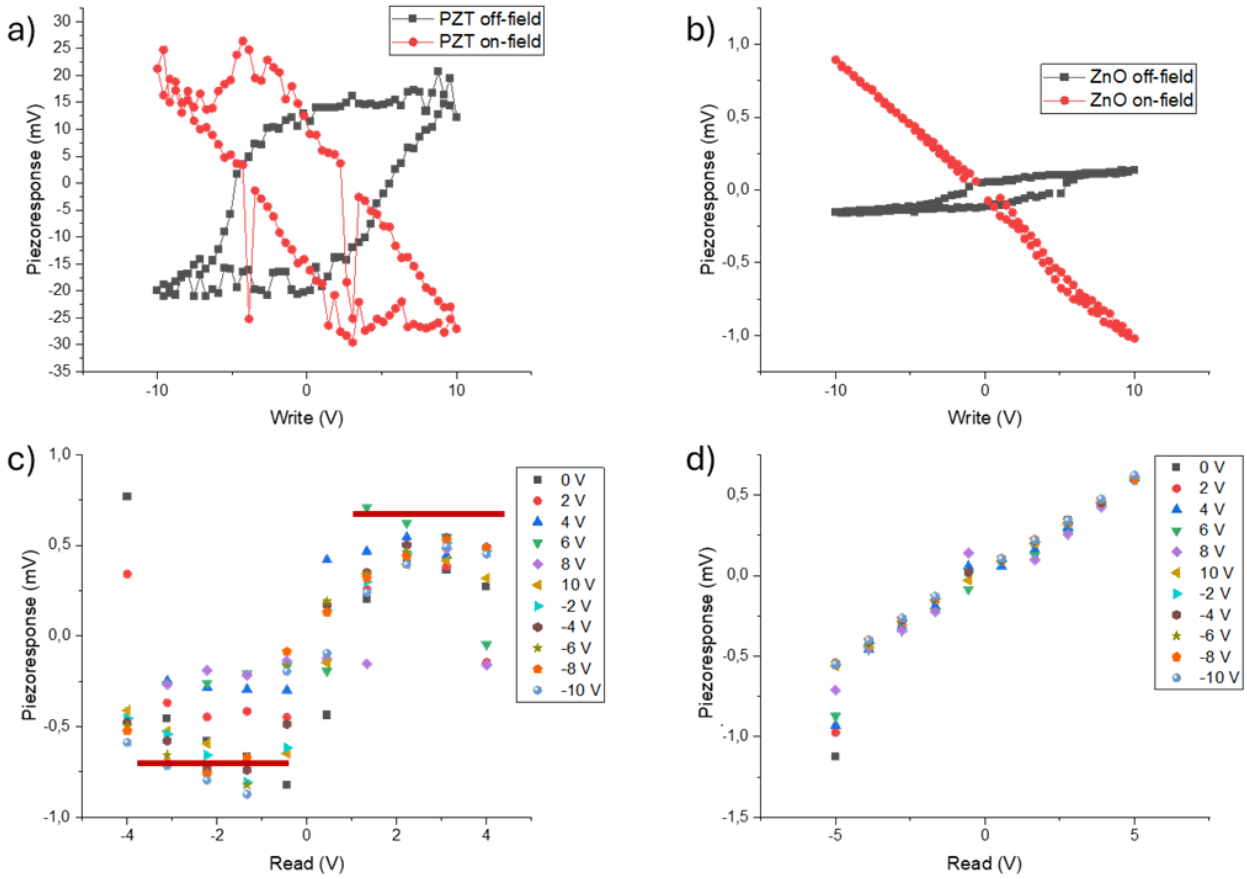

***Figure 62** : On- and off-field loops collected on a) PZT thin film and b) ZnO thin film. cKPFM measurement on c) PZT and d) ZnO.*

Regarding the ZnO, which is a known piezoelectric, non-ferroelectric material, a pseudo-ferroelectric off-field loop can be generated by intentionally enhancing the contribution of electrostatic effects, achieved by increasing the hold time of the poling segments from 10 ms to 30 ms and reducing the force setpoint from 70 to 25 nN. It mimics the behaviour of PZT (**Figure 62 b**). However, the on-field results show the disappearance of this pseudo-ferroelectric hysteresis, confirming its artefactual origin.

Another way to visualize the dependence of the PFM response from a sample on the applied polarisation voltage is to collect contact KPFM data using a set of ssPFM loops. Each loop shows a different initial value of the off-field loops (called reading voltage). By reconstructing the surface displacement in relation to the reading voltage for distinct poling values from the script, a bi-state equilibrium between the two extreme reading voltage values is observed, as illustrated in **Figure 62 c** by the two red lines. Conversely, a non-ferroelectric material such as ZnO displays a continuous, non-saturating response between the two extremes (**Figure 62 d**).

7.2 Single point ssPFM measurement

7.2.1 PVDF-TrFE

As shown in the PFM imaging section, all samples examined in this work exhibit naturally occurring ferroelectric domains and remain polarizable within the voltage range used. To further probe their properties, local ferroelectric hysteresis loops were taken in with ssPFM, an unambiguous method to confirm ferroelectric switching at the nanoscale.

Each ssPFM measurement consists of 6–10 consecutive loops. A representative example acquired at a random location on the polymer thin film is displayed in **Figure 63 a**. The first loop typically shows a reduced response compared to subsequent cycles, reflecting the initial alignment of dipoles before reaching a stable switching regime. For the statistical analysis, the first cycle is then excluded to calculate the averaged loops shown in **Figure 63 b–d**. The resulting mean amplitude, phase, and piezoresponse loops display the expected signatures of a ferroelectric polymer: a butterfly-shaped amplitude curve, a 180° phase reversal, and a negatively oriented piezoresponse consistent with the negative piezoelectric coefficient of PVDF-TrFE, respectively.

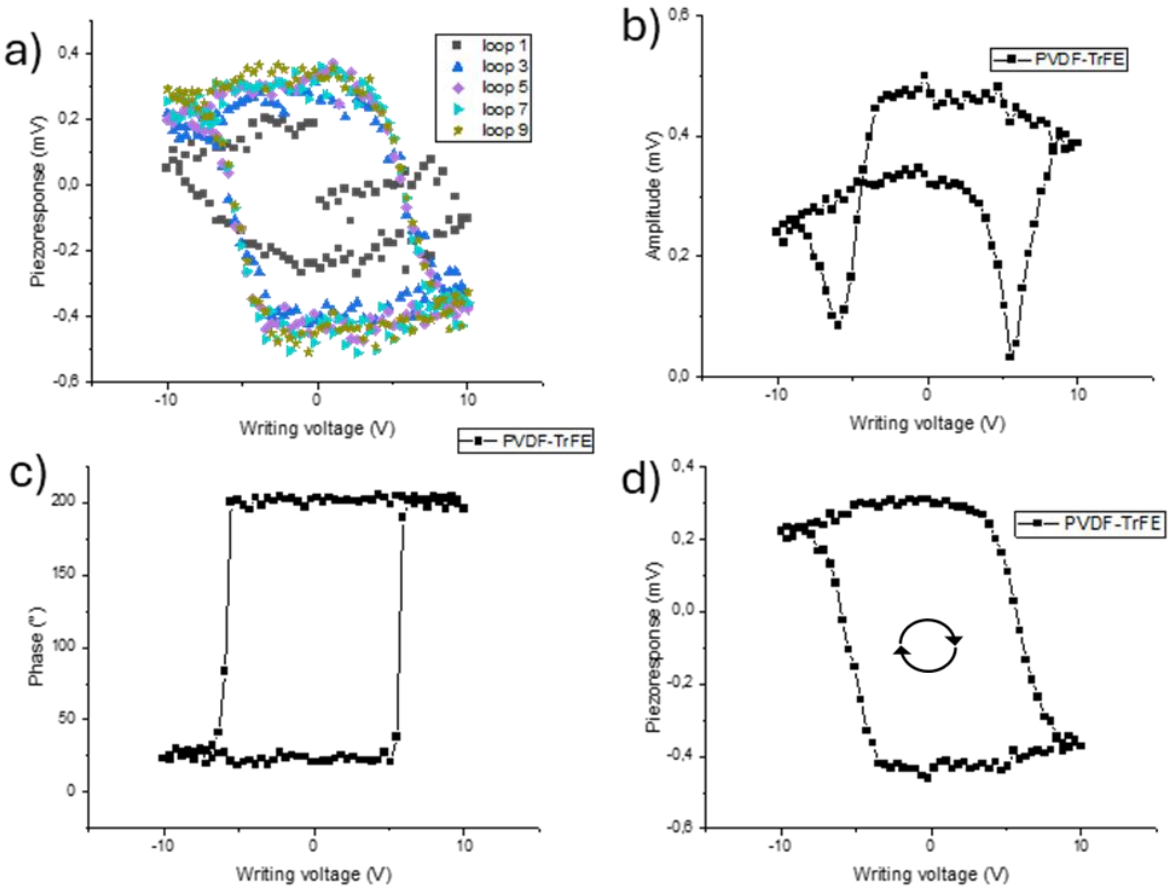

Figure 63 *: Ferroelectric loops on PVDF-TrFE: (a) different Piezoresponse loops collected during a single ssPFM measurement. (b) Mean Amplitude loop, (c) Mean Phase loop and (d) Mean Piezoresponse loop.*

For each off-field data on the isolated compounds or the composites, the on-field results were also captured at the same time. These results show that hysteresis remains through the reduction of the coercive voltage (**Figure 64 a**). It leans toward the conclusion that the measured loop arises from the ferroelectricity of the polymer. The cKPFM results further confirm this conclusion, showing the expected bi-state equilibrium (**Figure 65 b**).

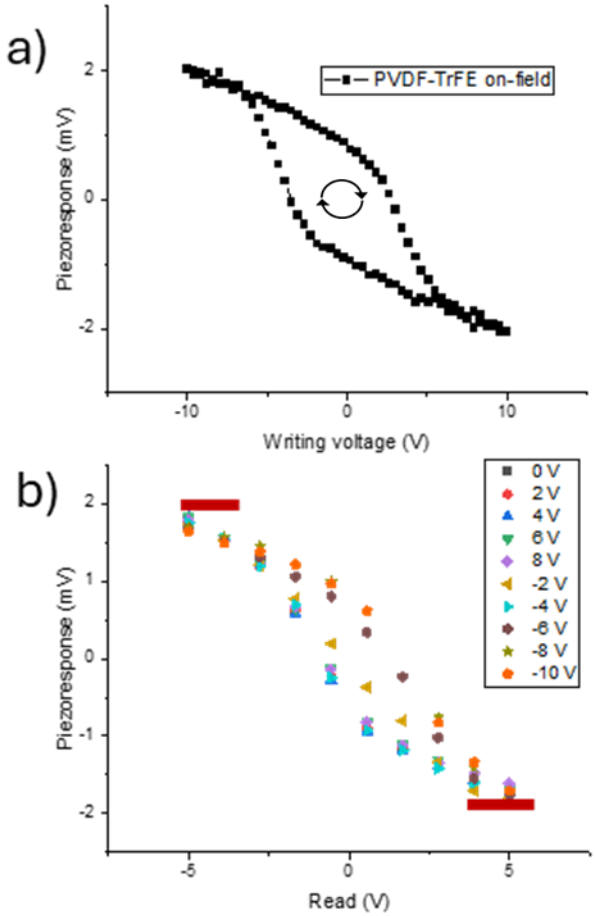

Figure 64 *: (a) On-field measurement and (b) cKPFM measurement on PVDF-TrFE samples.*

7.2.1.1 Thickness limitation

When studying ferroelectric thin films, one central question concerns the influence of film thickness on the detectability and magnitude of the piezoresponse, particularly in the polymer matrix. This particularity was investigated by performing measures on a PVDF-TrFE film prepared at 10 wt% instead of the usual 5 wt% and selecting a region near the film edge to capture a continuous thickness gradient. ssPFM hysteresis loops were recorded at regular intervals of 750 nm starting from the thinnest areas toward the thicker ones. The **Figure 65 a** and b illustrate this point from a sample where the edge thickness is approximately 50 nm, and each successive step shows an increase of roughly 20 nm.

From these measures emerge:

- First, the coercive voltage increases with thickness as expected (**Figure 65 c**). Switching a thicker ferroelectric layer requires a larger poling voltage to reverse the polarisation. In this study, the polymer switches no longer within the accessible

voltage range beyond a critical thickness of 110 nm. The value stays on a fixed piezoresponse, particularly visible when the thickness is over 150nm. But this limitation has no influence on our experiments because the thickness of all films in the nanocomposite of our research lies between 20 and 60 nm.

- Second, the maximum piezoresponse amplitude also strongly depends on the film thickness. Comparing the 50 nm and 110 nm regions reveals a reduction of up to 30% in the piezoresponse for the thicker film. Several factors may contribute to this behaviour. Thinner films show a more uniform electric field distribution across their reduced thickness, leading to more efficient polarisation switching. Additionally, thinner films are mechanically more compliant, leading to an enhanced electromechanical deformation and consequently to an increase in the piezoresponse [194].

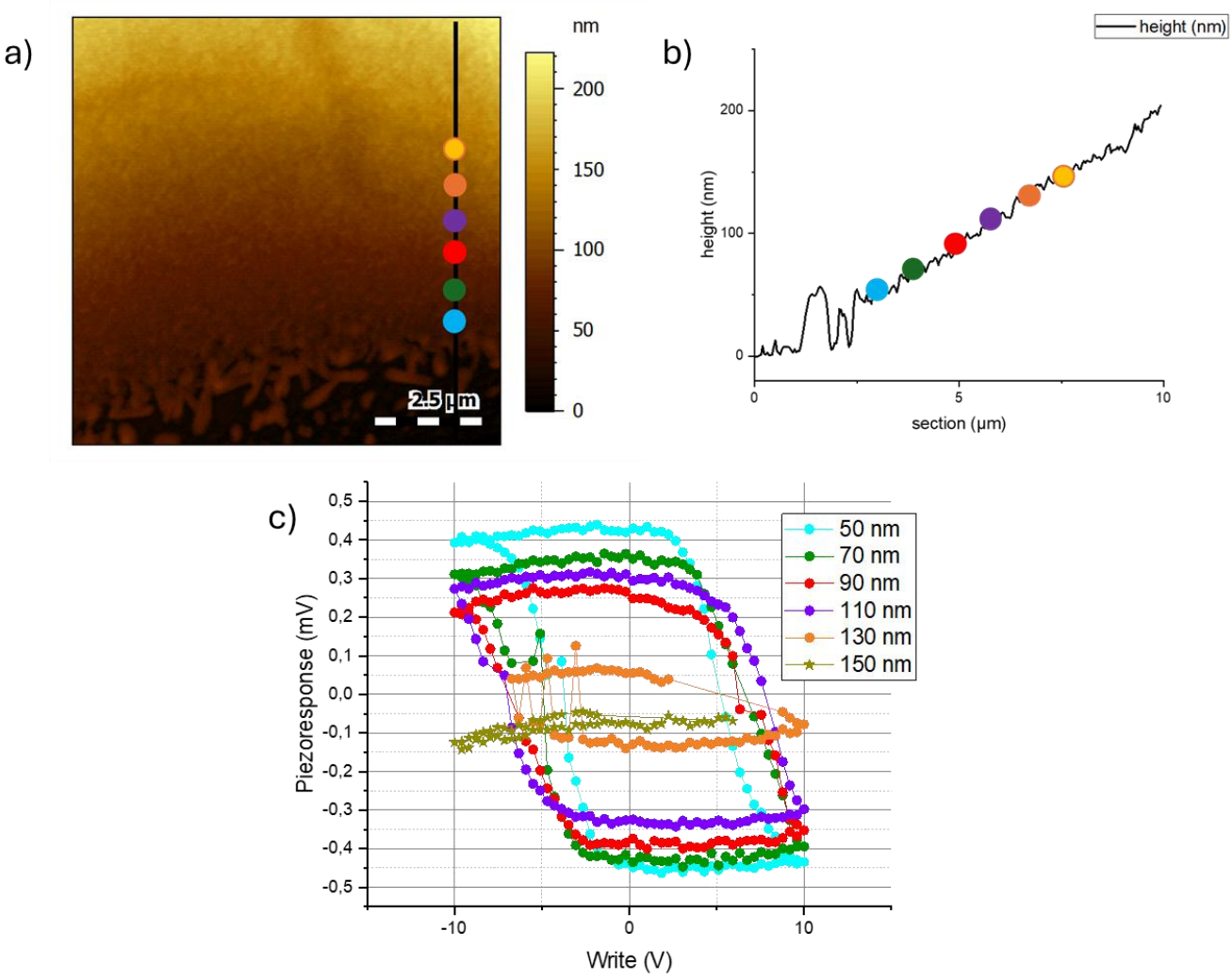

***Figure 65** : Influence of the thickness on the polarizability of the samples. (a) Topography of a film of PVDF-TrFE (5mg-ml) with relative position of the polarisation curves. (b) Thickness cross-section and the relative's position and (c) Ferroelectric loops at each relative position.*

7.2.2 BFO particles

Compared to the polymer thin films, ssPFM measurements on BFO nanoparticles reveal a broader diversity of behaviours. The most common response is a ferroelectric loop comparable in shape to that of PVDF-TrFE, especially in BFO mechanically maintained in PEDOT:PSS thin film and in the full nanocomposite to a lesser extent (illustrated by the blue topographical point in **Figure 66** and its corresponding amplitude in **Figure 66 b**), but inverted in sign, reflecting the opposite polarity of the BFO piezoelectric coefficient (**Figure 66 c-d**). Furthermore, other behaviours are also observed, like in the green area of **Figure 66 a** where the region shows a strong piezoresponse but no polarizability in the studied range (**Figure 66 e-f**), or like in the red area of **Figure 66 a** where no piezoresponse was detected. The lack of response can be explained by the fact that the area appearing as particles in imaging is some of the conductive polymer.

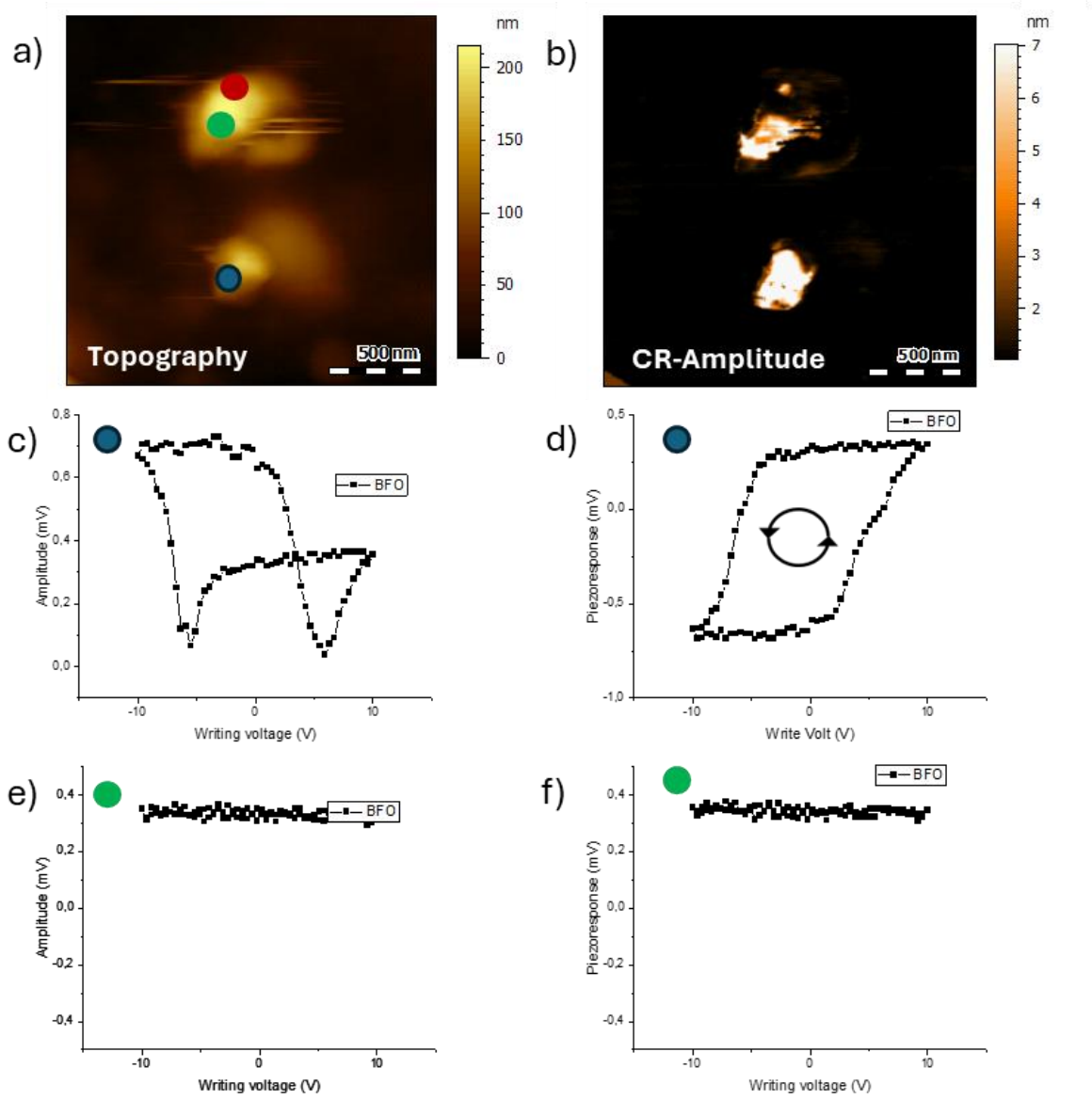

Figure 66 *: CR-PFM imaging of -BFO-PEDOT:PSS sample (a) Topography, (b) Amplitude. Indicated in blue, green, and red are, respectively the first, second, and third positions of ssPFM measurement. Ferroelectric loops on BFO particles (c) Amplitude, and (d) Piezoresponse of position 1 (blue), (e) Amplitude, and (f) Piezoresponse of position 2 (green).*

Looking at the ferroelectric verification, the on-field results for the blue area are similar to those of PZT, with an open hysteresis (**Figure 67 a**). Furthermore, the cKPFM results show the expected bi-state equilibrium (**Figure 67 b**). It is noticed that the V_{read} values are far greater than the rest of the measures in reason of its high hardness to poll than the PVDF-TrFE. Secondly, for the green area, we observe the same polarisability in on-field and in off-field. Furthermore, there is no bi-state equilibrium observed with the other ferroelectric measures. There is only a continuum of state that corresponds to the observations with ZnO. Moreover, the data at one fixed polarisation state appear

unswitchable with the technical conditions of our measurement apparatus. These observations strengthen the assumption that some part of the particles cannot be switched in the studied range. The red area even though visibly collected on what is supposed to be a BFO particle does not show any measurable responses.

All these results highlight limitations of single-point ssPFM measurements when applied to heterogeneous or multiphase materials. While adequate for uniform thin films, single-pixel loops fail to capture the spatial complexity of nanocomposites, making spatial mapping essential to reveal true trends [195].

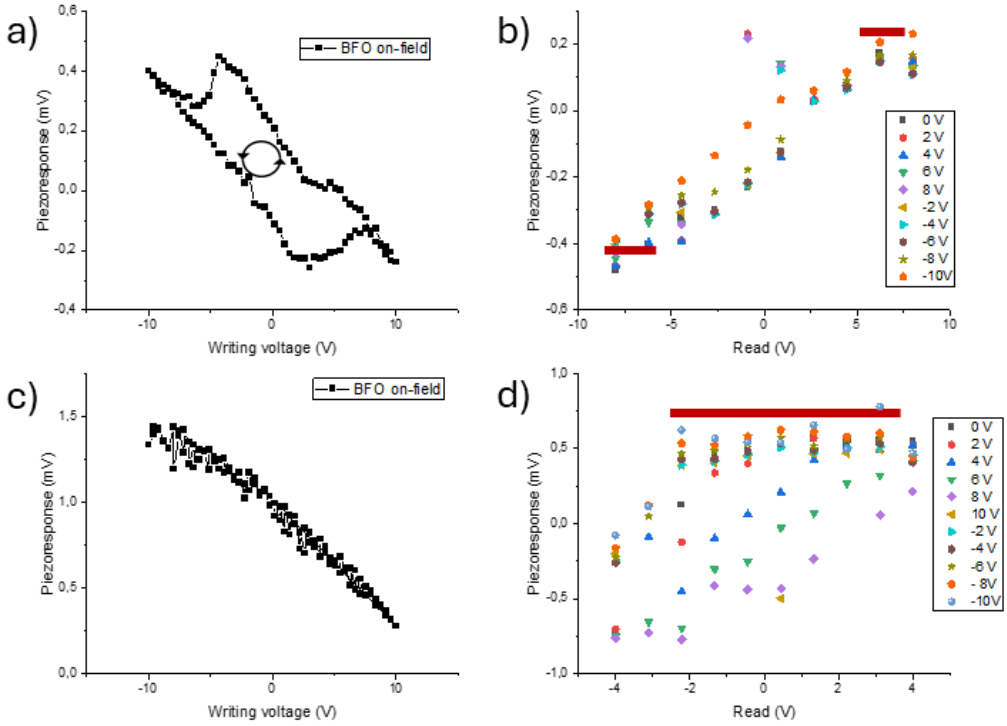

***Figure 67**:(a) On-field measurement and (b) cKPFM measurement on BFO particles position 1 (blue), (c) On-field measurement and (d) cKPFM measurement on BFO particles position 2 (green).*

7.3 ssPFM clustering

In most ssPFM studies, data are collected at a single location [196–198], providing only a local assessment of the ferroelectric response. Very few reports make use of the full cartographic capabilities of ssPFM measurement [199]. Similarly, some researchers working on related nanocomposite systems typically present only one representative loop per constituent phase [200,201]. However, our approach is to use a clustering ssPFM software to analyse ferroelectric trends in the different regions of the studied heterostructures. It is the recently developed pyssPFM software [184]. Since on- and off-

field are easily collectable simultaneously, both their trends are presented for all measures as a regular verification of the true ferroelectric nature of the signal.

7.3.1 PVDF-TrFE thin film

For the pure PVDF-TrFE film (**Figure 68**), the off-field piezoresponse loops extracted from a 4×4 ssPFM grid closely resemble those obtained from a single-point measurement (**Figure 68 c-d**). Only minor variations in coercive voltage are observed, plausibly attributable to small local differences in film thickness.

Dividing the data into 2 clusters using the pyssPFM software (**Figure 68 b**) does not significantly modify the resulting average piezoresponse loops, aside from small variations in loop amplitude (**Figure 68 e-f**). This behaviour is expected for a uniform polymer film, where the absence of sharp thickness gradients prevents strong local variations of the ferroelectric response within the scanned area.

The on-field mean loop saved alongside the off-field mean shows the same open and electrostatically pinched hysteresis reported in singular measurements. This highlights the true ferroelectric nature of the measure signal.

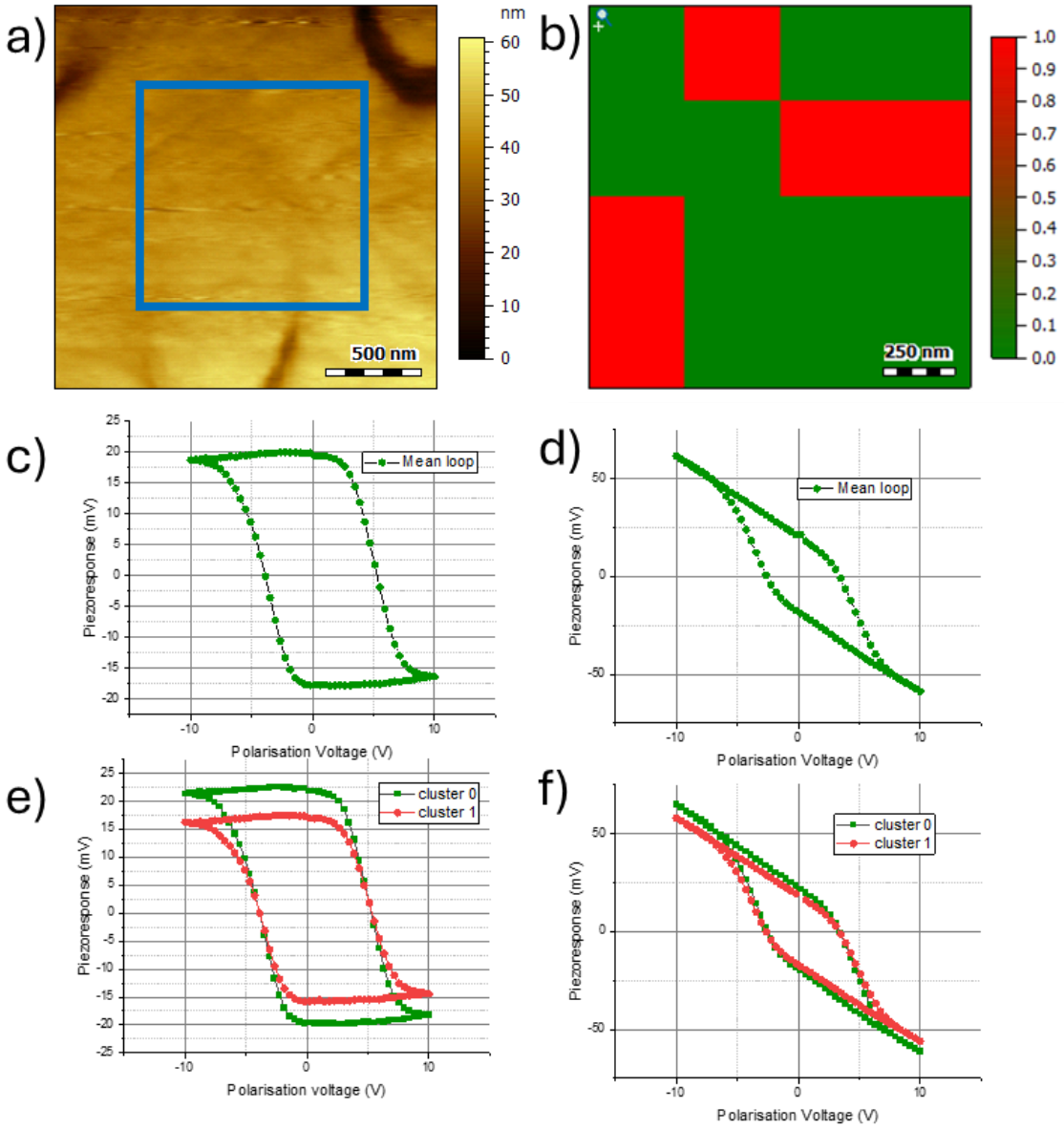

Figure 68 *: (a) Topographical image of PVDF-TrFE sample. The blue square marks the region used for ssPFM mapping, 4×4 curves over 1μm² area. (b) PyssPFM clustering for k=2. (c) Mean off-field loop and (d) Mean on-field loop of all 16 measurements. (e) Mean off-field loops and (f) Mean on-field loops for each cluster when k=2.*

7.3.2 BFO-PEDOT:PSS

The ssPFM analysis of the BFO particles within the conductive polymer matrix is presented in **Figure 69** and **Figure 70**. When the number of clusters is fixed at two (**Figure 70 a**), the distinction between the two main components becomes clear (**Figure 70 c-d**). The first cluster corresponds to the active BFO particles, which exhibit well-defined piezoresponse loops with consistent on- and off-field behaviour. The second cluster comprises both the non-responsive regions of the stabilizing polymer matrix clearly

visible as low-amplitude zones in the PFM images and some non-responsive BFO areas, most likely corresponding to particle edges or grains that are electrically isolated from the electrode.

Increasing the number of clusters reveals a further subdivision within the BFO population (**Figure 70 b**). A dominant cluster largely like to the initial one encompasses the majority of responsive BFO grains. However, secondary cluster but smaller exhibits markedly off-centred loops characterized by predominantly positive piezoresponse values (**Figure 70 e-f**). Notably, comparison with the corresponding PFM phase images (**Figure 69 c-d**) saved before and after the ssPFM measurement shows that the secondary cluster mainly coincides with regions of BFO particles that do not undergo a phase reversal during poling. These particles do not appear to be particularly bigger than the other ones. The limitation does then not seem to arise from the size of the particles. These areas likely correspond to grains with unfavourable crystallographic orientation or to particles partially encapsulated by the PEDOT:PSS layer, which would hinder efficient electrical contact and domain switching.

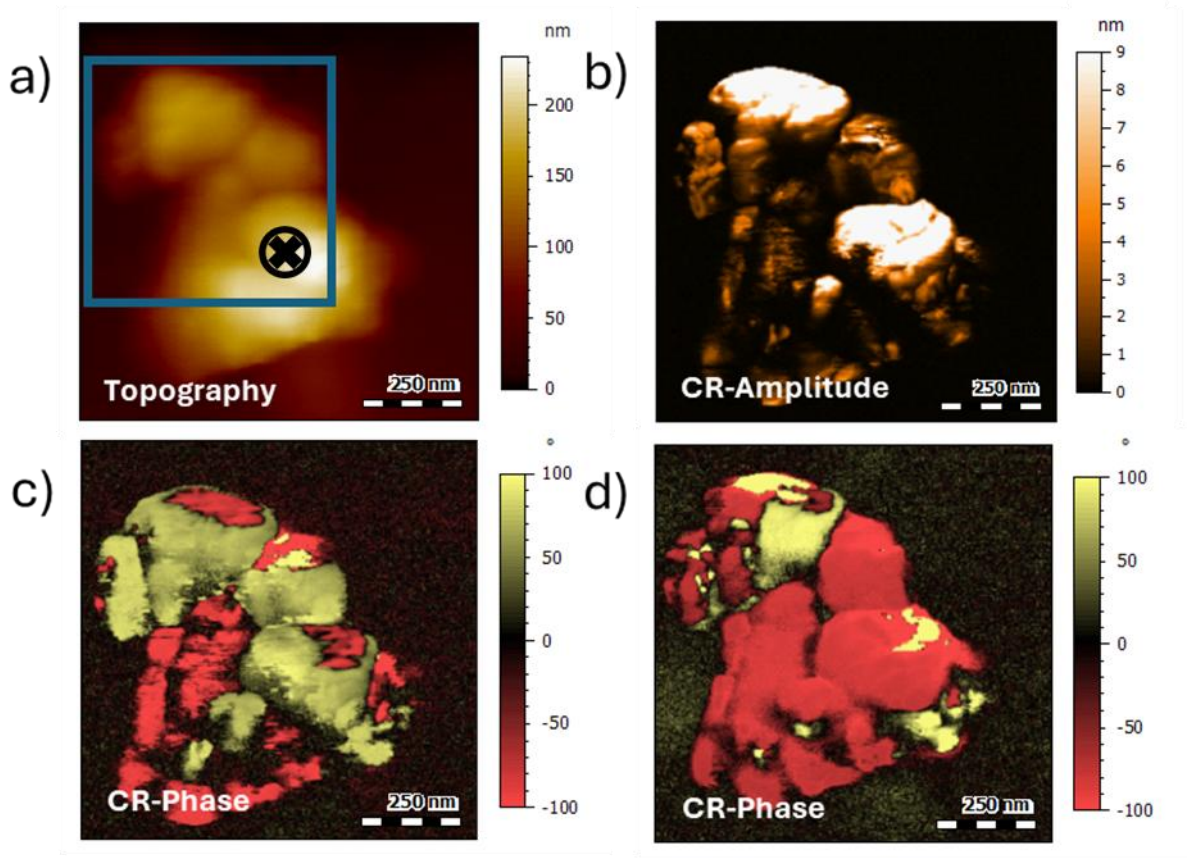

***Figure 69** :(a) Topography of BFO aggregates. The blue square marks the region used for ssPFM mapping, 8×8 curves over 500 nm². (b) Amplitude image without polarisation. (c) Phase image before polarisation and (d) Phase image after polarisation.*

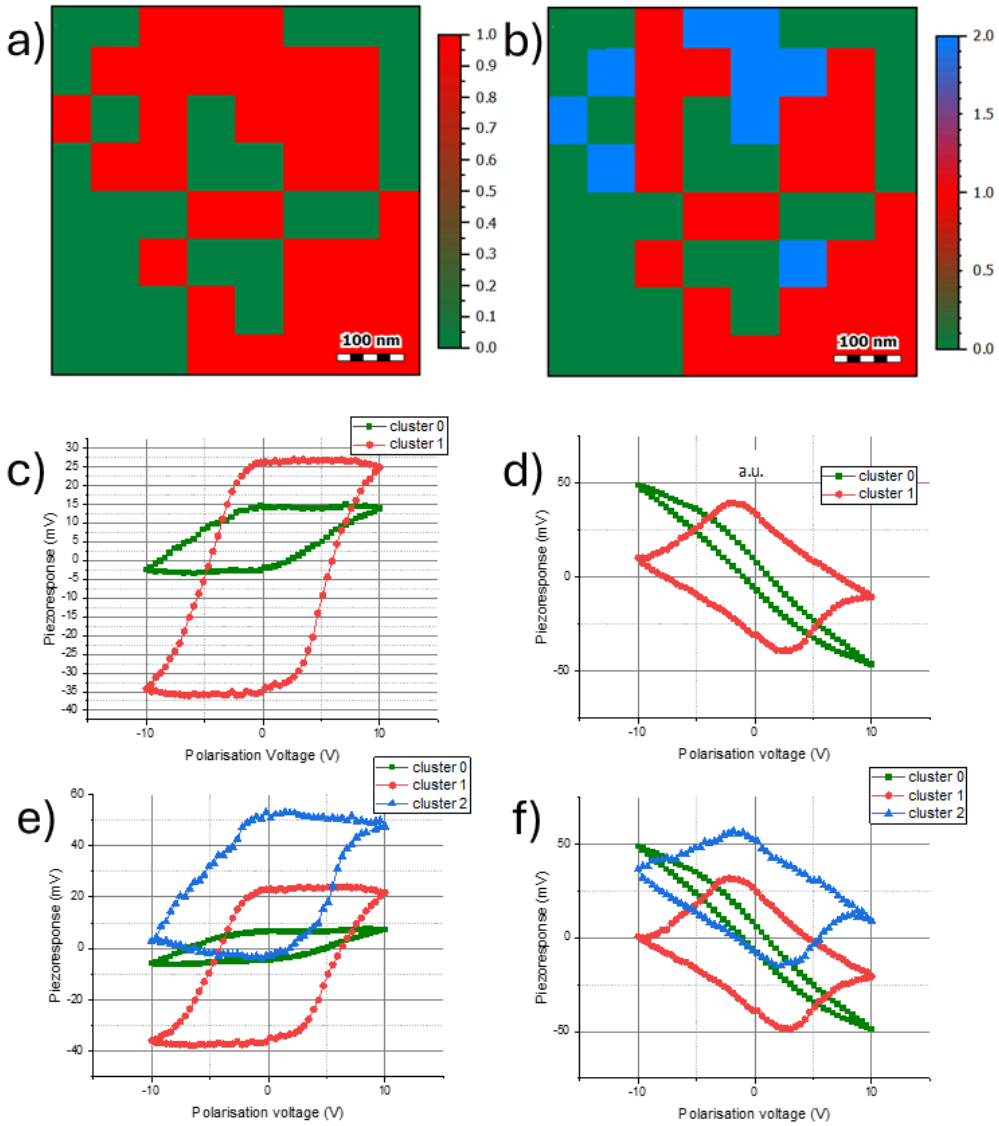

***Figure 70**: (a) PyssPFM clustering for k=2 and (b) PyssPFM clustering for k=3. (c) Mean off-field loops and (d) Mean on-field loops for each cluster when k=2. (e) Mean off-field loops and (f) Mean on-field loops for each cluster when k=3.*

7.3.3 Ferroelectric nanocomposite

With the hybrid ferroelectric nanocomposite (**Figure 71**), the identification of the two main behaviours is relatively straightforward, as both components are clearly distinguished by the orientation of their hysteresis loops. The polymer exhibits a counterclockwise loop orientation, consistent with that observed in pure PVDF-TrFE thin films, whereas the BFO displays a clockwise loop orientation (**Figure 71 e-f**). The corresponding on-field loops closely resemble those recorded for the individual materials. Similar to was observed for BFO in the conductive matrix, a third population emerges within the BFO aggregate regions and characterized by uncentred and hardly polarizable loops (**Figure 71 d**). These areas display a strong apparent piezoresponse but

lack a clear phase inversion under applied field conditions, as illustrated in the phase images (**Figure 71 c**). It should be noted that the phase images and the ssPFM mapping do not perfectly overlap. This defect can be attributed to experimental drift occurring during the measurement.

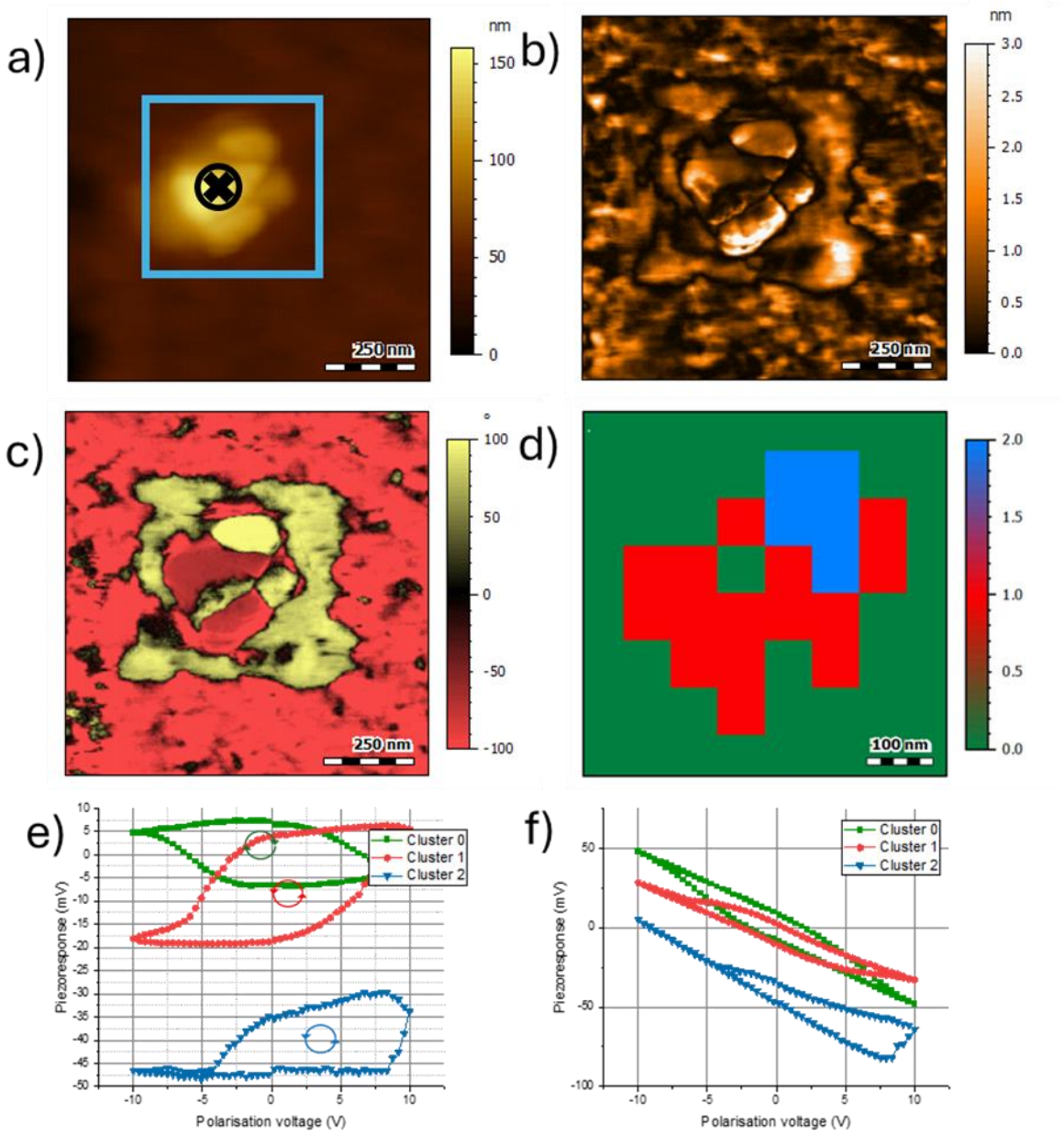

***Figure 71** : (a) Topographical image of PVDF-TrFE/BFO composite sample. The blue square marks the region used for ssPFM mapping, 8×8 curves over 500nm² area. (b) Amplitude and (c) Phase. (d) PyssPFM clustering for k=3. (e) Mean off-field loops and (f) Mean on-field loops for each cluster when k=3.*

The issue of unpolarizable grains within the accessible voltage range appears more pronounced in the composite system than in the individual components. Some grains

exhibit both positive and negative phase orientation depending on the initial orientation of their domains, without showing full switching behaviour (**Figure 72**). This likely results from the superposition of two relatively thick dielectric layers, which hinders efficient poling within the applied voltage range.

The difficulty in quantifying the coercive voltage is plausibly linked to thickness effects. Nevertheless, this explanation alone may not suffice because certain regions, particularly the upper portions of some aggregates, still exhibit a clear response within the studied voltage window.

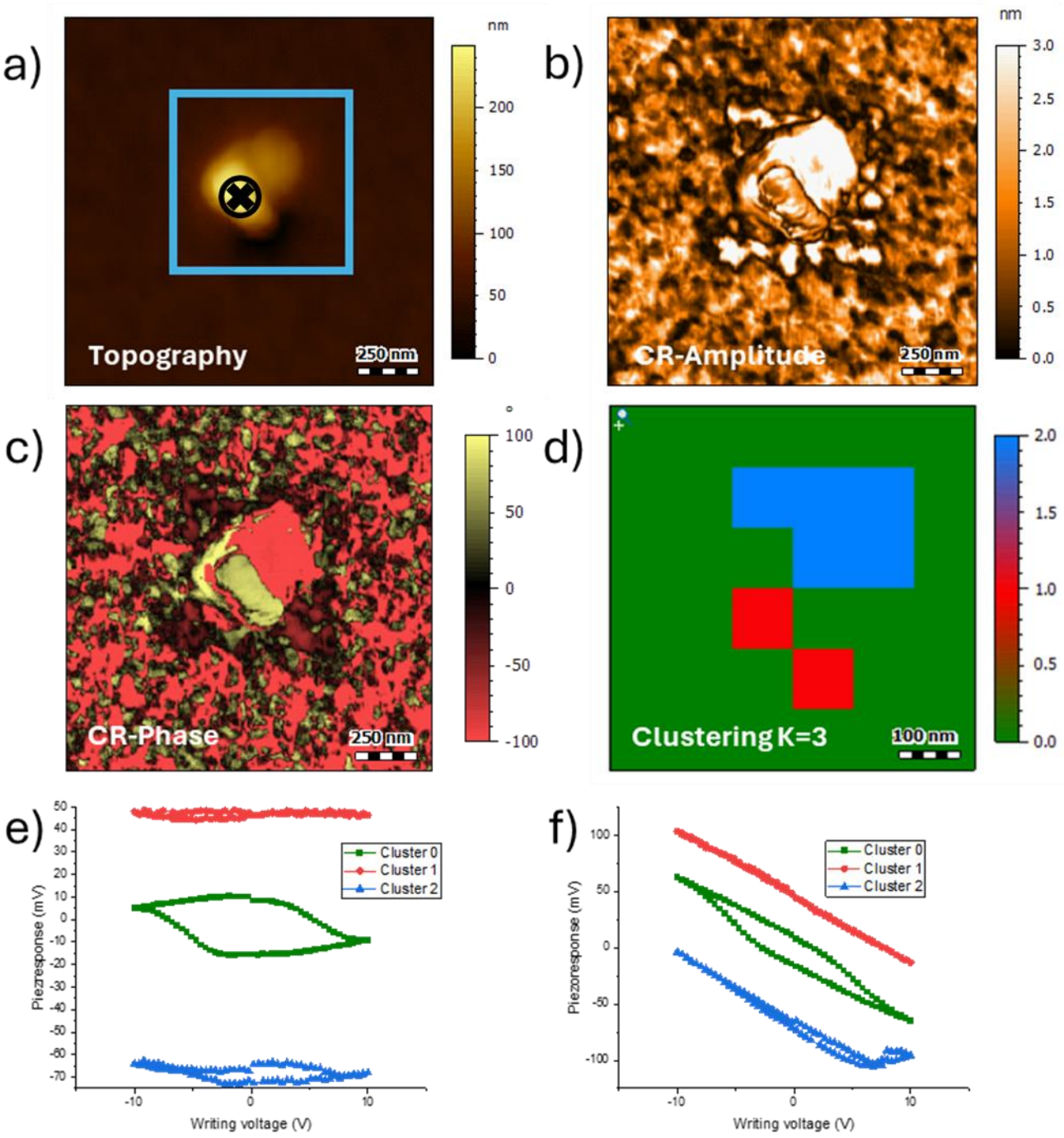

Figure 72 *: (a) Topographical image of PVDF-TrFE/BFO composite sample in a non-polarizable region. The blue square marks the region used for ssPFM mapping, 8×8 curves over a 500 nm² area. (b) Amplitude and (c) Phase. (d) PyssPFM clustering for k=3. (e) Mean off-field loops and (f) Mean on-field loops for each cluster when k=3.*

7.3.3.1 Subsurface particles

An important consideration for nanocomposite systems such as those investigated here concerns the presence of particles embedded below the polymer surface. It is

particularly relevant to determine whether such subsurface inclusions can be detected and whether they influence the local electromechanical response of the matrix.

Heterodyne KPFM provides a suitable approach to identify these buried particles through variations in the surface potential. As shown in **Figure 73**, a clear contrast is observed between the polymer matrix and the BFO particles. On another hand, several low-potential regions are visible and do not seem to correspond to any feature in the topography. This fact indicates the presence of particles located beneath the surface. Even though a slight deformation is observed in some cases, most remain undetectable by topography alone.

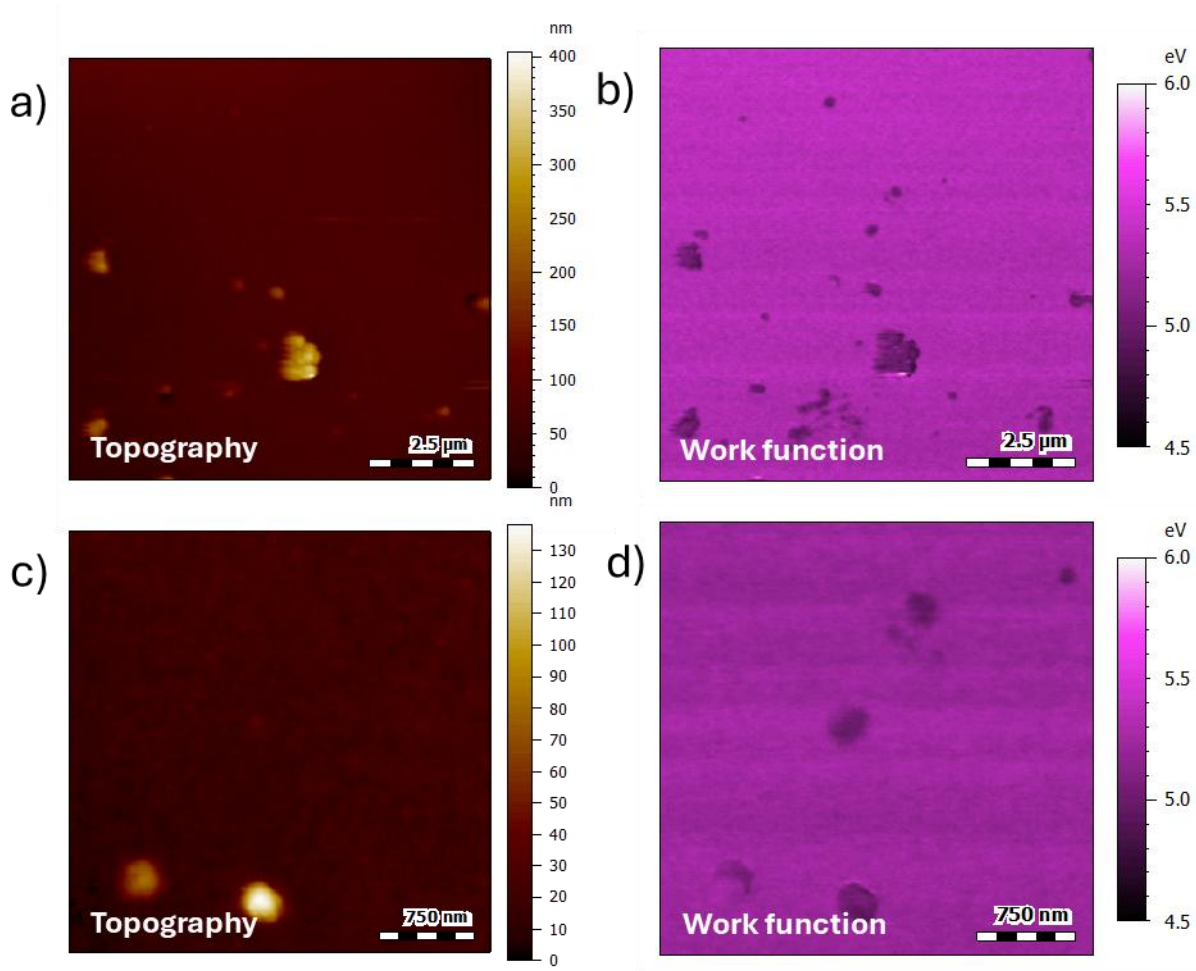

***Figure 73** : Heterodyne KPFM measurement on the ferroelectric nanocomposites. (a) Topography and (b) Work function of a 10 µm ^{2} area. (c) Topography and (d) Work function of a 3 µm ^{2} area.*

When the same regions are analysed by PFM, no characteristic BFO response is detected. A small perturbation in the phase image is only observed (**Figure 74 a–c**). The ssPFM maps further confirm that the only identifiable switching behaviour corresponds to the PVDF-TrFE matrix. The presence of the embedded particles gives rise solely to a modest

reduction of the piezoresponse amplitude (**Figure 74 d–e**), with no measurable ferroelectric contribution from the particles themselves.

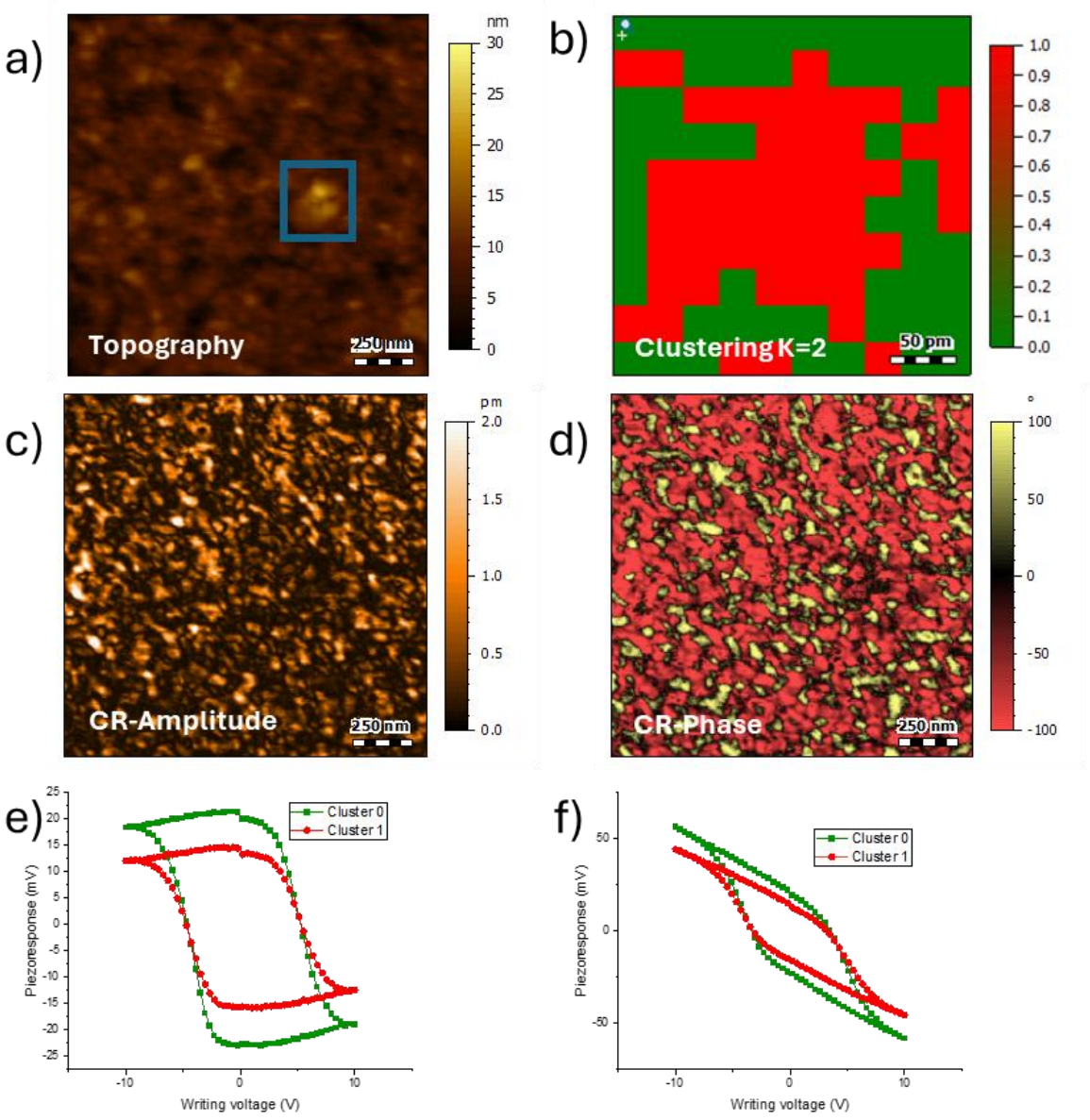

Figure 74 *: (a) Topographical image of PVDF-TrFE/BFO composite sample over underground particles. The blue square marks the region used for ssPFM mapping, 10×10 curves over a 250 nm² area. (b) Amplitude and (c) Phase. (d) PyssPFM clustering for k=2. (e) Mean off-field loops and (f) Mean on-field loops for each cluster when k=2.*

7.4 *"A priori"* ferroelectric samples from the literature

As illustrated in the previous results, the utmost caution is required when claiming that a material is ferroelectric or not based only on PFM measurement. Indeed, it is not rare to find recent studies that use the great resolution offered by the PFM measurement to assess the ferroelectric properties of very small or thin samples and which could not be

obtained with other ferroelectric assessments. Nonetheless, a lot of them do not check the authentic nature of the measure signal. It was also the case concerning the ferroelectric nature of lanthanide tungsten oxide and Tellurium nanowire, which are challenged in the LPNE laboratory

7.4.1 Lanthanide tungsten oxide

Lanthanide-based tungsten oxide (abbreviated as Ln_2WO_6) is a specific class of materials. Studied by the UCCS laboratory from Artois University, Ln_2WO_6 were thoroughly investigated as thin film deposed by pulsed laser ablation, using a variety of structural and crystallographic techniques, as well as by PFM [202–204]. It shows apparent polarizability with square imaging in conventional PFM imaging (**Figure 75 a-b**) and apparent hysteresis loops in spectroscopic mode (**Figure 75 c**). It was registered as a class of ferroelectric materials with a weak piezoelectric coefficient.

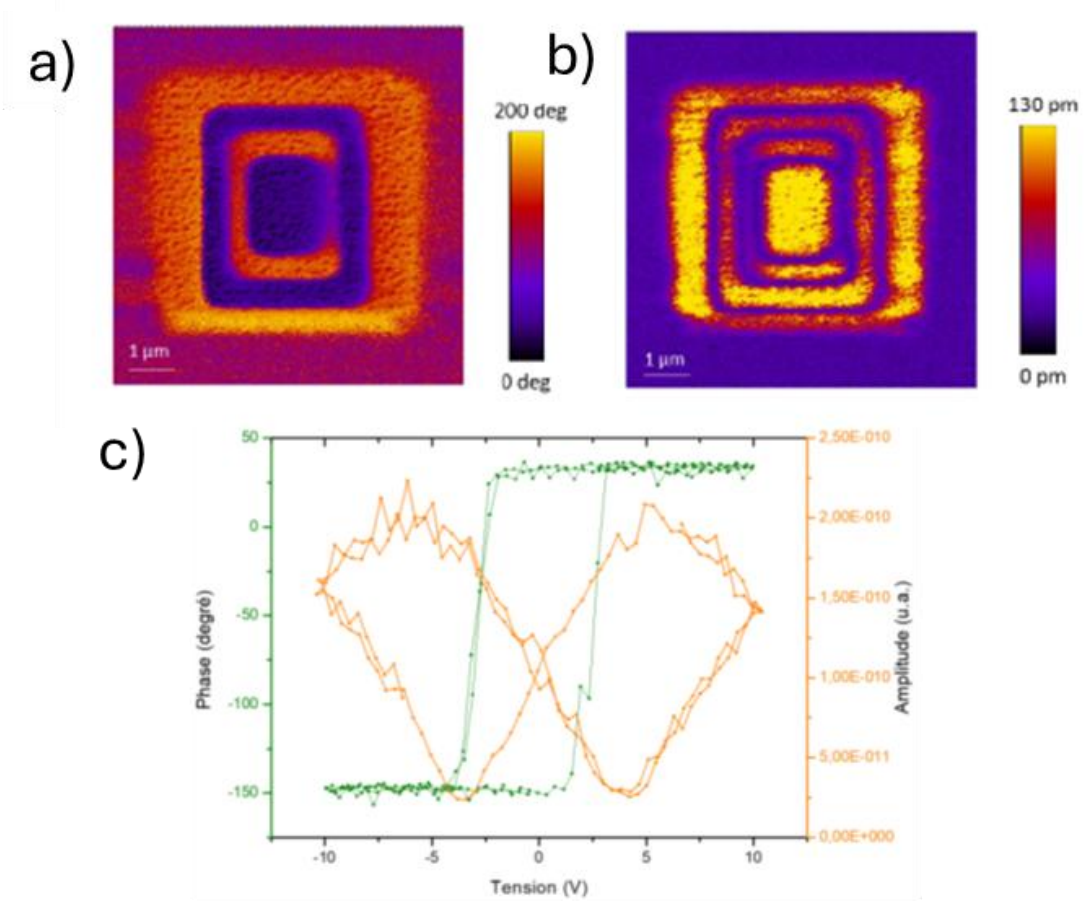

***Figure 75** : PFM data collected on the Gd_2WO_6: (a) Phase, (b) Amplitude, and (c) Amplitude/Phase loops collected at the UCCS Artois. Figure adapted from [202].*

In the prospect of a collaboration between UCCS and LPNE, some samples were also characterised by the LPNE as calibration samples for the numerous PFM techniques. The first one of the batch was the Gd_2WO_6. The first set of measurements from this sample

showed comparable ferroelectric square poling (**Figure 76 a-b**) and hysteresis loops (**Figure 76 c**) as those one previously reported on it.

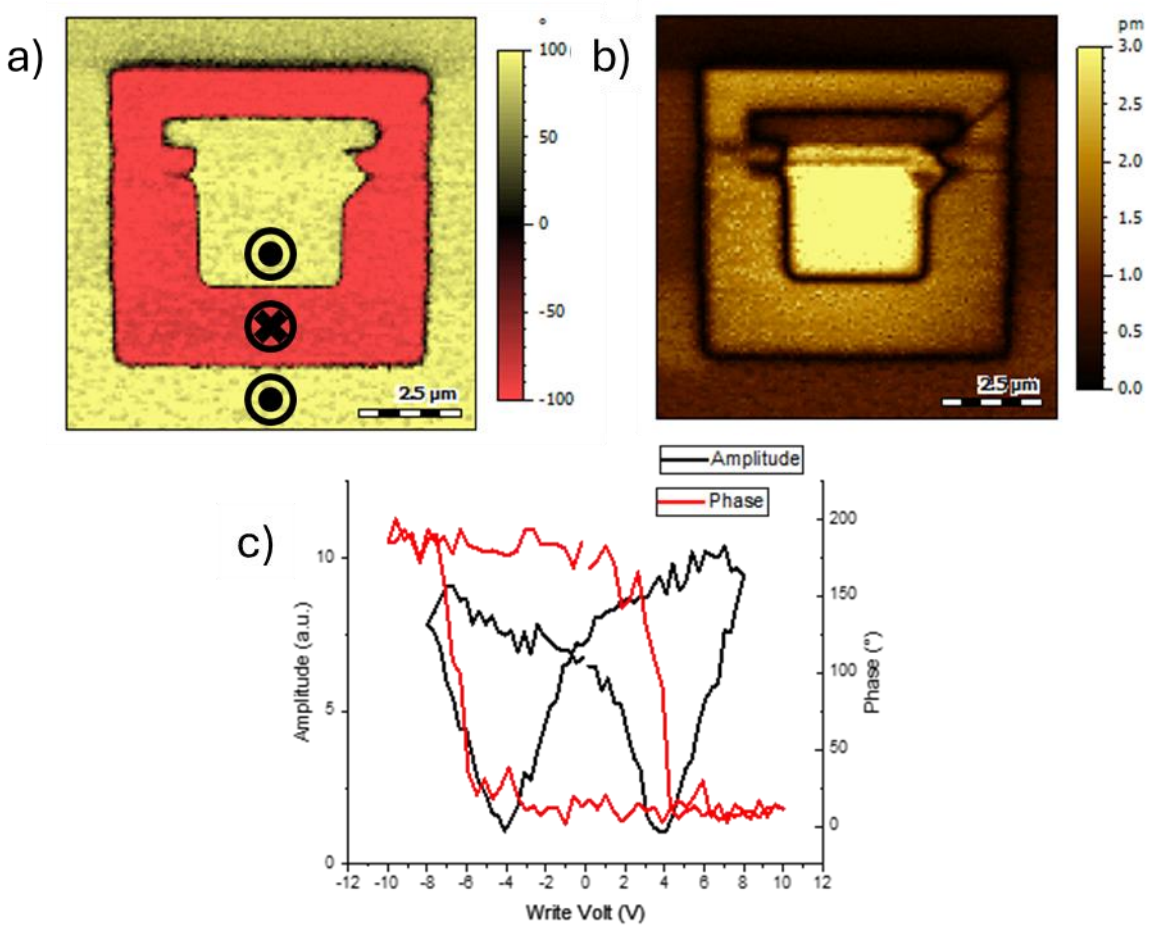

Figure 76 *:(a) Phase, (b) Amplitude and (c) Amplitude/Phase loops collected at the LPNE UMONS.*

However, it was noticed that the polarisation square tends to disappear after a short period of a few minutes (**Figure 77**). This can be interpreted as the nature of piezoelectric response originating purely from electrostatic forces.

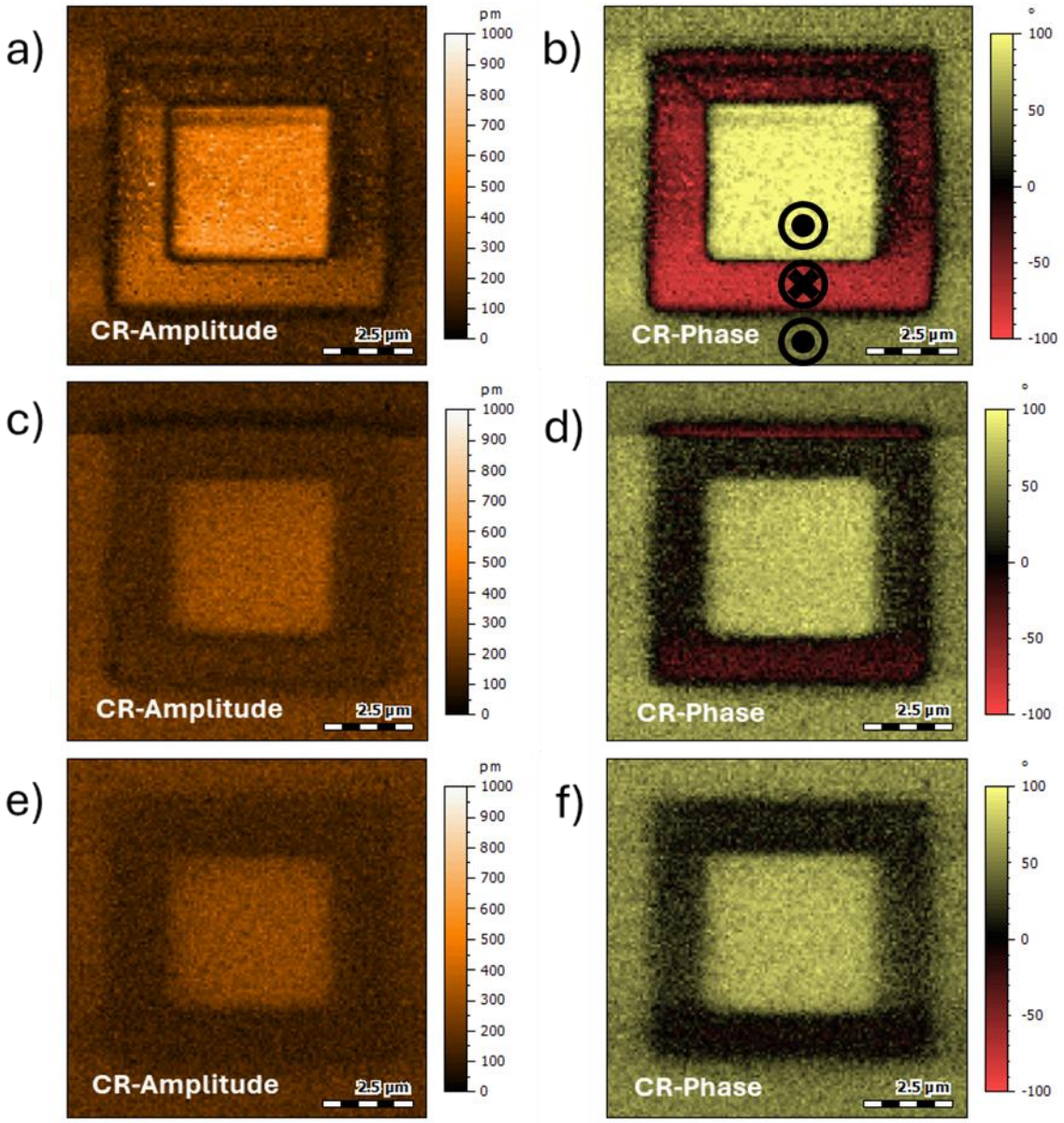

Figure 77 *: Polarisation square on Gd_2WO_6 sample, (a) Amplitude and (b) Phase right after the polarisation, (c) Amplitude and (d) Phase 20 minutes after polarisation, (e) Amplitude and (f) Phase 30 minutes after polarisation.*

To confirm this observation, both on- and off-field mode measurements, as well as loops at different V_{dc0} steps to reconstruct the cKPFM measure were investigated. From all those, it was revealed that even though an apparent hysteresis could be observed in the off-field loops, the on-field one shows a shrinking close to the total disappearance of any hysteresis (**Figure 78 a-b**). Instead of having the expected bi-state equilibrium, as there is the case with cKPFM, there is a continuum of state. All these added together tend to show that what was first interpreted as ferroelectricity in the Artois samples is only a parasitic response. The ferroelectric nature of the signal of all other samples from this family (Nd_2WO_6, Pr_2WO_6, ...) has also been assessed, and all of them show the same trend.

It is important to note that even though the ferroelectric response is most likely parasitic, it does not mean that the samples are not piezoelectric. Nevertheless, the very weak piezoelectric coefficient (less than 3 pm/V) expected from those materials tends to complicate the interpretation of the nature of the signal since it gets close to the detection limit of the SPM technique.

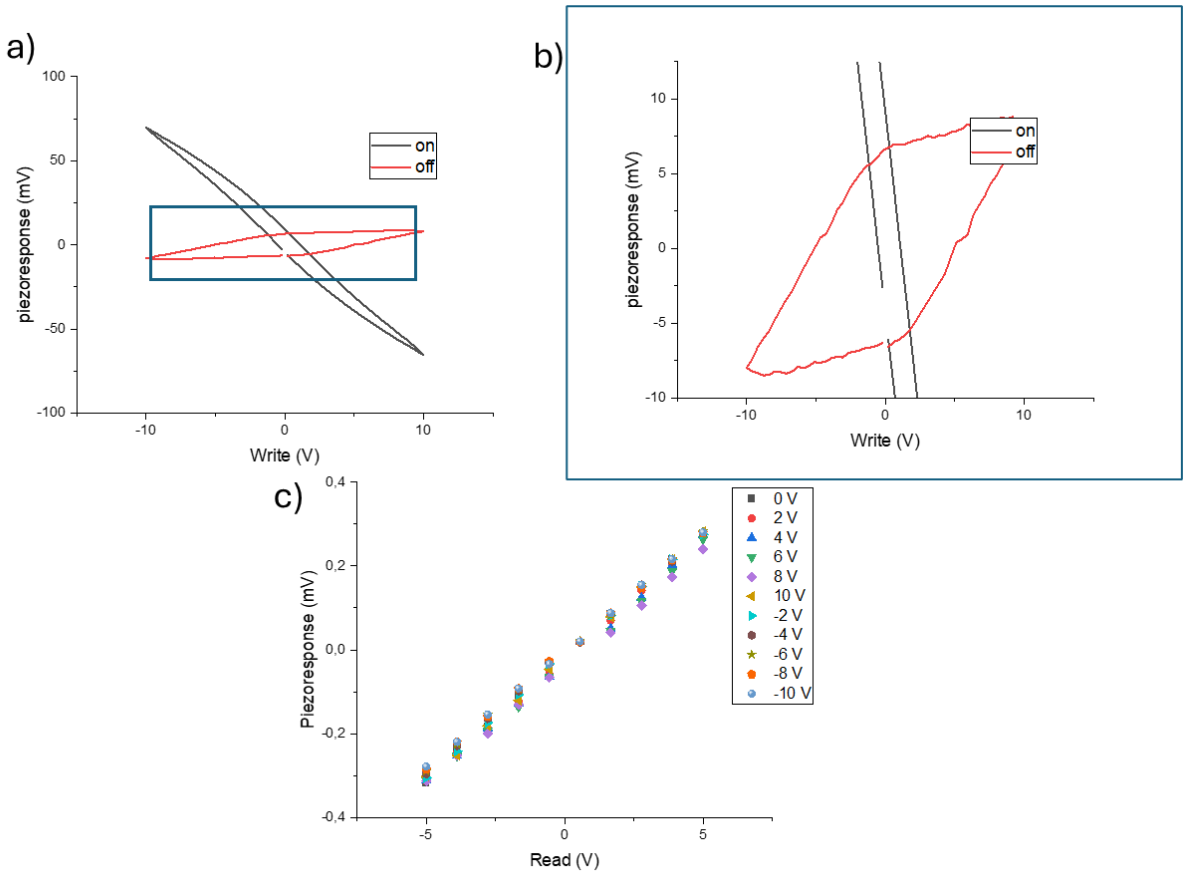

***Figure 78** : ssPFM measurement on the Gd_2WO_6 sample. a) On and off-field measurement, b) Zoom of the on and off-field measurement and c) cKPFM measurement.*

7.4.2 Single-material ferroelectric Tellurium nanowires

It has been recently reported that Tellurium nanowires may present ferroelectric properties [205]. In this paper, the authors have described the potential ferroelectricity from those mono-element materials is attributed to the displacement of ions, which is created by the interlayer interaction between lone-pair electrons. This atomic displacement leads to a separation of the mass centre of charges, resulting in a broken symmetry and thus in a spontaneous electric polarisation. DFT simulation was also used and showed that the ferroelectric polarisation can be attributed to off-centre ion displacements along the inclined edge surface of Te. The researchers used PFM and ssPFM measurements to prove their hypothesis.

A research group from India (Indian Association for the Cultivation of Science (IACS)) also investigated the dielectric properties of similar Tellurium nanowires and observed some ferroelectric loop responses on their nanowires. In the context of a collaboration with the Indian group for an alternative lead-free composite for energy harvesting, samples were sent to the LPNE to check for their potential ferroelectric properties.

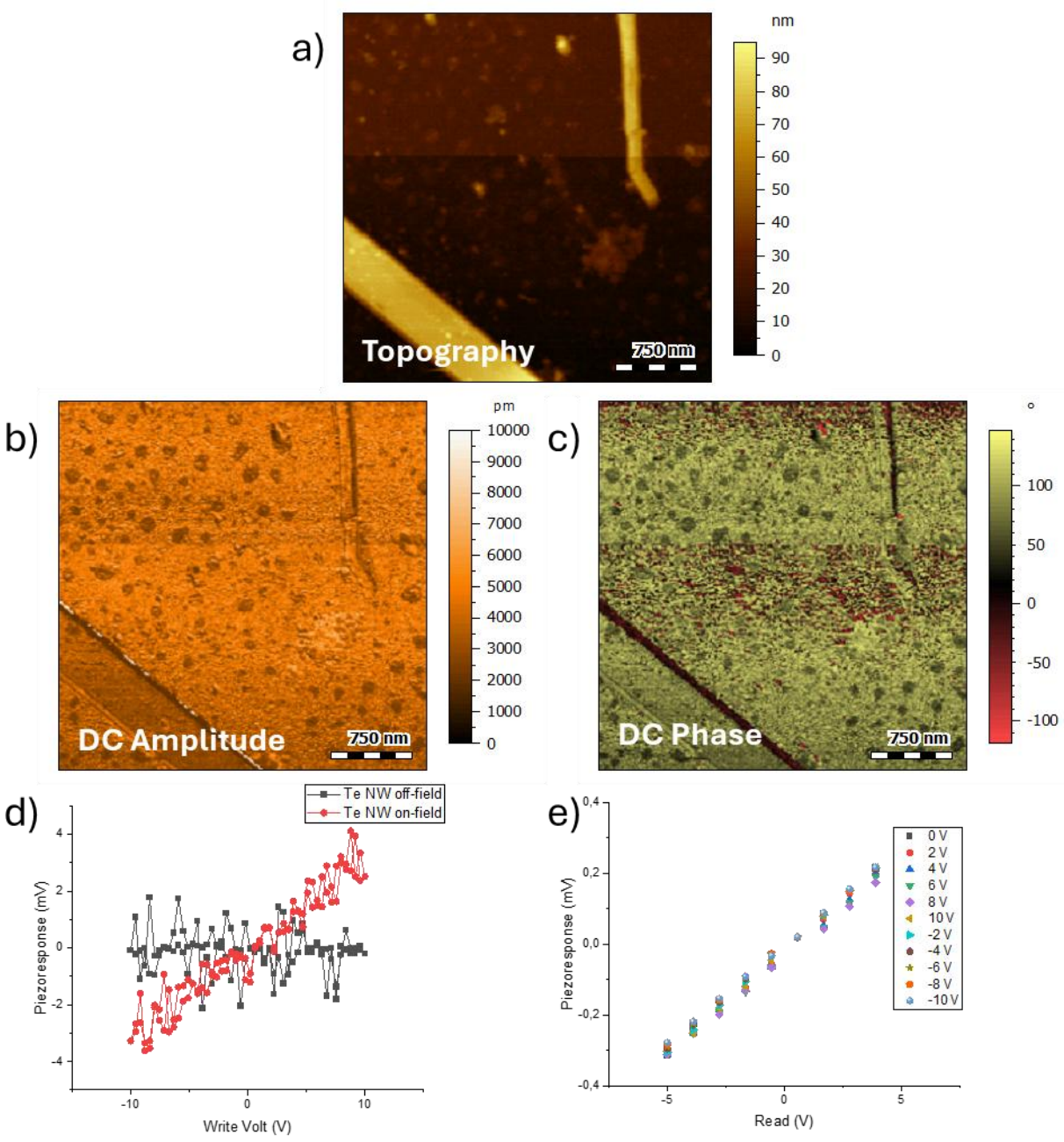

Figure 79 *: PFM measurement on Te nanowires sample. a) Topography, b) Amplitude, and c) Phase. ssPFM measurement on Te NW d) On an off-field loops and e) cKPFM.*

No ferroelectric responses are observable from the analyses performed at the LPNE. PFM images do not show any particular response on the nanowire, and ssPFM measurements do not present any ferroelectric hysteresis type of loops, either in on or even in off-field.

The cKPFM results present a continuum of state (**Figure 79**). All results point to non-ferroelectric materials.

Nevertheless, since it is not the same sample of nanowire as the original publication, a different preparation technique may have led to a very different development of the material arrangement. However, a closer look at the measurements presented in the research paper reveals some contradictions, particularly in the article with the reference [205]:

- First, there is an important shrink from the hysteresis between the on- and off-field phase loop that the researchers didn't describe from their observations (**Figure 80 a-d**).
- Second, while the research team claims they can polarise the nanowire with a polarisation voltage of ± 2.5 V and so are supposed to present a coercive voltage smaller than 2.5V, they present coherent ferroelectric loops as recorded with a V_{ac} value of 3V, raising the suspicion of an artefactual response (**Figure 80 a-d**).
- Third, the team also presents results where the centre of the hysteresis loop shifts on the writing voltage axis as a function of whether the area they work on is polarised or not (**Figure 80 e-f**). However, the only explanation in this case is that the loop arises from electrostatic forces.
- Fourth, they postulate that ferroelectricity is only observable at the edge of the NW since there is a thickness limitation. But they present phase images with a total phase inversion on the whole NW. This edge limitation makes more think about bad contact effect where the tip at the edge does not have an appropriate contact with the system and consequently raises dissimilar responses than intended.
- Fifth, the amplitude images associated with the phase data presented by the researchers (**Figure 81**) show an attenuation of the amplitude signal of the nanowire when polarised. However, the substrates (Au-coated SiO_2 (285 nm)/Si substrates and N-doped conductive silicon (Si) substrates) are known non-ferroelectric materials and present an increase in the amplitude in comparison.
- Sixth, there is most likely also a setup problem. They look to work at the edge of their systems, but they use tips (like SCM-PIT V2) that have quite an actual large radius for the size of the area they analyse.

All those facts lead us to interpret with caution what this research group had identified as ferroelectricity responses, and which most likely arises from an artefactual response. On the other hand, it is still possible that this sample shows some ferroelectric-like behaviours at the nanoscale, but the results presented in the article cannot be used to confirm that and require a lot of prudence for the PFM results analyses.

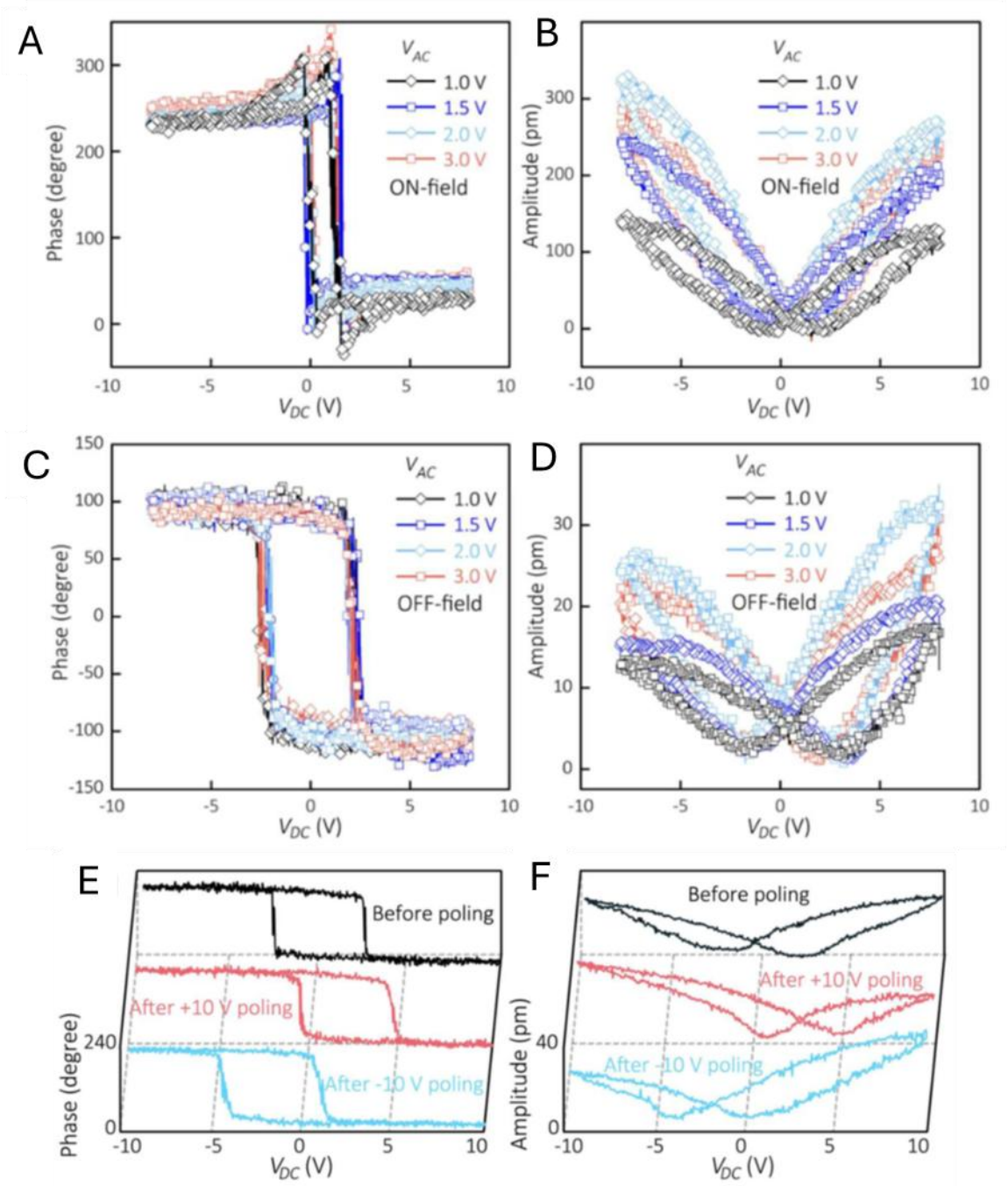

Figure 80 *: On-field (a) Phase loops and (b) Amplitude loops at different* V_{ac}*.*

Off-field (c) Phase loops and (d) Amplitude loops at different V_{ac}*.*

Off-field (e) phase loops and (f) Amplitude loops over unpolarized and polarized area (+-10V). Figure adapted from the supporting information of [205].

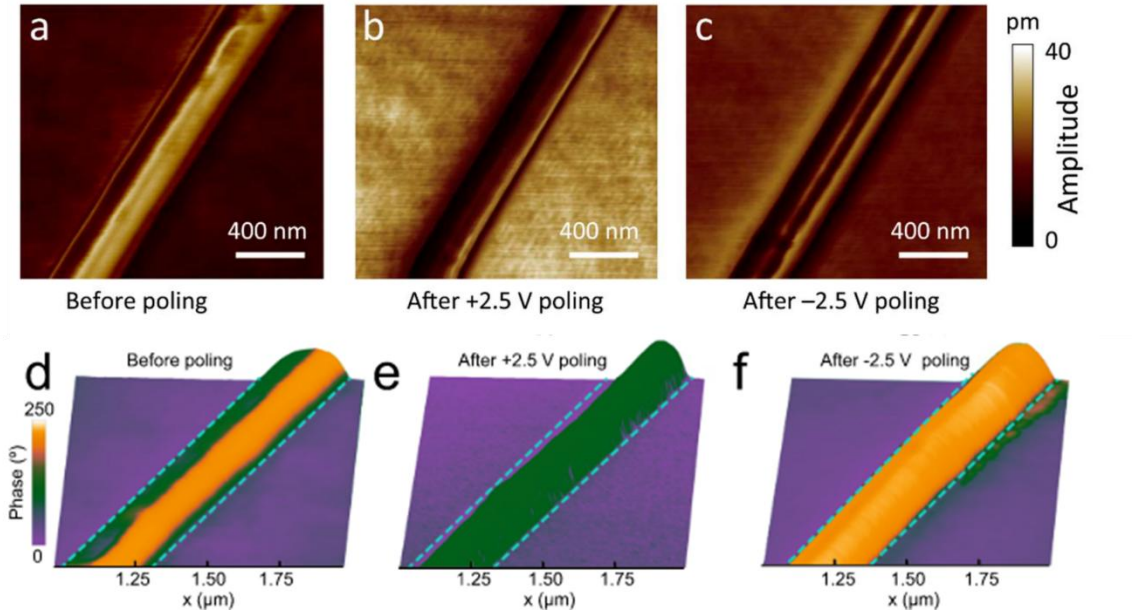

Figure 81 *; , Amplitude mapping measured by vertical PFM (a) Before polarisation, (b) After poling at +2.5 V and (c) After poling at –2.5 V. Corresponding phase images (d) Before polarisation, (e) After poling at +2.5 V and (f) After poling at –2.5 V. Figure adapted from the supporting information of [205].*

7.5 Conclusion

This chapter addressed the critical issue of reliably identifying ferroelectric behaviour at the nanoscale using switching-spectroscopy PFM. Measurements performed on reference materials highlighted that ferroelectric-like hysteresis loops can be generated under favourable experimental conditions even in non-ferroelectric systems. These observations underline the necessity of combining on-field and off-field analyses together with complementary electrostatic validation to avoid misinterpretation of PFM data.

Applied to PVDF–TrFE thin films, ssPFM measurements revealed robust and reproducible ferroelectric switching, supported by well-defined hysteresis loops, stable off-field responses, and clear bistable states in cKPFM measurements. In contrast, BFO nanoparticles exhibited a highly heterogeneous behaviour, with switchable ferroelectric responses coexisting with non-switchable areas. Spatially resolved clustering analysis enabled the discrimination of genuinely ferroelectric regions from non-responsive or non-switchable areas within both isolated systems and hybrid nanocomposites.

The importance of rigorous ferroelectric verification was further illustrated through the re-examination of previously reported ferroelectric materials, including Ln_2WO_6 compounds and Tellurium nanowires. In these systems, apparent ferroelectric hysteresis loops were observed; however, the absence of consistent off-field switching and electrostatic validation demonstrated that these responses could not be attributed to intrinsic ferroelectricity. These examples emphasize how insufficient spectroscopic validation may lead to the misclassification of materials and highlight the necessity of verification protocols.

Overall, this chapter demonstrates that switching-spectroscopy PFM constitutes an essential tool for the reliable identification of ferroelectric behaviour in complex and heterogeneous nanoscale systems.

Chapter 8: Estimation of the local surface displacement of complex heterostructure.

Quantifying nanoscale surface displacement in PFM remains a major challenge, as the reliability of piezoelectric coefficient extraction is still debated within the community. Although many studies have attempted to estimate d_{33} using PFM configurations inspired by macroscopic measurements [201,206–208], the presence of multiple parasitic signals intrinsic to PFM calls these results into question [162]. Electrostatic interactions between the biased tip and the sample surface induce cantilever bending that does not arise from genuine piezoelectric deformation. As previously discussed, extensive precautions must be taken to minimise such contributions.

Moreover, the detection principle of optical beam deflection (OBD) based SPM equipment, as used in the quasi totality of studies (as well as in this one), does not directly measure surface displacement. Instead, it measures cantilever bending, which is influenced by external mechanical or electrostatic forces. For this reason, it is not possible to claim to measure a true surface displacement, nor to evaluate the intrinsic piezoelectric coefficient d_{33}, but only an apparent one (d_{33}^{app}).

This chapter examines how this apparent coefficient may be extracted and reliably assessed with an approach derived from ssPFM. The need to use a calibration sample as an external reference will be addressed together with the spatial limitations of point spectroscopy when applied to complex three-dimensional systems with multiple electromechanical responses. The second part of the Chapter introduces DataCube-PFM. It is a spectroscopy–mapping approach enabling the measurement of apparent surface displacement (D) at each pixel over a controlled frequency range, while simultaneously recording local mechanical properties in a stabilised manner. Its advantages and limitations will be illustrated on the samples studied in this work.

8.1 d_{33}^{app} at fixed position

8.1.1 Illustration on the PVDF-TrFE thin film

Over the years, a wide range of strategies has been explored to extract piezoelectric coefficients from PFM measurements including the extraction of surface displacement from PFM images [86], the conversion of amplitude or piezoresponse loops, either on-field [12,209,210] or off-field [208] and the determination of the slope of amplitude versus V_{ac} at selected locations [211], [49,212].

Among these techniques, fixed-position measurements remain the most reliable because they avoid topographic crosstalk. Since ssPFM inherently acquires data at a fixed tip location and includes SHO fitting of the piezoresponse, the conversion of ssPFM data is a straightforward and robust approach to estimate the apparent displacement D.

However, many studies perform these measurements on-field. However, this practice should be strongly discouraged because the electrostatic force F_{es} substantially modifies the measured amplitude. In PVDF–TrFE, the on-field measurements nearly double the

apparent displacement compared with the off-field case (50 pm vs 30 pm for V_{ac} = 1 V) while failing to reach a true saturation behaviour (**Figure 82 a-b**).

To further minimise the electrostatic influence, ssPFM-style measurements are collected while no DC poling voltage is applied. By running the ssPFM routine over a pre-polled area while fixing the poling voltage to the minimum possible value during the acquisition (10 mV), hundreds of frequency sweeps are obtained for a given V_{ac} immediately after a conventional ssPFM sequence (**Figure 82 c**). These values show excellent internal consistency. Measurements acquired in this post-ssPFM regime exhibit a ~20–25% reduction in signal across all V_{ac} values, likely due to partial discharge relaxation. Plotting amplitude as a function of V_{ac} yields a slope of approximately −22.6 ±0.4 pm/V(**Figure 82 d**), which is a value of d_{33}^{app} consistent with the manufacturer-reported coefficient for this polymer [213].

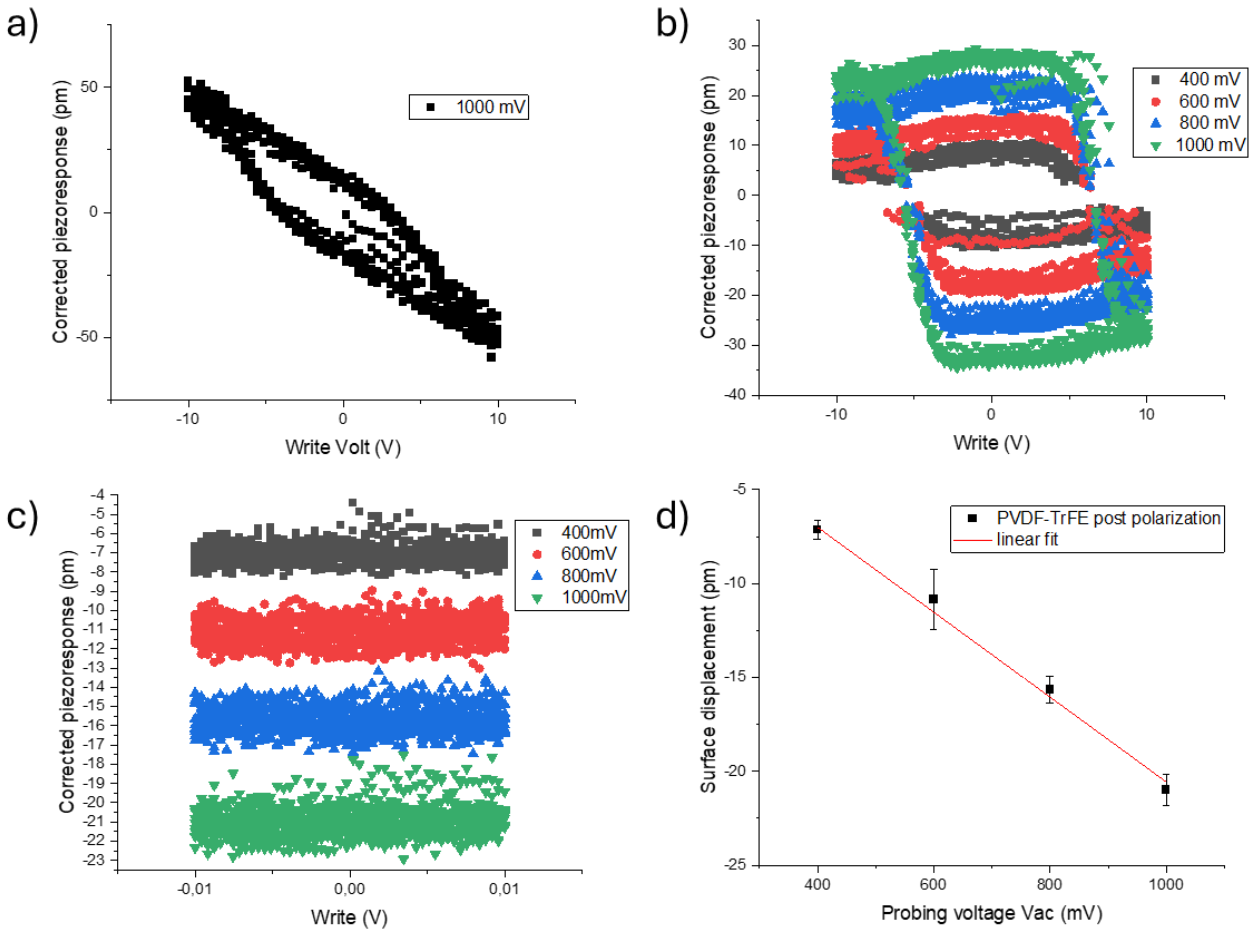

***Figure 82** : (a) On-field ssPFM measurement converted into picometres on the PVDF–TrFE thin film, acquired with V_{ac} = 1 V and V_{dc} swept between −10 and +10 V. (b) Off-field ssPFM measurements converted into picometres, recorded with V_{ac} between 0.4–1 V and V_{dc} between −10 and +10 V. (c) Off-field ssPFM measurements converted into picometres, acquired using quasi-zero poling voltage (V_{dc} = ±10 mV), with V_{ac} between 0.4–1 V. (d) Corresponding linear regression of D-values as a function of V_{ac} for the estimation of d_{33}^{app}.*

Repeating the measurement on nine randomly selected poled locations over a 1 μm² region yields consistent values for five of the positions (**Figure 83**). For the remaining four, the extracted d_{33}^{app} sharply decreases or becomes inaccessible, presumably due to drift during acquisition, which causes the tip to progressively shift away from the centre of the polarised region.

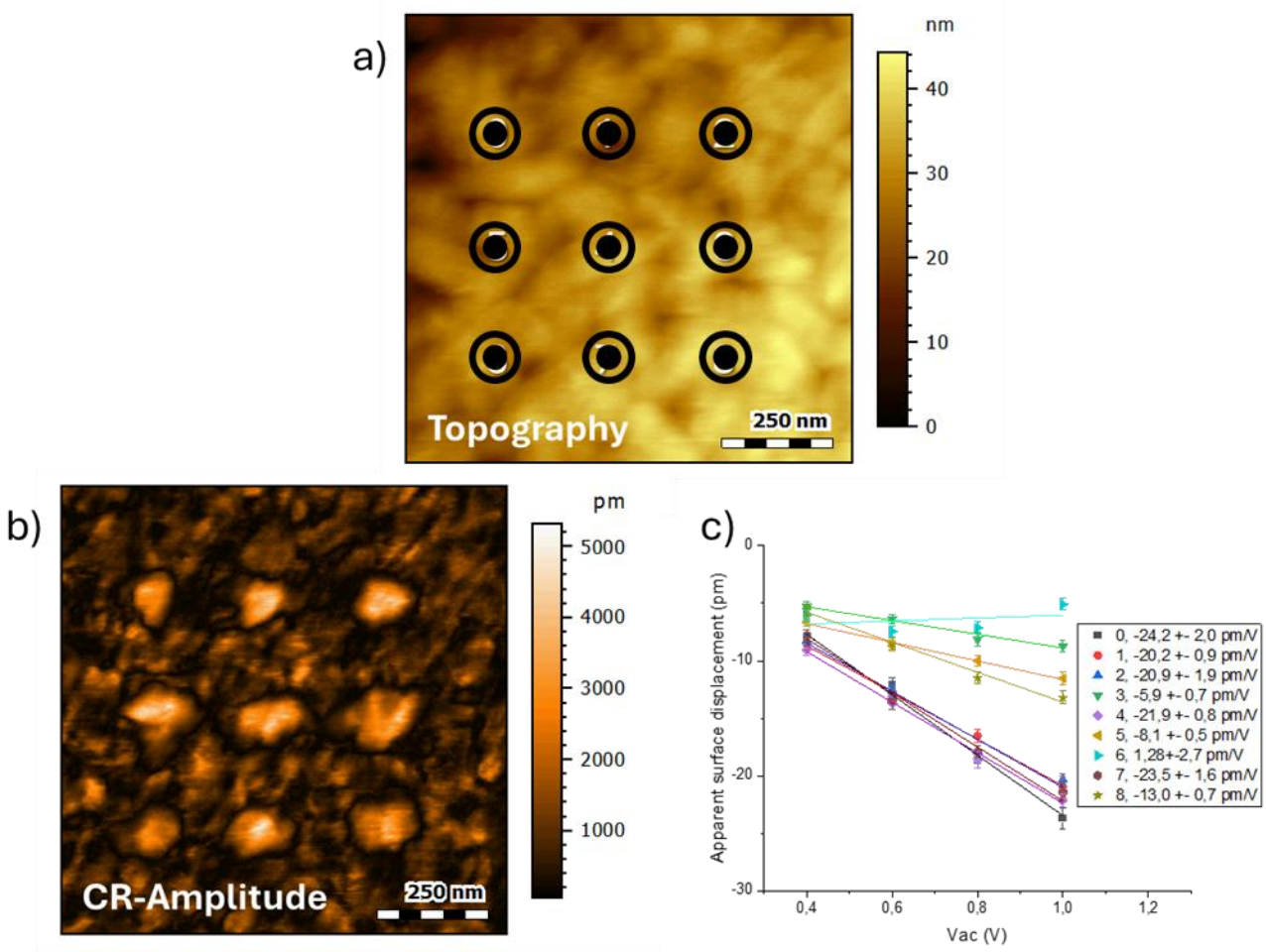

***Figure 83** : Evaluation of d_{33}^{app} over nine previously poled locations in PVDF–TrFE. (a) Topography image indicating the nine analysed spots. (b) CR-PFM Amplitude image acquired after ssPFM poling. (c) D-values as a function of V_{ac} for all positions.*

8.1.1.1 Tip calibration on known piezoelectric materials

Before proceeding further, it is essential to emphasise that AFM tips tend to wear off during PFM measurements, particularly under the relatively high set-point forces required in this study. Such abrasion directly affects the accuracy and comparability of the extracted piezoelectric coefficients. To ensure consistency between measurements, each tip is systematically calibrated against a reference material with a well-established d_{33} value.

For this research, a ZnO thin film was provided by Imen Ben Khaled, a PhD student affiliated with LPNE and UPHF (University of Valenciennes, France). The piezoelectric coefficient d_{33} of this reference film was independently measured by laser interferometry. This technique relies on the detection of sample vibrations induced by an applied electrical excitation through the measurement of the phase shift between the incident and reflected laser beams (**Figure 84 a**). When the sample deforms under the applied voltage, the optical path length changes, leading to a modification of the interference pattern. The effective piezoelectric coefficient can then be estimated as

$$d_{33} = \frac{\Delta L}{V}$$

Eq. 49

where ΔL is the displacement measured by interferometry while a probing voltage V is applied to the sample.

The ZnO film used for this study presented a measured d_{33} value of 5.8 ± 1.3 pm/V (**Figure 84 b**). When the mechanical calibration is correctly done, and the tip remains sharp, the PFM-derived value closely matches the reference, as shown for Tip 1 in **Figure 84 c**. In contrast, a worn tip or no optimal calibration yielded underestimated values, such as the 3.22 pm/V measured for Tip 2. In such cases, all data acquired with that tip are corrected by applying a multiplicative factor equal to the ratio of the true ZnO coefficient to the measured one (5.76/3.22 ≈ 1.8).

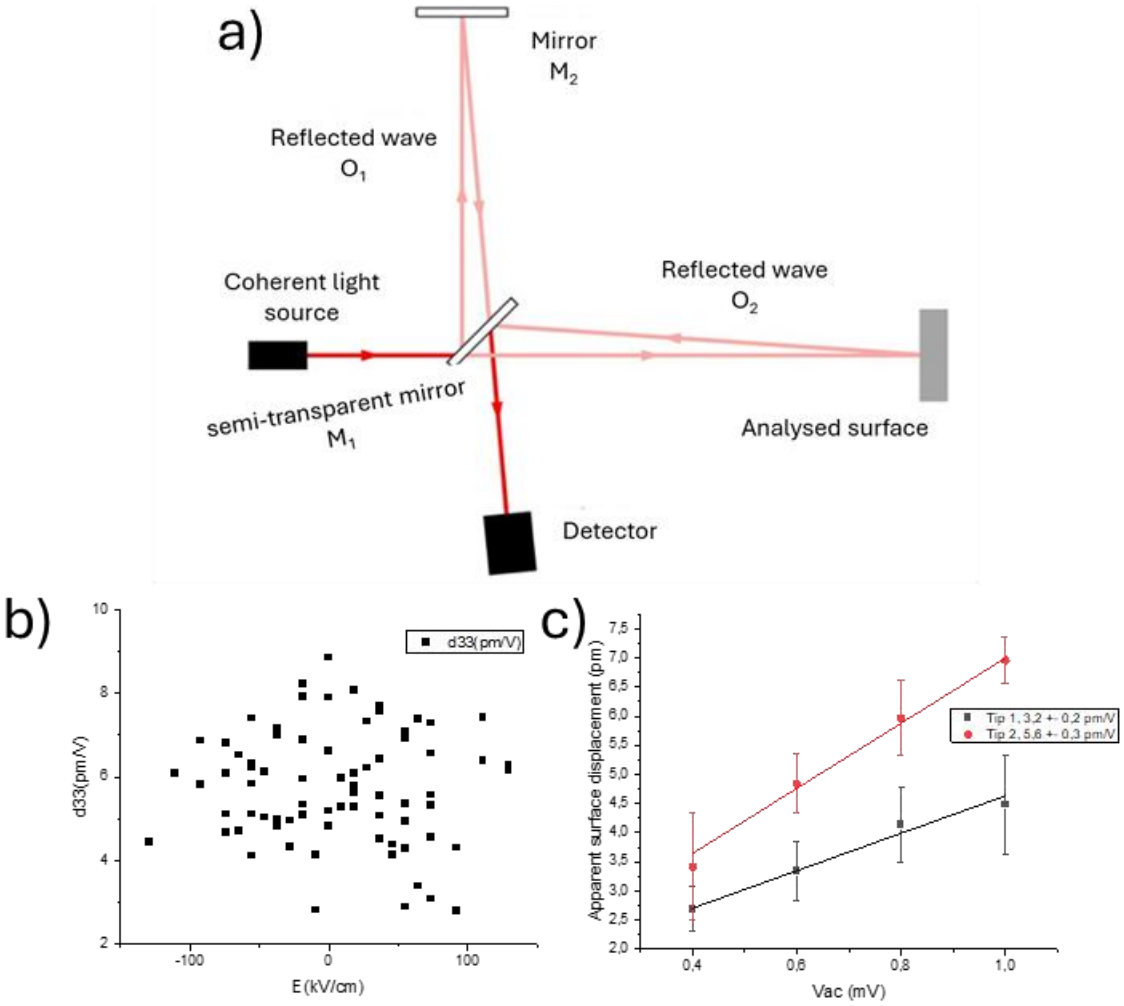

***Figure 84** : (a) Working principle of the Michelson interferometer. (b) Determination of the d_{33} coefficient of the ZnO calibration thin film using laser interferometry, when a probing voltage of 1V is applied. (c) PFM-derived d_{33} values for the same ZnO film obtained with two AFM probes illustrating the influence of tip wear and calibration accuracy.*

8.1.2 BFO particles, and the complexity of spectroscopy on 3D structures

Determining the piezoelectric coefficient of BFO at the nanoscale is particularly challenging. Reported values in the literature vary widely. Some studies claim coefficients as high as 60–120 pm/V. However, a closer examination reveals that many of the high values originate from measurements likely performed on-field. At least, that is what the characteristic "pinched" shape of their piezo loops suggests, which strongly undermines their reliability [214,215]. More consistent studies, including those combining direct and indirect PFM measurements [49] and theoretical predictions [216], place the intrinsic coefficient of BFO particles closer to 20–40 pm/V.

The estimation of d_{33}^{app} on BFO nanoparticles (**Figure 85**) reveals a broad distribution of responses. However, as shown before, not all particles within an aggregate switch under

the applied polarisation voltage (**Figure 85 c**). It indicates heterogeneous electrical contact or distinct crystalline orientations. For particles that can be reliably poled, the extracted d_{33}^{app} typically lies in the 25–35 pm/V range (**Figure 85 d**, data A-D). In contrast, unpoled regions often show either no measurable response or even a negative apparent coefficient (**Figure 85 d**, data C-B). It is consistent with insufficient electrical contact or unswitchable grains within the applied bias range.

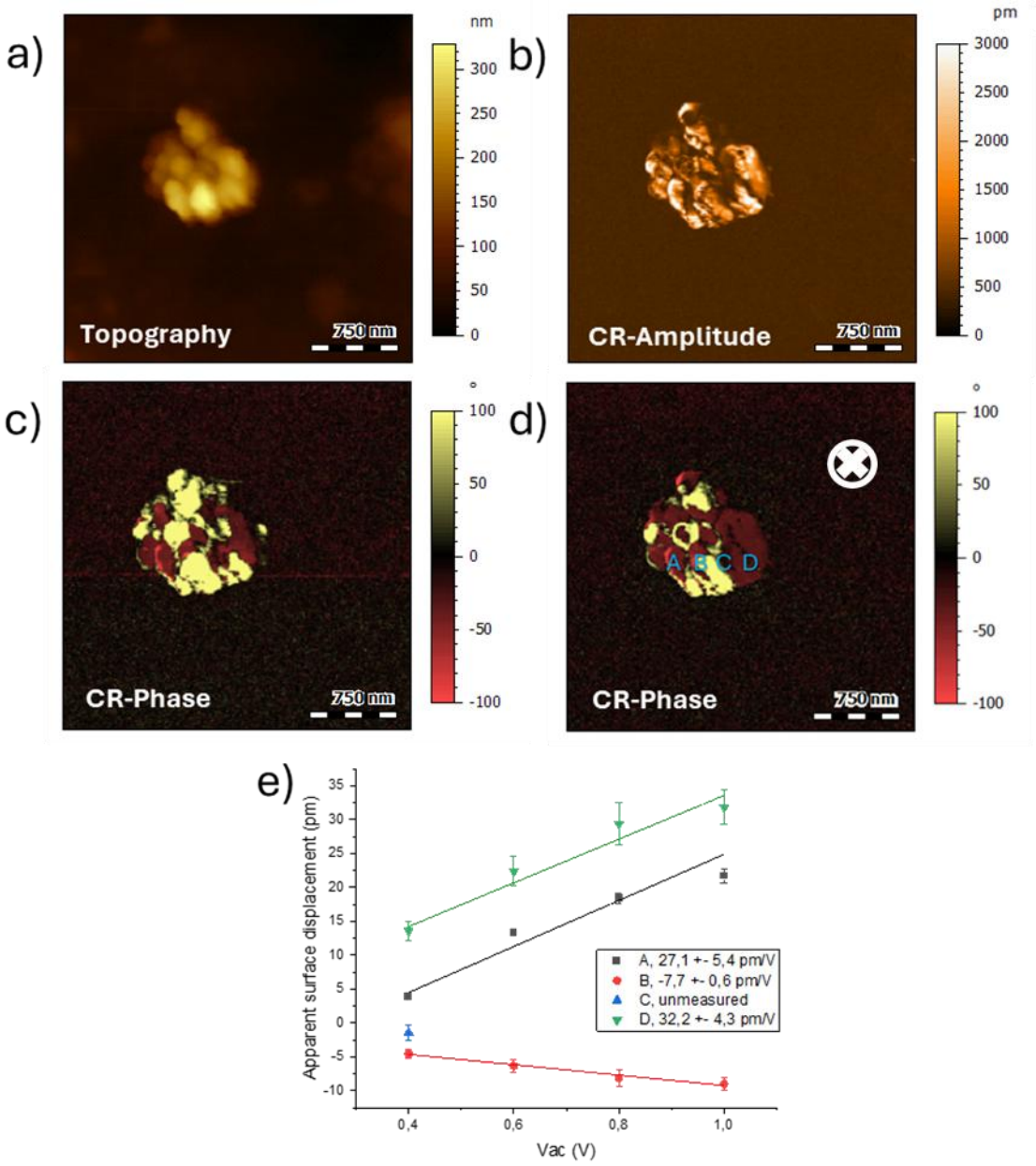

***Figure 85** : BFO nanoparticle aggregate embedded in PEDOT:PSS.(a) Topography, (b) CR-PFM amplitude after ssPFM poling, (c) Phase prior to poling, and (d) Phase after poling, indicating the specific sites analysed for d_{33}^{app}. (e) D-values plotted as a function of V_{ac} for all positions.*

8.1.3 PVDF-TrFE/BFO nanocomposite

The ferroelectric nanocomposites exhibit behaviour closely resembling that of their individual constituents. Within the PVDF-TrFE matrix, the d_{33}^{app} remains relatively uniform, ranging from −17 to −24.5 pm/V. In contrast, the BFO grains show substantial variability: some regions appear unresponsive (area B), others display negative response (area D, approx. −20 pm/V), while switchable grains achieve values between 15 and 35 pm/V (areas A and B).

This complexity is exacerbated by the relatively long duration of ssPFM measurements (∼1 minute per point) during which drift may shift the tip away from the intended feature. Consequently, apparent coefficients extracted from BFO nanoparticles must be interpreted cautiously, considering switching heterogeneity and instrumental instabilities.

From these observations, it becomes clear that although single-point spectroscopy offers a meaningful estimation for flat, homogeneous materials. Its spatial and temporal limitations make it poorly suited for complex, heterogeneous structures. This motivates the development of mapping-based approaches, discussed in the next section.

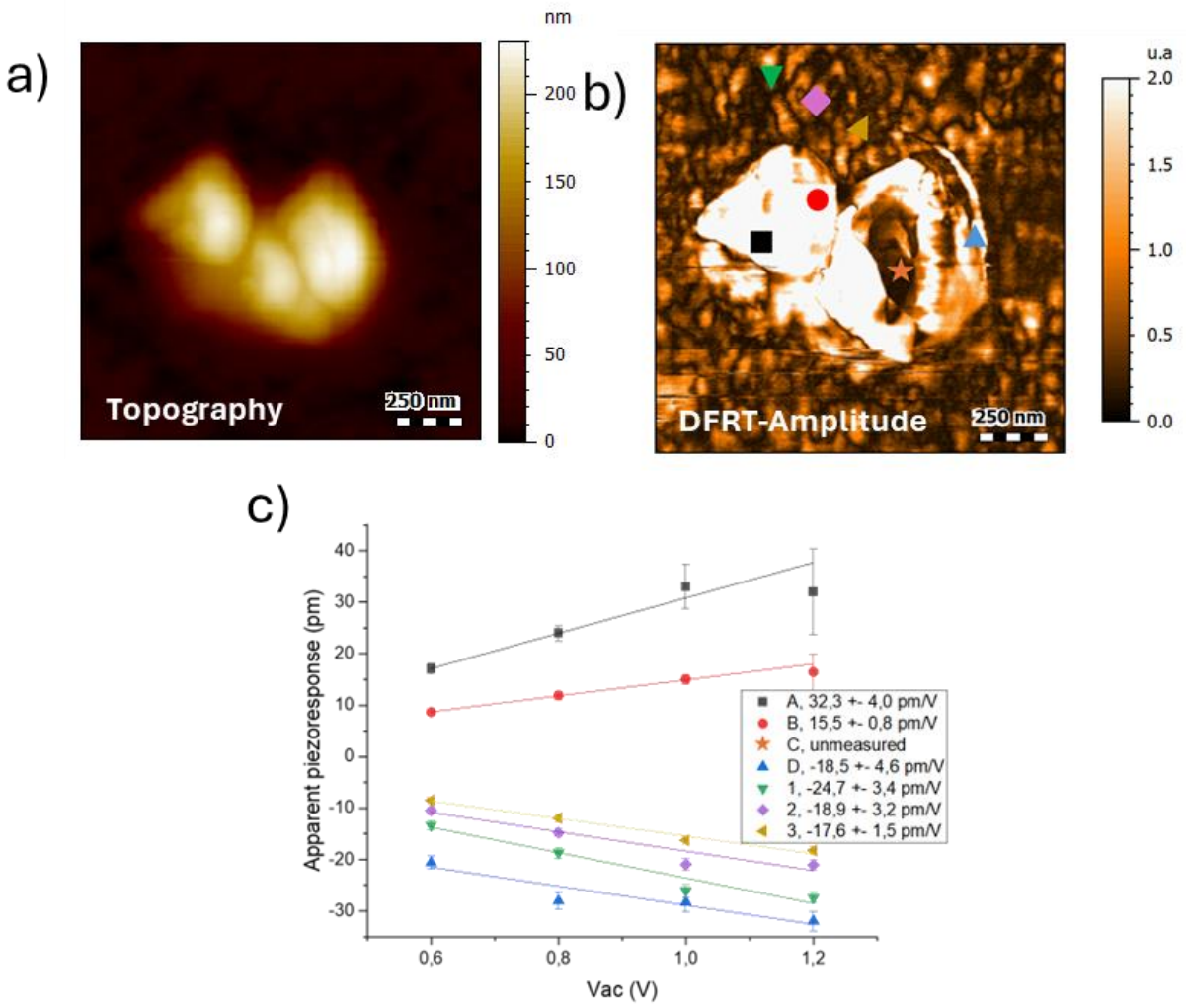

***Figure 86** : DFRT-PFM imaging of a multi-grain BFO aggregate embedded in PVDF–TrFE. Vertical mode (CR frequency range 250–350 kHz): (a) Topography, (b) Amplitude. (c) D-values as a function of V_{ac} in all spots highlighted in b.*

8.2 Data-cube PFM

As demonstrated in the previous section, earlier approaches provide access to an d_{33}^{app} that is generally reliable for uniform thin films. However, their applicability decreases markedly when the material exhibits complex, multiphase, three-dimensional features. In such systems, a precise interpretation requires simultaneous access to topography and to the key PFM parameters (amplitude, quality factor, and phase) evaluated at every pixel at the local contact-resonance frequency

Data-cube PFM (DataCube-PFM, or FFV-PFM) is an acquisition mode developed by Bruker in which each pixel exhibits a complete force–distance curve with an extended hold segment in contact and during which a full frequency sweep is performed. This approach provides all the parameters required to evaluate the apparent piezoresponse in a single

measurement while simultaneously mapping the sample topographical and mechanical properties. Thereby, it offers a clearer insight into the local tip–sample interaction.

However, it is important to note that data presentation was optimised for phase imaging from -90 to 90° for all previous measurements. It corresponds to down-oriented and up-oriented ferroelectric domains. The up and down domains in DataCube PFM, on the other hand, are optimized between 0 and 180°. For consistency across the dataset, all DataCube phase images presented here are converted to follow the same convention as the previous modes. All DataCube-PFM measurements are performed with an AC excitation voltage V_{ac} = 1 V.

8.2.1 PVDF-TrFE thin film

8.2.1.1 Mechanical and PFM imaging tool

A comparison between conventional CR-PFM and DataCube-PFM on the PVDF–TrFE thin film (**Figure 87**) reveals that the topography obtained with DataCube is substantially more stable. The fibrillar microstructure is clearly resolved. Despite using equivalent set-point forces (50 nN), no scratching or mechanical damage is observed in DataCube mode, conversely to CR-PFM (**Figure 87 a–b**). This improvement most likely arises from the controlled approach–retract sequence intrinsic to the DataCube acquisition. It reduces lateral shear forces and limits sample deformation or abrasion

Comparing the amplitude (**Figure 87 c-d**) and phase measurements (**Figure 87 e-f**) between both modes reveals analogous ferroelectric domains, although the CR-PFM dataset is sub-optimally tuned. It is evidenced by the reduced phase contrast. DataCube-PFM provides a clearer domain distribution because it can track the CR-frequency in the given frequency range. It should also be emphasised that several domains exhibit almost no amplitude response. It corresponds to the lower detection limit of the system at the applied excitation voltage, but not to an absence of piezoelectricity.

The complementary mechanical channels, the adhesion (**Figure 87 g**), and the modulus (**Figure 87 h**) show values consistent with expectations. The adhesion force (~30 nN) matches the one obtained in PeakForce Tapping, and the modulus extracted from the Maugis model appears particularly underestimated (< 1 GPa). This discrepancy is most likely because the used probe is not specifically calibrated for quantitative mechanical measurements. Nevertheless, the resulting contrast remains qualitatively meaningful and provides valuable information on local mechanical heterogeneity.

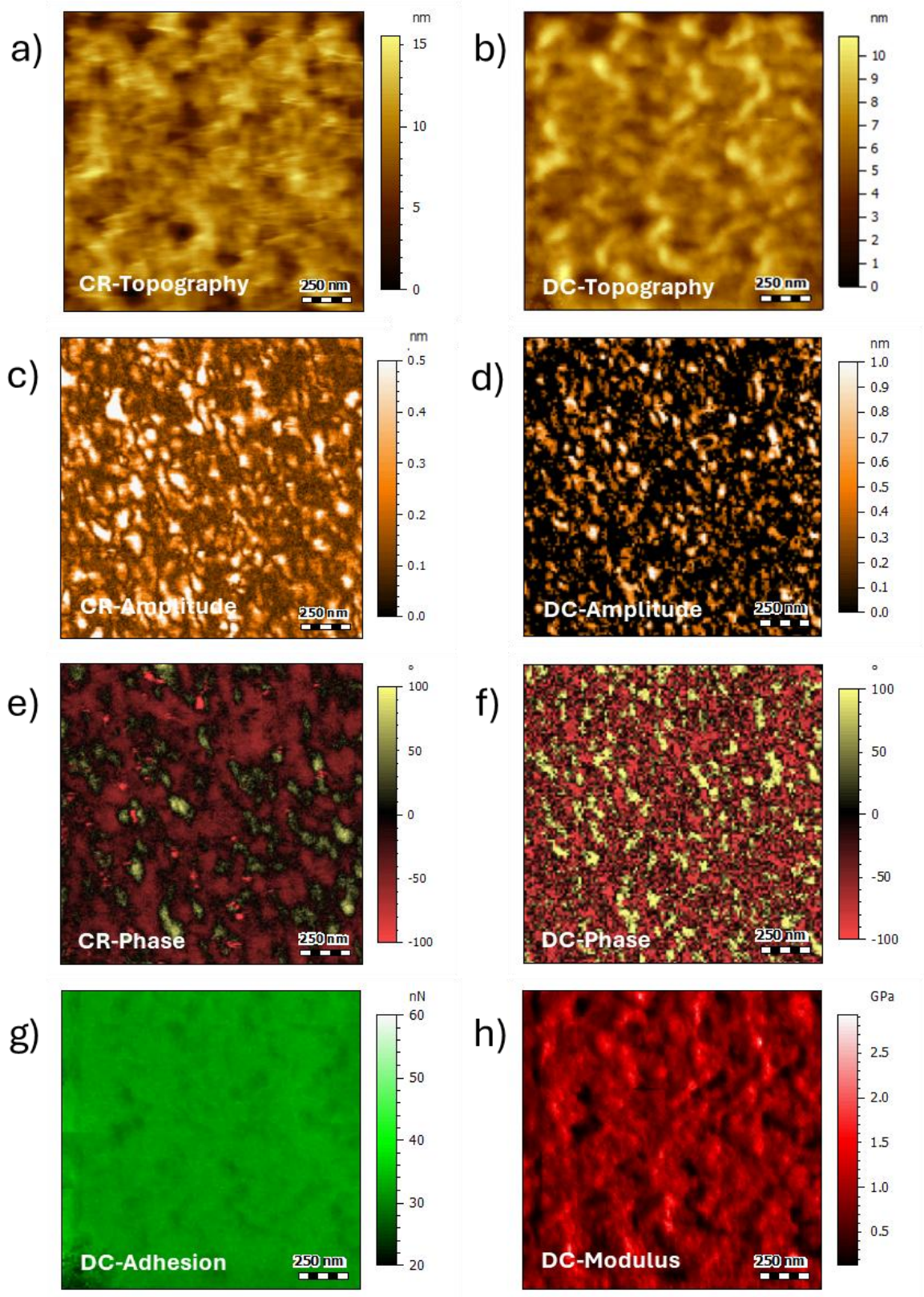

Figure 87 *: Comparison of CR-PFM and DataCube-PFM on the same 1.5 µm² area of PVDF-TrFE. Measurement in CR-PFM at CR frequency = 270 kHz, (a) Topography, (c) Amplitude, and (e) Phase. Measurement in DataCube PFM with a frequency range from 250 to 350 kHz, (b) Topography, (d) Amplitude, and (f) Phase. (g) Adhesion and (h) Modulus measurement associated with the DataCube measurement.*

8.2.1.2 Apparent surface displacement recalculation

Following local ssPFM polarisation performed in a separate region, a clear homogenisation of the PVDF–TrFE response is observed across the amplitude, phase, and quality-factor channels in the DataCube dataset (**Figure 88 b–d**). The D distribution is reconstructed using these three parameters and according to the relation described *vide infra,* **section 3.1.3.**

The resulting displacement mapping (**Figure 88 e**) agrees well with the values extracted from ssPFM-derived analyses. It provides a substantial more detailed spatial distribution around the written ferroelectric domain (**Figure 88 f**). A clustering software developed in LPNE for data analysis is used to separate the data between the poled (cluster 1) and unpoled (cluster 0) data (**Figure 88 g**). The histogram of *D*-value is presented in Figure 88 h. The observed spread in *D* value is directly linked to the spatial distribution of the polarisation (**Figure 88 f**). It ranges from only a few picometres at the edges of the poled area to approximately −20 pm at its centre and is fully consistent with the finite spatial extent of the poling field. This observation helps rationalise the small instabilities previously reported in some d_{33} measurements (**Figure 83**).

Overall, DataCube-PFM provides a more precise, spatially continuous, and mechanically stable representation of the local electromechanical response of PVDF–TrFE. It highlights clear advantages over single-point and conventional resonance-tracking approaches for quantitative nanoscale analysis.

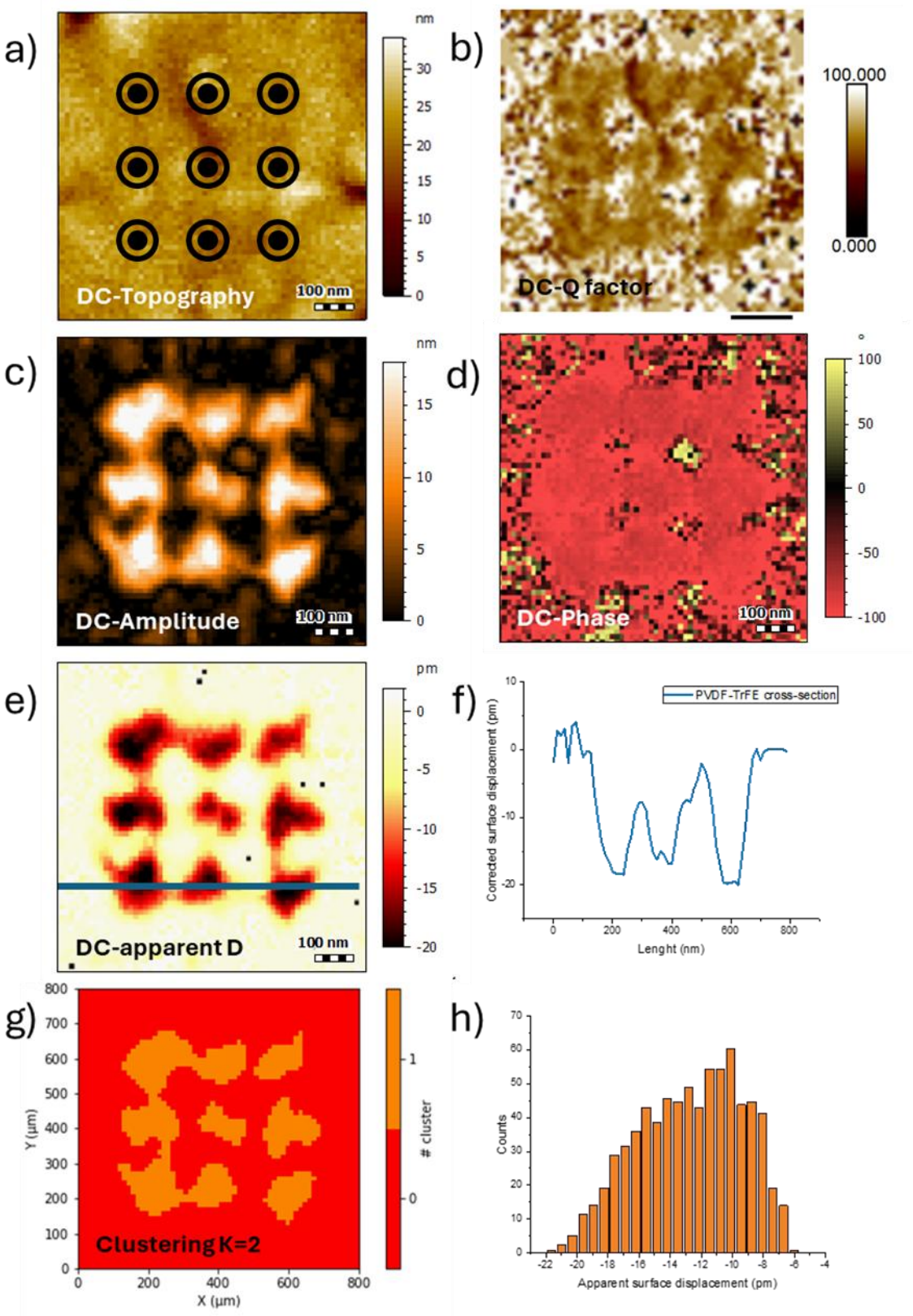

Figure 88 *: DataCube-PFM measurement on PVDF-TrFE sample after local ssPFM poling. (a) Topography, (b) Q factor, (c) Amplitude, (d) Phase, and (e) Reconstructed image of the D-value. (f) Section of the D-value. (g) Cluster mapping for k cluster = 2. (h) Histogram of D-value in cluster 1 after polarisation.*

8.2.2 BFO particles in PEDOT:PSS thin film

8.2.2.1 Mechanical and PFM imaging tool

The comparison between CR-PFM and DataCube-PFM performed on BFO particles embedded in PEDOT:PSS reveals substantially larger discrepancies than those observed for the PVDF–TrFE thin film. **Figure 89 a** shows a small BFO aggregate trapped inside the PEDOT:PSS matrix. After optimisation of the contact-resonance frequency in CR-PFM, two main phase regions are identified within the aggregate: one “up” and one “down”, each associated with a smaller secondary down-oriented region (**Figure 89 b**). The associated amplitude image (**Figure 89 c**) displays an additional peculiarity where nanoparticles belonging to the dominant up-oriented domain exhibit noticeably higher amplitude than the rest of the cluster. It suggests an uneven electromechanical response.

However, DataCube-PFM reveals a markedly different phase distribution. Although three regions are present, the up-oriented domain is substantially more extended. The down-oriented region is reduced (**Figure 89 d**). Only the small down-domain observed previously remains consistent across both imaging modes. The amplitude in DataCube-PFM (**Figure 89 e**) is considerably more homogeneous across the particles except at domain boundaries, where the expected signal discontinuities associated with domain walls are observed.

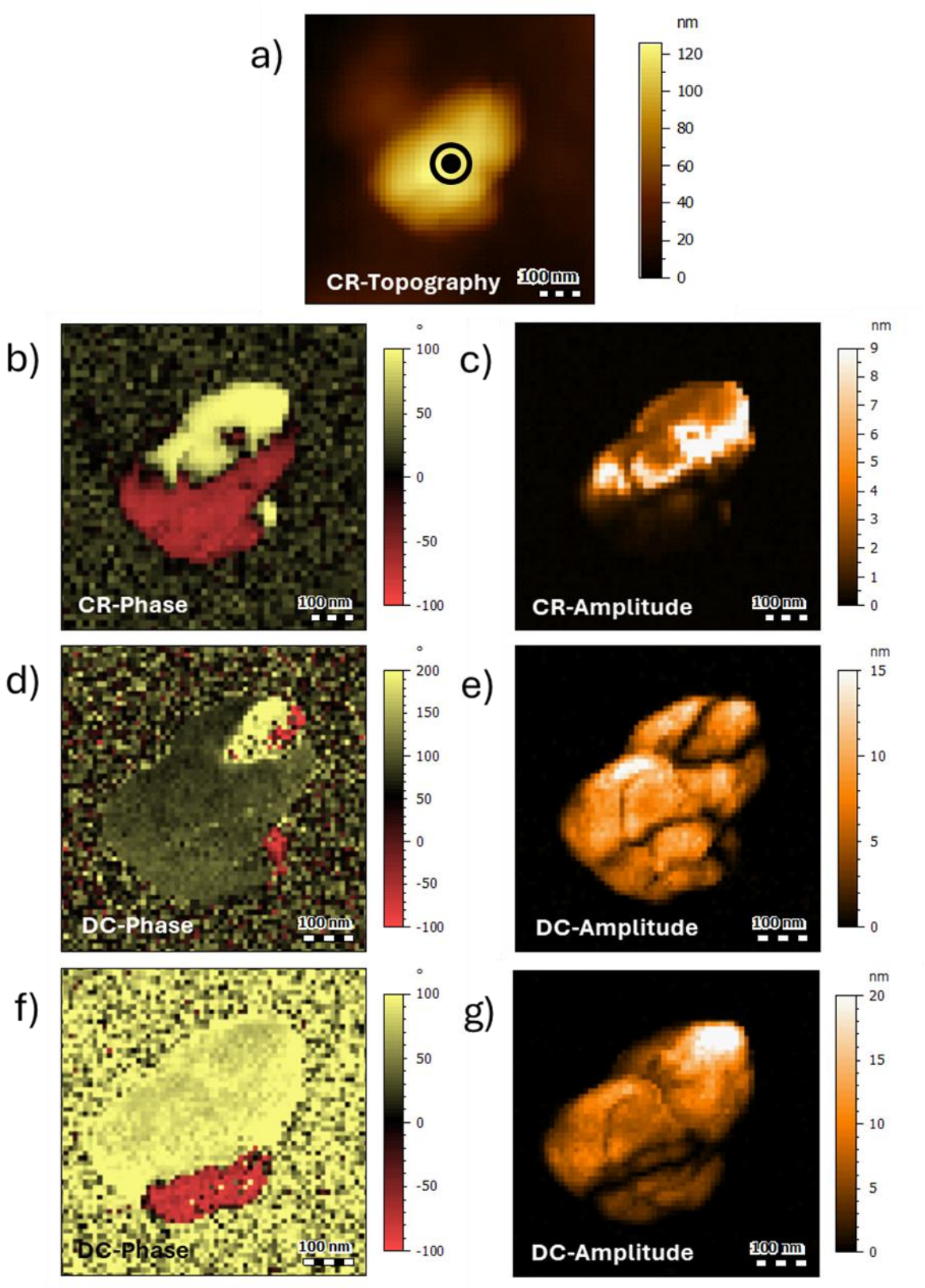

Figure 89 *: Comparison of CR-PFM and DataCube-PFM on a cluster of BFO. Measurement in CR-PFM, at CR frequency = 305 kHz, (a) Topography, (b) Amplitude, and (c) Phase. Measurement in DataCube PFM with a frequency range from 250 to 350 kHz before poling, (d) Amplitude, and (e) Phase. Measurement in DataCube PFM with a frequency range from 250 to 350 kHz after poling at -10 V, (f) Amplitude and (g) Phase.*

On another hand, the extended down-domain displays an apparent phase inversion spanning from –90° to 270° (**Figure 89 d**). Although this inversion alters the visual appearance of the phase map, it does not modify the physical interpretation of the domain orientation. This behaviour arises from the inherent phase unwrapping conditions in this measurement mode and does not reflect any actual change in the ferroelectric polarisation state.

These discrepancies most likely originate from the pronounced non-uniformity of the contact-resonance frequency across the BFO aggregates (**Figure 90 a**). Such spatial variations induce local phase reversals in conventional CR-PFM, leading to artificial inversions between different regions of the cluster. This artifact fully accounts for the mismatch observed between CR-PFM and DataCube-PFM. The strong spatial fluctuation of the resonance frequency across the BFO particles further supports the assumption that conventional CR-PFM is poorly suited to heterogeneous, multiphase systems. The quality factor also varies across the region (**Figure 90 c**), although no clear correlation with either the local modulus or the resonance frequency is observed.

The mechanical channels obtained from DataCube-PFM show trends like those previously observed for PVDF–TrFE. The adhesion map (**Figure 90 e**) is consistent with PeakForce Tapping measurements with adhesion forces of approximately 15 nN on the particles. The modulus values (**Figure 90 f**) are again underestimated because the probe was not optimised for quantitative mechanical measurements. A small feature visible in the top-left region of the adhesion map relates well to the topography and likely corresponds to a shallow subsurface particle.

A further and unusual characteristic of the DataCube datasets is the presence of a systematic directional asymmetry in the modulus. A side of the scanned region corresponding to the approach direction appears consistently softer. This effect is reproducible and appears across all channels influenced by mechanical contact, including resonance frequency and quality factor (**Figure 90 a**). This systematic appearance is referred to as the “moon phase effect”. It most likely arises from lateral forces acting during scanning and appears to be inherent to the measurement configuration.

After poling the region at −10 V, no significant change is observed in the mechanical adhesion and modulus channels (**Figure 90 d and f**). The CR-Frequency modulus also shows very few changes. Only a small number of pixels near domain walls become unmeasurable. The same is for the *Q* factor. It only shows a minute augmentation after polarisation (**Figure 90 d**).

The DataCube-PFM maps indicate that most BFO particles reorient towards the up-polarised state upon poling, in agreement with the expected ferroelectric behaviour. However, some regions appear to polarise in the opposite direction (**Figure 89 f**). Because this behaviour lacks a physically consistent explanation, it is almost certainly artefactual

and originates from the same lateral-force-related mechanism responsible for the “moon phase effect”.

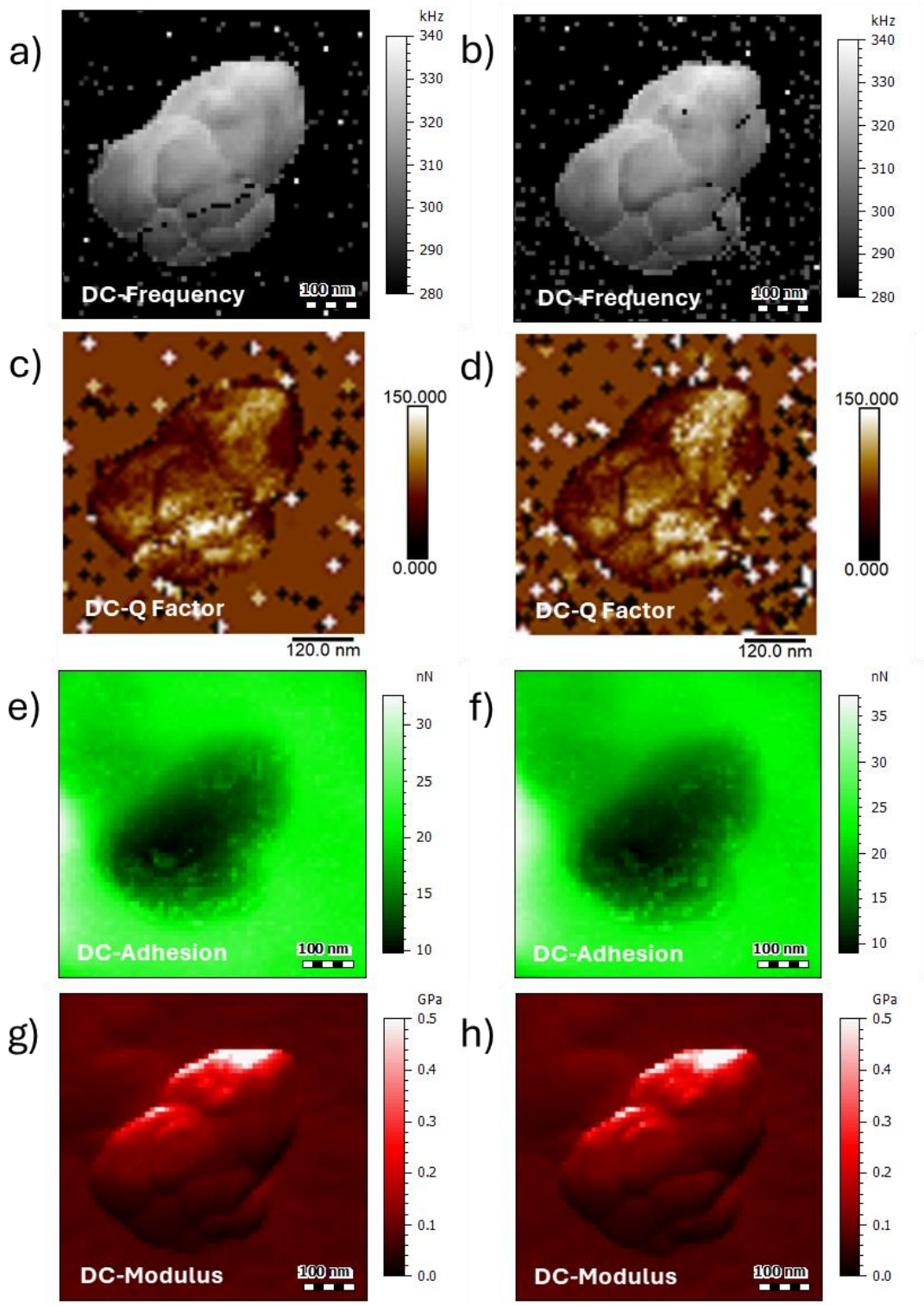

Figure 90 *: Mechanical DataCube-PFM measurement on a BFO aggregate (scan at 90°) before poling (a) CR-Frequency, (c) Q factor, (e) Adhesion, and (g) Young modulus. DataCube-PFM measurement on a BFO aggregates (scan at 90°) after poling at -10V (b) CR-Frequency, (d) Q-factor, (f) Adhesion, and (h) Young modulus.*

8.2.2.2 Apparent surface displacement recalculation

The reconstructed *D*-value maps are shown in **Figure 91 a** for the unpoled data and **Figure 91 b** for the post-poled state. Because the BFO response is the only relevant one for this analysis, the clustering software is used to divide the data and to isolate the response corresponding to the BFO. The cluster mapping is presented in **Figure 91 c**. The cluster of BFO phases is identified as cluster 1. Corresponding histograms for *D* mapping before and after clustering are presented in **Figure 91 d-e**.

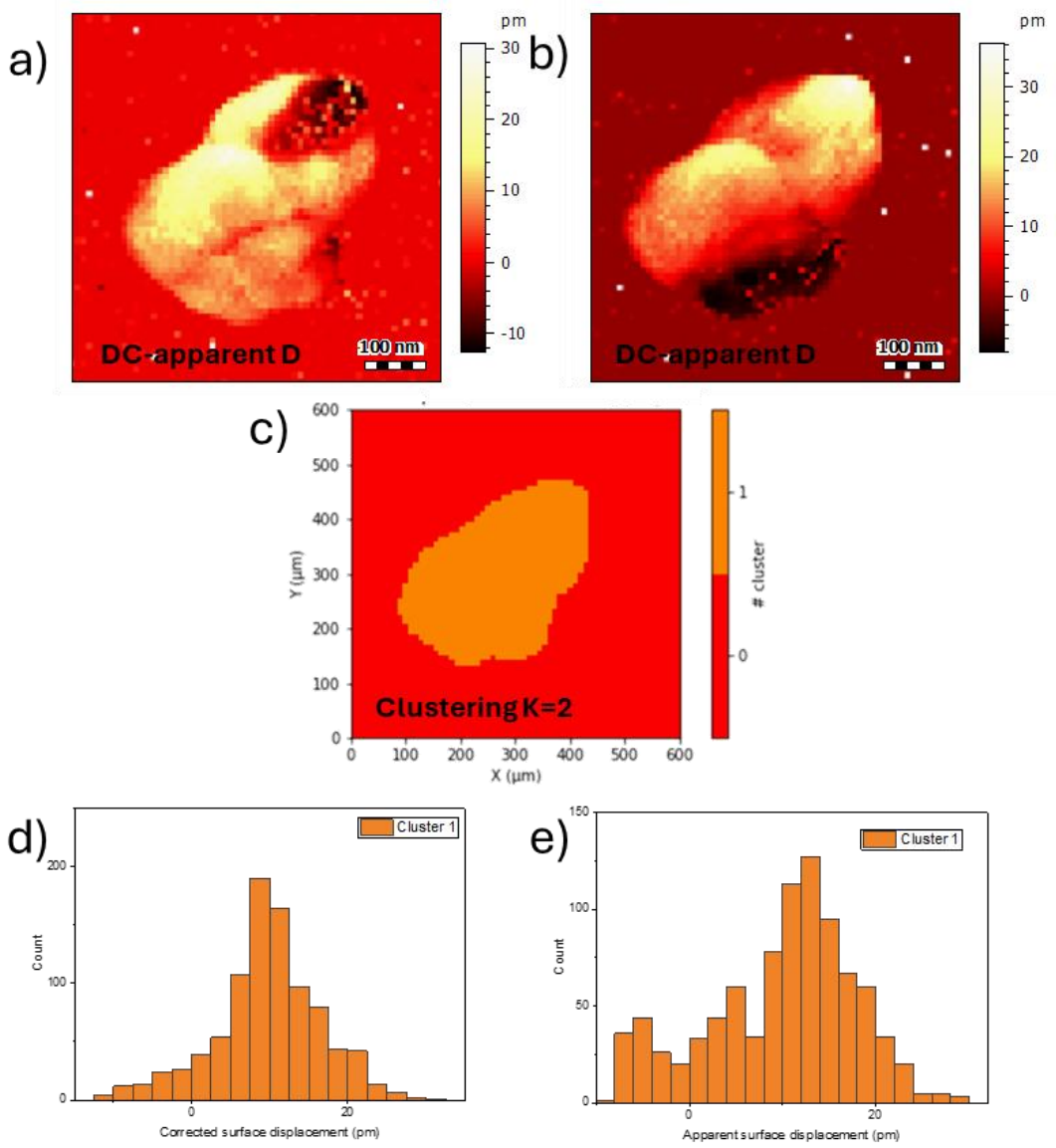

***Figure 91** : Reconstructed images of the D-values of the BFO particles (a) Before poling and (b) After poling. Cluster mapping for k cluster = 2 (c) Before poling and (d) After poling, and the D-value distribution in cluster 1 (e) Before poling and (f) After poling.*

Prior to poling, the D-values span a broad range from negative values associated with down-oriented domains to small positive displacements of a few picometres and up to approximately 25 pm, with a central value around 10 pm. After poling, the BFO particles exhibit an overall stronger electromechanical response with a central displacement near 15 pm and maxima approaching 30 pm (**Figure 91 f**). These values fall within the expected range for BFO. Residual negative displacements are still observed and correspond to newly formed down-oriented regions after poling. As observed for the mechanical channels, the reconstructed displacement maps also display a directional asymmetry that is consistent with the previously described “moon effect”.

8.2.3 PVDF-TrFE/BFO nanocomposite

8.2.3.1 DataCube vs CR-PFM

DataCube-PFM mapping performed on the PVDF–TrFE/BFO nanocomposites provides substantial additional insight into the local electromechanical behaviour of the system. **Figure 92** focuses on a relatively high aggregate of BFO particles embedded within the PVDF–TrFE matrix. **Figure 92 b–c** shows the CR-PFM images optimised for the BFO particles with the contact-resonance frequency set at approximately 310 kHz. Ferroelectric domains within the BFO grains are readily identifiable. However, domains within the polymer matrix are identifiable but appear faint because the excitation frequency is not optimised for the softer phase.

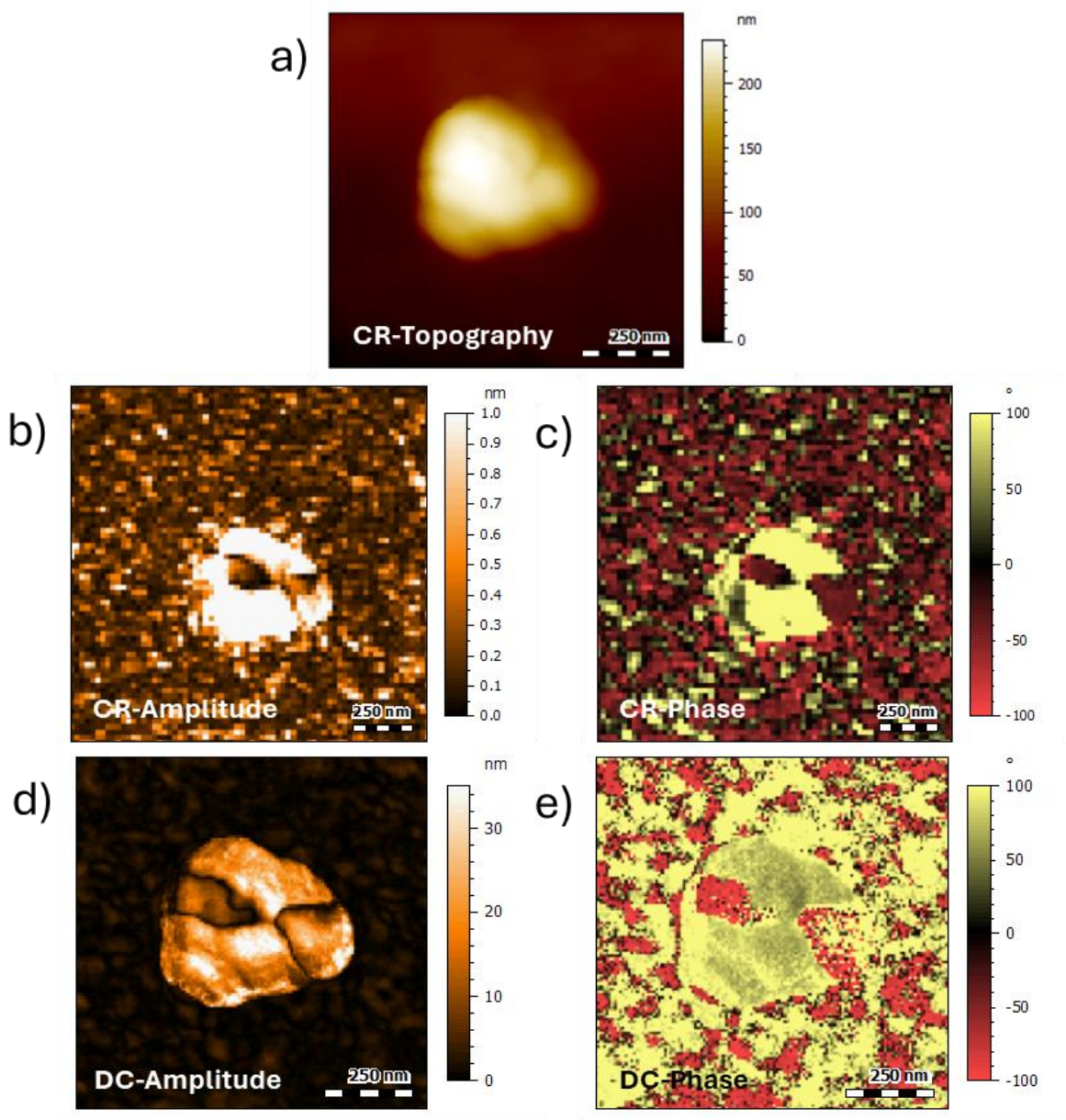

***Figure 92** : Comparison of CR-PFM and DataCube-PFM on a cluster of BFO inside the PVDF-TrFE matrix. Measurement in CR-PFM at CR frequency = 330 kHz, (a) Topography, (b) Amplitude, and (c) Phase. Measurement in DataCube PFM with a frequency range from 270 to 380 kHz before poling, (d) Amplitude, and (e) Phase.*

The corresponding DataCube-PFM amplitude and phase images are shown in **Figure 92 d–e**. Similar ferroelectric domain structures are observed on both components of the composite. However, the apparent up- and down-polarisation contrast in the polymer matrix appears inverted with respect to the one visualised in CR-PFM. This inversion originates from the contact-resonance optimisation in CR-PFM because the resonance frequency tuned for the particles is significantly higher than that of the polymer matrix (see **Figure 93 a**).

Mechanical mapping of the composite exhibits trends consistent with those observed in the individual constituent materials. The resonance frequency and quality factor are systematically lower in the polymer matrix than in the BFO particles (**Figure 93 a–b**). They reflect their lower stiffness. Polarised regions of the polymer exhibit more uniform resonance frequency and Q-factor values than unpoled areas. It agrees with previous reports. The DataCube adhesion map (**Figure 93 c**) shows the expected behaviour already observed in PeakForce Tapping measurements with lower adhesion on the particles than on the polymer matrix. Additionally, a pronounced tip-effect is observed around the particle boundaries. It likely arises from the finite size and topographic relief of the aggregates. The Young's modulus map (**Figure 93d**) exhibits the same directional asymmetry ("moon phase effect") described in the previous section.

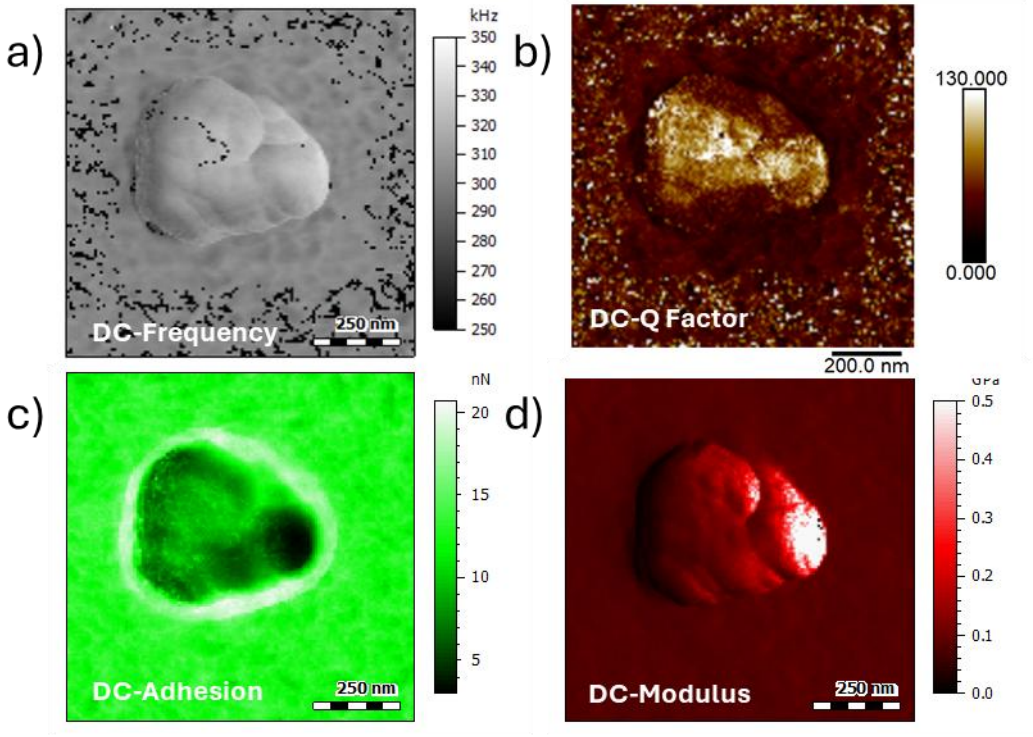

***Figure 93** : Mechanical DataCube-PFM measurement on a BFO aggregates inside the PVDF-TrFE matrix (a) CR-Frequency, (b) Q factor, (c) Adhesion and (d) Young modulus.*

The BFO grain, evidenced by pyssPFM clustering in this region, is non-polarisable within the voltage range investigated (**Figure 94 a–b**). In contrast, the PVDF–TrFE matrix undergoes a clear and global polarisation (**Figure 94 c–d**).

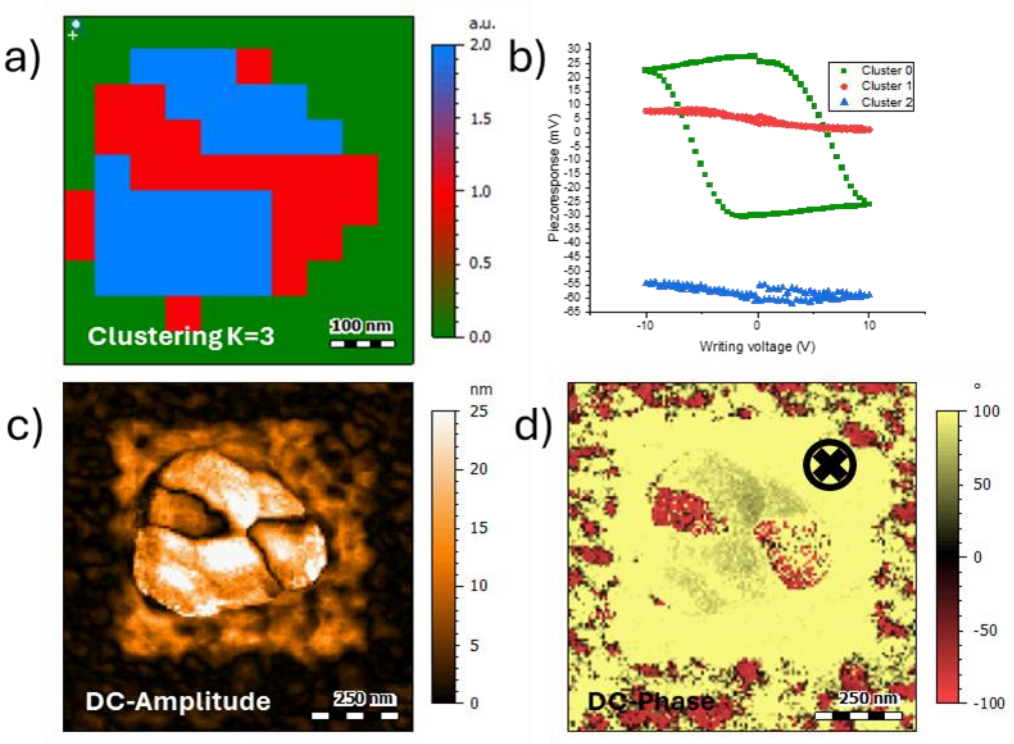

Figure 94 *:(a) PyssPFM clustering, K = 3. (b) Mean off-field loops. (c) DataCube-PFM amplitude and (d) DataCube-PFM phase after pyssPFM clustering.*

D mapping and clustering of the data are presented in **Figure 95 a-c**. When focusing specifically on the polymer response (cluster 0 **Figure 95 d-e**), a global decrease in D-value is observed with the mean value shifting from approximately 0 pm to −10 pm and minimum values approaching the expected −20 pm after poling. On the other hand, the BFO particles show only minimal changes in apparent displacement. Both distinct populations identified by ssPFM clustering remain clearly distinguishable in the histograms corresponding to cluster 1 (**Figure 95 f–g**). This observation further supports the heterogeneous switching behaviour of the BFO grains within the composite.

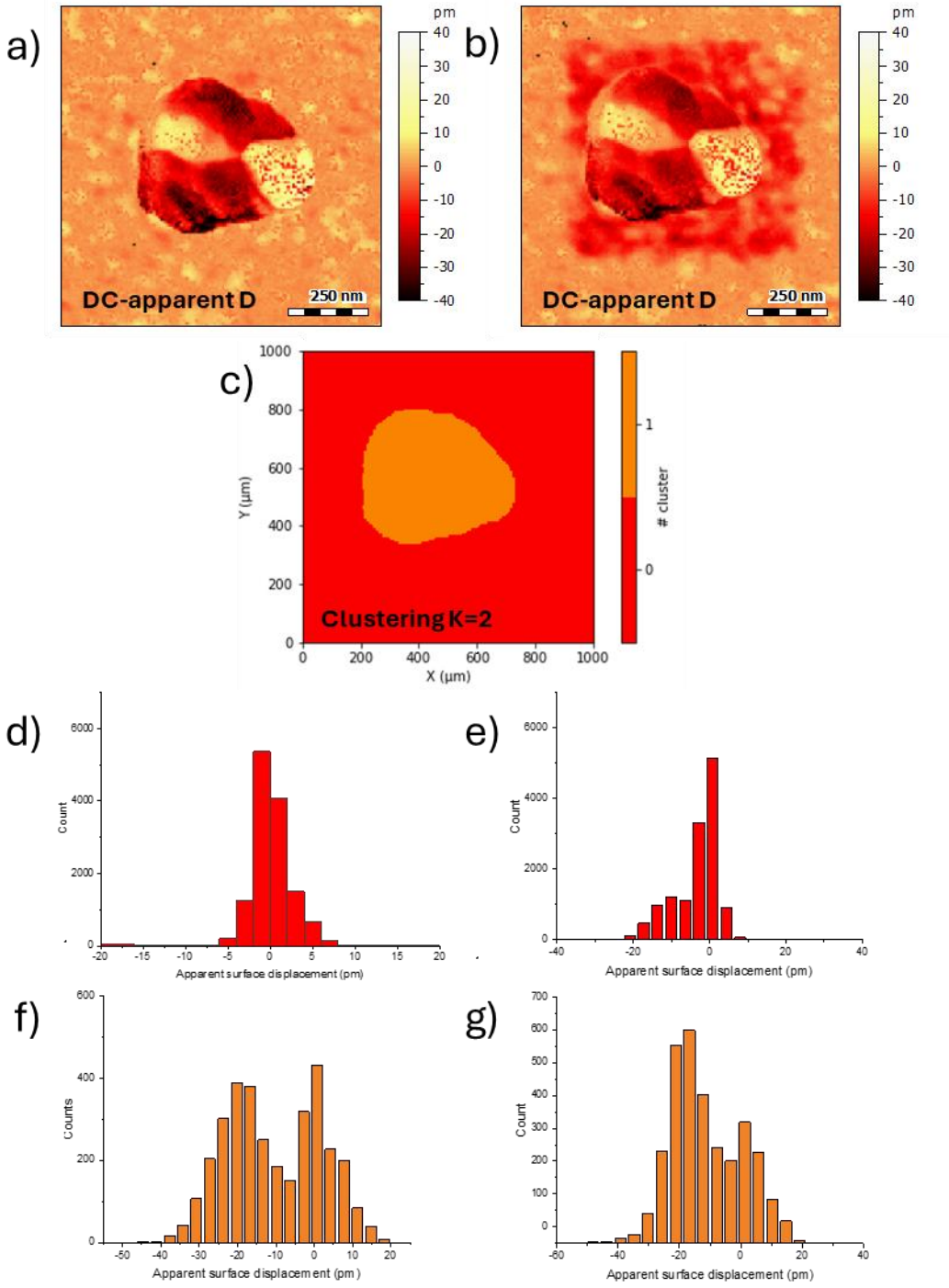

Figure 95 *: Reconstructed images of the D-value of the BFO/PVDF-TrFE (a) before polarisation and (b) After ssPFM polarisation. (c) Cluster mapping for k cluster = 2. Histogram for D-values before polarisation (d) Cluster 0 and (e) Cluster 1. Histogram for D-values after polarisation (f) Cluster 0 and (g) Cluster 1.*

8.2.3.2 DataCube vs DFRT

Figure 96 and **Figure 97** show DataCube measurements acquired over the same area investigated with DFRT-PFM and local d_{33}^{app} point spectroscopy. To facilitate direct

comparison, DataCube-PFM and DFRT-PFM images of the same region are juxtaposed in **Figure 96**. Due to the intrinsically longer acquisition time of DataCube-PFM, the spatial resolution is reduced. The DataCube dataset requires slightly more than one hour to acquire at a resolution of 64 × 64 pixels (**Figure 96 a–b**) whereas the DFRT-PFM mapping is completed in approximately 20 minutes with a resolution of 256 × 256 pixels (**Figure 96 c–d**). Despite the lower spatial resolution, the same ferroelectric domain structure is clearly observed within the polymer matrix in both datasets. Furthermore, the domain patterns observed on the surfaces of the BFO particles are consistent with those previously reported in DFRT-PFM, but without the phase overshoot artifacts. Regions that previously appeared "blurry" or ambiguous in DFRT-PFM phase images are no longer present in the DataCube-PFM data. This improvement arises from the intrinsic nature of the DataCube acquisition mode in which force–distance curves provide more stable contact conditions on rough or heterogeneous surfaces compared with continuous-contact driven modes at the expense of acquisition speed.

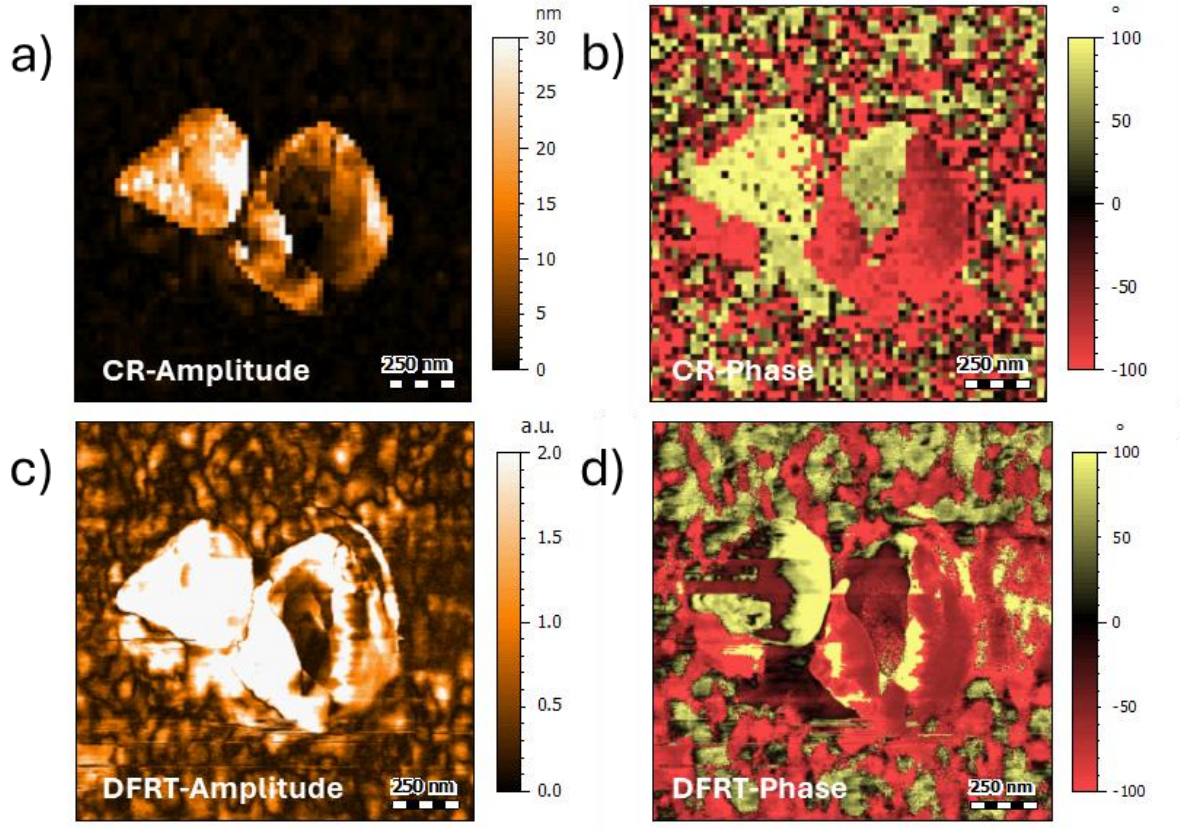

***Figure 96** : (a) DataCube-PFM Amplitude and (b) DataCube-PFM Phase. (c) DFRT-PFM Amplitude and (d) DFRT-PFM Phase.*

The same area is polarised at +10 V and re-imaged with DataCube-PFM (**Figure 97 a–b**). The polymer matrix shows a global increase in amplitude and a homogenisation of the phase response whereas the BFO grains display a much broader range of behaviours.

Regions that were previously non-responsive remain essentially inactive while previously down-oriented regions are partially switched to the up-oriented state. Therefore, the reconstructed D-value of the polymer matrix (cluster 0, **Figure 97 f**) exhibits a global decrease with a mean value around −20 pm after poling. In this case, the minimum displacement values are not considered because the polarisation state is spatially uniform. The cluster corresponding to the BFO particles (cluster 1, **Figure 97 g–h**) shows a clear shift towards positive displacement values with a mean around +15 pm and maxima reaching 30–40 pm.

Finally, a strong consistency is observed between the apparent piezoelectric coefficients extracted from local point spectroscopy and those obtained from DataCube displacement mapping (**Figure 91** vs **Figure 97 d**). This agreement confirms the robustness and reliability of the DataCube-PFM approach for quantitative analysis in complex, heterogeneous ferroelectric systems.

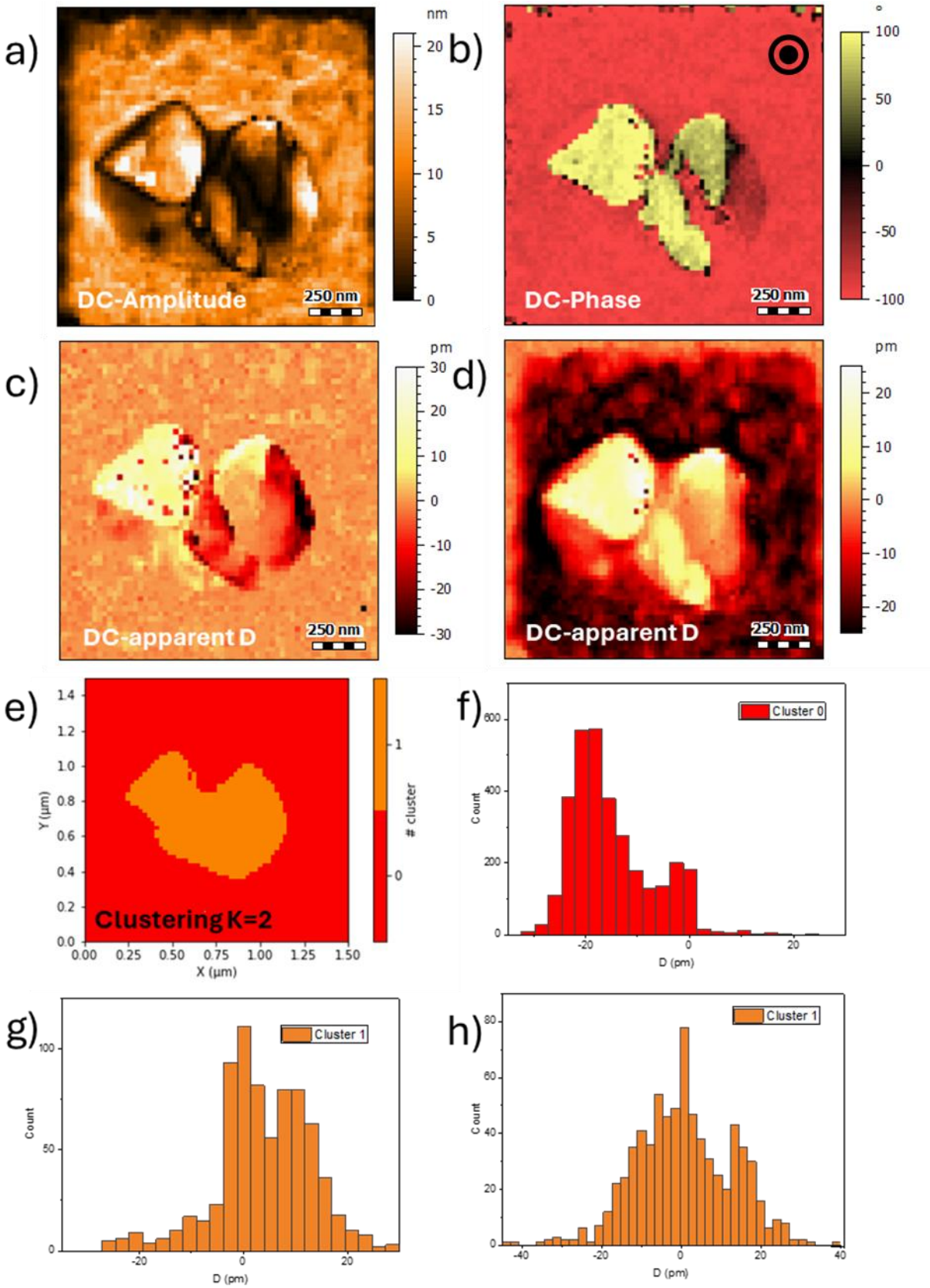

Figure 97 *: (a) DataCube-PFM Amplitude and (b) DataCube-PFM Phase after polarizing the whole area at +10V. D-mapping (c) Before and (d) After polarisation. (e) Cluster mapping for k cluster = 2. Histogram for D-value (f) Cluster 0 after polarisation, (g) Cluster 1 before polarisation, and (h) Cluster 1 after polarisation.*

8.3 Conclusion

This chapter addressed the quantification of electromechanical displacement at the nanoscale and the associated limitations of conventional AFM measurements. It was shown that PFM measurements provide access only to an apparent piezoelectric coefficient, strongly influenced by experimental conditions and tip–sample interactions. Fixed-position ssPFM spectroscopy performed under quasi-zero DC bias was identified as the most reliable approach for homogeneous thin films, yielding consistent apparent coefficients for PVDF–TrFE. When applied to BFO nanoparticles and nanocomposites, single-point measurements revealed pronounced spatial heterogeneity, limiting their representativeness. To overcome these limitations, DataCube-PFM was introduced as a spectroscopy–mapping approach enabling spatially resolved reconstruction of apparent surface displacement while simultaneously accessing mechanical properties. This method improved measurement stability and reduced resonance-related artefacts, providing a more robust framework for the quantitative assessment of complex ferroelectric nanocomposites.

Chapter 9: Conclusions & Perspectives

9.1 Conclusions

The central objective of this study was the characterisation of complex ferroelectric responses of a hybrid ferroelectric nanocomposite at the nanoscale, with particular emphasis on understanding how geometry, surface roughness, and multi-phase interfaces influenced PFM-based measurements. To address this question, a PVDF–TrFE/Bismuth ferrite oxide ($BiFeO_3$, BFO) nanocomposite was selected as a model system. Both the composite and its individual constituents were fabricated by spin-coating. This method enabled the preparation of thin and practically uniform films suitable for AFM-based measurements at moderate polarisation voltages. BFO nanoparticles were synthesised using a sol–gel route. They were embedded either in a PEDOT:PSS matrix or directly within the PVDF–TrFE polymer matrix. PEDOT:PSS was used for its mechanical stabilisation and conductive properties. Throughout this work, particular attention was paid to differentiating genuine electromechanical signals from artefacts arising from electrostatic forces, mechanical heterogeneity, and instrumental limitations. Rather than relying exclusively on conventional PFM imaging, advanced techniques including DFRT-PFM, ssPFM combined with pyssPFM clustering, and DataCube-PFM were applied to achieve a reliable and spatially resolved interpretation of the nanoscale ferroelectric response.

This study was structured into four main analysis chapters. The first focused on the dispersion and proper integration of nanoparticles within polymer matrices, as well as on the limitations imposed by the applicable voltage range. The second chapter presented the imaging of ferroelectric domains simultaneously within both phases of the composite with the help of the DFRT-PFM mode. The third addressed the verification of the genuine ferroelectric nature of the measured signals using local ssPFM measurements, together with the spatial distribution of these properties through clustering analysis. The last chapter dealt with the quantification of surface displacement in PFM, both through local spectroscopy and through extended spatial mapping using the DataCube-PFM mode.

The first analyses focused on sample synthesis and structural characterisation. X-ray diffraction confirmed the formation of rhombohedral-phase BFO particles. Environmental SEM and AFM imaging demonstrated that spin-coated PVDF–TrFE thin films exhibited a homogeneous fibrillar morphology characteristic of well-crystallised ferroelectric polymer phases. In the hybrid nanocomposites, the images showed effective and homogeneous embedding of BFO particles within the polymer matrix, although some degree of aggregation persisted. Thickness measurements combining AFM scratch tests and ellipsometry revealed film thicknesses spatially varying between 20 and 60 nm. PeakForce Tapping measurements further confirmed the successful integration of the two phases and provided a clear contrast in Young's modulus as well as adhesion between polymer and particles. Local conductive-AFM measurements demonstrated the absence of leakage currents in both PVDF–TrFE and BFO within the voltage range used for

PFM, ensuring that all electromechanical measurements could be performed without risk of local electrical breakdown.

The second set of results concentrated on the investigation of the naturally occurring ferroelectric domain structures of PVDF–TrFE, BFO particles, and their hybrid nanocomposite. Conventional CR-PFM revealed well-defined elongated up- and down-oriented domains in PVDF–TrFE, independent of the underlying fibrillar morphology. Local poling experiments confirmed switchability and highlighted substantial lateral spreading of the polarised regions. However, CR-PFM imaging of BFO particles embedded in PEDOT:PSS or PVDF–TrFE proved noticeably more challenging. Only a subset of particles displayed a measurable piezoresponse, while strong roughness and contact instabilities frequently generated ambiguous amplitude and phase contrasts. DFRT-PFM partially mitigated these issues by improving resonance tracking and enabling simultaneous vertical and lateral imaging. However, this technique revealed phase-flip artifacts associated with mechanical instabilities and PID overshoot, particularly on rough and heterogeneous regions, thereby restricting the reliability of domain interpretation in such systems.

In the third part, the challenge of reliably identifying ferroelectric behaviour at the nanoscale was addressed using switching-spectroscopy PFM. Measurements performed on reference materials (PZT and ZnO) demonstrated that ferroelectric-like hysteresis loops could be artificially generated in non-ferroelectric systems under favourable experimental conditions. This highlighted the necessity of complementary validation through off-field versus on-field loop comparison and cKPFM measurements. Applied to PVDF–TrFE, ssPFM revealed robust and reproducible ferroelectric switching with well-defined hysteresis both on and off field, as well as a clear bistable state in cKPFM measurements. Thickness-dependent studies showed that both coercive voltage and piezoresponse amplitude strongly depended on film thickness, although all films remained switchable in the investigated range. In contrast, BFO nanoparticles exhibited highly heterogeneous behaviour ranging from fully switchable ferroelectric responses, with similar on- and off-field and cKPFM values to bulk BFO, to strong but non-polarisable signals or complete absence of response. These variations reflected differences in electrical coupling, crystallographic orientation, and local environment. Spatially resolved ssPFM clustering successfully discriminated active ferroelectric regions from non-responsive or artefactual ones in both isolated systems and full nanocomposites. In parallel, the re-examination of previously reported ferroelectric materials, such as Ln_2WO_6 compounds and tellurium nanowires, illustrated how insufficient spectroscopic validation could lead to the misclassification of non-ferroelectric materials.

The last analysis chapter addressed the fundamental difficulty of quantifying nanoscale electromechanical displacement with PFM and clarified why only an apparent piezoelectric coefficient, d_{33}^{app}, could be extracted with OBD-based AFM systems. Fixed-

position ssPFM spectroscopy performed off-field and under quasi-zero DC bias was identified as the most robust approach for homogeneous thin films, provided that tip wear was carefully accounted for through calibration on a ZnO reference. Applied to PVDF–TrFE, this approach yielded consistent d_{33}^{app} values in agreement with reference data (approximately −20 pm/V). When extended to BFO nanoparticles and nanocomposites, single-point spectroscopy revealed pronounced heterogeneity, with switchable, non-switchable, and artefactual responses coexisting within individual aggregates. This resulted in a wide distribution of apparent d_{33}^{app}values ranging from −20 up to 34 pm/V, and in some cases, undetermined values. To overcome the spatial limitations of point measurements, DataCube-PFM was introduced as a spectroscopy–mapping approach enabling pixel-wise reconstruction of apparent surface displacement while simultaneously tracking local mechanical properties. DataCube-PFM improved mechanical stability, reduced resonance-related artefacts, and eliminated phase overshoot effects encountered in DFRT-PFM. It also provided mechanical information useful for identifying the underlying nature of the materials. The resulting displacement maps were fully consistent with single-point d_{33}^{app} estimates, demonstrating the ability of DataCube-based mapping to reliably and physically meaningfully assess the electromechanical behaviour of complex, heterogeneous ferroelectric systems.

As a general conclusion, this study demonstrated the reliable nanoscale characterisation of ferroelectric nanocomposites while accounting for their complex geometry, local surface roughness, and rigidity, which strongly influenced all PFM measurements. Using PVDF–TrFE/BFO thin films as a model system, it was shown that conventional PFM alone was insufficient to unambiguously identify ferroelectric behaviour in heterogeneous and three-dimensional structures. Advanced approaches combining DFRT-PFM, switching-spectroscopy PFM with data clustering, and DataCube-PFM proved essential to stabilise measurements, discriminate genuine electromechanical responses from artefacts, and achieve meaningful spatial quantification. The advantages and drawbacks of the different PFM techniques were summarised in **Table 5**. Overall, this work established robust methodological guidelines for interpreting PFM data in complex ferroelectric nanocomposite systems.

***Table 5** : Summary of the different PFM modes used during this thesis*

PFM Mode	Advantages	Drawbacks
Conventional CR-PFM	• Fast imaging with high spatial resolution • Well suited for visualising ferroelectric domain structures on flat, homogeneous samples • easy to use	• Sensitive to surface roughness and mechanical heterogeneity • Not suited for quantitative mapping
DFRT-PFM	• Improved stability due to dynamic tracking of contact resonance • Enables simultaneous vertical and lateral domain imaging • Better suited for heterogeneous samples than CR-PFM	• Susceptible to PID overshoot and phase-flip artefacts • Reduced reliability on very rough topographies (possible ambiguous phase contrast)
ssPFM	• Direct probing of local ferroelectric switching behaviour • Off-field measurements reduce electrostatic contributions • Complementaries on-field and cKPFM measurement enable discrimination between ferroelectric and artefactual responses • Convertible in quantitative measurement	• Single-point measurements, lack spatial representativity • Time-consuming for mapping
Data-cube PFM	• Force–distance-based approach ensures stable contact on rough surfaces • Simultaneous access to electromechanical and mechanical properties • Reduced resonance-related artefacts and phase overshoot • Access to quantitative mapping of the surface displacement	• Long acquisition times • Lower spatial resolution compared to conventional imaging modes • Limited to a qualitative mechanical approach

9.2 Perspectives

While this work provides a comprehensive methodology for the investigation of ferroelectric nanocomposite properties, it has intentionally been centered on a single model system, namely PVDF–TrFE/BFO thin films. To strengthen the conclusions of this study, it will be relevant to broaden it to a larger range of investigated materials and architectures. As examples, replacing BFO nanoparticles with other ferroelectric oxides, such as $BaTiO_3$, or with purely piezoelectric fillers like ZnO embedded within the PVDF–TrFE matrix would allow a more systematic evaluation of the respective roles of intrinsic ferroelectricity and linear piezoelectricity in PFM-based measurements. Such studies could help distinguish material-dependent effects from measurement-induced artefacts and refine the interpretation of PFM contrast in heterogeneous systems. Similarly, substituting PVDF–TrFE with alternative ferroelectric polymer matrices could provide valuable insight into the influence of matrix stiffness, dielectric properties, crystallinity, and switching behaviour on both local electromechanical response and stability of SPM measurements.

In addition to ferroelectric and piezoelectric systems, extending these methodologies to flexoelectric materials represents a particularly promising perspective. Flexoelectricity is expected to be strongly enhanced at the nanoscale and may contribute significantly to PFM signals, especially in mechanically heterogeneous or curved systems. Investigating nominally non-ferroelectric materials exhibiting strong flexoelectric responses would provide an ideal testbed to assess the sensitivity and limits of PFM-based techniques, as well as to clarify the interplay between flexoelectric, electrostatic, and true piezoelectric contributions in measured signals.

Concerning the sample morphology, the nanocomposite investigated in this thesis exhibits significant local surface roughness due to partially emerging particle aggregates. Because these features strongly affect contact mechanics, resonance stability, and the reliability of PFM imaging, future studies should therefore focus on systems with flatter surfaces while preserving multiphase complexity. Optimized deposition strategies aimed at improved particle embedding, alternative multilayer architectures, cryo-microtomed cross-sections, or the investigation of ferroelectric polymer blends will certainly help to boost the quality and reproducibility of such samples. Improved morphological control would also facilitate more direct comparison with the theoretical simulation of electromechanical coupling at heterogeneous interfaces.

Beyond planar thin films, the approaches developed in this study could also be extended to more complex three-dimensional heterostructures. As DataCube-PFM has proven effective for quantifying electromechanical responses on rough and heterogeneous surfaces, it appears particularly promising for the study of nanowires, nanopillars, or vertically aligned composite systems. These geometries are of strong technological interest but remain extremely challenging for conventional PFM due to steep topography, large variations in contact area, and limited measurement stability. Force–distance-based spectroscopy–mapping approaches could significantly improve the reliability of nanoscale electromechanical characterisation in such systems. Further improvements

may also be achieved through recently developed PeakForce-based PFM modes, which could enhance mechanical tracking during DataCube-like measurements. Such advances would open the way to the nanoscale characterisation of functional device-relevant architectures, including flexible sensors, soft robotic architectures, and actuators based on ferroelectric or piezoelectric nanocomposites.

Finally, quantitative displacement extraction remains an open challenge in nanoscale PFM. Although this thesis demonstrates that apparent surface displacement can be robustly reconstructed using force–curve-based approaches, absolute quantification is still limited by the use of optical beam deflection detection and by uncertainties related to electrostatic interactions and cantilever dynamics. Combining similar force–distance methodologies with alternative SPM detection schemes, such as interferometric displacement sensing, would allow a more rigorous validation of the measured signals and help disentangle true surface displacement from electrostatic or cantilever-bending artefacts. Coupling such measurements with advanced modelling or correlative techniques could further enhance confidence in quantitative nanoscale electromechanical measurement.

Altogether, these perspectives highlight that the methodologies developed in this thesis form a versatile and transferable framework rather than a system-specific study. By extending them to new materials, morphologies, physical mechanisms, and device architectures, they have the potential to significantly contribute to the reliable nanoscale characterisation of complex ferroelectric, piezoelectric, and flexoelectric systems and to bridge the gap between fundamental understanding and technological application.

Chapter 10: Bibliography

[1] World Energy Outlook 2024 – Analysis, IEA (2024). https://www.iea.org/reports/world-energy-outlook-2024 (accessed January 4, 2026).

[2] X. Wang, *Piezoelectric nanogenerators—Harvesting ambient mechanical energy at the nanometer scale*, Nano Energy 1 (**2012**) 13–24. https://doi.org/10.1016/j.nanoen.2011.09.001.

[3] F.R. Fan, W. Tang, Z.L. Wang, *Flexible Nanogenerators for Energy Harvesting and Self-Powered Electronics*, Advanced Materials 28 (**2016**) 4283–4305. https://doi.org/10.1002/adma.201504299.

[4] *Wind and water provide most renewable electricity,* (n.d.). https://ec.europa.eu/eurostat/web/products-eurostat-news/-/ddn-20210108-1 (accessed January 5, 2026).

[5] J. Briscoe, S. Dunn, *Piezoelectric nanogenerators – a review of nanostructured piezoelectric energy harvesters*, Nano Energy 14 (**2015**) 15–29. https://doi.org/10.1016/j.nanoen.2014.11.059.

[6] R. Bhatnagar, V. Yadav, U. Kumar, M.F. Carrasco, P*iezoelectric Energy Harvesting: From Fundamentals to Advanced Applications*, Energy Tech 13 (**2025**). https://doi.org/10.1002/ente.202401455.

[7] H. Liu, J. Zhong, C. Lee, S.-W. Lee, L. Lin, *A comprehensive review on piezoelectric energy harvesting technology: Materials, mechanisms, and applications*, Applied Physics Reviews 5 (**2018**). https://doi.org/10.1063/1.5074184.

[8] C. Dagdeviren, P. Joe, O.L. Tuzman, K.-I. Park, K.J. Lee, Y. Shi, Y. Huang, J.A. Rogers, *Recent progress in flexible and stretchable piezoelectric devices for mechanical energy harvesting, sensing and actuation*, Extreme Mechanics Letters 9 (**2016**) 269–281. https://doi.org/10.1016/j.eml.2016.05.015.

[9] J. Zhang, Y. He, C. Boyer, K. Kalantar-Zadeh, S. Peng, D. Chu, C.H. Wang, *Recent developments of hybrid piezo–triboelectric nanogenerators for flexible sensors and energy harveste*rs, Nanoscale Adv. 3 (**2021**) 5465–5486. https://doi.org/10.1039/d1na00501d.

[10] E. Aksel, J.L. Jones, *Advances in Lead-Free Piezoelectric Materials for Sensors and Actuators*, Sensors 10 (**2010**) 1935–1954. https://doi.org/10.3390/s100301935.

[11] S. Banerjee, S. Bairagi, S. Wazed Ali, *A critical review on lead-free hybrid materials for next generation piezoelectric energy harvesting and conversion*, Ceramics International 47 (**2021**) 16402–16421. https://doi.org/10.1016/j.ceramint.2021.03.054.

[12] N.T. Beigh, D. Mallick, Low-Cost, *High-Performance Piezoelectric Nanocomposite for Mechanical Energy Harvesting*, IEEE Sensors J. 21 **(2021**) 21268–21276. https://doi.org/10.1109/JSEN.2021.3100869.

[13] D. Petrukhin, V. Salnikov, A. Nikitin, I. Sidane, S. Slimani, S. Alberti, D. Peddis, A. Omelyanchik, V. Rodionova, *Effect of Bismuth Ferrite Nanoparticles on Physicochemical Properties of Polyvinylidene Fluoride-Based Nanocomposites*, J. Compos. Sci. 8 (**2024**) 329. https://doi.org/10.3390/jcs8080329.
[14] H. Wang, Z. Li, S. Shi, X. Fan, Z. Sun, J. Liu, P. Li, J. Zhai, Z. Pan, *Harnessing piezoelectric and flexoelectric synergies in one-dimensional heterostructure nanofibers for nano-energy harvesting and self-powered sensors*, Chemical Engineering Journal 474 (**2023**) 145470. https://doi.org/10.1016/j.cej.2023.145470.
[15] J.-H. Bae, S.-H. Chang, PVDF-*based ferroelectric polymers and dielectric elastomers for sensor and actuator applications*: a review, Funct. Compos. Struct. 1 (**2019**) 012003. https://doi.org/10.1088/2631-6331/ab0f48.
[16] P. Adhikary, D. Mandal, *Piezoelectric Materials Based on Polymers and Their Composites*, in: R. Gupta (Ed.), Handbook of Energy Materials, Springer Nature Singapore, Singapore, **2022**: pp. 1–37. https://doi.org/10.1007/978-981-16-4480-1_74-1.
[17] A.S.M.A. Haseeb, ed., E*ncyclopedia of materials: electronics*, Elsevier, Amsterdam Boston Heidelberg London New York Oxford, **2023**.
[18] J. Martinez-Vega, ed., *Dielectric materials for electrical engineering*, ISTE, London, **2010**.
[19] G. Blaise, D. Treheux, *Physics of Dielectrics, in: Dielectric Materials for Electrical Engineering*, **2013**: pp. 1–16. https://doi.org/10.1002/9781118557419.ch01.
[20] G. Blaise, *Fundamental approach to the storage of energy in dielectrics*, in: Proceedings of **1995** IEEE 5th International Conference on Conduction and Breakdown in Solid Dielectrics, IEEE, Leicester, UK, n.d.: pp. 324–328. https://doi.org/10.1109/icsd.1995.523002.
[21] H. Zhang, H. Tan, *Dielectric Materials for Capacitive Energy Storage*, 1st ed., CRC Press, Boca Raton, **2024**. https://doi.org/10.1201/9781003454496.
[22] X. Hao, *A review on the dielectric materials for high energy-storage application*, J. Adv. Dielect. 03 (**2013**) 1330001. https://doi.org/10.1142/s2010135x13300016.
[23] Manoj Gupta, Wong Wai Leong, Eugene, *Microwave Heating of Other Materials, in: Microwaves and Metals*, John Wiley & Sons, Ltd, **2007**: pp. 159–182. https://doi.org/10.1002/9780470822746.ch5.
[24] J. Curie, P. Curie, D*éveloppement par compression de l'électricité polaire dans les cristaux hémièdres à faces inclinées*, bulmi 3 (**1880**) 90–93. https://doi.org/10.3406/bulmi.1880.1564.
[25] G. Lippmann, *Principe de la conservation de l'électricité, ou second principe de la théorie des phénomènes électriques*, J. Phys. Theor. Appl. 10 (**1881**) 381–394. https://doi.org/10.1051/jphystap:0188100100038100.
[26] A. Khan, R. Joshi, M.K. Sharma, C.-J. Huang, J.-H. Yu, Y.-L. Wang, Z.-H. Lin, T*he potential of organic piezoelectric materials for next-generation implantable*

biomedical devices, Nano Trends 6 (**2024**) 100032. https://doi.org/10.1016/j.nwnano.2024.100032.
[27] M. Smith, S. Kar-Narayan, *Piezoelectric polymers: theory, challenges and opportunities*, International Materials Reviews 67 (**2022**) 65–88. https://doi.org/10.1080/09506608.2021.1915935.
[28] C. Covaci, A. Gontean, P*iezoelectric Energy Harvesting Solutions: A Review*, Sensors 20 (**2020**) 3512. https://doi.org/10.3390/s20123512.
[29] A. Farahani, A. Zarei Hanzaki, H.R. Abedi, L. Tayebi, E. Mostafavi, *Polylactic Acid Piezo-Biopolymers: Chemistry, Structural Evolution, Fabrication Methods, and Tissue Engineering Applications*, Journal of Functional Biomaterials 12 (**2021**) 71. https://doi.org/10.3390/jfb12040071.
[30] K. Maity, D. Mandal, *Piezoelectric polymers and composites for multifunctional materials*, in: Advanced Lightweight Multifunctional Materials, Elsevier, **2021**: pp. 239–282. https://doi.org/10.1016/B978-0-12-818501-8.00001-9.
[31] S.B. Lang, D.K. Das-Gupta, *Chapter 1 - Pyroelectricity: Fundamentals and applications, in: H.S. Nalwa (Ed.), Handbook of Advanced Electronic and Photonic Materials and Devices*, Academic Press, Burlington, **2001**: pp. 1–55. https://doi.org/10.1016/B978-012513745-4/50036-6.
[32] H. Cui, W. He, Q. Pei, R. Ma, 16 - *Electrocaloric effects in ferroelectric polymers, in: K. Asadi (Ed.), Organic Ferroelectric Materials and Applications*, Woodhead Publishing, **2022**: pp. 535–570. https://doi.org/10.1016/B978-0-12-821551-7.00016-6.
[33] D. Zhang, H. Wu, C.R. Bowen, Y. Yang, *Recent Advances in Pyroelectric Materials and Applications,* Small 17 (**2021**). https://doi.org/10.1002/smll.202103960.
[34] J. Valasek, P*iezo-Electric and Allied Phenomena in Rochelle Salt*, Phys. Rev. 17 (**1921**) 475–481. https://doi.org/10.1103/PhysRev.17.475.
[35] K. Asadi, ed., *Organic ferroelectric materials and applications*, Woodhead Publishing, an impreint of Elsevier, Oxford, **2022.**
[36] S. Kasap, P. Capper, eds., Springer *Handbook of Electronic and Photonic Materials*, Springer International Publishing, Cham, **2017.** https://doi.org/10.1007/978-3-319-48933-9.
[37] J. Park, D.-G. Lee, S. Hur, J.M. Baik, H.S. Kim, H.-C. Song, *A Review on Recent Advances in Piezoelectric Ceramic 3D Printing*, Actuators 12 (**2023**) 177. https://doi.org/10.3390/act12040177.
[38] B. Wang, Y. Gu, S. Zhang, L.-Q. Chen, *Flexoelectricity in solids: Progress, challenges, and perspectives*, Progress in Materials Science 106 (**2019**) 100570. https://doi.org/10.1016/j.pmatsci.2019.05.003.
[39] S.M. Kogan, *Piezoelectric effect during inhomogeneous deformation and acoustic scattering of carriers in crystals*, Sov. Phys. Solid State 5 (**1964**) 2069–2070.
[40] L. Wang, S. Liu, X. Feng, C. Zhang, L. Zhu, J. Zhai, Y. Qin, Z.L. Wang, *Flexoelectronics of centrosymmetric semiconductor*s, Nat. Nanotechnol. 15 (**2020**) 661–667. https://doi.org/10.1038/s41565-020-0700-y.

[41] S. Huang, L. Qi, W. Huang, L. Shu, S. Zhou, X. Jiang, *Flexoelectricity in dielectrics: Materials, structures and characterizations*, J. Adv. Dielect. 08 (**2018**) 1830002. https://doi.org/10.1142/S2010135X18300025.
[42] S.V. Kalinin, A.N. Morozovska, *Focusing light on flexoelectricity, Nature Nanotechnology* 10 (**2015**) 916–917. https://doi.org/10.1038/nnano.2015.213.
[43] Front Matter, in: *Advanced Lightweight Multifunctional Materials*, Elsevier, **2021**: https://doi.org/10.1016/b978-0-12-818501-8.01001-5.
[44] R.E. Newnham, *Properties of Materials: Anisotropy, Symmetry, Structure*, Oxford University Press, **2004**. https://doi.org/10.1093/oso/9780198520757.001.0001.
[45] A.O.D. Santos, W.H. Yaegashi, R. Marcon, B.B. Li, R.V. Gelamo, L.P. Cardoso, J.M. Sasaki, M.A.R. Miranda, F.E.A. Mello, R*ochelle salt piezoelectric coefficients obtained by x-ray multiple diffraction*, J. Phys.: Condens. Matter 13 (**2001**) 10497–10505. https://doi.org/10.1088/0953-8984/13/46/318.
[46] K. Uchino, *Comprehensive Composite Materials: Piezoelectric Composites*. Elsevier Amsterdam, The Netherlands (**2000**).
[47] J. Wang, S. Wang, X. Li, L. Li, Z. Liu, J. Zhang, Y. Wang, *High piezoelectricity and low strain hysteresis in PMN–PT-based piezoelectric ceramics*, Journal of Advanced Ceramics 12 (**2023**) 792–802. https://doi.org/10.26599/JAC.2023.9220720.
[48] Y. Qi, T.D. Nguyen, P.K. Purohit, M.C. McAlpine, *Stretchable Piezoelectric Nanoribbons for Biocompatible Energy Harvesting*, in: Stretchable Electronics, John Wiley & Sons, Ltd, **2012**: pp. 111–139. https://doi.org/10.1002/9783527646982.ch5.
[49] J.M. Vila-Fungueiriño, A. Gómez, J. Antoja-Lleonart, J. Gázquez, C. Magén, B. Noheda, A. Carretero-Genevrier, *Direct and converse piezoelectric responses at the nanoscale from epitaxial $BiFeO_3$ thin films grown by polymer assisted deposition*, Nanoscale 10 (**2018**) 20155–20161. https://doi.org/10.1039/C8NR05737K.
[50] S. Korkmaz, I.A. Kariper, *BaTiO3-based nanogenerators: fundamentals and current status*, J Electroceram 48 (**2022**) 8–34. https://doi.org/10.1007/s10832-021-00266-3.
[51] R.J. Ross, J. Kan, X. Wang, J. Blankenburg, J.I. Stockhausen, R.F. Pellerin, *Wood and Wood-Based Materials as Sensors—A Review of the Piezoelectric Effect in Wood*, U.S. Department of Agriculture, Forest Service, Forest Products Laboratory, Madison, WI, **2012**. https://doi.org/10.2737/FPL-GTR-212.
[52] T. Yucel, P. Cebe, D.L. Kaplan, *Structural Origins of Silk Piezoelectricity*, Adv Funct Materials 21 (**2011**) 779–785. https://doi.org/10.1002/adfm.201002077.
[53] A. Farahani, A. Zarei-Hanzaki, H.R. Abedi, L. Tayebi, E. Mostafavi, *Polylactic Acid Piezo-Biopolymers: Chemistry, Structural Evolution, Fabrication Methods, and Tissue Engineering Applications*, Journal of Functional Biomaterials 12 (**2021**). https://doi.org/10.3390/jfb12040071.

[54] K. Uchino, *Comprehensive Composite Materials: Piezoelectric Composites*. Elsevier Amsterdam, The Netherlands (**2000**).
[55] A. Tuluk, T. Mahon, S. Van Der Zwaag, P. Groen, *Estimating the true piezoelectric properties of BiFeO3 from measurements on BiFeO3-PVDF terpolymer composites*, Journal of Alloys and Compounds 868 (**2021**) 159186. https://doi.org/10.1016/j.jallcom.2021.159186.
[56] B. Jaffe, W.R. Cook, H. Jaffe, *THE PEROVSKITE STRUCTURE, in: Piezoelectric Ceramics*, Elsevier, **1971**: pp. 49–51. https://doi.org/10.1016/B978-0-12-379550-2.50008-9.
[57] H. Simons, J. Daniels, W. Jo, R. Dittmer, A. Studer, M. Avdeev, J. Rödel, M. Hoffman, *Electric-field-induced strain mechanisms in lead-free 94%(Bi1/2Na1/2)TiO3–6%BaTiO3,* Applied Physics Letters 98 (**2011**) 082901. https://doi.org/10.1063/1.3557049.
[58] T. Dawa, B. Sajjadi, *Exploring the potential of perovskite structures for chemical looping technology: A state-of-the-art review*, Fuel Processing Technology 253 (**2024**) 108022. https://doi.org/10.1016/j.fuproc.2023.108022.
[59] E. Fukada, *Piezoelectricity of Wood*, J. Phys. Soc. Jpn. 10 (**1955**) 149–154. https://doi.org/10.1143/jpsj.10.149.
[60] E. Fukada, *History and recent progress in piezoelectric polymers*, IEEE Trans. Ultrason., Ferroelect., Freq. Contr. 47 (**2000**) 1277–1290. https://doi.org/10.1109/58.883516.
[61] L. Huang, X. Zhuang, J. Hu, L. Lang, P. Zhang, Y. Wang, X. Chen, Y. Wei, X. Jing, *Synthesis of Biodegradable and Electroactive Multiblock Polylactide and Aniline Pentamer Copolymer for Tissue Engineering Applications*, Biomacromolecules 9 (**2008**) 850–858. https://doi.org/10.1021/bm7011828.
[62] S.C. Mathur, J.I. Scheinbeim, B.A. Newman, *Piezoelectric properties and ferroelectric hysteresis effects in uniaxially stretched nylon-11 films*, Journal of Applied Physics 56 (**1984**) 2419–2425. https://doi.org/10.1063/1.334294.
[63] V.S. Bystrov, E. Seyedhosseini, S. Kopyl, I.K. Bdikin, A.L. Kholkin, *Piezoelectricity and ferroelectricity in biomaterials: Molecular modeling and piezoresponse force microscopy measurements*, Journal of Applied Physics 116 (**2014**) 066803. https://doi.org/10.1063/1.4891443.
[64] Y. Choi, J. Koo, J.A. Rogers, *Inorganic materials for transient electronics in biomedical applications*, MRS Bull. 45 (**2020**) 103–112. https://doi.org/10.1557/mrs.2020.25.
[65] G.-T. Hwang, M. Byun, C.K. Jeong, K.J. Lee, *Flexible Piezoelectric Thin-Film Energy Harvesters and Nanosensors for Biomedical Applications*, Advanced Healthcare Materials 4 (**2015**) 646–658. https://doi.org/10.1002/adhm.201400642.
[66] S. Guerin, S.A.M. Tofail, D. Thompson, *Organic piezoelectric materials: milestones and potential*, NPG Asia Mater 11 (**2019**) 10. https://doi.org/10.1038/s41427-019-0110-5.
[67] T. Vijayakanth, D.J. Liptrot, E. Gazit, R. Boomishankar, C.R. Bowen, *Recent Advances in Organic and Organic–Inorganic Hybrid Materials for Piezoelectric*

Mechanical Energy Harvesting, Adv Funct Materials 32 (**2022**). https://doi.org/10.1002/adfm.202109492.
[68] H. Kawai, *The Piezoelectricity of Poly (vinylidene Fluoride)*, Japanese Journal of Applied Physics 8 (**1969**) 975. https://doi.org/10.1143/JJAP.8.975.
[69] S. Mohammadpourfazeli, S. Arash, A. Ansari, S. Yang, K. Mallick, R. Bagherzadeh, *Future prospects and recent developments of polyvinylidene fluoride (PVDF) piezoelectric polymer; fabrication methods, structure, and electro-mechanical properties*, RSC Adv. 13 (**2023**) 370–387. https://doi.org/10.1039/D2RA06774A.
[70] B. Mohammadi, A.A. Yousefi, S.M. Bellah, *Effect of tensile strain rate and elongation on crystalline structure and piezoelectric properties of PVDF thin films*, Polymer Testing 26 (**2007**) 42–50. https://doi.org/10.1016/j.polymertesting.2006.08.003.
[71] K. Tashiro, M. Kobayashi, *Structural phase transition in ferroelectric fluorine polymers: X-ray diffraction and infrared/Raman spectroscopic study, Phase Transitions* 18 (**1989**) 213–246. https://doi.org/10.1080/01411598908206864.
[72] F. Oliveira, Y. Leterrier, J. Månson, O. Sereda, A. Neels, A. Dommann, D. Damjanovic, *Process influences on the structure, piezoelectric, and gas-barrier properties of PVDF-TrFE copolymer*, J Polym Sci B Polym Phys 52 (**2014**) 496–506. https://doi.org/10.1002/polb.23443.
[73] X. Li, J. Pan, F. Macedonio, C. Ursino, M. Carraro, M. Bonchio, E. Drioli, A. Figoli, Z. Wang, Z. Cui, *Fluoropolymer Membranes for Membrane Distillation and Membrane Crystallization*, Polymers 14 (**2022**) 5439. https://doi.org/10.3390/polym14245439.
[74] A. Chatterjee, A. Das, K. Saha, U. Jeong, *Nanofiller-Induced Enhancement of PVDF Electroactivity for Improved Sensing Performance*, Advanced Sensor Research 2 (**2023**) 2200080. https://doi.org/10.1002/adsr.202200080.
[75] N. Chamankar, R. Khajavi, A.A. Yousefi, A. Rashidi, F. Golestanifard, *A flexible piezoelectric pressure sensor based on PVDF nanocomposite fibers doped with PZT particles for energy harvesting applications*, Ceramics International 46 (**2020**) 19669–19681. https://doi.org/10.1016/j.ceramint.2020.03.210.
[76] A. Tripathy, N.P. Maria Joseph Raj, B. Saravanakumar, S.-J. Kim, A. Ramadoss, *Tuning of highly piezoelectric bismuth ferrite/PVDF-copolymer flexible films for efficient energy harvesting performance*, Journal of Alloys and Compounds 932 (**2023**) 167569. https://doi.org/10.1016/j.jallcom.2022.167569.
[77] Y. Cho, J. Jeong, M. Choi, G. Baek, S. Park, H. Choi, S. Ahn, S. Cha, T. Kim, D.-S. Kang, J. Bae, J.-J. Park, *BaTiO3@PVDF-TrFE nanocomposites with efficient orientation prepared via phase separation nano-coating method for piezoelectric performance improvement and application to 3D-PENG*, Chemical Engineering Journal 427 (**2022**) 131030. https://doi.org/10.1016/j.cej.2021.131030.

[78] A. Sarhan, A. Hassan, M.I. Abdelhamid, T. Fahmy, A. *Habib, Investigation and optimization of the piezoelectric nanocomposite ZnO/PVVH/P(VDF-TrFE) for energy harvesting application*s, Sci Rep 15 (**2025**) 20246. https://doi.org/10.1038/s41598-025-04099-w.

[79] S. Stoyanova, E. Ivanov, L.R. Hegde, A. Georgopoulou, F. Clemens, F. Bedoui, R. Kotsilkova, P*VDF Hybrid Nanocomposites with Graphene and Carbon Nanotubes and Their Thermoresistive and Joule Heating Properties*, Nanomaterials 14 (**2024**) 901. https://doi.org/10.3390/nano14110901.

[80] S.K. Ghosh, T.K. Sinha, B. Mahanty, D. Mandal, *Self-poled Efficient Flexible "Ferroelectretic" Nanogenerator: A New Class of Piezoelectric Energy Harvester*, Energy Tech 3 (**2015**) 1190–1197. https://doi.org/10.1002/ente.201500167.

[81] V. Bystrov, E. Paramonova, X. Meng, H. Shen, J. Wang, T. Lin, V. Fridkin, *Ferroelectric Thin Films and Composites Based on Polyvinylidene Fluoride and Graphene Layers: Molecular Dynamics Study*, Coatings 14 (**2024**). https://doi.org/10.3390/coatings14030356.

[82] A. Tripathy, N.P. Maria Joseph Raj, B. Saravanakumar, S.-J. Kim, A. Ramadoss, *Tuning of highly piezoelectric bismuth ferrite/PVDF-copolymer flexible films for efficient energy harvesting performance*, Journal of Alloys and Compounds 932 (**2023**) 167569. https://doi.org/10.1016/j.jallcom.2022.167569.

[83] D. Bhadra, Md.G. Masud, S. Sarkar, J. Sannigrahi, S.K. De, B.K. Chaudhuri, S*ynthesis of PVDF/$BiFeO_3$ nanocomposite and observation of enhanced electrical conductivity and low-loss dielectric permittivity at percolation threshold*, J Polym Sci B Polym Phys 50 (**2012**) 572–579. https://doi.org/10.1002/polb.23041.

[84] S. Dash, R.N.P. Choudhary, M.N. Goswami, *Enhanced dielectric and ferroelectric properties of PVDF-BiFeO3 composites in 0–3 connectivity*, Journal of Alloys and Compounds 715 (**2017**) 29–36. https://doi.org/10.1016/j.jallcom.2017.04.310.

[85] M.S. Ravisankar, U.P.M. Rasi, *Study of local piezo and ferroelectric characteristics of PVDF + Bi25FeO40 composite nanodots using piezoforce microscopy*, J Mater Sci: Mater Electron 35 (**2024**) 312. https://doi.org/10.1007/s10854-024-12038-0.

[86] M. Fortunato, H.C. Bidsorkhi, C.R. Chandraiahgari, G. De Bellis, F. Sarto, M.S. Sarto, *PFM Characterization of PVDF Nanocomposite Films With Enhanced Piezoelectric Response*, IEEE Trans. Nanotechnology 17 (**2018**) 955–961. https://doi.org/10.1109/TNANO.2018.2833201.

[87] R. Sahoo, D. Duraisamy, N.P.M.J. Raj, A.N. Rao, S. Mohanty, G.N. Venkatesan, S.-J. Kim, A. Ramadoss, A*coustic sensor based on a PVDF-TrFE/BTO composite structure with improved ferroelectric and piezoelectric properties*, Surfaces and Interfaces 44 (**2024**) 103747. https://doi.org/10.1016/j.surfin.2023.103747.

[88] M.A. Signore, S.K. Padmanabhan, L. Velardi, A. Serra, M. Stoppa, L. Francioso, A. Licciulli, *Preparation and characterization of bacterial cellulose-ZnO piezoelectric nanocomposites studied using Piezoresponse Force Microscopy (PFM)*, Applied

Surface Science 692 (**2025**) 162734.
https://doi.org/10.1016/j.apsusc.2025.162734.
[89] G. Binnig, H. Rohrer, S*canning tunneling microscopy, Surface Science* 126 (**1983**) 236–244.
https://doi.org/10.1016/0039-6028(83)90716-1.
[90] J. Tersoff, D.R. Hamann, *Theory of the scanning tunneling microscope*, Phys. Rev. B 31 (**1985**) 805–813.
https://doi.org/10.1103/PhysRevB.31.805.
[91] G. Binnig, C.F. Quate, Ch. Gerber, *Atomic Force Microscope*, Phys. Rev. Lett. 56 (**1986**) 930–933.
https://doi.org/10.1103/PhysRevLett.56.930.
[92] K. Haase, A.E. Pelling, *Investigating cell mechanics with atomic force microscopy*, J. R. Soc. Interface. 12 (**2015**) 20140970.
https://doi.org/10.1098/rsif.2014.0970.
[93] D. Wang, T.P. Russell, *Advances in Atomic Force Microscopy for Probing Polymer Structure and Properties*, Macromolecules 51 (**2018**) 3–24.
https://doi.org/10.1021/acs.macromol.7b01459.
[94] E. Uhlmann, V. Mihotovic, A. Coenen, *Modelling the abrasive flow machining process on advanced ceramic materials*, Journal of Materials Processing Technology 209 (**2009**) 6062–6066.
https://doi.org/10.1016/j.jmatprotec.2009.06.019.
[95] A. Dazzi, C.B. Prater, AFM-IR: *Technology and Applications in Nanoscale Infrared Spectroscopy and Chemical Imaging*, Chem. Rev. 117 (**2017**) 5146–5173.
https://doi.org/10.1021/acs.chemrev.6b00448.
[96] R. Garcia, *Nanomechanical mapping of soft materials with the atomic force microscope: methods, theory and applications*, Chem. Soc. Rev. 49 (**2020**) 5850–5884.
https://doi.org/10.1039/D0CS00318B.
[97] D. Denning, J. Guyonnet, B.J. Rodriguez, *Applications of piezoresponse force microscopy in materials research: from inorganic ferroelectrics to biopiezoelectrics and beyond*, International Materials Reviews 61 (**2016**) 46–70.
https://doi.org/10.1179/1743280415Y.0000000013.
[98] J.J. Sáenz, N. García, P. Grütter, E. Meyer, H. Heinzelmann, R. Wiesendanger, L. Rosenthaler, H.R. Hidber, H.-J. Güntherodt, *Observation of magnetic forces by the atomic force microscope*, Journal of Applied Physics 62 (**1987**) 4293–4295.
https://doi.org/10.1063/1.339105.
[99] C. Shen, *Atomic Force Microscopy for Energy Research*, 1st ed., CRC Press, Boca Raton, **2022**.
https://doi.org/10.1201/9781003174042.
[100] G. Seychal, P. Nickmilder, V. Lemaur, C. Ocando, B. Grignard, P. Leclère, C. Detrembleur, R. Lazzaroni, H. Sardon, N. Aranburu, J.-M. Raquez, *A novel approach to design structural natural fiber composites from sustainable CO 2 - derived polyhydroxyurethane thermosets with outstanding properties and circular features*, Composites Part A: Applied Science and Manufacturing 185 (**2024**) 108311.
https://doi.org/10.1016/j.compositesa.2024.108311.

[101] L. Yang, P. Nickmilder, H. Verhoogt, T. Hoeks, P. Leclère, *Probing Viscoelastic Properties and Interfaces in High-Density Polyethylene Vitrimers at the Nanoscale Using Dynamic Mode Atomic Force Microscopy*, ACS Appl. Mater. Interfaces 16 (**2024**) 38501–38510. https://doi.org/10.1021/acsami.4c06809.
[102] D.G. Yablon, ed., *Scanning probe microscopy for industrial applications: nanomechanical characterization*, Wileys, Hoboken, New Jersey, **2014**.
[103] P. Nguyen-Tri, P. Ghassemin, P. Carriere, A.A. Assadi, D.D. Nguyen, *Recent Progressive Use of Advanced Atomic Force Microscopy in Polymer Science: A Review*, (**2020**). https://doi.org/10.20944/preprints202003.0082.v1.
[104] B. Cappella, G. Dietler, *Force-distance curves by atomic force microscopy*, Surface Science Reports 34 (**1999**) 1–104. https://doi.org/10.1016/S0167-5729(99)00003-5.
[105] D. Hussain, K. Ahmad, J. Song, H. Xie, A*dvances in the atomic force microscopy for critical dimension metrology*, Meas. Sci. Technol. 28 (**2017**) 012001. https://doi.org/10.1088/0957-0233/28/1/012001.
[106] V. Agmo Hernández, *An overview of surface forces and the DLVO theory*, ChemTexts 9 (**2023**) 10. https://doi.org/10.1007/s40828-023-00182-9.
[107] J. Ángyán, J. Dobson, G. Jansen, T. Gould, eds., *Introduction, in: London Dispersion Forces in Molecules, Solids and Nano-Structures: An Introduction to Physical Models and Computational Methods*, The Royal Society of Chemistry, **2020**. https://doi.org/10.1039/9781782623861-00001.
[108] J. Freund, J. Halbritter, J.K.H. Hörber, H*ow dry are dried samples? Water adsorption measured by STM*, Microscopy Research and Technique 44 (**1999**) 327–338. https://doi.org/10.1002/(SICI)1097-0029(19990301)44:5%3C327::AID-JEMT3%3E3.0.CO;2-E.
[109] P. Lambert, ed., Surface Tension in Microsystems: *Engineering Below the Capillary Length*, Springer Berlin Heidelberg, Berlin, Heidelberg, **2013**. https://doi.org/10.1007/978-3-642-37552-1.
[110] V. Agmo Hernández, *An overview of surface forces and the DLVO theory*, ChemTexts 9 (**2023**) 10. https://doi.org/10.1007/s40828-023-00182-9.
[111] S. Hong, J. Woo, H. Shin, J.U. Jeon, Y.E. Pak, E.L. Colla, N. Setter, E. Kim, K. No, *Principle of ferroelectric domain imaging using atomic force microscope*, Journal of Applied Physics 89 (**2001**) 1377–1386. https://doi.org/10.1063/1.1331654.
[112] S. Hong, H. Shin, J. Woo, K. No, *Effect of cantilever–sample interaction on piezoelectric force microscopy*, Applied Physics Letters 80 (**2002**) 1453–1455. https://doi.org/10.1063/1.1454219.
[113] S. Wang, C. Hao, *Principle and Application of Peak Force Tapping Mode Atomic Force Microscope*, in: B. J. Jansen, H. Liang, J. Ye (Eds.), International Conference on Cognitive Based Information Processing and Applications (CIPA 2021), Springer Singapore, Singapore, **2022**: pp. 671–679.

https://doi.org/10.1007/978-981-16-5854-9_86.
[114] S. Nahar, A. Schmets, G. Schitter, A. Scarpas, *Quantitative nanomechanical property mapping of bitumen micro-phases by peak-force Atomic Force Microscopy*, in: Asphalt Pavements, CRC Press, **2014**: pp. 1397–1406. https://doi.org/10.1201/b17219-169.
[115] Hertz, *On the Contact of Elastic Solids*, Crelle's Journal 92 (n.d.) 156–171.
[116] T.D.B. Jacobs, C. Mathew Mate, K.T. Turner, R.W. Carpick, *Understanding the Tip–Sample Contact: An Overview of Contact Mechanics from the Macro - to the Nanoscale, in: D.G. Yablon (Ed.), Scanning Probe Microscopy in Industrial Applications*, 1st ed., Wiley, **2013**: pp. 15–48. https://doi.org/10.1002/9781118723111.ch2.
[117] I.N. Sneddon, *The relation between load and penetration in the axisymmetric boussinesq problem for a punch of arbitrary profile*, International Journal of Engineering Science 3 (**1965**) 47–57. https://doi.org/10.1016/0020-7225(65)90019-4.
[118] P.D. Garcia, R. Garcia, *Determination of the Elastic Moduli of a Single Cell Cultured on a Rigid Support by Force Microscopy*, Biophysical Journal 114 (**201**8) 2923–2932. https://doi.org/10.1016/j.bpj.2018.05.012.
[119] B.V. Derjaguin, V.M. Muller, Y.P. Toporov, E*ffect of contact deformations on the adhesion of particles*, Journal of Colloid and Interface Science 53 (**1975**) 314–326. https://doi.org/10.1016/0021-9797(75)90018-1.
[120] K.L. Johnson, K. Kendall, A.D. Roberts, *Surface energy and the contact of elastic solids*, Proceedings of the Royal Society of London. A. Mathematical and Physical Sciences 324 (**1971**) 301–313. https://doi.org/10.1098/rspa.1971.0141.
[121] G. Haugstad, *Atomic force microscopy: exploring basic modes and advanced applications*, John Wiley & Sons, Hoboken, N.J, **2012**. https://doi.org/10.1002/9781118360668.
[122] D. Maugis, A*dhesion of spheres: The JKR-DMT transition using a dugdale model*, Journal of Colloid and Interface Science 150 (**1992**) 243–269. https://doi.org/10.1016/0021-9797(92)90285-T.
[123] K.L. Johnson, J.A. Greenwood, *An Adhesion Map for the Contact of Elastic Spheres*, Journal of Colloid and Interface Science 192 (**1997**) 326–333. https://doi.org/10.1006/jcis.1997.4984.
[124] G. Benstetter, A. Hofer, D. Liu, W. Frammelsberger, M. Lanza, *Fundamentals of CAFM Operation Modes, in: Conductive Atomic Force Microscopy*, John Wiley & Sons, Ltd, **2017**: pp. 45–77. https://doi.org/10.1002/9783527699773.ch3.
[125] M.P. Murrell, M.E. Welland, S.J. O'Shea, T.M.H. Wong, J.R. Barnes, A.W. McKinnon, M. Heyns, S. Verhaverbeke, *Spatially resolved electrical measurements of SiO2 gate oxides using atomic force microscopy*, Applied Physics Letters 62 (**1993**) 786–788. https://doi.org/10.1063/1.108579.
[126] C. Li, S. Minne, B. Pittenger, A. Mednick, *Simultaneous Electrical and Mechanical Property Mapping at the Nanoscale with PeakForce TUNA*, **2011**.

[127] W. Melitz, J. Shen, A.C. Kummel, S. Lee, K*elvin probe force microscopy and its application*, Surface Science Reports 66 (**2011**) 1–27. https://doi.org/10.1016/j.surfrep.2010.10.001.
[128] B. Ofuonye, J. Lee, M. Yan, C. Sun, J.-M. Zuo, I. Adesida, *Electrical and microstructural properties of thermally annealed Ni/Au and Ni/Pt/Au Schottky contacts on AlGaN/GaN heterostructures*, Semicond. Sci. Technol. 29 (**2014**) 095005. https://doi.org/10.1088/0268-1242/29/9/095005.
[129] G. Shao, *Work Function and Electron Affinity of Semiconductors: Doping Effect and Complication due to Fermi Level Pinning*, Energy & Environ Materials 4 (**2021**) 273–276. https://doi.org/10.1002/eem2.12218.
[130] B. Grévin, F. Husainy, D. Aldakov, C. Aumaître, *Dual-heterodyne Kelvin probe force microscopy*, Beilstein J. Nanotechnol. 14 (**2023**) 1068–1084. https://doi.org/10.3762/bjnano.14.88.
[131] N. Balke, P. Maksymovych, S. Jesse, A. Herklotz, A. Tselev, C.-B. Eom, I.I. Kravchenko, P. Yu, S.V. Kalinin, *Differentiating Ferroelectric and Nonferroelectric Electromechanical Effects with Scanning Probe Microscopy*, ACS Nano 9 (**2015**) 6484–6492. https://doi.org/10.1021/acsnano.5b02227.
[132] N. Balke, S. Jesse, P. Yu, Ben Carmichael, S.V. Kalinin, A. Tselev, *Quantification of surface displacements and electromechanical phenomena via dynamic atomic force microscopy*, Nanotechnology 27 (**2016**) 425707. https://doi.org/10.1088/0957-4484/27/42/425707.
[133] M.A. Signore, L. Francioso, C. De Pascali, A. Serra, D. Manno, G. Rescio, F. Quaranta, E. Melissano, L. Velardi, I*mprovement of the piezoelectric response of AlN thin films through the evaluation of the contact surface potential by piezoresponse force microscopy*, Vacuum 218 (**2023**) 112596. https://doi.org/10.1016/j.vacuum.2023.112596.
[134] Z. Huang, G. Leighton, *Interferometry for Piezoelectric Materials and Thin Films, in: M.G. Cain (Ed.), Characterisation of Ferroelectric Bulk Materials and Thin Films*, Springer Netherlands, Dordrecht, **2014:** pp. 87–113. https://doi.org/10.1007/978-1-4020-9311-1_5.
[135] Guillaume.F. Nataf, M. Guennou, G. Scalia, X. Moya, T.D. Wilkinson, J.P.F. Lagerwall, *High-contrast imaging of 180° ferroelectric domains by optical microscopy using ferroelectric liquid crystals*, Applied Physics Letters 116 (**2020**) 212901. https://doi.org/10.1063/5.0008845.
[136] P. Güthner, K. Dransfeld, *Local poling of ferroelectric polymers by scanning force microscopy*, Applied Physics Letters 61 (**1992**) 1137–1139. https://doi.org/10.1063/1.107693.
[137] E. Soergel, *Piezoresponse force microscopy (PFM)*, J. Phys. D: Appl. Phys. 44 (**2011**) 464003. https://doi.org/10.1088/0022-3727/44/46/464003.
[138] S. Jesse, A.P. Baddorf, S.V. Kalinin, *Switching spectroscopy piezoresponse force microscopy of ferroelectric materials*, Applied Physics Letters 88 (**2006**) 062908. https://doi.org/10.1063/1.2172216.

[139] O. Kwon, D. Seol, H. Qiao, Y. Kim, *Recent Progress in the Nanoscale Evaluation of Piezoelectric and Ferroelectric Properties via Scanning Probe Microscopy*, Advanced Science 7 (**2020**) 1901391. https://doi.org/10.1002/advs.201901391.
[140] S.M. Purushothaman, M.F. Tronco, B. Kottathodi, I. Royaud, M. Ponçot, N. Kalarikkal, S. Thomas, D. Rouxel, *A review on electrospun PVDF-based nanocomposites: Recent trends and developments in energy harvesting and sensing applications*, Polymer 283 (**2023**) 126179. https://doi.org/10.1016/j.polymer.2023.126179.
[141] A. Gruverman, B.J. Rodriguez, S.V. Kalinin, *Electromechanical Behavior in Biological Systems at the Nanoscale*, in: S. Kalinin, A. Gruverman (Eds.), Scanning Probe Microscopy, Springer New York, New York, NY, **2007**: pp. 615–633. https://doi.org/10.1007/978-0-387-28668-6_23.
[142] S. Magonov, *Piezoresponse Force Microscopy in Its Applications*, **2013**. https://api.semanticscholar.org/CorpusID:53462372.
[143] U. Rabe, S. Amelio, M. Kopycinska, S. Hirsekorn, M. Kempf, M. Göken, W. Arnold, *Imaging and measurement of local mechanical material properties by atomic force acoustic microscopy*, Surface & Interface Analysis 33 (**2002**) 65–70. https://doi.org/10.1002/sia.1163.
[144] F. Mege, *AFM à contact résonant : développement et modélisation*, Theses, Université de Grenoble, **2011**. https://theses.hal.science/tel-00618676.
[145] G. Stan, S. Krylyuk, A.V. Davydov, M.D. Vaudin, L.A. Bendersky, R.F. Cook, *Contact-resonance atomic force microscopy for nanoscale elastic property measurements: Spectroscopy and imaging*, Ultramicroscopy 109 (**2009**) 929–936. https://doi.org/10.1016/j.ultramic.2009.03.025.
[146] B.J. Rodriguez, C. Callahan, S.V. Kalinin, R. Proksch, *Dual-frequency resonance-tracking atomic force microscopy*, Nanotechnology 18 (**2007**) 475504. https://doi.org/10.1088/0957-4484/18/47/475504.
[147] A. Cui, P.D. Wolf, Y. Ye, Z. Hu, A. Dujardin, Z. Huang, K. Jiang, L. Shang, M. Ye, H. Sun, J. Chu, *Probing electromechanical behaviors by datacube piezoresponse force microscopy in ambient and aqueous environments*, Nanotechnology 30 (**2019**) 235701. https://doi.org/10.1088/1361-6528/ab0866.
[148] B. Pittenger, *Characterizing Ferroelectric Materials with SS-PFM and DCUBE PFM*, **2023**. https://doi.org/10.13140/RG.2.2.19958.88648.
[149] D. Seol, B. Kim, Y. Kim, *Non-piezoelectric effects in piezoresponse force microscopy*, Current Applied Physics 17 (**2017**) 661–674. https://doi.org/10.1016/j.cap.2016.12.012.
[150] L. Collins, Y. Liu, O.S. Ovchinnikova, R. Proksch, *Quantitative Electromechanical Atomic Force Microscopy*, ACS Nano 13 (**2019**) 8055–8066. https://doi.org/10.1021/acsnano.9b02883.
[151] A. Gomez, T. Puig, X. Obradors, *Diminish electrostatic in piezoresponse force microscopy through longer or ultra-stiff tips*, Applied Surface Science 439 (**2018**) 577–582. https://doi.org/10.1016/j.apsusc.2018.01.080.

[152] J.P. Killgore, L. Robins, L. Collins, *Electrostatically-blind quantitative piezoresponse force microscopy free of distributed-force artifacts*, Nanoscale Adv. 4 (**2022**) 2036–2045. https://doi.org/10.1039/D2NA00046F.
[153] Q.N. Chen, Y. Ou, F. Ma, J. Li, *Mechanisms of electromechanical coupling in strain based scanning probe microscopy*, Applied Physics Letters 104 (**2014**) 242907. https://doi.org/10.1063/1.4884422.
[154] S. Badur, D. Renz, M. Cronau, T. Göddenhenrich, D. Dietzel, B. Roling, A. Schirmeisen, *Characterization of Vegard strain related to exceptionally fast Cu-chemical diffusion in Cu2Mo6S8 by an advanced electrochemical strain microscopy method*, Scientific Reports 11 (**2021**) 18133. https://doi.org/10.1038/s41598-021-96602-2.
[155] N. Balke, S. Jesse, A.N. Morozovska, E. Eliseev, D.W. Chung, Y. Kim, L. Adamczyk, R.E. García, N. Dudney, S.V. Kalinin, *Nanoscale mapping of ion diffusion in a lithium-ion battery cathode*, Nature Nanotechnology 5 (**2010**) 749–754. https://doi.org/10.1038/nnano.2010.174.
[156] Q.N. Chen, Y. Ou, F. Ma, J. Li, *Mechanisms of electromechanical coupling in strain based scanning probe microscopy*, Appl. Phys. Lett. (**2014**).
[157] J. Yu, E.N. Esfahani, Q. Zhu, D. Shan, T. Jia, S. Xie, J. Li, Quadratic electromechanical strain in silicon investigated by scanning probe microscopy, Journal of Applied Physics 123 (**2018**) 155104. https://doi.org/10.1063/1.5023407.
[158] Y. Kim, A. Kumar, A. Tselev, I.I. Kravchenko, H. Han, I. Vrejoiu, W. Lee, D. Hesse, M. Alexe, S.V. Kalinin, S. Jesse, *Nonlinear Phenomena in Multiferroic Nanocapacitors: Joule Heating and Electromechanical Effects*, ACS Nano 5 (**2011**) 9104–9112. https://doi.org/10.1021/nn203342v.
[159] A. Abdollahi, N. Domingo, I. Arias, G. Catalan, *Converse flexoelectricity yields large piezoresponse force microscopy signals in non-piezoelectric materials*, Nat Commun 10 **(2019**) 1266. https://doi.org/10.1038/s41467-019-09266-y.
[160] D. Lee, A. Yoon, S.Y. Jang, J.-G. Yoon, J.-S. Chung, M. Kim, J.F. Scott, T.W. Noh, *Giant Flexoelectric Effect in Ferroelectric Epitaxial Thin Films*, Phys. Rev. Lett. 107 (**2011**) 057602. https://doi.org/10.1103/PhysRevLett.107.057602.
[161] R.K. Vasudevan, N. Balke, P. Maksymovych, S. Jesse, S.V. Kalinin, *Ferroelectric or non-ferroelectric: Why so many materials exhibit "ferroelectricity" on the nanoscale*, Applied Physics Reviews 4 (**2017**) 021302. https://doi.org/10.1063/1.4979015.
[162] D. Seol, B. Kim, Y. Kim, N*on-piezoelectric effects in piezoresponse force microscopy*, Current Applied Physics 17 (**2017**) 661–674. https://doi.org/10.1016/j.cap.2016.12.012.
[163] N. Balke, P. Maksymovych, S. Jesse, I.I. Kravchenko, Q. Li, S.V. Kalinin, *Exploring Local Electrostatic Effects with Scanning Probe Microscopy: Implications for Piezoresponse Force Microscopy and Triboelectricity*, ACS Nano 8 (**2014**) 10229–10236. https://doi.org/10.1021/nn505176a.

[164] H. Miranda, E. de Obaldía, E. Ching-Prado, *Synthesis and Characterization of Polycrystalline Bifeo3 Deposited by Sol-Gel Technique*, in: 2022 8th International Engineering, Sciences and Technology Conference (IESTEC), **2022**: pp. 802–809. https://doi.org/10.1109/IESTEC54539.2022.00131.
[165] A. Khorsand Zak, A.M. Hashim, *Synthesis strategies for BFO nanostructures: A comprehensive review on techniques, challenges, and future perspectives*, Inorganic Chemistry Communications 177 (**2025**) 114337. https://doi.org/10.1016/j.inoche.2025.114337.
[166] S.M.H. Shah, S. Riaz, A. Akbar, S. Atiq, S. Naseem, E*ffect of Solvents on the Ferromagnetic Behavior of Undoped $BiFeO_3$ Prepared by Sol-Gel*, IEEE Trans. Magn. 50 (**2014**) 1–4. https://doi.org/10.1109/TMAG.2014.2309720.
[167] D. Bhadra, Md.G. Masud, S. Sarkar, J. Sannigrahi, S.K. De, B.K. Chaudhuri, *Synthesis of PVDF/$BiFeO_3$ nanocomposite and observation of enhanced electrical conductivity and low-loss dielectric permittivity at percolation threshold*, J Polym Sci B Polym Phys 50 (**2012**) 572–579. https://doi.org/10.1002/polb.23041.
[168] J.K. Kim, S.S. Kim, W.-J. Kim, S*ol–gel synthesis and properties of multiferroic BiFeO3*, Materials Letters 59 (**2005**) 4006–4009. https://doi.org/10.1016/j.matlet.2005.07.050.
[169] S.J.J. Kay, N. Chidhambaram, A. Thirumurugan, S. Shanavas, P. Sakthivel, R.S. Rimal Isaac, *Stoichiometric balancing of bismuth ferrite-perovskite nanoparticles: comparative investigations on biogenic versus conventional chemical synthesis*, J Mater Sci: Mater Electron 34 (**2023**) 2034. https://doi.org/10.1007/s10854-023-11486-4.
[170] V.F. Cardoso, G. Minas, S. Lanceros-Méndez, *Multilayer spin-coating deposition of poly(vinylidene fluoride) films for controlling thickness and piezoelectric response*, Sensors and Actuators A: Physical 192 (**2013**) 76–80. https://doi.org/10.1016/j.sna.2012.12.019.
[171] M. Fakhry, O. Soppera, D. Berling, *Innovative Elaboration of Polyvinylidene Fluoride Thin Films via Dip-Coating: Beta Phase Optimization, Humidity Control, Nanoparticles Addition, and Topographic Analysis*, Micro 5 (**2025**) 12. https://doi.org/10.3390/micro5010012.
[172] A. Salimi, A.A. Yousefi, *Conformational changes and phase transformation mechanisms in PVDF solution-cast films*, J Polym Sci B Polym Phys 42 (**2004**) 3487–3495. https://doi.org/10.1002/polb.20223.
[173] S. Bodkhe, P.S.M. Rajesh, F.P. Gosselin, D. Therriault, *Simultaneous 3D Printing and Poling of PVDF and Its Nanocomposites*, ACS Appl. Energy Mater. 1 (**2018**) 2474–2482. https://doi.org/10.1021/acsaem.7b00337.
[174] S. Apelt, S. Höhne, E. Mehner, C. Böhm, M. Malanin, K. Eichhorn, D. Jehnichen, P. Uhlmann, U. Bergmann, *Poly(vinylidene fluoride-co-trifluoroethylene) Thin Films after Dip- and Spin-Coating*, Macro Materials & Eng 307 (**2022**) 2200296. https://doi.org/10.1002/mame.202200296.
[175] A.K. Muraleedharan, K. Co, M. Vallet, A. Zaki, F. Karolak, C. Bogicevic, K. Perronet, B. Dkhil, C. Paillard, C. Fiorini-Debuisschert, F. Treussart, *Ferroelectric Texture of*

Individual Barium Titanate Nanocrystals, ACS Nano 18 (**202**4) 18355–18367. https://doi.org/10.1021/acsnano.4c02291.
[176] A. Arrigoni, L. Brambilla, C. Bertarelli, G. Serra, M. Tommasini, C. Castiglioni, *P(VDF-TrFE) nanofibers: structure of the ferroelectric and paraelectric phases through IR and Raman spectroscopies*, RSC Adv. 10 (**2020**) 37779–37796. https://doi.org/10.1039/D0RA05478J.
[177] J. Seo, J.Y. Son, W.-H. Kim, *Structural and ferroelectric properties of P(VDF-TrFE) thin films depending on the annealing temperature*, Materials Letters 238 (**2019**) 294–297. https://doi.org/10.1016/j.matlet.2018.11.156.
[178] M. Krutko, H.M. Poling, M. Sheth, S. Kongsomros, A.E. Bryan, M. Sharma, A. Singh, H.A. Reza, K.A. Wikenheiser-Brokamp, T. Takebe, M.A. Helmrath, G.M. Harris, L. Esfandiari, *Thermal Annealing Enhances Piezoelectricity and Regenerative Potential of PVDF-TrFE Nanofiber Scaffolds*, Adv Materials Technologies 10 (**2025**) e01513. https://doi.org/10.1002/admt.202401513.
[179] J.L. Carter, C.A. Kelly, M.J. Jenkins, *Processing optimization of PEDOT:PSS and PEDOT:PSS/Tween 80 films*, Polym J 55 (**2023**) 253–260. https://doi.org/10.1038/s41428-022-00740-x.
[180] S. Jena, N.K. Sahoo, *Evolutionary Design, Deposition and Characterization Techniques for Interference Optical Thin-Film Multilayer Coatings and Devices*, in: S. Kumar, D.K. Aswal (Eds.), Recent Advances in Thin Films, Springer Singapore, Singapore, **2020**: pp. 281–343. https://doi.org/10.1007/978-981-15-6116-0_10.
[181] J.A. Chávez, J. Landaverde, R.L. Landaverde, V. Tejnecký, *Monitoring and behavior of unsaturated volcanic pyroclastic in the Metropolitan Area of San Salvador*, El Salvador, SpringerPlus 5 (**2016**) 536. https://doi.org/10.1186/s40064-016-2149-x.
[182] T.Q. Tran, F. Zuttion, V. Valero, S. Taupin, R. Salva, J. Portal, G.S. Luengo, P. Leclère, *Acrylic Films in Cosmetics: Decoding the Structural Mechanism of a High-Performing Skin Coating*, ACS Appl. Mater. Interfaces 17 (**2025**) 59873–59883. https://doi.org/10.1021/acsami.5c13170.
[183] I. Drewek, A. Pietka, T.Q. Tran, M. Blazhynska, A. Jeništova, C. Chipot, A. Barth, M. Surin, P. Leclère, R. Wattiez, R.N. Muller, D. Stanicki, S. Laurent, M*olecular self-assembly mediates the flocculation activity of benzimidazole derivatives against E. coli*, Sci Rep 15 (**2025**) 28600. https://doi.org/10.1038/s41598-025-13837-z.
[184] H. Valloire, P. Quéméré, N. Vaxelaire, H. Kuentz, G. Le Rhun, Ł. Borowik, *Enhancing ferroelectric characterization at nanoscale: A comprehensive approach for data processing in spectroscopic piezoresponse force microscopy*, Journal of Applied Physics 135 (**2024**) 194101. https://doi.org/10.1063/5.0197226.
[185] S.M. Neumayer, S. Saremi, L.W. Martin, L. Collins, A. Tselev, S. Jesse, S.V. Kalinin, N. Balke, *Piezoresponse amplitude and phase quantified for electromechanical characterization*, Journal of Applied Physics 128 (**2020**) 171105. https://doi.org/10.1063/5.0011631.

[186] K. El Hami, H. Yamada, K. Matsushige, *Nanoscopic measurements of the electrostriction responses in P(VDF/TrFE) ultra-thin-film copolymer using atomic force microscopy*:, Appl Phys A 72 (**2001**) 347–350. https://doi.org/10.1007/s003390000702.
[187] D. Disnan, F. Bacher, S. Berger, M. Schneider, U. Schmid, M*icrostructural influence on thermal stability of ferroelectric properties in P(VDF-TrFE) spin cast thin films*, Polymer 298 (**2024**) 126894. https://doi.org/10.1016/j.polymer.2024.126894.
[188] P. Poncet, F. Casset, A. Latour, F. Domingues Dos Santos, S. Pawlak, R. Gwoziecki, A. Devos, P. Emery, S. Fanget, *Static and Dynamic Studies of Electro-Active Polymer Actuators and Integration in a Demonstrator*, Actuators 6 (**2017**) 18. https://doi.org/10.3390/act6020018.
[189] A.S. Borowiak, N. Baboux, D. Albertini, B. Vilquin, G. Saint Girons, S. Pelloquin, B. Gautier, *Electromechanical response of amorphous LaAlO3 thin film probed by scanning probe microscopies*, Applied Physics Letters 105 (**2014**) 012906. https://doi.org/10.1063/1.4889853.
[190] J. Seo, J.Y. Son, W.-H. Kim, *Structural and ferroelectric properties of P(VDF-TrFE) thin films depending on the annealing temperature*, Materials Letters 238 (**2019**) 294–297. https://doi.org/10.1016/j.matlet.2018.11.156.
[191] W.J. Hu, D.-M. Juo, L. You, J. Wang, Y.-C. Chen, Y.-H. Chu, T. Wu, *Universal Ferroelectric Switching Dynamics of Vinylidene Fluoride-trifluoroethylene Copolymer Films*, Sci Rep 4 (**2014**) 4772. https://doi.org/10.1038/srep04772.
[192] P. Sharma, D. Wu, S. Poddar, T.J. Reece, S. Ducharme, A. Gruverman, *Orientational imaging in polar polymers by piezoresponse force microscopy*, Journal of Applied Physics 110 (**2011**) 052010. https://doi.org/10.1063/1.3623765.
[193] S. Gonzalez Casal, X. Bai, K. Alhada-Lahbabi, B. Canut, B. Vilquin, P. Rojo Romeo, S. Brottet, D. Albertini, D. Deleruyelle, M. Bugnet, I. Canero Infante, B. Gautier, *Mechanical Switching of Ferroelectric Domains in 33-200 nm-Thick Sol-Gel-Grown $PbZr_{0.2}Ti_{0.8}O_3$ Films Assisted by Nanocavities*, Adv Elect Materials 8 (**2022**) 2200077. https://doi.org/10.1002/aelm.202200077.
[194] Mohd. Amaan, H. Vardhan, M. Saini, Km. Komal, B. Singh, *Effect of Thickness and Doping on Energy Harvesting Performance of PVDF-Based Nanogenerator*, in: M. Kumar, A.K. Singh, S. Sharma, D. Kumar (Eds.), Recent Advances in Functional Materials, Volume 2, Springer Nature Singapore, Singapore, **2025**: pp. 349–357.
[195] D. Carranza-Celis, A. Cardona-Rodríguez, J. Narváez, O. Moscoso-Londono, D. Muraca, M. Knobel, N. Ornelas-Soto, A. Reiber, J.G. Ramírez, *Control of Multiferroic properties in BiFeO3 nanoparticles*, Sci Rep 9 (**2019**) 3182. https://doi.org/10.1038/s41598-019-39517-3.
[196] G. Tian, D. Chen, H. Fan, P. Li, Z. Fan, M. Qin, M. Zeng, J. Dai, X. Gao, J.-M. Liu, *Observation of Exotic Domain Structures in Ferroelectric Nanodot Arrays Fabricated via a Universal Nanopatterning Approach*, ACS Appl. Mater. Interfaces 9 (**2017**) 37219–37226. https://doi.org/10.1021/acsami.7b12605.

[197] G. Tian, D. Chen, J. Yao, Q. Luo, Z. Fan, M. Zeng, Z. Zhang, J. Dai, X. Gao, J.-M. Liu, *$BiFeO_3$ nanorings synthesized via AAO template-assisted pulsed laser deposition and ion beam etching*, RSC Adv. 7 (*2017*) 41210–41216. https://doi.org/10.1039/C7RA07677K.
[198] K. Feng, X. Liu, D. Si, X. Tang, A. Xing, M. Osada, P. Xiao*, Ferroelectric BaTiO 3 dipole induced charge transfer enhancement in dye-sensitized solar cells*, Journal of Power Sources 350 (**2017**) 35–40. https://doi.org/10.1016/j.jpowsour.2017.03.049.
[199] S. Jesse, B.J. Rodriguez, S. Choudhury, A.P. Baddorf, I. Vrejoiu, D. Hesse, M. Alexe, E.A. Eliseev, A.N. Morozovska, J. Zhang, L.-Q. Chen, S.V. Kalinin, *Direct imaging of the spatial and energy distribution of nucleation centres in ferroelectric materials*, Nature Mater 7 (**2008**) 209–215. https://doi.org/10.1038/nmat2114.
[200] V.D. Tran, H.-C. Truong, T.V. Nguyen, P. Leclère, T.-T. Duong, T.H. Bui, V.Q. Nguyen, *Piezoelectric responses of PVDF-KBT electrospun nanocomposite fibres via nanoscale mapping*, Ceramics International 49 (**2023**) 38288–38296. https://doi.org/10.1016/j.ceramint.2023.09.161.
[201] A. Baji, Y.-W. Mai, Q. Li, Y. Liu, *Nanoscale investigation of ferroelectric properties in electrospun barium titanate/polyvinylidene fluoride composite fibers using piezoresponse force microscopy*, Composites Science and Technology 71 (**2011**) 1435–1440. https://doi.org/10.1016/j.compscitech.2011.05.017.
[202] L. Mégane, Synthèse, *caractérisations structurales et propriétés de matériaux diélectriques A2WO6 (A = lanthanide, Bi) sous forme massive et en couches minces pour la récupération d'énergie*, n.d.
[203] T. Carlier, M.-H. Chambrier, A. Da Costa, F. Blanchard, T. Denneulin, M. Létiche, P. Roussel, R. Desfeux, A. Ferri, *Ferroelectric State in an α-Nd_2 WO_6 Polymorph Stabilized in a Thin Film*, Chem. Mater. 32 (**2020**) 7188–7200. https://doi.org/10.1021/acs.chemmater.0c01405.
[204] M. Lheureux, M.-H. Chambrier, K.D. Francesca, B. Vargas, L. Yedra, A. Da Costa, T. Carlier, F. Blanchard, S. Estradé, F. Peiro, P. Roussel, J.-F. Blach, A. Ferri, R. Desfeux, *Thin-Film Stabilization of a Ferroelectric Orthorhombic α-Pr2WO6 Polymorph*, ACS Appl. Electron. Mater. 4 (**2022**) 5234–5245. https://doi.org/10.1021/acsaelm.2c00913.
[205] J. Zhang, J. Zhang, Y. Qi, S. Gong, H. Xu, Z. Liu, R. Zhang, M.A. Sadi, D. Sychev, R. Zhao, H. Yang, Z. Wu, D. Cui, L. Wang, C. Ma, X. Wu, J. Gao, Y.P. Chen, X. Wang, Y. Jiang, *Room-temperature ferroelectric, piezoelectric and resistive switching behaviors of single-element Te nanowires*, Nat Commun 15 (**2024**) 7648. https://doi.org/10.1038/s41467-024-52062-6.
[206] D. Viehland, J.F. Li, Y. Yang, T. Costanzo, A. Yourdkhani, G. Caruntu, P. Zhou, T. Zhang, T. Li, A. Gupta, M. Popov, G. Srinivasan, *Tutorial: Product properties in multiferroic nanocomposites*, Journal of Applied Physics 124 (**2018**) 061101. https://doi.org/10.1063/1.5038726.
[207] J. Park, M.H. Lee, D.J. Kim, M.-H. Kim, W.-J. Kim, D. Do, J.H. Jeon, B.H. Park, T.K. Song*, High piezoelectric performance of lead-free $BiFeO_3$ –$BaTiO_3$ thin films grown by a pulsed laser deposition method*, RSC Adv. 6 (**2016**) 106899–106903. https://doi.org/10.1039/C6RA22271D.

[208] X. Liu, X. Kuang, S. Xu, X. Wang, *High-sensitivity piezoresponse force microscopy studies of single polyvinylidene fluoride nanofibers*, Materials Letters 191 (**2017**) 189–192. https://doi.org/10.1016/j.matlet.2016.12.066.
[209] H. Zhu, Y. Yang, W. Ren, M. Niu, W. Hu, H. Ma, J. Ouyang, *Rhombohedral BiFeO3 thick films integrated on Si with a giant electric polarization and prominent piezoelectricity*, Acta Materialia 200 (**2020**) 305–314. https://doi.org/10.1016/j.actamat.2020.09.022.
[210] S. Wu, J. Zhang, X. Liu, S. Lv, R. Gao, W. Cai, F. Wang, C. Fu, Micro-Area F*erroelectric, Piezoelectric and Conductive Properties of Single BiFeO3 Nanowire by Scanning Probe Microscopy*, Nanomaterials 9 (**2019**) 190. https://doi.org/10.3390/nano9020190.
[211] H.H. Singh, N. Khare, *Improved performance of ferroelectric nanocomposite flexible film based triboelectric nanogenerator by controlling surface morphology, polarizability, and hydrophobicity*, Energy 178 (**2019**) 765–771. https://doi.org/10.1016/j.energy.2019.04.150.
[212] D. Cavallini, M. Fortunato, G.D. Bellis, M.S. Sarto, *PFM Characterization of Piezoelectric PVDF/ZnONanorod thin films*, in: 2018 IEEE 18th International Conference on Nanotechnology (IEEE-NANO), IEEE, Cork, Ireland, **2018**: pp. 1–3. https://doi.org/10.1109/NANO.2018.8626362.
[213] *Piezoelectric Materials | P(VDF-TRFE)* | Arkema Piezotech, (n.d.). https://piezotech.arkema.com/en/Products/piezoelectric-copolymers/ (accessed **December 7, 2025**).
[214] S. Shanthy, S.K. Singh, *MULTIFERROIC $BiFeO_3$ FILMS: CANDIDATE FOR ROOM TEMPERATURE MICRO BIOSENSOR*, Integrated Ferroelectrics 99 (**2008**) 77–85. https://doi.org/10.1080/10584580802107726.
[215] J. Wang, H. Zheng, Z. Ma, S. Prasertchoung, M. Wuttig, R. Droopad, J. Yu, K. Eisenbeiser, R. Ramesh, *Epitaxial BiFeO3 thin films on Si*, Applied Physics Letters 85 (**2004**) 2574–2576. https://doi.org/10.1063/1.1799234.
[216] M. Graf, M. Sepliarsky, R. Machado, M.G. Stachiotti, *Dielectric and piezoelectric properties of BiFeO3 from molecular dynamics simulations*, Solid State Communications 218 (**2015**) 10–13. https://doi.org/10.1016/j.ssc.2015.06.002.